

LOW RESISTIVITY PAY; THE ROLE OF CHLORITE IN CONTROLLING RESISTIVITY RESPONSES

Joanne Tudge

Petrophysics traditionally uses Archie's equation to estimate the amount of hydrocarbons initially in place. This relies on the increase in resistivity when non-conductive hydrocarbons replace conductive saline fluids in the pore space. However, if clay minerals are present in sufficient abundance, they can lower the resistivity to such an extent as to compensate for the increase in resistivity caused by the presence of hydrocarbons.

The study reservoir (A), of the Berkine Basin, Algeria, is an example of this "low resistivity contrast". No discernable change in the resistivity between the water-bearing and the hydrocarbon-bearing sections of the sandstone reservoir results in a continuous overestimation of the water saturation.

Chlorite is a known cause of "low resistivity contrast" and is prevalent throughout the study reservoir sandstones. The low cation exchange capacity of chlorites means known shaly-sand models do not apply. Therefore it is necessary to develop an alternative method for estimating saturation in the study reservoir.

To understand where the resistivity may be most affected the distribution of the chlorite within the reservoir must be determined. Detailed analysis of the sedimentary data identified a link between the chlorite-rich sandstones and the upper shoreface depositional environment.

Discriminant statistical analysis of the log data was successful in identifying the upper shoreface, chloritic sandstones from the lower shoreface sandstones and offshore mudstones. This provided a classification scheme to identify the chlorite-rich intervals from log data in uncored wells.

Analysis of capillary pressure curves, with respect to the depositional environments, identified a strong correlation between the chlorite occurrence and core-based petrophysical characteristics. This allowed for Leverett-J saturation height functions to be developed for the upper shoreface, chlorite-rich sandstones and lower shoreface sandstones. Transformation of these Leverett-J functions to the wireline log scale allowed saturation estimations to be calculated that account for the chlorite presence and don't require the resistivity measurement.

ACKNOWLEDGEMENTS

Initially my thanks must go to my supervisors at the University of Leicester; Prof Mike Lovell and Dr Sarah Davies for their guidance and support. Acknowledgements go to ConocoPhillips (previously Burlington Resources) for providing the data and remit for the project as well as funding, as well as the London Petrophysical Society (LPS) for their funding contributions, and continuing scientific support. My thanks go in particular to Mike Millar, my appointed LPS supervisor, for his many contributions and support. Also to Iain McNeill who thought up the original project remit and, along with Mike Lovell, made the whole project possible.

In addition I acknowledge and thank Prof Peter Harvey for answering never-ending questions about statistical analysis, and also Dr Richard England for general science discussion and all-round support. I must thank my fellow postgraduates, particularly Peter Fitch and Andrew Shore for light relief, coffee breaks and general support through the last 4 years. And finally I must thank my family, who without their support and understanding I would not have been able to do this.

Contents

Acknowledgements

1. Introduction	1
<i>1.1 Background.....</i>	<i>1</i>
<i>1.2 Aims and Objectives of the Thesis.....</i>	<i>3</i>
<i>1.3 Thesis Structure.....</i>	<i>4</i>
2. Review – Measurements.....	6
<i>2.1 Wireline Log Data.....</i>	<i>6</i>
2.1.1 Gamma Ray Measurements.....	10
2.1.2 Density Measurement.....	14
2.1.3 Neutron Porosity Measurement.....	17
2.1.4 Resistivity Measurement.....	19
2.1.5 Acoustic (Sonic) Measurement.....	23
<i>2.2 Core-Data Measurements.....</i>	<i>24</i>
2.2.1 Core-derived Archie Parameters.....	25
2.2.2 Capillary Pressure Curves.....	31
2.2.3 Saturation Height Derivation.....	36
2.2.4 Porosity Distributions.....	38
2.2.5 Polished Thin Section Analysis.....	39
2.2.6 SEM Analysis.....	40
2.2.7 X-ray Diffraction Analysis.....	41
3. Review – Chlorite	43
<i>3.1 Introduction.....</i>	<i>43</i>
<i>3.2 Background.....</i>	<i>43</i>

3.2.1	Chemical Composition.....	44
3.2.2	Cation-Exchange-Capacity.....	46
3.3	<i>Formation</i>	47
3.3.1	Alteration of Kaolinite.....	50
3.3.2	Alteration from Berthierine.....	51
3.3.4	Direct precipitation from pore waters.....	52
3.4	<i>Effect on Reservoir Quality</i>	52
3.5	<i>Summary</i>	55
4.	Geological Setting/Sedimentology	57
4.1	<i>Regional Setting</i>	57
4.1.1	Geological History of the Ghadames Basin.....	59
4.1.2	Field-scale Geological Background.....	62
4.2	<i>Sedimentary Facies</i>	63
4.3	<i>Sedimentary Core-Data Measurements</i>	71
4.3.1	Polished Thin Section Analysis	73
4.3.2	SEM Analysis.....	77
4.3.3	XRD Analysis.....	83
4.3.4	Facies Discussion.....	85
4.4	<i>Porosity Distributions</i>	87
4.5	<i>Conclusions</i>	91
5.	Wireline Log Analysis	92
5.1	<i>Initial/Standard Log Analysis</i>	93
5.1.1	Data Quality.....	93
5.1.2	Log-based Lithology Analysis.....	97
5.1.3	Thomas-Stieber Analysis.....	124

5.2	<i>Log-analysis Relationship to Chlorite Occurrence</i>	127
5.3	<i>Log-analysis Relationship to Sedimentary Facies</i>	132
5.3.1	Density – Neutron cross-plot for Facies.....	132
5.3.2	Gamma-ray – Sonic cross-plot relationship to facies.....	134
5.4	<i>Statistical Analysis</i>	135
5.4.1	Iterative Non-hierarchical Cluster Analysis.....	139
5.4.2	Discriminant Analysis.....	145
5.5	<i>Conclusions</i>	151
6.	Petrophysical Interpretation	155
6.1	<i>Introduction</i>	155
6.2	<i>Petrophysical Core Data</i>	155
6.2.1	Archie Petrophysical Parameters.....	156
6.2.2	Saturation exponents (n).....	159
6.2.3	Clay-corrected Parameters.....	161
6.2.4	Core Sw Values and $S_{w_{irr}}$ analysis.....	163
6.3	<i>Petrophysical Log Data</i>	166
6.3.1	Porosity Calculations.....	166
6.3.2	Pickett Plots.....	173
6.3.3	Permeability.....	175
6.4	<i>Log-derived Saturation Estimation</i>	178
6.4.1	Archie-derived Saturation Calculation.....	178
6.4.2	Waxman-Smits Saturation Calculation.....	179
6.4.3	Juhász (Waxman-Smits) Saturation Calculation.....	182
6.4.4	Log-derived Water Saturation Estimates Comparison.....	183
6.5	<i>Saturation Height Functions</i>	185

6.5.1 Work-flow for Sw-height Analysis.....	186
6.5.2 Composite J-function derived Sw profile.....	191
6.6 Comparison of Saturation Results.....	196
6.7 Conclusions.....	197
7. Conclusions.....	199

Appendices

Appendix I – Glossary.....	i
Appendix II – Facies.....	iv
Appendix III – Resistivity Index.....	xxxix
Appendix IV – Capillary Pressure Curves.....	xlvi
Appendix V – Oil Density Calculations.....	lvi
Appendix VI – Bibliography.....	lix

1. Introduction

1.1 Background

Estimation of the quantity of hydrocarbons within a reservoir is crucial in the exploration and production of oil and gas reserves. This calculation is based on the (stock tank) oil initially in place equation (STOIIP), or its equivalent for gas, and depends on knowing the gross rock volume, the proportion of rock that is reservoir quality, the porosity and water saturation, and a formation volume factor (Tiab and Donaldson, 1996). Of these, two petrophysical parameters, the porosity and the water saturation can be estimated from core and downhole log data. A third petrophysical parameter, the permeability, is not included in this static equation, but defines the fluid flow potential of the reservoir and is essential in appraising the production characteristics; it is also used with the porosity when defining the quality of the reservoir. The porosity is simply the proportion of space within a rock which can be filled with fluids, for example water or hydrocarbons. The permeability is the ease with which fluids flow, primarily through the interconnected pores (Serra and Serra, 2003; Tiab and Donaldson, 1996) unless the formation is fractured. The water saturation (S_w) relates to the hydrocarbon saturation ($1 - S_w$).

Multiple factors can affect the porosity and permeability of a reservoir, which in turn affect the volume of producible hydrocarbons. Siliclastic rocks, composed of sandstones and mudstones, are common hydrocarbon reservoirs, with the sandstones within the sequences acting as the reservoirs and the mudstones as seals due to their very low permeability. The porosity and permeability are affected by grain size and shape, the presence of clay grains in the rock, degree of cementation and fractures (Tiab and Donaldson, 1996). The latter, where the fractures are open, is the only one which can increase the porosity and permeability.

Water saturation is most commonly interpreted from the wireline log data, based on the electrical resistivity measurement. Archie (1942) defined an empirical relationship between the electrical resistivity of a rock (R_t) and the saturating fluid (R_w), its porosity (ϕ) and the water saturation (S_w), where m is the porosity exponent, a is a constant and n is the saturation exponent ;

$$S_w^n = \left(\frac{a}{\phi^m} \right) \left(\frac{R_w}{R_t} \right) \quad (1.1)$$

This relationship, discussed in more detail in chapters 2 and 6, is known as Archie's equation, and is the basis for hydrocarbon estimation in clean siliclastic reservoirs where there are no clays present, as saline water in pore spaces exhibits lower resistivity (higher conductivity) than high resistivity (non-conducting) hydrocarbons.

In this project we are interested in how the presence of clay minerals in sandstones affects the porosity, water saturation estimation and permeability in a sandstone reservoir. When clay grains form on the edges of sandstone grains, after deposition, they can prevent the formation of cements and preserve porosity with increasing depth. In narrow pore throats they can restrict the permeability, especially if the clays present are 'swelling clays', which expand in the presence of water. The presence of clay minerals in sandstones can affect the resistivity measurement as they are conductive; therefore when present in abundance they can lower the resistivity values. A common result of these clay grain-coatings is to have high porosity sandstone at depth, which form good hydrocarbon reservoirs. However, the low resistivity associated with the clays can counteract the increase in resistivity when hydrocarbons are present, such that the resistivity exhibited across the hydrocarbon-bearing zone is indistinguishable or lower than the water-bearing zone. This effect is known as "*low resistivity pay*", and is sometimes referred to as "*low resistivity contrast*" (Worthington, 2000).

1.2 Aims and Objectives of this thesis

The problem of “*low resistivity pay*” is not new, and many studies have been done to try and address the problem; namely the overestimation of water saturation in the presence of hydrocarbons (Durand et al., 2001; Henn et al., 2001; Hill and Milburn, 1956; Juhász, 1979; Waxman and Smits, 1968; Worthington, 2000). Worthington (2000) outlines six causes, from a petrophysical prospective, of low resistivity pay zones: 1) laminated sand-shale sequences; 2) low-salinity formation water; 3) electronic conduction within the rock matrix; 4) fine grains; 5) internal microporosity and 6) superficial microporosity. The latter three are all related to capillarity, and produce a high surface area which manifests as a shale effect.

The focus of this study is the uppermost Carboniferous reservoir (A) of the Berkiné Basin, Eastern Algeria. The A reservoir is a known “*low resistivity pay*” reservoir as the hydrocarbon-bearing, and producing, zones cannot be distinguished from the water-bearing zones (McNeill, 2006). The presence of grain-coating chlorites has previously been identified as the cause of this low resistivity (Hughes et al., 2003; McNeill, 2006), however, the abundance and distribution of the chlorite within the reservoir is not known.

The main aim of this project, to refine the saturation estimations in the A reservoir, can be split into two separate objectives: 1) understanding the occurrence and distribution of the grain-coating chlorite; and 2) developing a saturation model which accounts for the low resistivity pay zones.

Objective 1 can be addressed by undertaking detailed sedimentary analysis, in connection with a review of published literature, on available core data, to answer the following questions:

- i) How do grain-coating chlorites form?
- ii) Is the chlorite in the A reservoir diagenetic or authigenic?

- iii) Is there a depositional environmental or facies control on the chlorite distribution within the A reservoir?
- iv) Does the presence of the grain-coating chlorite affect the porosity distributions (i.e. porosity) of the sediment?

Objective 2 can be best addressed through detailed analysis of the wireline log data, while considering the following questions:

- v) Can the presence of chlorite be predicted from the wireline log data, either with or without input from core data?
- vi) Does a saturation-height model provide a more realistic estimate of water saturation than the resistivity measurement estimation?

Through the thesis the above questions are addressed and answered, with the aim of improving our understanding of the role of chlorite in creating low resistivity pay zones in the A reservoir.

1.3 Thesis Structure

The thesis structure follows a progression from the sedimentary analysis through to petrophysical analysis. Chapters 2 and 3 are reviews of the background information necessary to the study, chapter 4 deals with the sedimentary interpretation, while chapters 5 and 6 discuss the petrophysical interpretations. Chapter 7 brings the petrophysical and sedimentological results together in conclusions to the project objectives.

Chapter 2 introduces the methodology behind the data used in the study. The wireline logging measurements, and the tools used are described, detailing the information they produce and its relevance. Chapter 2 also provides a brief outline of the core-data measurements used in this study.

Chapter 3 outlines the data available in the literature regarding the formation, occurrence of sedimentary grain-coating chlorites and the known influence of chlorite on reservoir properties. This chapter helps to focus the sedimentary interpretation and analysis undertaken, the details of which are in Chapter 4.

Chapter 5 describes the basic lithological analysis of the wireline log data. Log-based lithology interpretations are described in the early sections of the chapter. The later sections of the chapter deal with the identification of chlorite, and sedimentary facies, from the wireline log data. The methods used are basic cross-plots of wireline log variables, and more complex statistical analysis using the core-based sedimentology as a model.

The petrophysical analysis for the porosity, permeability and saturations are discussed in Chapter 6. Both core and log-based porosity models are described, and permeability calculations explored. The bulk of the chapter deals with the saturation estimations. The necessary parameters for Archie calculations are derived from core data, and the stages of saturation calculations are discussed in detail. The latter half of the chapter deals with the derivation of the core-based saturation height functions, and their conversion to the log scale. A final discussion compares the different saturation estimates from Archie to core saturation-height functions.

Chapter 7 brings the main conclusions of the previous chapters together and discusses them with regard to the original objectives outlined in section 1.2.

2. Review – Measurements

In this project the parameters of interest are porosity, permeability and saturation, as well as the presence or absence of clays in sandstones. These parameters can be obtained from both log and core data, and can be measured either directly or indirectly. In this project it is how these measurements, e.g. resistivity, are affected by the presence or absence of clays that is of interest.

2.1 Wireline Log Data

Reservoir characterization can take place on several scales: reservoir scale (100m – km), borehole scale (m), individual sedimentary bed scale (cm – dm), and pore scale (mm – μm). Log data provide information at the borehole scale and can also provide information at the bed scale, and estimation of some pore scale parameters. To obtain the measurements used in this study a borehole is drilled into the subsurface reservoir, and in the uncased (open) borehole wireline logging tools are dropped to the bottom. As the tool string is slowly pulled back up the hole measurements are made at regular intervals. The measurements obtained are often geophysical (e.g. nuclear, electrical, sonic) but can be used to estimate a number of parameters, from lithology on the bed scale, to porosity, and pore fluid on the pore scale.

For this project, the available log data (see Chapter 5 for details) consists of caliper, spectral gamma ray (thorium, potassium, and uranium), density, and neutron porosity, deep, medium and shallow resistivity and sonic travel-time measurements. The gamma ray log data measures three elements (thorium, potassium and uranium) of the chemistry of the rock and typically can be used to estimate lithology and clay content. Porosity can be estimated from the neutron, density and sonic tools, while pore fluid type, and therefore saturation, can be estimated from the resistivity measurement. Basic parameters for each tool and its specific use within the scope of this project will be

discussed below. Table 2.1 summarises the different tools, relevant to this study, by well. More detailed information on the exact specifications and capabilities of each tool discussed here can be found through the Baker Atlas (www.bakerhughesdirect.com) or Schlumberger websites (www.slb.com).

Tool	Contractor	Measurement	Wells
HDIL (High Definition Induction Tool)	Baker Atlas	Resistivity	<i>MLNW-3; MLNW-5; MLNW-6; MLN-5</i>
ZDL (Z-Densilog)	Baker Atlas	Caliper, Density, PEF	<i>MLNW-3; MLNW-5; MLNW-6; MLN-5</i>
CN (Compensated Neutron)	Baker Atlas	Neutron Porosity	<i>MLNW-3; MLNW-5; MLNW-6; MLN-5</i>
DAC (Digital Array Acoustilog)	Baker Atlas	Sonic Travel Time	<i>MLNW-3; MLNW-5; MLNW-6; MLN-5</i>
DSL (Digital Spectralog)	Baker Atlas	Spectral Gamma Ray	<i>MLNW-3; MLNW-5; MLNW-6; MLN-5</i>
AITH (Array Induction Tool - H)	Schlumberger	Resistivity	<i>MLNW-1; MLNW-2; MLNW-4</i>
HILT (High Resolution Integrated Logging Tool)	Schlumberger	Caliper, Density, PEF, Spectral gamma-ray	<i>MLNW-1; MLNW-2; MLNW-4</i>
APS (Accelerator Porosity Sonde)	Schlumberger	Neutron Porosity	<i>MLNW-1; MLNW-2; MLNW-4</i>
DSST (Dipole Shear Sonic Imager Tool)	Schlumberger	Sonic Travel Time	<i>MLNW-1; MLNW-2; MLNW-4</i>

Table 2.1: Summary of logging tool, contractor and measurements used in this study and the relevant Well-number

Depth of investigation of a tool is simply defined as: *“The radial distance away from the measure point at the borehole at which the formation is having an effect on the tool reading”* (Rider, 2004; Serra and Serra, 2003).

Although rather vague this definition allows us to compare different tool measurements. For tools which emit a signal into the formation the depth of investigation can be equal to the transmitter and receiver spacing, e.g. the sonic tool. For the density tool depth is limited by how far the gamma-rays can travel into the formation, which is a function of the electron density. Other factors can influence the depth of investigation, but these

vary with measurement and will be discussed with the appropriate individual measurements (later in this chapter).

The vertical resolution of tools is subject to much discussion, and varies with formation and environment characteristics. A definitive definition is problematic given the conflicting information from the literature. The qualitative definition of vertical resolution is:

“The minimum thickness of formation (bed) that can be distinguished and fully characterized by a tool under operational conditions” (Hearst et al., 1999; Lofts and Page, 2002; Serra and Serra, 2003; Theys, 1991).

One approach is to simply equate the physical distance between the transmitters/sources and receivers/detectors on the tool to the vertical resolution; however this can yield significant errors (Rider, 2004; Theys, 1991). However, Theys (1991) provides a more quantitative theoretical definition, illustrated in figure 2.1:

“The full width at half maximum of the response of the measurement to an infinitesimally short event”

In practice this is not always the case; as an individual bed is more likely to be resolved when the contrast between the bed and the surrounding formation is greatest.

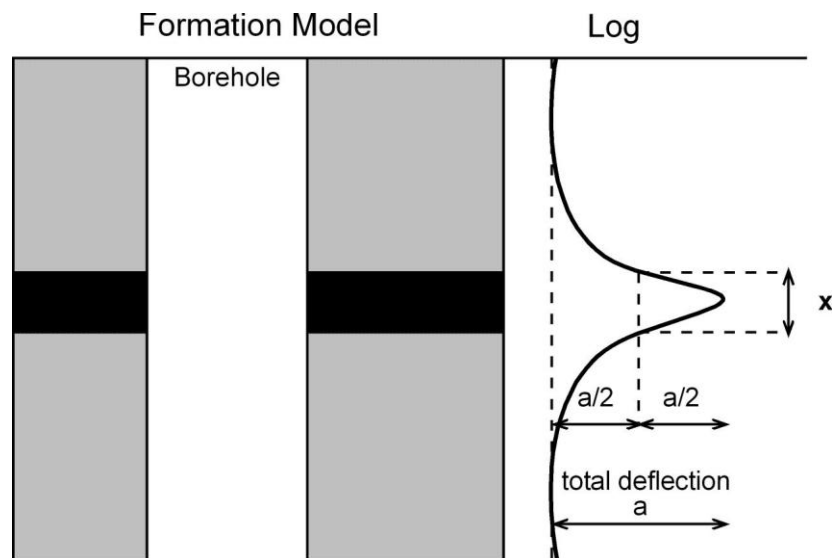


Figure 2.1: Graphical representation of the theoretical definition of vertical resolution (x) (modified from Theys, 1991)

This quantitative definition requires a vertical resolution that is specific to the field under study to be determined. This can be achieved by running the logging tools over an interval containing different bed thicknesses and comparing to core data, as suggested by Theys (1991). However it is more common to approximate a vertical resolution per tool.

The vertical resolution of a tool is most important when attempting to accurately correlate sharp bed boundaries identified in core to the logging data. Assuming the simplest case of a vertical borehole with horizontal bedding, no matter how sharp the lithological boundary is in the core it will appear gradational by the logging tool. A tool measures a volume of the formation and so, as a bed boundary is approached, a percentage of the signal received is responding to the lithologies above and below the boundary. This gradation from one bed to another is known as the “shoulder effect”, and can be lessened, or accentuated, based on logging speed. If a section is logged too fast the bed boundaries become more smeared, increasing the shoulder effects (Figure 2.2). If the beds are dipping through a vertical borehole, or a deviated or horizontal borehole is drilled through horizontal beds or inclined beds the shoulder effects will also

be exaggerated. In this project the wells are assumed vertical, and the bedding is near horizontal.

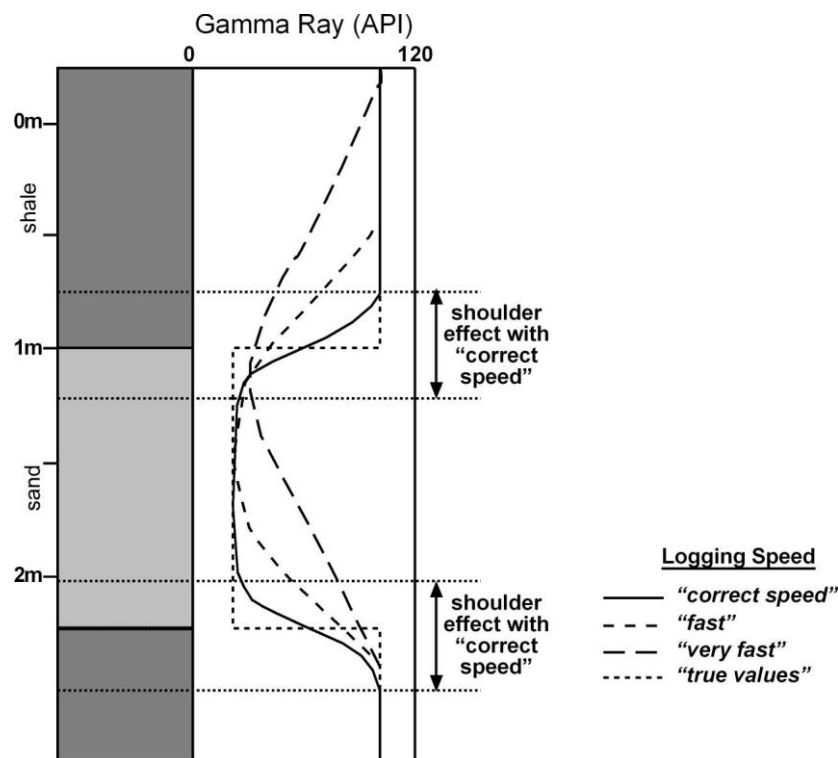


Figure 2.2: The influence of logging speed on shoulder effects and bed boundary definition (modified from Rider, 2004).

Accurately placing a bed boundary is a matter of interpretation, through knowing the vertical resolution of a tool as well as logging speed. However, one possible solution is to place the boundary at the point of maximum change in value (maximum slope) (Rider, 2004).

2.1.1 Gamma Ray Measurements

Gamma ray measurements rely on the detection of natural gamma radiation from the formation, and are most commonly used as a proxy for shale content (Hampson et al., 2005; Heslop, 1974; Humphreys and Lott, 1990; Rider, 2004). There are two main types of gamma ray logging tool, total gamma ray (GR) and spectral gamma ray (SGR). Gamma ray tools rely on recording count-rates and both types have similar depths of investigation, suffer minor environmental effects, and are calibrated to artificial “shale”

formation in laboratories (Ellis, 1987). The total gamma ray simply measures the total radioactivity of the formation. The spectral gamma ray log records the individual mass concentrations of potassium (^{40}K) in weight percent (wt%), with thorium (^{232}Th) and uranium (principally ^{238}U) in parts per million (ppm) (Ellis, 1987).

Spectral Gamma Ray

The three measured elements of the spectral gamma ray tools each have distinct emission spectra (Figure 2.3) which can be detected by the logging tool. However, the gamma rays are likely to have interacted with the formation and drilling mud prior to detection by the tool, leading to a weakening and broadening of the emission spectra (Figure 2.3b) (Hurst, 1990; Rider, 2004). Through calibration of the logging tool with artificial formations, with known element abundances, it is possible to relate the relative contributions of each element, as recorded by the logging tool, to the abundance of each element (Edmundson and Raymer, 1979; Hurst, 1990; Rider, 2004).

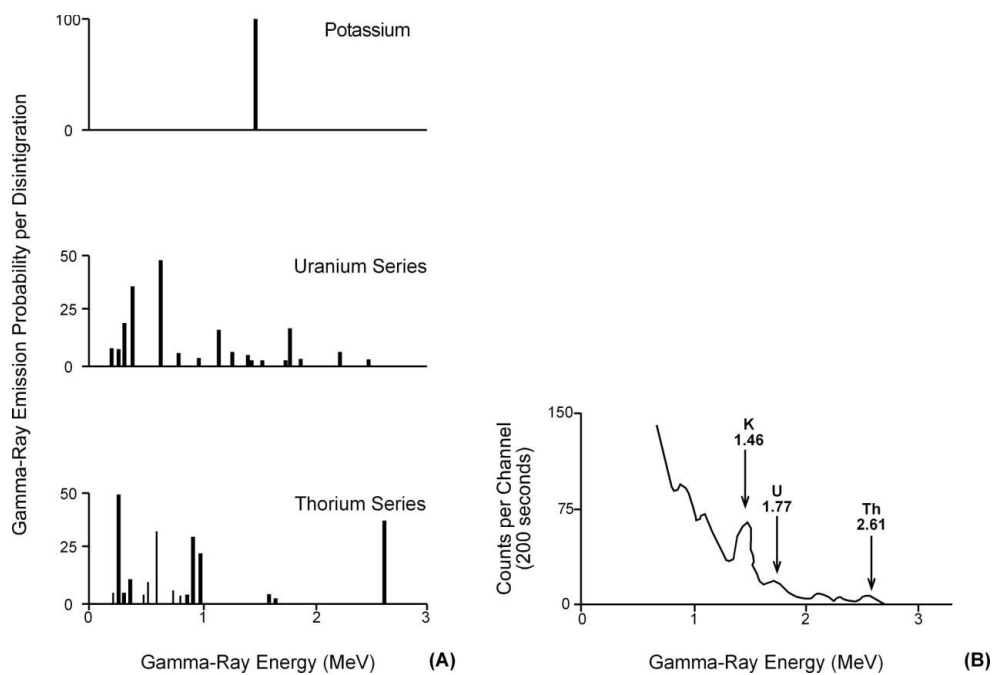


Figure 2.3: (a) Emission spectra of three components of a spectral gamma ray, and (b) the “real” nature of the spectra that makes identification more subjective (modified from Hurst, 1990)

The volume of investigation of a gamma ray tool is, in theory, the extent of the formation, as the detected gamma rays could originate from anywhere in the formation. However, typically a depth of investigation is assumed to be around 30cm with a vertical resolution of 1 metre. This introduces errors into the reading, which become more pronounced at higher logging speeds, since the faster the tool is moving, the less chance of detecting radiation (Ellis, 1987; Hurst, 1990; Rider, 2004). Therefore the logging speed should always be in mind when interpreting spectral gamma ray plots.

For qualitative analysis, the gamma ray log provides a “quick look” method for identifying shale zones (Theys, 1991). The spectral gamma ray is commonly used to discern clay mineralogy within a shale formation, and more commonly the presence of clay minerals in sandstones (Hampson et al., 2005; Hurst, 1990; Pirmez et al., 1997)

Thorium and potassium concentrations are most closely linked to clay mineral content and identification, because many clay minerals contain potassium, and thorium is often adsorbed onto clay minerals (Hearst et al., 1999). A plot of Thorium (Th) vs. Potassium (K) can be used to indicate the presence of individual clay minerals (Figure 2.4), based on the principle that potassium, for example, is present in feldspar, mica and illite, but not in chlorite, kaolinite or montmorillonite (Deer et al., 1992; Hearst et al., 1999). Thorium content relies on the adsorption capacity of the individual clay minerals, and can be influenced by its availability in pore waters. Due to the intrinsic variability within and between clays, the neat divisions (Figures 2.4 and 2.5) of Thorium vs. Potassium plots should be viewed with caution (for a more detailed discussion of the pitfalls see Hurst (1990)). More specifically for this study, the identification of chlorite is even less reliable from such plots, because chlorite contains little to no potassium, and has a low adsorption capacity for thorium, and is therefore more difficult to discern on the plots (Hurst, 1990).

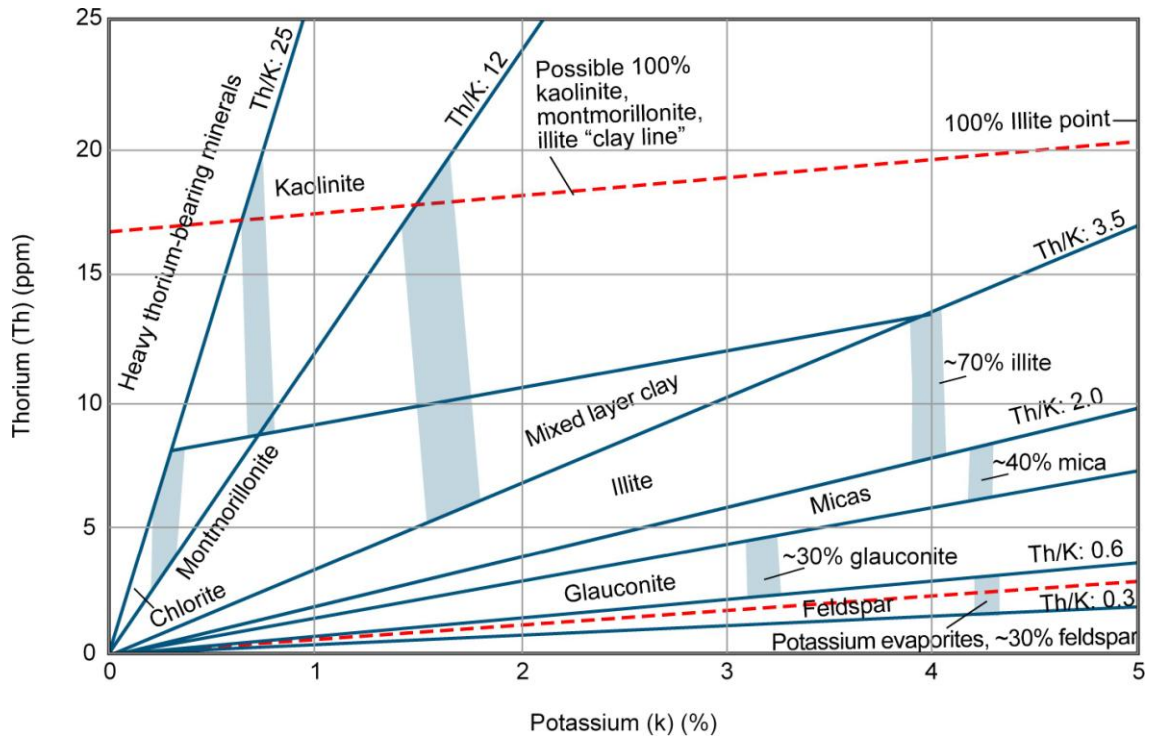


Figure 2.4: Schlumberger Th vs. K plot, with clay fields shown (www.slb.com)

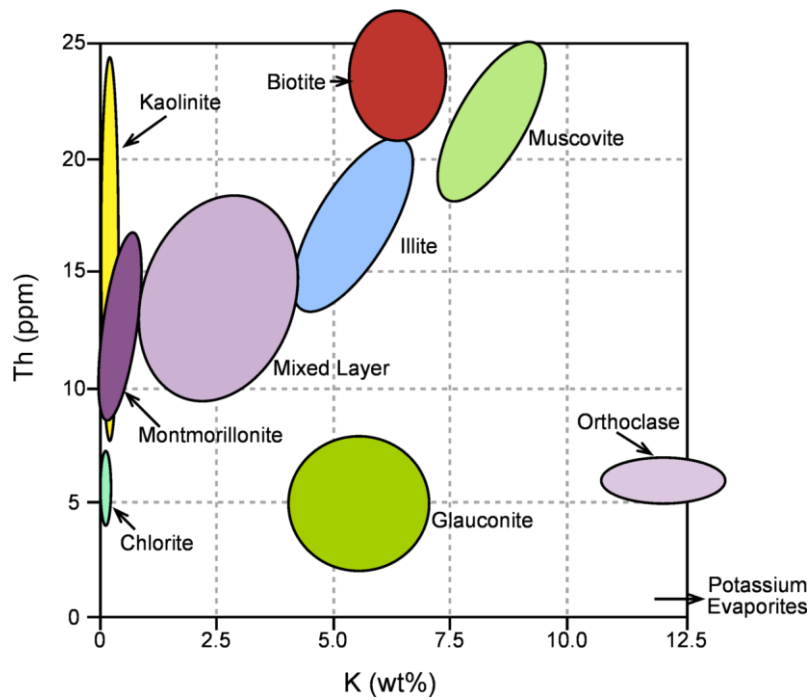


Figure 2.5: Th vs. K showing clay fields (modified from Serra and Serra, 2003)

2.1.2 Density Measurement

The principle of the density tool is the attenuation of gamma rays focussed from a source into the formation which measures the electron density of the formation. The dominant interaction between the source gamma rays and the formation is through Compton scattering (Ellis, 2003a; Hearst et al., 1999) where the gamma rays are attenuated by their interaction with electrons in the formation, which provides a measure of the electron density of the formation (Ellis, 2003a). Through a simple relationship, shown on the graph below (Figure 2.6) it is possible to obtain bulk density from the electron density (Ellis, 2003a), note that although linear the relationship does not pass through the origin (0, 0).

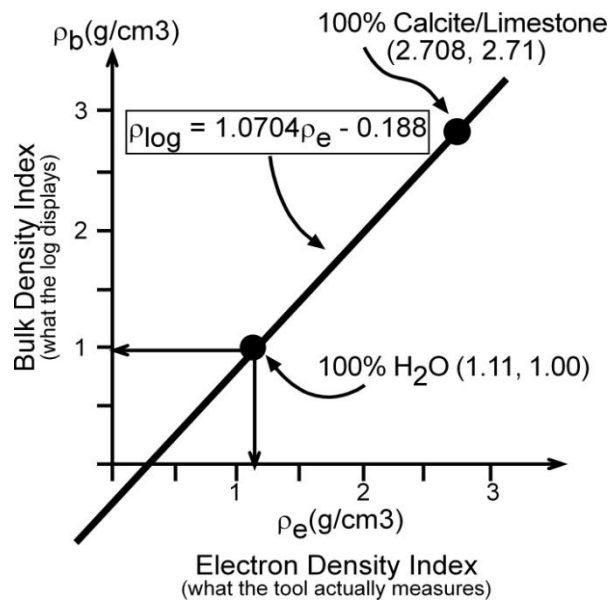


Figure 2.6: Graph showing the relationship between electron density and bulk density. Since H has a ratio of 11% higher than its bulk density a simple correction is applied to all logging density tools – the equation shown on the graph (modified from Ellis, 2003a).

In practice the energy emitted from a gamma ray source is a spectrum where different interactions occur in relation to the energy, and the atomic number of the atom interacting with (Figure 2.7). At lower gamma ray energies photoelectric absorption dominates the process in sedimentary rocks (Bertozzi et al., 1981). At very high

energies ‘pair production’ occurs, but this is of no consequence for density logging tools as the source energy is kept below the limit (Ellis, 2003a).

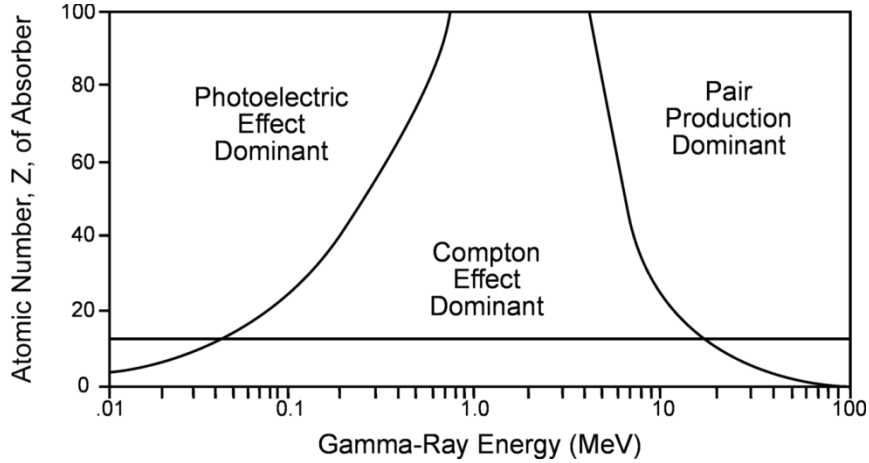


Figure 2.7: Regions of influence of three types of gamma ray interactions (modified from Ellis, 1987)

The amount of absorption due to the photoelectric effect can be estimated by comparing the propagation of gamma rays at high and low energies (Bertozzi et al., 1981; Ellis, 2003a). Knowing the photoelectric factor (PEF) of a formation can help distinguish between three of the common minerals, and is often used, in conjunction with the gamma ray data, to distinguish the mineralogy of a formation (See chapter 5). However, the presence of barite in heavy drilling mud, with its very efficient low-energy gamma ray adsorbing capabilities, can render the PEF measurement useless, because as equation 2.1 shows the higher the atomic number (i.e. heavier atoms) the higher the PEF value (Ellis, 2003a). In this study, with the exception of one well, barite-rich drilling mud was used; therefore the PEF curves are of no use in interpretation.

$$PEF = \left(\frac{Z}{10} \right)^{3.6} \quad (2.1)$$

In dense formations the Compton scattering attenuation is high (e.g. low porosity limestone) and fewer gamma rays reach the detector, while if more of the formation is water-filled pore space (and therefore H atoms) a lower density is recorded (Rider, 2004) (Figure 2.6).

A formation (e.g. sandstone) is composed of the grains that make up the rock (rock matrix) and the fluid within the pore space (porosity, ϕ). The bulk density (ρ_b) measurement is volumetrically proportional to the rock matrix density (ρ_{ma}), the pore fluid density (ρ_f) and the amount of pore space available, and is linked by the simple relationship:

$$\rho_b = \phi \cdot \rho_f + (1 - \phi) \rho_{ma} \quad (2.2)$$

As a result of this simple relationship it is possible, and commonly used, to calculate the porosity of the rock, assuming the fluid and matrix densities are known or can be estimated. Some common matrix densities are shown below (Table 2.2); although a better estimate of rock matrix density can be obtained from core analysis.

Mineral	Density (g.cm³)
<i>Quartz</i>	2.65
<i>Feldspar</i>	2.62 – 2.76
<i>Calcite</i>	2.71
<i>Dolomite</i>	2.85
<i>Montmorillonite</i>	2.0 – 2.7
<i>Chlorite</i>	2.60 – 3.22
<i>Halite</i>	2.16
<i>Anhydrite</i>	2.96
<i>Pyrite</i>	5.0

Table 2.2: Some typical density values for common minerals (modified from Rider, 2004)

For lithology determination the density tool is most effective when used in conjunction with the neutron porosity measurements (see chapter 5).

2.1.3 Neutron Porosity Measurement

The neutron porosity tool works on a similar principle of attenuation as the density tool, but uses neutrons instead of gamma rays, with the neutrons interacting with the nucleus rather than the electrons. In a process known as elastic scattering the neutrons interact with nuclei and undergo energy loss, with the mass of the target struck controlling the amount of energy lost (Ellis, 2003b, , 2004). The maximum energy loss is a function of the relative mass of a neutron compared to the mass of the isotope it collides with (Figure 2.8): the most effective isotope being hydrogen as it requires the least number of collisions to reduce the energy to nearly zero (Ellis, 2003b, 2004). Some average collision counts are shown for common minerals in Table 2.3, these simulations provide average estimates based on collision at a variety of random angles (Ellis, 2003b, 2004). Thermal absorption is another important interaction, as the more a neutron interacts with target nuclei the lower its thermal energy becomes, until it “disappears” and becomes what is known as an epithermal neutron (Ellis, 2003b, 2004).

Moderator	Number of Collisions
<i>H</i>	14.5
<i>C</i>	91.3
<i>O</i>	121
<i>Ca</i>	305
<i>H₂O</i>	15.8
<i>Limestone 0% Porosity</i>	132
<i>Limestone 20% Porosity</i>	29.7

Table 2.3: Average number of collisions required with different atoms to slow down the neutrons (modified from Rider, 2004)

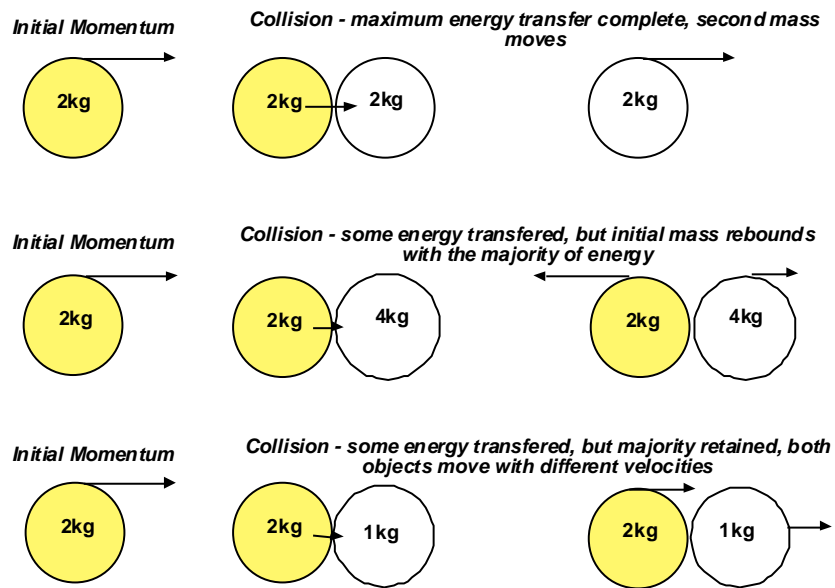


Figure 2.8: Schematic representation of the behaviour of neutrons when colliding with other atoms of different masses, assuming each collision is head on

The sensitivity of elastic scattering energy loss to hydrogen is exploited in neutron porosity devices, where a measurement of the spatial distribution of thermal or epithermal, depending on the tool, neutrons resulting from interaction of high energy neutrons with a formation can be related to its hydrogen content (Ellis, 2003b, 2004; Ellis, 1987; www.slb.com). Therefore if the formation pore space is filled with hydrogen, in the form of water or liquid hydrocarbons, then the measurement is, in effect, yielding porosity. Since gas contains a lower concentration of hydrogen if present in the pore space it will yield a lower porosity than really exists. At the other end of the scale shales will often appear falsely highly porous on a neutron porosity plot, this is largely due to the hydrogen concentration associated with the shale matrix, existing in either the clay mineral structure or as bound water (Ellis, 1987).

Therefore the neutron porosity measurements, in this project, are primarily used in conjunction with the density measurements, to determine lithology and gas intervals. Using this dual approach the unwanted effects of shale (*excess porosity*) can be compensated for.

2.1.4 Resistivity Measurement

The electrical resistivity of a rock is described as the ability of a fluid-saturated rock to impede the flow of an electric current through that rock, i.e. it is the inverse of the conductivity, a measure of how well electrical current is conducted. The resistivity measurement is an invaluable tool for petrophysical analysis, and was the original electrical log run by Schlumberger in 1927 (www.slb.com). The resistivity tool gives information on the porous nature of the formation and, more importantly, the pore-filling fluids, although it is also dependent on pore geometry, formation stress and temperature, the rock composition and the interstitial fluids (Edmundson, 1988b; Tiab and Donaldson, 1996). Since sedimentary rocks are generally only capable of transmitting electrical currents via the fluids contained within either the pore water or that adsorbed onto grains, the resistivity log is essentially an indicator of the fluids in the pore spaces; able to detect the presence of hydrocarbons (oil and gas are not differentiated) or saline water. Ions from dissociated salts within the fluids allow the current to flow, and as such the salinity of the fluids greatly affects the resistivity; an increase in salinity leads to a reduction in resistivity (Edmundson, 1988b). The presence of hydrocarbons increases the resistivity, as they are non-conductors, and therefore effectively the equivalent to the rock matrix. However as stated previously, the presence of pore-lining clays can affect the resistivity by providing an “extra” conduit for the current to pass through (Ellis, 1987). Therefore if a saline pore-fluid is replaced by oil/gas the current may still be passed through the water associated with clays and thus the presence of hydrocarbons does not cause a significant reduction in resistivity, as illustrated in Figure 2.9.

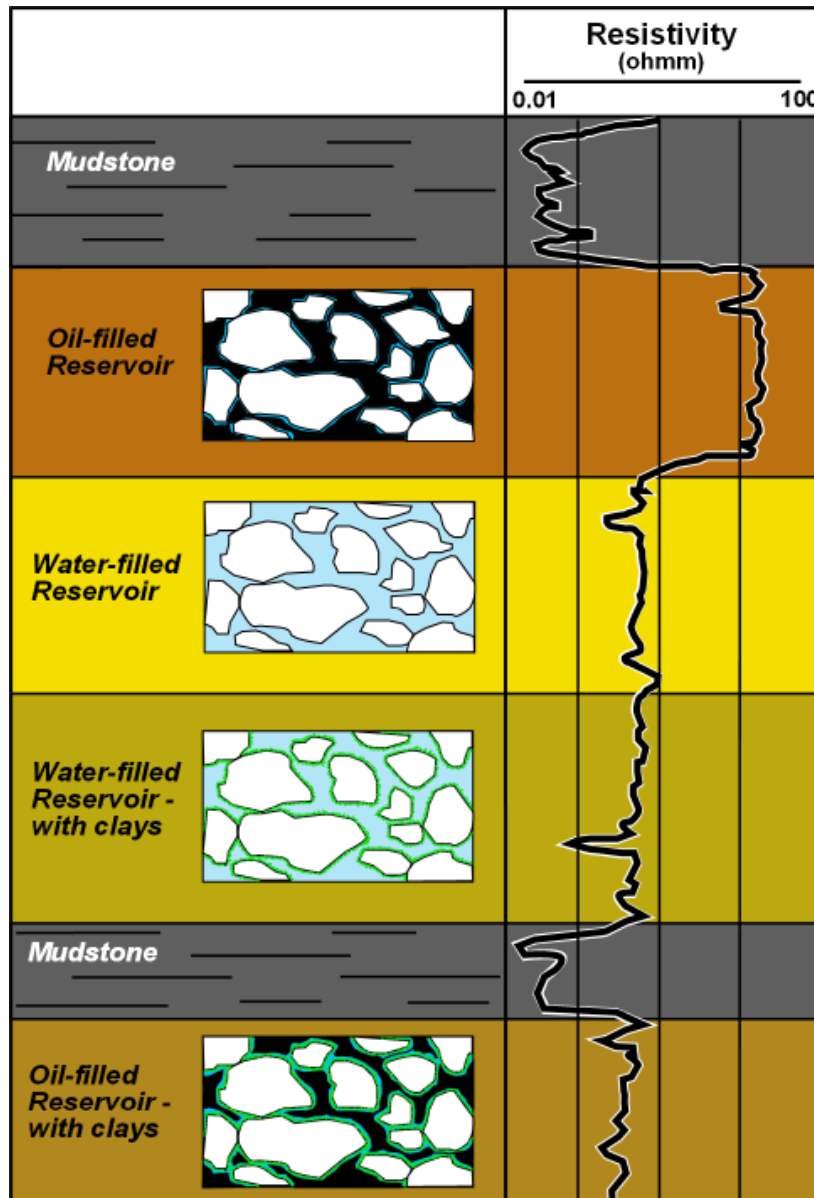


Figure 2.9: Schematic resistivity profiles for water and oil bearing clean and clay-rich sandstone reservoirs.

There are several ways of measuring the resistivity, the two most common tools being either the laterolog, where current is passed into the formation through galvanic contact, or induction tools where the current is generated by electromagnetic fields. Common practice is to use the laterolog tool with water-based mud, and the induction tool with oil-based mud. In this project the induction tool was used with oil-based mud drilling fluid, and therefore will be our focus. The induction tool uses a transmitter coil to set up an alternating magnetic field, which induces current flow in the earth (Figure 2.10). The

current generates a second magnetic field detected by a receiver coil. The magnitude and character of the magnetic field is governed by the frequency of the transmitted current, which gives information on the electric properties in the vicinity near the borehole (Ellis, 1987; Hearst et al., 1999; Rider, 2004). One advantage of an induction tool is its suitability for logging in environments where heavy drilling mud is used, as in this case. A further advantage of the induction tool are the multiple depths of investigation available, from short and long-spacing arrays (Hearst et al., 1999; Xiao et al., 2002). The induction tool, on average, can resolve a bed with minimum thickness of ~60cm, although processing can sometimes increase this resolution (Xiao et al., 2002).

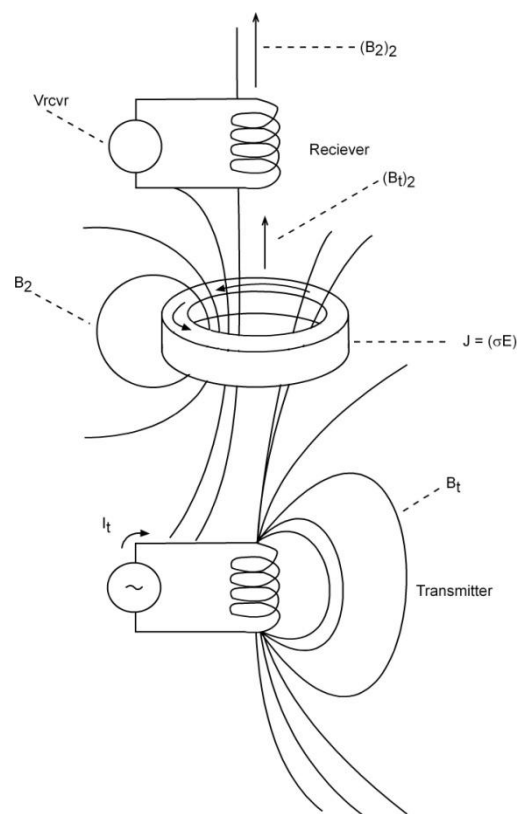


Figure 2.10: Principle of an induction tool (modified from Ellis, 1987, pg 105)

	Discipline	Used for	Knowing
Quantitative	<i>Petrophysics</i>	<i>Fluid Saturations:</i>	<i>Formation water resistivity (R_w)</i>
		<i>Formation (S_w)</i>	<i>Mud-Filtrate resistivity (R_{mf})</i>
		<i>Invaded Zone (S_{xo})</i>	<i>Porosity (Ø) (and F)</i>
		<i>i.e. detect hydrocarbons</i>	<i>Temperature</i>
Semi-Quantitative and Qualitative	<i>Geology</i>	<i>Textures</i>	<i>Calibration with laboratory samples</i>
		<i>Lithology</i>	<i>Mineral Resistivities</i>
		<i>Correlation</i>	
	<i>Sedimentology</i>	<i>Facies,</i>	<i>Gross Lithologies</i>
		<i>Bedding characteristics</i>	
	<i>Reservoir Geology</i>	<i>Compaction,</i>	<i>Normal pressure trends</i>
		<i>Overpressure and shale porosity</i>	
	<i>Geochemistry</i>	<i>Source rock identification</i>	<i>Sonic and density log values</i>
<i>Source rock maturation</i>		<i>Formation temperature</i>	

Table 2.4: The principle uses of the resistivity and conductivity logs (modified from Rider, 2004)

From the many possible uses of the resistivity measurement (Table 2.4) the main use, in this project, is to obtain an estimate for the hydrocarbon saturation of the sandstone formation. Through a series of experiments and equations, Archie (1942) determined a relationship between the measured total resistivity (R_t), the resistivity of the saturating fluid (R_w), the porosity (ϕ) and the water saturation (S_w) of a formation:

$$R_t = \frac{a.R_w}{\phi^m S_w^n} \quad (2.3)$$

Archie's equation, as this is known, is more commonly rearranged and used to calculate the water saturation of a formation, and thus the hydrocarbon saturation ($1 - S_w$):

$$S_w = \sqrt[n]{\frac{a.R_w}{\phi^m .R_t}} \quad (2.4)$$

The use of Archie equation is explained in more detail in the core analysis part of this chapter (section 2.2.1) and chapter 6.

2.1.5 Acoustic (Sonic) Measurement

The sonic tool measures the transit time of a sound wave through the formation (i.e. slowness), as the velocity (inverse transit time) and attenuation of sound waves in a formation can depend on the formation's porosity, density, texture, saturation and fluid type, as it is sensitive to the presence of gas (Hearst et al., 1999; Market, 2008; Pirmez et al., 1997). The full waveform acoustic tool provides many different velocity readings, including compressional and shear velocity. Shear velocity is of interest in geomechanical studies but does not propagate through fluids (water, oil, gas); the compressional velocity is the main interest in hydrocarbon reservoirs for the estimation of porosity.

The basic design of an acoustic tool consists of an acoustic transmitter and receiver, which record the time between the transmitter firing and first detection of a signal producing only compressional velocity measurements (Ellis, 1987). The acoustic tools are often designed so that the signal travelling through the formation arrives at the detector before the signals travelling through the tool casing or the borehole mud (Ellis, 1987). A large enough separation between the transmitter and receiver ensures against the mud-arrival being first, while the tool case is usually grooved to slow down the signal from the case (Ellis, 1987; Zhu et al., 2008).

One of the main derivatives of the transit time measurement is the porosity (ϕ) of the formation, calculated by the Wyllie equation (Wyllie et al., 1958; Wyllie et al., 1956). Wyllie's time-average equation relates the velocity of the bulk material (V_b), to the rock matrix velocity (V_{ma}) and pore fluid velocity (V_f):

$$\frac{1}{V_b} = \frac{\phi}{V_f} + \frac{1-\phi}{V_{ma}} \quad (2.5)$$

There are limits to the use of the equation; it only should apply to formations under sufficient pressure as to have reached their terminal velocity; intergranular porosities larger than 0.35 are unreliable; the rock must be fully saturated with fluid of at least the velocity of water (i.e. not gas-filled); and the rock cannot be fractured or vuggy (Hearst et al., 1999). In this project, the rock is of sufficient depth and does not exhibit vuggy or fractured porosity (Hughes et al., 2003), therefore the Wyllie equation can be used as a porosity measurement assuming matrix and fluid velocities are considered constant.

The acoustic measurement is not particularly useful for lithological determination unless both compressional and shear velocities are available (Ellis, 1987). However, a strong dependence on the shale fraction of sedimentary rocks is observed (Hearst et al., 1999; Pirmez et al., 1997) and therefore these data could be useful in separating the clay-rich sandstones from the clean sandstones in this study.

2.2 Core-Data Measurements

Core data was available in two categories: conventional core analysis providing basic physical information and special core analysis (SCAL) providing additional data e.g. electrical parameters (Table 2.5). Additionally, thin sections provide visual information (section 2.2.5 and 2.2.6), and XRD measurements (section 2.2.7) provide qualitative and semi-quantitative information on the composition of the formation rock, especially clay minerals.

Conventional Core Analysis	Special Core Analysis
Porosity	Dean Stark Water Saturation
Permeability	Capillary Pressure Curves
Grain Density	Mercury Injection – pore size distributions
	Formation Factor, Porosity Exponent (m)
	Resistivity Index, Saturation Exponent (n)
	Excess Conductivity (Co/Cw)

Table 2.5: Parameters measured through conventional and special core analysis

2.2.1 Core-derived Archie Parameters

One of the main deliverables from core analysis is the determination of electrical parameters (a, m, and n), relating to the Archie equation, and the formation factor (FF) and resistivity index (RI) for use in the saturation calculation (previous section). These also include the clay-corrected versions (FF*, m* and n*).

Formation factor and cementation exponents

The formation factor was originally defined by (Sundberg, 1980) and first experimentally demonstrated by Archie (1942) in clean sandstones, as the ratio of the rock resistivity when fully water saturated (R_o) to the resistivity of the saturating water:

$$FF = \frac{R_o}{R_w} \quad (2.6)$$

Through measurements on samples of porosity and formation factor Archie (1942) determined an empirical relationship between the two variables:

$$FF = \frac{a}{\phi^m} \quad (2.7)$$

The intercept a was taken by Archie to be 1 (discussed below), and the m exponent represents the negative trend of the slope. Archie (1942) originally showed that commonly $m = 2$ in clean un-cemented sandstones, however it soon became clear that m was a function of the degree of cementation of sandstone, increasing as cementation increased (Edmundson, 1988a; Lasswell, 2006). As a result, m reflects the pore geometry and inter-pore connections, and the default of 2 should only be used as a guide if no other information is available.

Since the water resistivity, rock resistivity and porosity are measurable parameters on core plugs, it is a simple matter to derive m and a values specific to the reservoir under study. A log-log plot of formation factor (FF) vs. porosity can produce core-derived m and a values (Archie, 1942). A true Archie rock will have $FF = 1$ when porosity = 1, because at this point the rock is equivalent to 100% water (i.e. it has no matrix) and often the “best-fit” will force through this (1, 1) origin, which yields $a = 1$. However, the presence of clay minerals/shale within a matrix of a rock can reduce the slope of the line, so a has a value greater than 1. The shallower the best fit line between formation factor and porosity (i.e. the smaller the m value) the higher the a has a value, and potentially the more shaly a rock is, as there is less of an increase in the resistivity of the rock with a decrease in porosity (Figure 2.11). This effect can also be achieved by an increase in the fluid salinity, although the best-fit line would still pass through the origin. Alternatively the less shale there is in a rock, the greater the increase in resistivity for a decrease in porosity and therefore the larger the m value and the steeper the gradient (Figure 2.11), this effect can also be achieved by decreasing the salinity of the rock – but in this case the best-fit line would still pass through the (1, 1) origin.

However, the a value cannot theoretically be less than 1, since the (1, 1) origin represents a rock composed of 100% water. Note that when comparing values of a and m , the two are inextricably linked and should be compared for different samples as a pair of numbers.

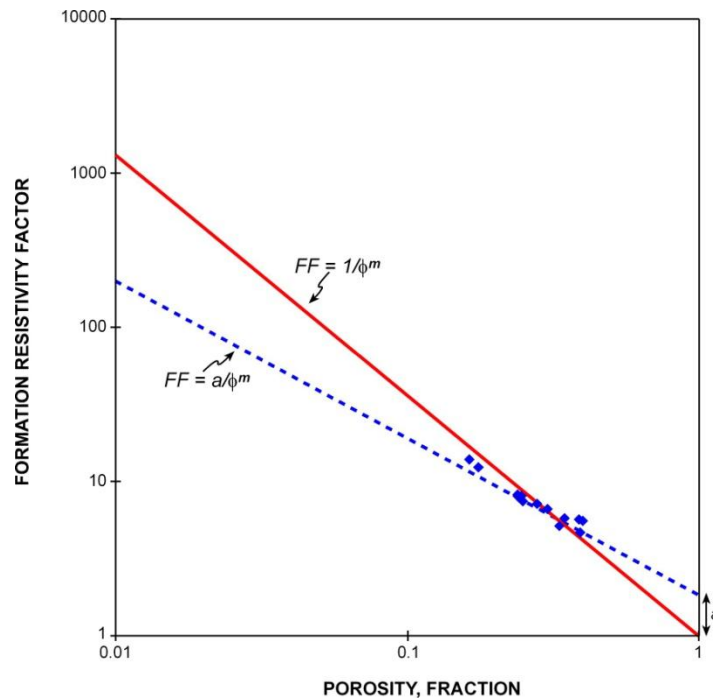


Figure 2.11: FF vs. Porosity cross-plot, illustrating m and a

Formation factor measurements are taken on multiple core plugs at different pressures. The standard formation factor vs. porosity plot (Figure 2.11) is usually composed of data points at a consistent pressure from each of the different samples. Often the ambient conditions are used because these are the conditions under which the porosity is measured. However some of the higher pressure measurements can provide a more accurate representation of the formation conditions. A representative pressure equivalent to the depth of the reservoir and ideally predictive of likely pressures during reservoir depletion should be used in calculations.

Clay corrected formation factor (F^) and porosity exponent (m^*)*

Since real rocks often are not as clean and therefore do not follow the simple conductivity behaviour as those from Archie’s experiments, a range of shaly-sand models have developed (Worthington, 1985). Most models are modifications to Archie’s equation, based on the idea of excess conductivity from clays within the formation (Waxman and Smits, 1968; Worthington, 1985). Work by Hill and Milburn (1956), among others, determined that the relationship between measured rock resistivity and the saturating water resistivity was curved in shaly sands, in contrast to the straight line devised by Archie in clay-free (‘clean’) sandstones. Waxman and Smits (1968) took this further to devise a method for correcting for the shale content of the sample, and produce what can be seen as “clay-corrected” versions of Archie’s original electrical parameters (Figure 2.12).

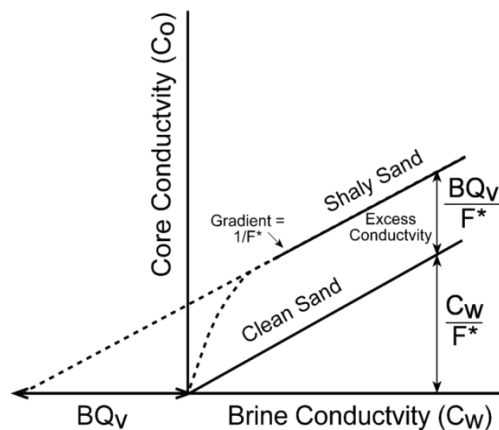


Figure 2.12: The Waxman-Smits C_o/C_w excess conductivity figure, illustrating the clean sand and shaly sand lines; note the curvature of the relationship at low brine conductivities (low pore fluid salinities) (modified from Worthington, 1985)

Figure 2.12 illustrates the relationship between a shaly-sandstone and a clean sandstone in terms of conductivity, and can be used to produce a clay-corrected formation factor (FF^*). The use of the C_o/C_w plot as an indicator of shale-content in a reservoir rock stems from Archie’s formation factor (FF) equation:

$$FF = \frac{R_o}{R_w} = \frac{C_w}{C_o} \quad (2.8)$$

Therefore a plot of measured C_w vs. C_o values for a single sample will yield a gradient of $1/FF$ passing through the origin assuming it is a clean fully brine-saturated sandstone sample (i.e. shale free). However, if the sample is unclean (i.e. shaly) then there will be an excess conductivity associated with the clay content, which will result in the C_w vs. C_o plot separating from the “clean” line and will no-longer pass through the origin of the graph, with the new C_w intercept (i.e. how much over-shoots the origin) as a measure of the excess conductivity (X). So the above equation becomes:

$$FF = \frac{C_w}{C_o} + X \quad (2.9)$$

In the Waxman-Smits (1968) shaly sand equation this excess conductivity (X) is quantified by the term BQ_v/FF^* , thus incorporating the excess conductivity associated with the clays in the S_w calculation (Waxman and Smits, 1968). In this format B is the equivalent conductance of sodium clay exchange cations, Q_v is the cation exchange capacity per unit pore volume, and FF^* is the formation factor for a shaly sand (Waxman and Smits, 1968; Worthington, 1985).

The clay corrected (intrinsic) formation factor (FF^*) can then be used in much the same way as a clean sand formation factor to determine a clay-corrected porosity exponent (m^*).

Resistivity Index vs. Water Saturation

Further work by Archie (Archie, 1942) involved partially saturated rocks, and allowed for the development of a relationship between the fraction of voids filled with water (S_w) and the resistivity of the resulting sand (R_t):

$$S_w = \left(\frac{R_o}{R_t} \right)^{1/n} \quad (2.10)$$

Archie proposed a factor (the resistivity index RI) to raise the rock's resistivity in the presence of hydrocarbons (Archie, 1942; Edmundson, 1988a):

$$R_t = \frac{RI}{R_o} \quad (2.11)$$

$$RI = \frac{R_t}{R_o} \quad (2.12)$$

$$RI = \frac{1}{S_w^n} \quad (2.13)$$

Where R_t is the true resistivity of the rock (measured value), R_o is the resistivity of the fully brine saturated rock, S_w is the water saturation and RI is the resistivity index. By combining equation (2.12) with equation (2.13) it is possible to generate a log-log plot of resistivity index (RI) vs. water saturation (Figure 2.13), in order to determine the saturation exponent (n) of the reservoir samples. Archie found that for clean unconsolidated sands the saturation exponent (n) approximated to 2 (Archie, 1942), and therefore this is often taken to be the default value, where core data is unavailable. Although, since n can vary and can exhibit different values at different saturations, often related to complex porosity distributions, ideally a reservoir specific value should be determined, using figure 2.13.

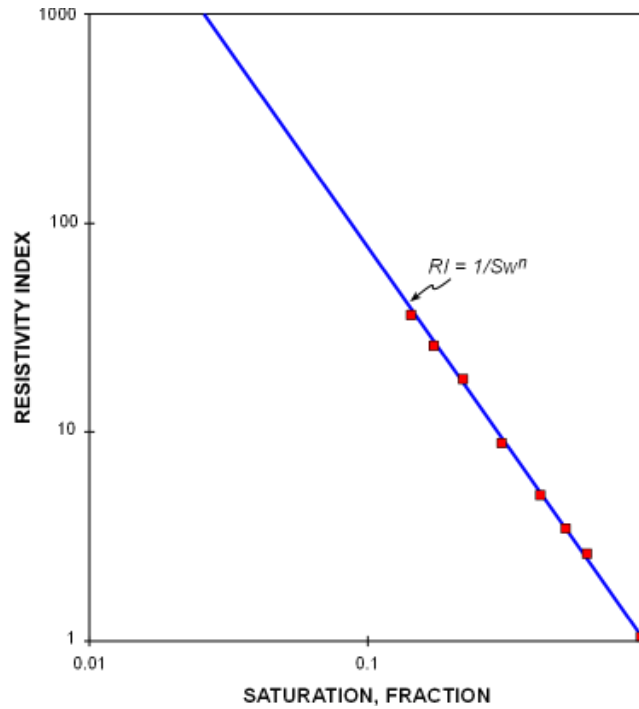


Figure 2.13: Resistivity index vs. Saturation to derive n , note the intercept is a real data point from the start of the experiment when the rock is fully brine saturated.

2.2.2 Capillary Pressure Curves

Capillary pressure is defined by Tiab and Donaldson (1996) as:

“the difference in pressure between two immiscible fluids across a curved interface at equilibrium”

The curved surface between the two fluids is a consequence of preferential wetting of the capillary walls by one of the phases (Tiab and Donaldson, 1996). In an oil reservoir it is generally assumed that water is the wetting phase, and the pore spaces are the capillaries. Therefore the sharpness of curvature of the surface is dependant on the size and geometry of the pore space, wettability, mineralogy of pore walls and the proportions (saturations) of fluids present (Calhoun et al., 1949; Leverett, 1941; Tiab and Donaldson, 1996). It is assumed that within a reservoir the wetting phase (water) and non-wetting phase (oil) are in equilibrium, the pressure required to disrupt the equilibrium is a function of water saturation. Therefore in a water-wet oil reservoir, if

pressure is applied to pore fluids there will be a point where all the oil has been displaced from the pores and the irreducible water saturation ($S_{w_{irr}}$) is reached (Calhoun et al., 1949; Leverett, 1941; Tiab and Donaldson, 1996). Information that is discernable from a capillary pressure curve is shown in Figure 2.14.

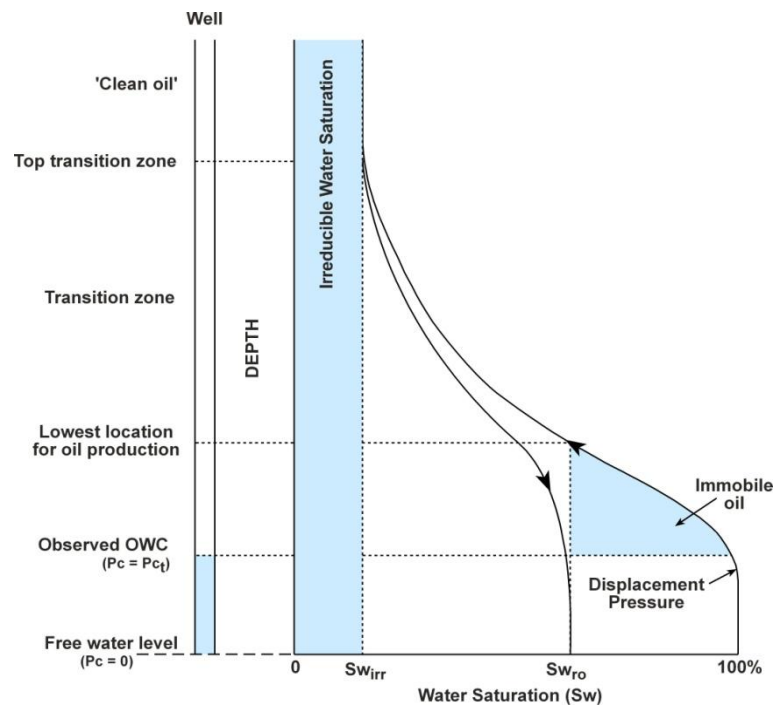


Figure 2.14: Schematic capillary pressure curve, highlighting the parameters determinable, i.e. irreducible water saturation ($S_{w_{irr}}$), transition zone, displacement pressure.

Capillary pressure curves can be produced using different methods; porous plate, centrifuge, which use real fluids and mercury injection, which uses mercury not real fluids. In this study, the capillary pressure curves were generated using the porous plate method and the centrifuge method.

Porous Plate Method

The porous plate method works on the principle of brine displacement by air or oil from a fully saturated sample. The samples are fully saturated with brine and placed on a saturated porous plate in a capillary pressure cell. To obtain the measurements required

for a capillary pressure curve, the sample is desaturated in stages via an increase in pressure, so that the air displaces brine. After each pressure increase the sample is left to regain saturation equilibrium and once this has been reached the sample is removed from the porous plate and weighed. The decrease in sample weight is an indication of the decrease in brine saturation. These measured weights are then used in conjunction with pore volume and brine density to calculate the brine saturations at each of the pressure points. This is done using:

$$S_{w_{change}} = \left[\frac{(W_1 - W_2)}{\rho_b} \right] / V_p \quad (2.14)$$

Where:

$W_1 - W_2$	=	Sample weight change at each capillary pressure, (g)
V_p	=	Pore Volume (cm ³)
ρ_b	=	Density of Brine (g/cm ³)

These calculated changes in brine saturation ($S_{w_{change}}$) are subtracted from the initial brine saturation to obtain the saturation values at each capillary pressure value. The saturation values are then plotted against the respective capillary pressure values to produce the capillary pressure curves (Craig, 2003; Tiab and Donaldson, 1996).

There is, however, the potential for error in these measurements (Lindsay, 2006), and three common errors are easily identifiable on the resultant capillary pressure curves. Sometimes initial brine displacement occurs with no saturation change for the first few pressure increases, which is caused by improper cleaning of the sample (Figure 2.15a). If during the measurements the sample loses contact with the porous plate, then the resultant curve will produce a straight line as no further desaturation will occur (Figure

2.15b). Grain loss in the sample during the weighing stage causes a “kick” in the graph (Figure 2.15c). However, this could also be an actual property of the sample, as a “kick” could be caused by the displacement of capillary blocking grains, such as clays.

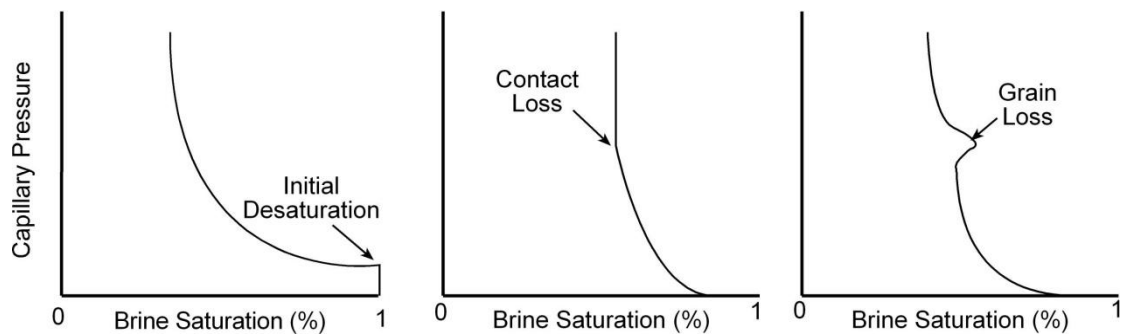


Figure 2.15: Schematic diagram of the main errors associated with the porous plate method as they appear on the capillary pressure curves: initial desaturation; contact loss; grain loss (Lindsay, 2006).

Centrifuge Method

The centrifuge method again uses a fully brine-saturated sample with oil as the displacing fluid. The saturated core plugs are mounted in a rotor bucket and surrounded by the displacing medium. The rotor is then spun at rates of rotation equivalent to capillary pressures, and the volume of displaced brine is measured. The core plug is then maintained at each capillary pressure until equilibration is achieved. The whole assemblage was weighed before and after the test so evaporitic losses can be detected. The capillary pressure and saturation data is then derived from the volumes of brine displaced, the core plug pore volume and the corresponding pressures (Craig, 2003; Tiab and Donaldson, 1996). Due to the wait time required for samples to reach equilibrium at each stage these measurements are time consuming, often requiring weeks to months per sample.

The capillary pressures at each interval are then calculated from the rate of rotation using (Craig, 2003):

$$Pc = 1.578 \times 10^{-7} \cdot (\rho_b - \rho_o) \cdot \left(R - \frac{L}{2}\right) \cdot L \cdot RPM^2 \quad (2.15)$$

Where:

- ρ_b = density of brine (g/cm³)
- ρ_o = density of oil (g/cm³)
- R = distance from centre of rotation to outer face of core plug (cm)
- L = length of core plug (cm)
- RPM = revolutions per minute

The changes in the brine saturation are calculated using:

$$S_{w \text{ change}} = \frac{(V_p - V_{displaced})}{V_p} \quad (2.16)$$

Where:

- V_p = pore volume (cm³)
- $V_{displaced}$ = volume of displaced fluid (cm³)

The change in average brine saturation is added to or subtracted from the initial brine saturation, to give either imbibition or drainage.

To then determine the end saturation values, a plot of $Pc \cdot S_{w \text{ avg}}$ vs. Pc is plotted, and the slope measured at each reported capillary pressure, and fed into the equation below:

$$S_w = \frac{d(Pc \cdot S_{avg})}{dPc} \quad (2.17)$$

These end saturation values can then be plotted against the respective capillary pressures to produce the final capillary pressure curves (Craig, 2003).

2.2.3 Saturation Height Derivation

Saturation height functions provide a way to calculate saturation without relying on resistivity measurements, and are based on the height above the free water level (FWL). Many varieties of saturation height functions are available; Skelt-Harrison, Leverett J-function, or FOIL function to name a few (Cuddy et al., 1993; Harrison and Jing, 2001; Leverett, 1941; Skelt and Harrison, 1995; Worthington, 2002). The Leverett J-function is based on core data but can also be used on log-data. Therefore providing a good calibration between the two data sets and thus is ideal for the saturation height models in this project.

It is possible to use core capillary pressure curves to calculate Leverett J-functions to develop a transform linking J-functions to water saturation (S_w). Thus, using a plot of water saturation vs. J-function, water saturation can be determined at any point for which the J-function value is known (Figure 2.16).

Work-flow for S_w -height analysis

1) Convert capillary pressure (psi) to reservoir conditions using equation (2.18), where σ is the interfacial tension (dynes/cm) and θ is the contact angle (degrees):

$$Pc_{res} = Pc_{lab} \times \frac{[\sigma \cos.\theta]_{res}}{[\sigma \cos.\theta]_{lab}} \quad (2.18)$$

2) Then convert Pc_{res} to height (h) above free water level (in metres), where the density of water (ρ_w) and oil (ρ_o) are in g/cc:

$$h = \frac{Pc_{res} \times 2.309}{(\rho_w - \rho_o)} \quad (2.19)$$

3) Can then calculate the J-function using equation (2.20), which uses a rock quality indicator with the permeability/porosity ($\sqrt{k/\Phi}$) term, since permeability (k) represents pore throat size (μm):

$$J = \left[\frac{0.217 \times Pc_{res}}{(\sigma \cos.\theta)_{res}} \right] \times \left(\sqrt{\frac{k}{\Phi}} \right) \quad (2.20)$$

4) Plot J-values against brine saturations, which will allow for the determination of saturation values at any point once the capillary pressure is known. If the capillary pressure is not measured it can be calculated from knowing the height above free water level (equation 2.19).

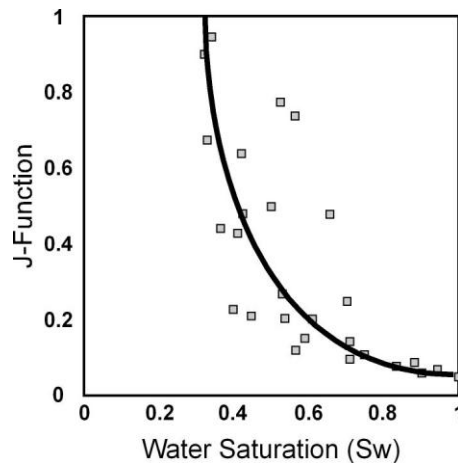


Figure 2.16: Schematic example of a J-function vs. water saturation (S_w) plot

However, the Leverett J-function is “inappropriate where there is a diversity of rock types within a reservoir” (Harrison and Jing, 2001; Leverett, 1941; Stiles, 1998) and data are needed from samples that exhibit the same rock-type or facies with the same properties. This is explored further in Chapter 6.

2.2.4 Porosity Distributions

In addition to the saturation estimations for the different facies it is important to note the porosity distributions of the different facies. The point here is to see if there is any associated distinctive porosity distributions, e.g. bi-modal, with the particular facies and through that association with the clay (chlorite) occurrence/content.

High Pressure Mercury Injection measurements can be used to determine many properties of a sample, for example capillary pressure data, pore-space distributions, grain density and bulk density. In this research, it is the pore-space distributions which are of interest. The measurements are made on core plugs, which are initially clean and dry. At this stage the samples are placed into a penetrometer, and then weighed. The penetrometer is then filled with mercury, and the bulk volume of the sample is determined at this point. Mercury is then injected into the sample at increasing incremental pressure. At each point the mercury intrusion was monitored while the pressure was held constant, and the pressure and total volume at that point is recorded.

It is possible that initial apparent intrusions at low pressure may be the result of the mercury conforming itself to the surface irregularities of the sample, which are not representative of the pore structure. Therefore the threshold pressure is identified where the rate of mercury injection increases rapidly. The cumulative volumes of mercury injected are expressed as a fraction of the total pore volume. The minimum pore throat radius which can be penetrated at each mercury displacement pressure can then be calculated using:

$$r = \frac{2\sigma \cdot \cos \theta \cdot C}{P_c} \quad (2.21)$$

Where:

- r = pore throat radius (μm)
- σ = interfacial tension between air and mercury (485 dynes/cm)
- θ = contact angle between air and mercury (140 degrees)
- P_c = capillary pressure (psia)
- C = conversion constant (0.145)

This allows a graph of pore volume injected vs. pore throat radius to be constructed, the differential of which produces the pore throat size distribution function, which is then smoothed and normalised. The normalised pore throat size distribution is then graphically presented alongside pore throat radius vs. saturation, and permeability distribution vs. pore throat radius. It is the pore throat radius vs. function distributions which is of interest for determining pore-space distributions (Lindsay, 2002).

2.2.5 Polished Thin Section Analysis

Polished thin sections provide a visual characterization of the sandstone samples, and aid in facies definition. A simple descriptive classification of the different sandstones enables the visual identification and presence of pore-lining clays – as a mild green rim to quartz grains. Point-counting allows for a semi-quantitative analysis of the composition.

2.2.6 SEM Analysis

Polished thin sections can be carbon-coated to allow analysis under the scanning electron microscope (SEM), this allows for a visual classification of the type of clays present in sandstone samples, as well as providing a semi-quantitative idea of mineral composition. The instrument used is the Hitachi S-3600N; an environmental scanning electron microscope (ESEM). In backscatter detector mode the visual identification of clays and grains is possible, at a range of magnifications. The visual identification of clays is possible as they each have distinct morphological characteristics (Figure 2.17), for example chlorite appears platy and can form rosettes, while kaolinite will have a bookish appearance (Welton, 1984).

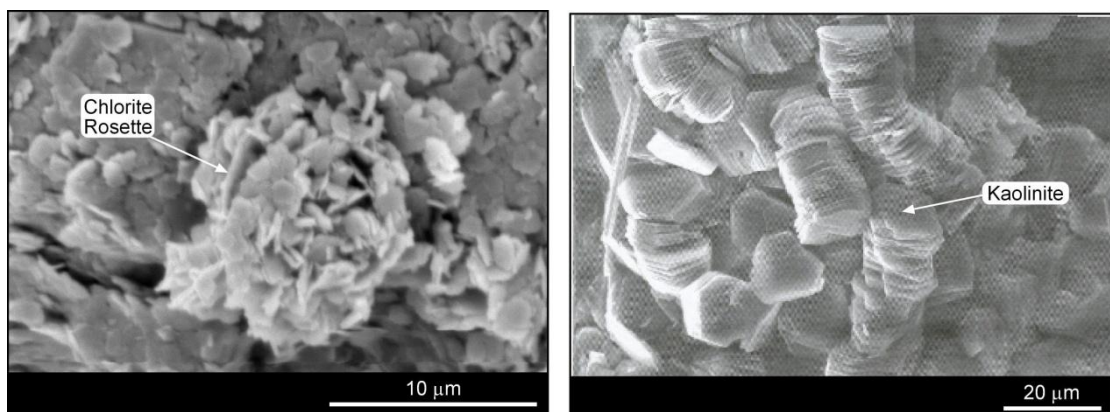


Figure 2.17: SEM images of some of the common clays and their characteristics – chlorite rosettes (left) and “bookish” kaolinite (right) (Milliken, 2003)

In X-ray detector mode it is possible to gain a semi-quantitative analysis of the mineralogy of the sample. When working in this mode, a beam current of 15kV and 70A was used, at a working distance of 15mm. For each sample, an area totalling 1 cm³ was mapped, at magnification x100, for elemental composition, with each area undergoing exposure to the x-ray beam for 20 minutes. The maps show the relative proportions of aluminium (Al), magnesium (Mg), carbon (C) (for pore-space), silica

(Si), manganese (Mn), iron (Fe), and titanium (Ti). This element mapping allows for semi-quantitative analysis of mineralogical composition, to be backed up by selecting individual points on specific grains and running a point spectral analysis. An example of an element map and associated point spectral analysis is shown in figure 2.18.

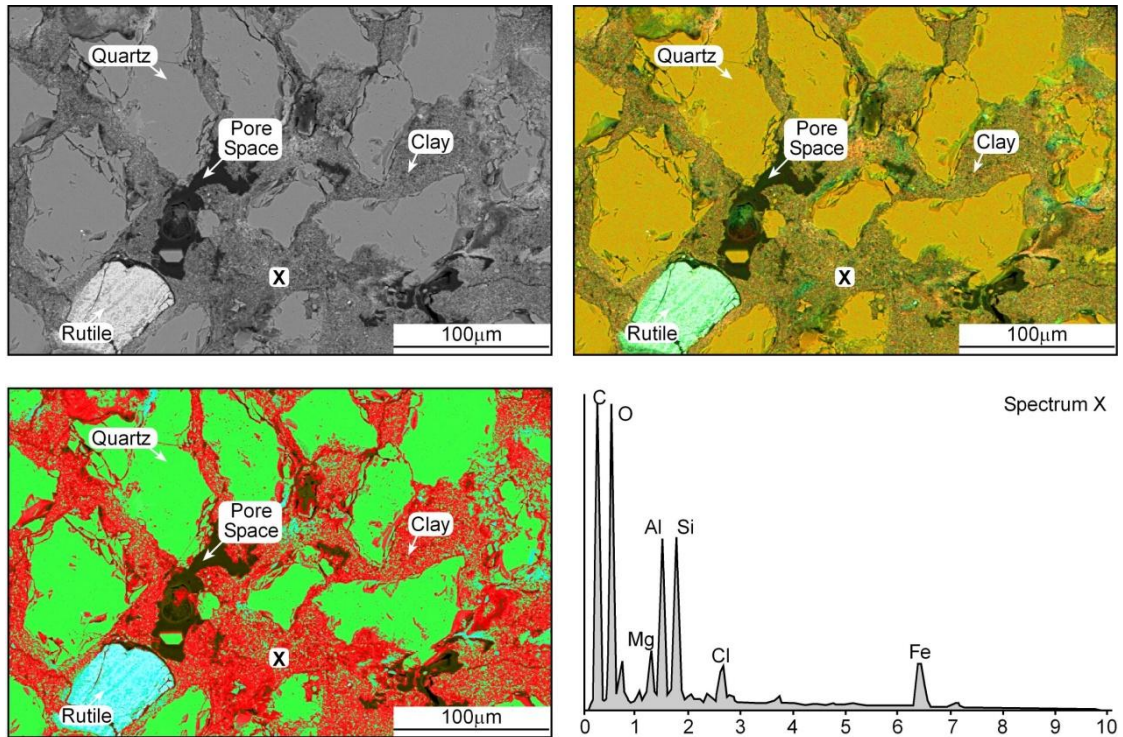


Figure 2.18: Element map of thin section, with locations of spectral composition from the grains, and spectra 3 as example.

2.2.7 X-Ray Diffraction Analysis

X-ray diffraction (XRD) measurements on the clay sized ($<2\mu\text{m}$) fraction of sandstones allows for quantitative analysis of the mineralogical composition (Brindley, 1952; Moore and Reynolds, 1997; Velde, 1992). Through the interaction of x-rays (2.5 – 35 degrees 2 theta) with a powdered sample the resulting x-ray diffraction pattern can be used to identify the presence of different clay minerals (Figure 2.19). Each of the main clay minerals, illite, smectite, kaolinite, chlorite, will have identifying peaks

corresponding to 001 basal reflectors (Moore and Reynolds, 1997). However, in cases where both chlorite and kaolinite are present the identifying peaks overlap (Figure 2.19); therefore the sample is heated to 550°C for 1hr. This causes kaolinite to become amorphous to X-rays therefore when the sample is re-run only chlorite spectra will be visible (Moore and Reynolds, 1997).

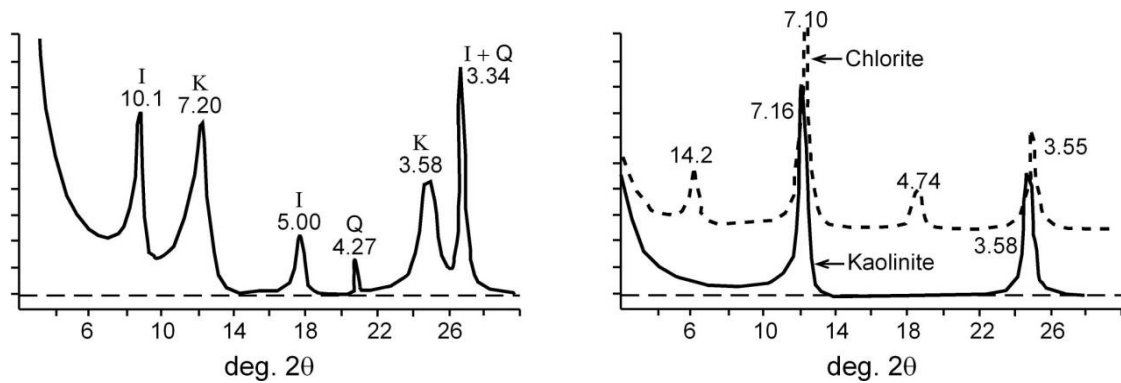


Figure 2.19: Example of X-ray diffraction (XRD) identification of left: bulk mineralogy for a sandstone sample: I = illite, K = kaolinite, Q = quartz, right: similarity between chlorite and kaolinite XRD profiles from the clay fraction of a sandstone sample (modified from Moore and Reynolds, 1997)

There are other examples of clay minerals occurring as mixed layers, e.g. smectite-illite, and the methods of differentiation are explained in Moore and Reynolds (1997). However, since the presence/absence of chlorite is the primary focus of this project, those methods, though run on the samples, are not described here.

3. Review - Chlorite

3.1 Introduction

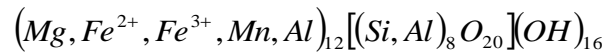
Of all the common sedimentary clays the presence of chlorite in a hydrocarbon reservoir is considered to cause the most problems due to its variable composition and cation exchange capacity (CEC). Sedimentary chlorite compositions range from iron-rich to magnesium-rich, and can form through various methods; these are discussed in this chapter. Understanding the petrographic identification, sedimentary origin and distribution of chlorite is necessary to understand its effect on the physical properties (porosity, permeability and saturation) of a reservoir, particularly where lower hydrocarbon saturation estimation can arise.

3.2 Background

In siliclastic sedimentary rocks clay is often classified based on grain size; $<2\mu\text{m}$ in diameter. Grains which fall into this size category often have the same sort of crystallographic (mineral) structure, known as phyllosilicate (Velde, 1992) or sheet-like, these include micas, talc, chlorite, serpentine, kaolinite, illite, smectite and vermiculite (Deer et al., 1992). Other minerals, such as quartz, can also exhibit a small, $<2\mu\text{m}$ grain size, therefore it is better to define clay minerals based on their chemical and mineralogical characteristics. “True” clay minerals constitute of the kaolinite group, illite group, smectite group and vermiculate; in addition to the sheet-like structure, they are all hydrous silicates and yield refractory materials at high temperatures (Brindley and Brown, 1980; Deer et al., 1992; Velde, 1992). In this project the term “clay” refers to the group of phyllosilicates.

3.2.1 Chemical Composition

The chlorite group is part of the phyllosilicate clays; it is an iron aluminium magnesium silicate hydroxide with the chemical formula:



Chlorites are sheet silicates that exhibit regularly alternating negatively charged tetrahedral – octahedral – tetrahedral 2:1 layers (Figure 3.1).

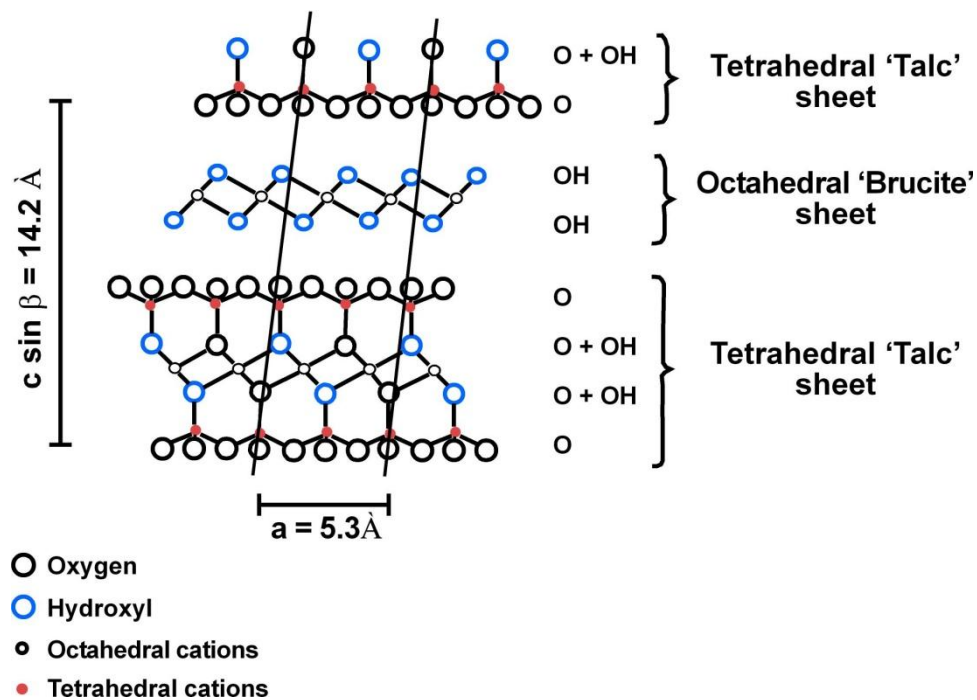
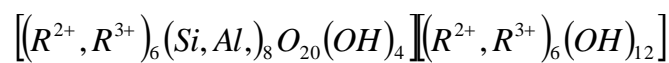


Figure 3.1: Idealized structure of chlorite (modified from Deer et al., 1992)

This leads to an alternative version of the above formula:



This formula illustrates the layered nature of chlorite, separated into the tetrahedral layers and octahedral layers respectively, while R^{2+} and R^{3+} represent the divalent (Mg, Fe) and trivalent (Al, Fe) cations respectively (Henn et al., 2001). By substituting different elements into the octahedral and tetrahedral sites in both layers charges can be created, thus creating a variable cation exchange capacity (CEC). As a result there are many varieties of chlorite, which can be divided into four main classifications: Clinocllore (Mg-rich); Chamosite (Fe-rich); Pennantite (Mn-rich) and Sudoite (Al-rich); the latter two being much less common varieties (Deer et al., 1992). Chlorite occurs as detrital metamorphic chlorite and authigenic and diagenetic sedimentary chlorites. As figure 3.2 illustrates, a compositional difference exists between metamorphic and diagenetic chlorites, with metamorphic chlorites exhibiting less compositional variation than diagenetic chlorites, particularly with Al-content (Velde, 1985).

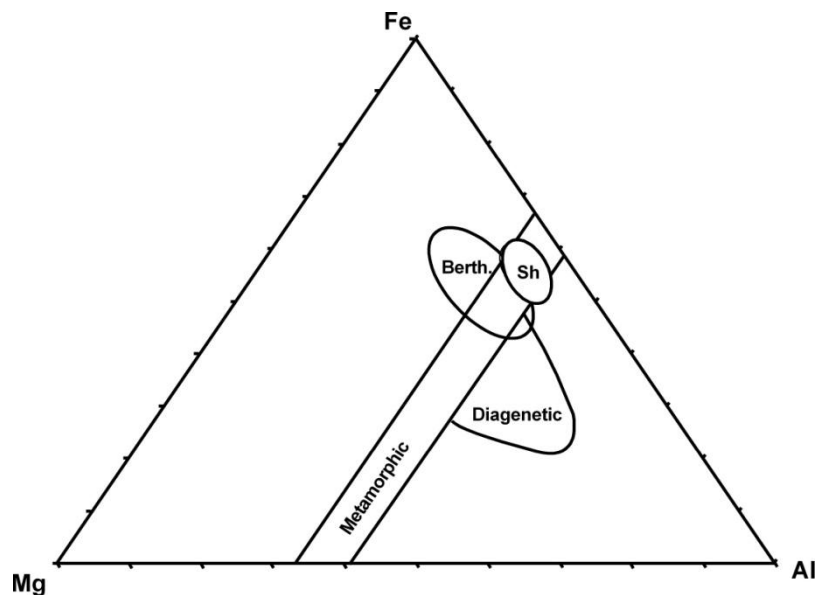


Figure 3.2: Al-Fe-Mg plot with the different compositional fields of metamorphic and diagenetic chlorites, Berth = berthierine, Sh = shale compositions (modified from Velde, 1985)

3.2.2 Cation-Exchange-Capacity

The cation exchange capacity (CEC) of clays is, quite simply, a measure of the amount of exchangeable ions on the reactive surfaces of the clays (Gall et al., 1983). In general clays have high cation exchange capacities and affect the physical properties and resistivity measurements of rocks. As a result many models have been built up around this effect, known as shaly sand models (Clavier et al., 1984; Poupon and Leveaux, 1971; Revil et al., 1998; Waxman and Smits, 1968). These will be discussed in more detail in chapter 6.

The cation exchange capacity of chlorite is of interest in this study, and limited literature is available. However, all documented examples indicate chlorite has low CEC values, lower than most other clays and iron-rich minerals, e.g. pyrite and glauconite (Clavier et al., 1984; Gall et al., 1983; Henn et al., 2001) (table 3.1). The charge in chlorites is created when Si^{4+} is replaced by Al^{3+} in the tetrahedral sheet, and R^{2+} is replaced by R^{3+} in the octahedral sheet (see chemical formula above) (Durand et al., 2001; Henn et al., 2001). Since the replacement ions create opposing charges in the sheets the sum of these fixed charges are low to nil (Henn et al., 2001). An additional charge can occur due to broken bonds or surface defects, which are compensated for by rearrangements with water molecules, creating OH groups, which can be exchanged for cations (Durand et al., 2001; Henn et al., 2001). However, this is usually a very weak CEC, and would not contribute greatly to the effect on resistivity.

Clay Mineral	Cation Exchange Capacity (meq/100g)	Reference
<i>Kaolinite</i>	2.0 – 4.9	<i>Van Olphen & Fripiat (1979)</i>
<i>Glauconite (montmorillonite)</i>	5.0 – 39.0	<i>Manghnani & Hower, (1964)</i>
<i>Illite</i>	26.6 – 69.0	<i>Van Olphen & Fripiat (1979)</i>
<i>Chlorite</i>	2.0 – 14.0	<i>Henn, et al.,(2001)</i>

Table 3.1: Some cation exchange values for common clays and iron-rich minerals

3.1 Formation

Deer, et al (1992) state that “*Chlorites are derived from the aggradation of less organised sheet minerals, by the degradation of pre-existing ferromagnesian minerals and by crystallisation from dilute solutions of their components*” (i.e. from pore fluids). Thus in sedimentary environments chlorites are most commonly diagenetic and are thought to form within the first 100m of burial, at temperatures <100°C (Hillier, 1994). The mode of formation of diagenetic chlorite can vary in relation to Mg or Fe dominance within the structure; i.e. chamosite (Fe-rich) or clinochlore (Mg-rich) form in different ways (Aagaard et al., 2000; Bjorlykke, 1998; Ehrenberg, 1993; Hillier, 1994; Pay et al., 2000; Ryan and Hillier, 2002). Hillier (1994) demonstrates that clinochlore (Mg-rich chlorite), for example, commonly forms via the alteration of smectite, and in particular environments: most commonly in aeolian sandstones or sabkhas within arid and evaporitic environments. The resultant Mg-rich chlorites will often exhibit honeycomb morphology, similar to that of their smectite precursor (Weibel, 1999). The Fe-variety (chamosite) occurs most commonly in sandstones deposited in marine to non-marine transitional environments, often with a precursor mineral originating from deposition (Table 3.2) (Hillier, 1994; Pay et al., 2000).

The formation of Fe-rich chlorite occurs either by the alteration of a precursor mineral, kaolinite or berthierine, with increasing burial depth, or from the direct precipitation from pore fluids. All methods require the addition of iron (Fe) and magnesium (Mg) ions. The Mg and Fe ions in the pore waters are believed to originate from the alteration of volcanoclastic lithic fragments to illite within the sandstone (Milodowski and Zalasiewicz, 1991; Ryan and Reynolds, 1996), or from the erosion of soil profiles by river waters, which then transport the ions in colloid form.

Stratigraphy	Age	Location	Depositional Environment	References
Frio or Vicksburg Formation	Oligocene	Texas & Louisiana	<i>Deltaic</i>	(Grigsby, 2001; Sullivan and McBride, 1991)
Wilcox Group	Palaeocene – Eocene	Texas Gulf Coast	<i>Deltaic: especially distributary channels</i>	(Boles and Franks, 1979)
Basal Belly River	L. Cretaceous	Western Canada, Alberta	<i>Deltaic: distributary channel mouth bar & interdistributary</i>	(Longstaffe, 1986)
Terry Sandstone	L. Cretaceous	Denver Basin, Colorado	<i>Near shore shallow marine</i>	(Pittman, 1988)
Frontier Formation	L. Cretaceous	Powder River Basin, Wyoming	<i>Reworked offshore marine bar</i>	(Tillman and Almon, 1979)
Tuscaloosa or Woodbine Formation	L. Cretaceous	Louisiana & Mississippi	<i>Fluvial to near-shore marine</i>	(Ryan and Reynolds, 1996)
Garn Formation	M. Jurassic	Haltenbanken, offshore Norway	<i>Braid Delta, merging with foreshore and shoreface deposits</i>	(Ehrenberg, 1993)
Tofte Formation	Toarcian	Haltenbanken, offshore Norway	<i>Shallow marine, deltaic</i>	(Ehrenberg, 1993)
Intra Dunlin Sand	E. Jurassic – Pliensbachian	Veselefrikk Field, offshore Norway	<i>Near shore marine, ebb tidal delta shoal or mouth bar</i>	(Ehrenberg, 1993)
Tilje Formation	E. Jurassic	Haltenbanken, offshore Norway	<i>Tidally influenced shallow marine deltaic</i>	(Ehrenberg, 1993)
Halse Formation	E. Jurassic	Bornholm, Denmark	<i>Shallow marine with ironstone layers</i>	(Larsen and Friis, 1991)
Statfjord Formation	Rhaetian-Sinemurian	Veselefrikk Field, offshore Norway	<i>Shallow marine middle – upper shoreface</i>	(Ehrenberg, 1993)
Spiro Sandstone	Pennsylvanian	Arkoma Basin, Oklahoma & Arkansas	<i>Variety of marine & non-marine fluvial & tidal channels</i>	(Gross et al., 1995; Lumsden et al., 1971)
Clair Group	Devonian – Carboniferous	Offshore Shetland Isles, UK	<i>Fluvial, aeolian & lacustrine</i>	(Pay et al., 2000)
Goru Formation	Cretaceous	Sawan Field, Indus Basin, Pakistan	<i>Shallow marine, volcanoclastic</i>	(Berger et al., 2009)
Skagerrak Formation	L. Triassic	Central Graben, North Sea	<i>Fluvial, with marginal marine</i>	(Humphreys et al., 1989; Weibel, 1999)
Jureia & Itajai-Acu Formations	U. Cretaceous	Santos Basin, Brazil	<i>Shallow marine & turbidites</i>	(Anjos et al., 2003)

Table 3.2: Examples of sandstones containing pore-lining chlorites and their associated depositional environment (modified from Hillier, 1994)

In shallow-marine environments the more common source of Fe and Mg ions is from a fresh-water i.e. fluvial, source (Figure 3.3). When the fluvial waters interact with oceanic waters (specifically the OH⁻ ions) the Fe and Mg ions flocculate, and are free to attach themselves to grains (Longstaffe, 1986). If flocculates attach themselves to clay grains they can be transported and deposited in the offshore mudstones, before undergoing reduction to be released back into mobile pore fluids (Boles and Franks, 1979). Alternatively, the ions can attach directly to quartz grains and react with the pre-existing grains once deposited in the sandbody. If direct precipitation of diagenetic chlorites occurs close to this fluvial supply of Fe, then a concentration of diagenetic chlorites in associated facies would be expected, and as table 3.2 illustrates, there is a dominance of pore-lining chlorites in fluvial and deltaic sandstones (e.g. Ehrenberg, 1993; Longstaffe, 1986).

Once the pore waters are saturated with Fe and Mg ions it is possible to form diagenetic chlorite in multiple ways, most of which require temperatures below 100°C, and occur early in the diagenetic evolution of the sandstones (Henn et al., 2001; Longstaffe, 1986).

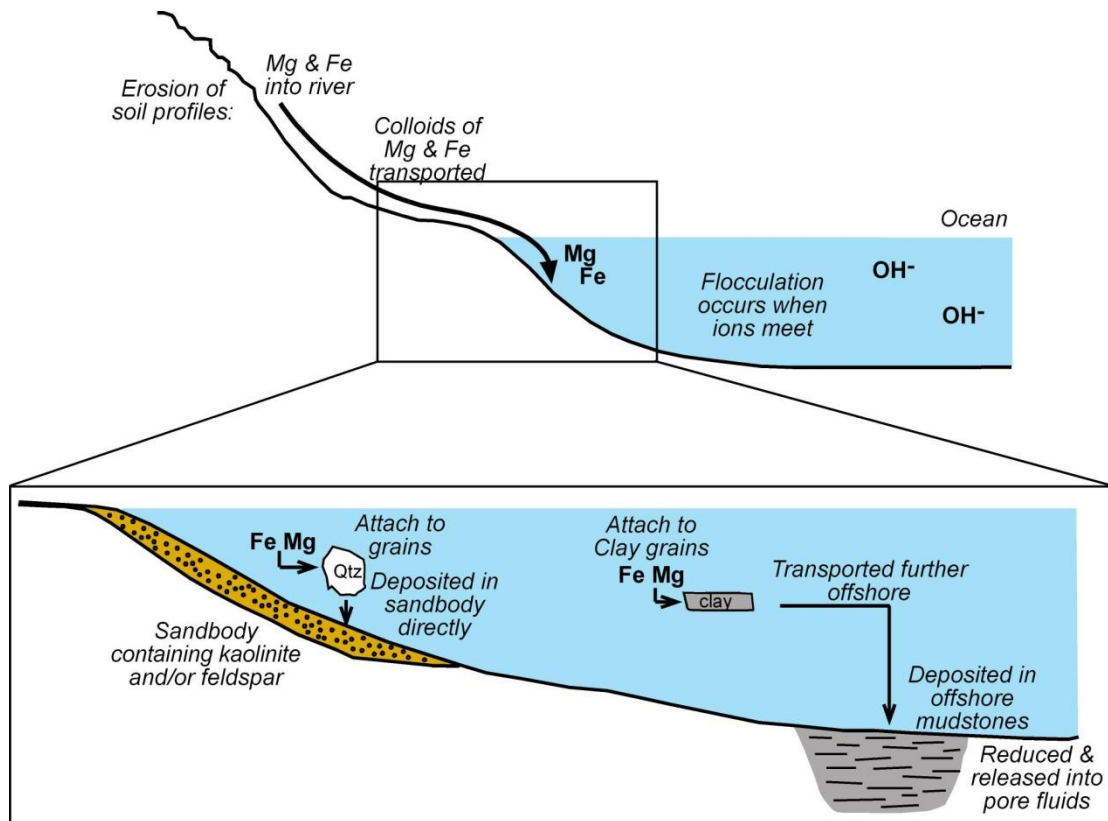
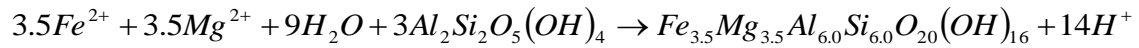


Figure 3.3: Schematic representation of environment of formation of chlorite, with possible methods of introducing Fe and Mg into the system.

3.3.1 Alteration of kaolinite

The dissolution of kaolinite may produce authigenic chlorite, particularly in shallow marine environments (Weibel, 1999). It has been observed that kaolinite often occurs within the mineral assemblage associated with pore-lining clays, and decreases in abundance as pore-lining chlorite increases (Aagaard et al., 2000; Bjorlykke, 1998; Pay et al., 2000; Weibel, 1999). Since kaolinite has a similar composition to chlorite, without the Mg or Fe, it would be possible that interaction with fluids rich in Fe/Mg ions could prompt the alteration of kaolinite to chlorite (Deer et al., 1992; Humphreys et al., 1989). Boles and Franks (1979) studied the composition of kaolinite and chlorite in the Wilcox sandstones and developed the following reaction to account for the decrease in kaolinite with increase in chlorite, based on the average chlorite composition:



As in the case of the Wilcox sandstones, the chlorites formed from kaolinite alteration will often exhibit a particularly high aluminium content (Boles and Franks, 1979; Humphreys et al., 1989; Norry, 2009, Pers. Comm.).

3.3.2 Alteration from berthierine

Another common precursor mineral is believed to be berthierine, which is already Fe-rich and often appears as anomalous Fe-rich clay in shallow marine settings (Humphreys et al., 1989; Ryan and Hillier, 2002). Multiple studies (Aagaard et al., 2000; Ehrenberg, 1993; Hillier, 1994) outline the presence of interstratified 7Å and 14Å layers in sandstones known to contain pore-lining chlorites. The 7Å Fe-rich clays occur at shallow depths, and are believed to be the precursor to chlorite. It has been suggested that chlorites gradually form at depths equal to ~100°C (Aagaard et al., 2000; Hillier, 1994). Studies have shown that the abundance of the 7Å mineral decreases with depth, and there is a corresponding increase in the 14Å mineral; chlorite (Ehrenberg, 1993). Ehrenberg (1993) theorises this increase in 14Å chlorite with depth implies the 7Å layers develop at surface or shallow marine conditions, and that the 7Å mineral undergoes progressive recrystallisation with increasing temperature up to ~100°C, confirmed by Aagaard et al, (2000). The 7Å mineral is popularly believed to be berthierine and therefore the precursor to chlorite due to its strong 7Å reflector and chemical similarity to chlorite (Deer et al., 1992). Berthierine is also found in the modern verdine facies and therefore forms near surface or early in the diagenetic process (Ryan and Hillier, 2002) and is associated with shallow marine,

fluvial and marine-non-marine transitional environments. It has also been suggested by Needham et al. (2005) that the chlorite precursor could be excreted as clay rims from worm fecal matter, before being subsequently altered to chlorite with increased burial depth.

3.3.3 Direct precipitation from pore waters

An alternative process is the formation of chlorites from the direct precipitation of pore-fluids, assuming the necessary ions are available. The Fe and Mg ions could originate from fresh-water input or from the breakdown of biotite grains, while the gradual dissolution of feldspars could provide the Al, Si ions. This direct precipitation could be influenced by meteoric waters flushing through early diagenetic sediment and, in shallow marine environments, meteoric water circulation may contribute to greater diagenesis near-shore (Bjorlykke, 1998; Hillier, 1994). This would create a changing profile of chlorite abundance from proximal (high chlorite concentration) to distal sand-bodies (low chlorite concentration), allowing for the identification of this process. Humphreys *et al* (1989) argue that this direct precipitation is more applicable to later pore-filling chlorites, and is not directly constrained by the original depositional environment. However, the present-day development of the verdine facies in shallow marine, deltaic environments supports the idea that the mixing of marine and fluvial/meteoric waters creates the specific geochemical conditions that encourage the formation of pore-lining chlorites, and therefore environment is specific to the development of sedimentary chlorites (Ryan and Hillier, 2002; Ryan and Reynolds, 1996).

3.4 Effect on Reservoir Quality

Oil companies are interested in sandstones containing an abundance of pore-lining clays (including chlorite), because early-formed clays are often associated with higher porosity. The formation of clay-coatings early in the burial history of sandstones can prevent later formation of quartz overgrowths, which can significantly reduce the porosity, by physically blocking the nucleation sites on the detrital quartz grains (Anjos et al., 2003; Hillier, 1994; Pittman et al., 1992). Normal compaction trends usually result in porosities of <10% by around 2000m depth, however higher porosities at depth (some >25% porosity) have been recorded in many locations including the Tuscaloosa sandstone, Louisiana (Pittman et al., 1992; Ryan and Reynolds, 1996), the Norphlet sandstone, Mississippi and Alabama (Dixon et al., 1989), the North Sea (Ehrenberg, 1993) and the Santos Basin, Brazil (Anjos et al., 2003) (Figure 3.4). These sandstones have a high proportion of grain-coating clays, commonly chlorite. For example in the Santos Basin, Brazil, chlorite is the main diagenetic component, occurring as pore-filling cement, replacing framework grains and most commonly as pore-lining cement (Anjos et al., 2003).

In some examples, double layers of chlorite coatings develop, producing a micro-porosity between the layers in addition to preserving the macro-porosity. Often sandstones containing grain with chlorite coatings will exhibit a distinct bi-modal porosity distribution, with peaks at micro (<0.1 μ m) and macro (>1.0 μ m) pore-throat radii (Anjos et al., 2003; Islam, 2009; Nadeau, 2000; Saner et al., 2006). In examples where these pore-lining clays have severely restricted quartz or carbonate cementation the sandstones can become mechanically weak and friable (Ryan and Reynolds, 1996; Saner et al., 2006).

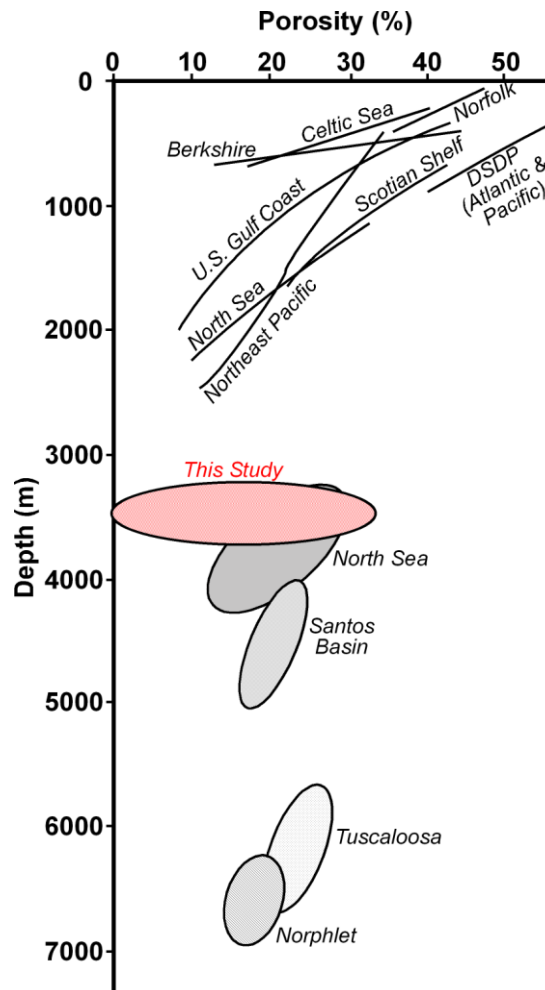


Figure 3.4: Some typical porosity compaction trends for sandstones, with high preserved porosity values from the Tuscaloosa sandstone, Norphlet sandstone, North Sea and Santos Basin sandstones with the A sandstone (*this study) for comparison (modified from Anjos et al., 2003).

In addition to affecting the porosity, grain-coating clays are commonly believed to constrict pore throats causing a reduction in permeability (Anjos et al., 2003; Howard, 1992; Islam, 2009; Schmid et al., 2004). Work by Islam (2009) illustrates a correlation between decreasing horizontal permeability and increasing chlorite content. The relationship between grain-coating clays and permeability is, however, more complex. Howard (1992) discusses whether it is the type of clay or the distribution within pore throats which has the greater effect on permeability. Through modelling permeability, pore throat radius, clay type and morphology Howard (1992) determined that blocky kaolinite can in fact reduce permeability more than fibrous

illite, as it physically blocks the pore-space in contrast to illite which creates drag-induced turbulence to flow. This is not always the case as, for example, in the Jauf Sandstone, Saudi Arabia, the presence of pore-bridging fibrous illites reduces the permeability more than the pore-lining chlorites (Saner et al., 2006). However, in general the presence of pore-lining clays reduces the permeability to less than that in an equivalent porosity clean sandstones (Luo et al., 2009).

Chlorite is often linked with low resistivity hydrocarbon reservoirs, where estimated water saturations are high as the high resistivity caused by hydrocarbons is masked by their presence (discussed in chapter 2). It is commonly thought that the cation exchange capacity (CEC) associated with clays is the cause of this low-resistivity. While this may be the case for clays such as kaolinite, illite and smectite with high CEC values, work by Henn et al (2001) suggests that the conductivity associated with the CEC in chlorites is too low to be a significant cause. However, the high irreducible water saturation associated with the micro-porosity caused by the pore-lining chlorites could be a factor (e.g. Anjos et al., 2003; Luo et al., 2009; Saner et al., 2006). These high irreducible water saturations commonly affect the measured borehole resistivity readings (inverse of conductivity), causing it to remain low in hydrocarbon-bearing sections in contrast to the water-bearing sections (Anjos et al., 2003; Luo et al., 2009; Rabaute et al., 2003).

3.5 Summary

Chlorite is a common sedimentary clay mineral, with a tetrahedral-octahedral-tetrahedral layer structure as part of the phyllosilicate (sheet) clays. Chemically it is an iron aluminium magnesium silicate hydroxide, with two dominant forms: clinocllore (Mg-rich) and chamosite (Fe-rich). The Fe-rich variety commonly forms in sedimentary environments in the transition between marine and non-marine

systems e.g. deltas. It is thought that they form either by the alteration of precursor kaolinite or berthierine, or by direct precipitation from pore waters. All methods require the addition of Mg or Fe ions, which are believed to be sourced from either the dissolution of volcanoclastic lithic fragments or from ions within fluvial waters, introduced from soil erosion. There is little difference to the resultant chlorites, although if formed via the alteration of kaolinite they will be particularly high in aluminium content.

This type of sedimentary chlorite forms early in the diagenetic history and, as such, affects the reservoir properties. By preventing quartz overgrowths higher porosities can be preserved where pore-lining chlorites are present, although the permeability can be reduced. Unlike other clays, the low cation exchange capacity of chlorites should not affect the resistivity enough to use shaly sand models; however, chlorites are still linked to low resistivity pay reservoirs and require more investigation.

In this case, however, it is thought that the chlorites may not be solely responsible for the low resistivity pay. The formation pore waters are known to have a very high salinity of >300000ppm (McNeill, 2006, Pers. Comm.), which would significantly lower the resistivity measurement. However, a lack of available data to test the formation waters effect, and following the original remit of the project, chlorite as the cause will be investigated.

4. Geological Setting/sedimentology

4.1 Regional Setting

The occurrence of chlorite in hydrocarbon reservoirs is not a new problem, but is relatively common, with many previous studies reporting grain-coating chlorites in sandstones with a range of geological ages and deposited in various sedimentary environments (Table 4.1). Some examples include the Upper Cretaceous Tuscaloosa Sandstone of Louisiana (Pittman et al., 1992); the Berea Sandstone; the Spiro Sandstone of the Red Oak field (Houseknecht and McGilvery, 1990) the Belly River sandstone of the Pembina Field (Longstaffe, 1986) and the Santos Basin, Brazil (Anjos et al., 2003).

In many of these previous studies, the presence of chlorite grain-coatings shows a strong, but variable dependence on the depositional environment or sub-environment. For example the chlorite coatings in the Berea Sandstone and the Spiro Sand occur in sandstones from the fluvial channels but not in the marine bars and sheet sands (Houseknecht and McGilvery, 1990), while in the Belly River sandstone, the chlorite preferentially develops in the sandstones deposited in the distributary channels (Longstaffe, 1986). The possible facies-controlled formation of grain-coating chlorites is discussed in more detail in chapter 3.

This study focuses on the Carboniferous sandstone (A) of the study field of the Berkine Basin, Algeria. The Berkine Basin is part of the greater Ghadames Basin (Figure 4.1), which is a large intracratonic sag basin on the North African platform, eastern Algeria (Underdown and Redfern, 2008).

<i>Age</i>	<i>Formation</i>	<i>Depositional Environment</i>	<i>Sandstone Composition</i>	<i>Location</i>	<i>Reference</i>
Cretaceous	Belly River	Deltaic	Volcanic Lithic Arenite	Alberta Basin, Canada	Carrigy & Mellon (1964)
Mississippian Jurassic	Big Injun Dogger-Beta	Deltaic ?	Lithic Arenite ?	West Virginia Holstein Trough, Germany	Heald (1965) Horn (1965)
Pennsylvanian	Spiro	Channel	Quartz Arenite	Arkoma Basin, Oklahoma	Pittman & Lumdsen (1968)
Mississippian	Berea	Fluvial/Bar	Quartz Arenite – Sublithic Arenite	West Virginia	Larese (1974)
Cretaceous	Horsetheif	Distributary channel/bar	Volcanic Lithic Arenite	Wyoming	Almon et al (1976)
Triassic	Unnamed	Fluvial	Subarkose	UK Sector, North Sea	Taylor (1978)
Pennsylvanian	Strawn	Deltaic	Sublithic Arenite	North-Central Texas	Land & Dutton (1978)
Cretaceous	Tuscaloosa	Fluvial/deltaic/bar	Lithic Arenite	Louisiana	Smith (1985); Thomson (1979)
Cretaceous	Frontier	Shelf ridges	Subarkose	Powder River Basin	Winn et al (1983)
Pennsylvanian	Granite Wash	Fan delta	Arkose	Mobeetie field, Texas	Dutton & Land (1985)
Miocene	Unnamed	Shallow marine	Lithic Arenite	Matagorda, offshore Texas	Thayer (1985)
Jurassic	Cotton valley	Marine	Mixed	Catahoula Creek field	Janks et al (1985)
Neogene	Surma group	?	?	Bengal Basin, Bangladesh	Imam & Shaw (1985)
Pennsylvanian	Springer	Shallow Marine	Quartz Arenite	Anadarko Basin	McBride et al (1987)
Cretaceous	Parkman	Marine	Subarkose	Powder River Basin	Dogan & Brenner (1983)
Jurassic	Norplet	Alluvial fan/eolian	Arkose- Subarkose	Florida, Alabama, Mississippi	Dixon et al (1989)
Pennsylvanian	Fanshawe	Deep fan	Lithic Arenite	Arkoma Basin, Oklahoma	Pittman & Wray (1989)

Table 4.1: Previous studies of reservoir sandstones containing chlorite coats, listing formation, depositional environment and location (modified from Pittman et al., 1992)

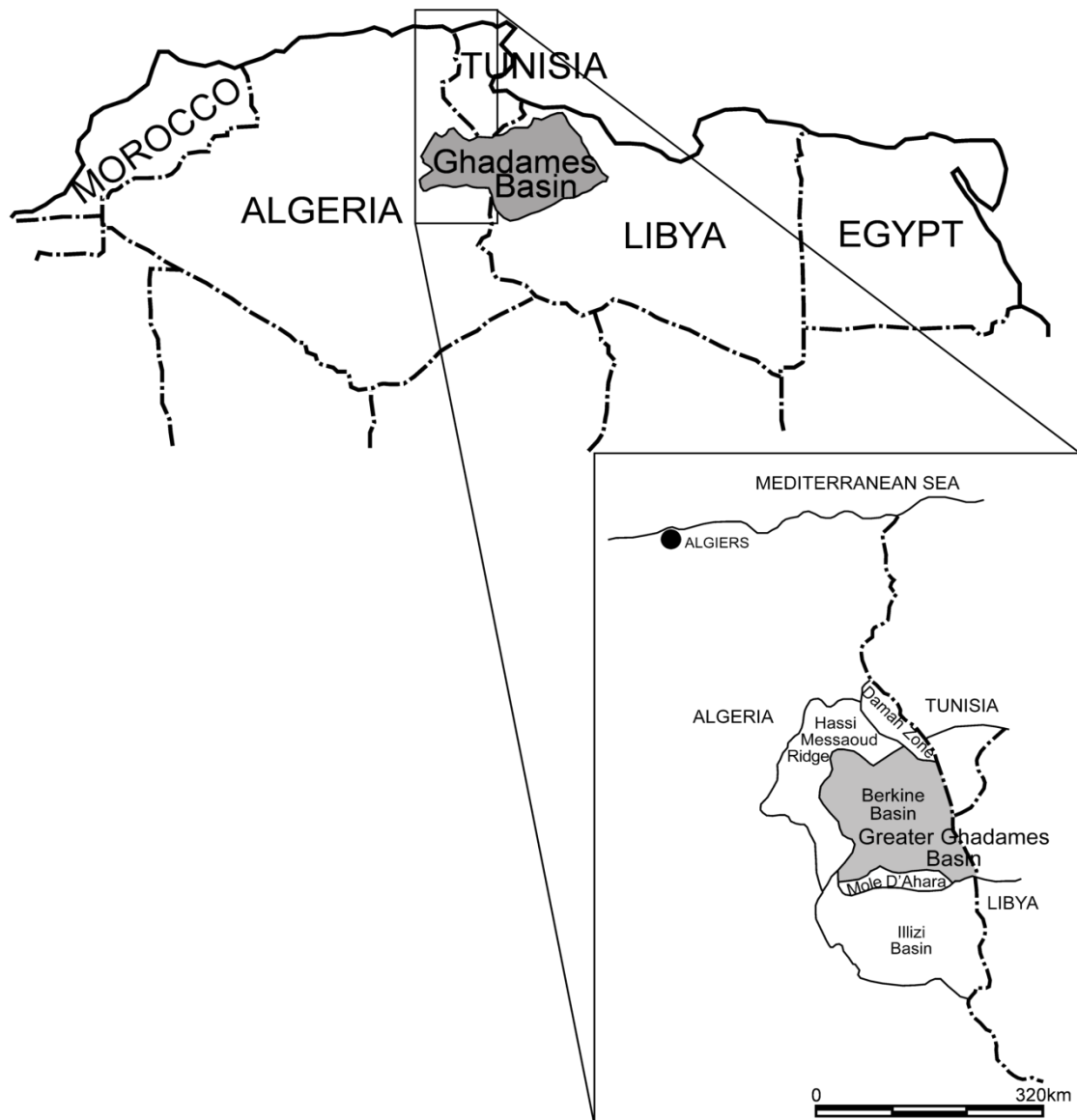


Figure 4.1: Locality map of the Berkine Basin, Greater Ghadames Basin in Eastern Algeria – with the study field highlighted (modified from Cochran and Petersen, 2001; Underdown and Redfern, 2008)

The Study field is the area of the Ghadames Basin currently being produced by ConocoPhillips (and other companies). Multiple wells penetrate the field targeting the Triassic TAG-I formation and the three Carboniferous reservoirs (A, B and C).

4.1.1 Geological History of the Ghadames Basin

The Ghadames Basin is a large intracratonic sag basin on the North African platform crossing Libya, Tunisia and Algeria. The North African margin has been affected by several tectonic events, with the Hercynian (Carboniferous – Permian) and Alpine

(Eocene) events exerting the strongest influence on the history of hydrocarbon generation in the basin (Underdown and Redfern, 2008).

Thick Palaeozoic strata (1500 – 3000m) are overlain by relatively thin Mesozoic and Cenozoic strata (300 – 700m) in the basin centre. These Mesozoic and Cenozoic strata thicken towards the north and west in areas where the Palaeozoic strata were severely eroded during the Hercynian orogeny (Underdown and Redfern, 2008) (Figure 4.2).

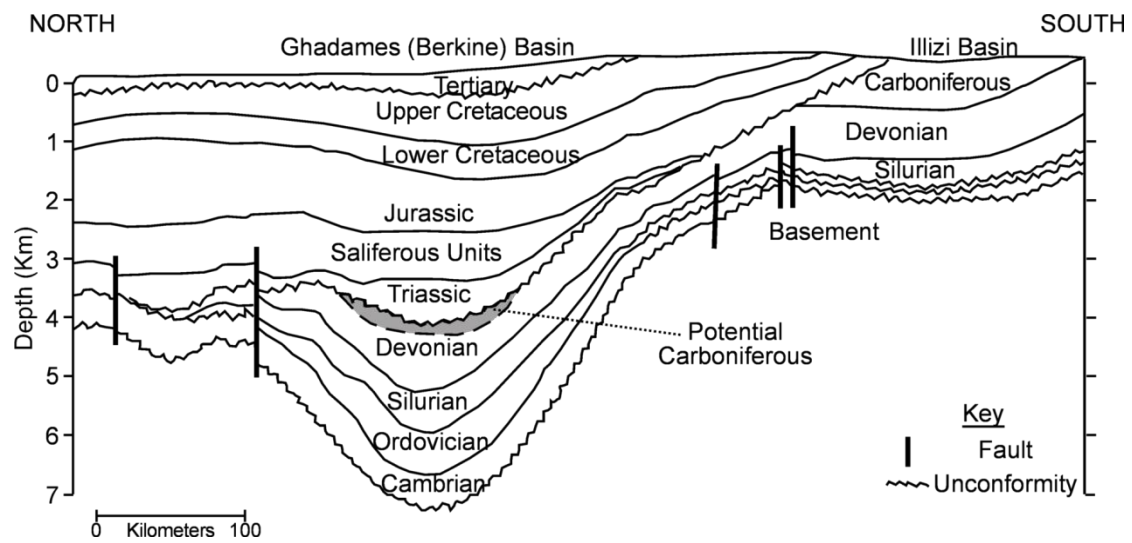


Figure 4.2: Cross-section of the Ghadames Basin (modified from Klett, 2000)

Continental siliciclastics were deposited throughout the Cambrian. A marine transgression and subsequent deposition of transgressive marine mudstones occurred during the Ordovician. An extensive glaciation across North Africa in the late Ordovician resulted in glacial-periglacial conditions on the southern margin of the Ghadames basin, while marine conditions continued further north. A major postglacial transgressive episode during the Early Silurian deposited regionally extensive marine mudstones (Tanezzuft Formation) which are the most important Palaeozoic source rock in the region, believed to have sourced 80 – 90% of the Palaeozoic hydrocarbons (Boote et al., 1998; Klett, 2000; Le Heron et al., 2009).

Regressive marine mudstones and sandstones were deposited in the Upper Silurian. In the south-east these sediments are truncated against the Caledonian unconformity which separates the Silurian deposits from the overlying Devonian succession (Underdown and Redfern, 2008). The lower Devonian is characterised by continental sandstones and mudstones and argillaceous transgressive marine mudstones. A regression in the late Devonian and Carboniferous deposited the shallow marine and deltaic sediments which are the focus of this study. Uplift related to the Hercynian orogeny resulted in the erosion of large parts of the Palaeozoic succession (Figure 4.2) and Mesozoic clastic, carbonate and evaporate sediments unconformably overly this Palaeozoic basin (Boote et al., 1998; Underdown and Redfern, 2008).

Triassic extension was related to the rifting of the Tethys Ocean and opening of the central Atlantic Ocean. Subsequent thermal subsidence during the Jurassic and Cretaceous resulted in the development of a north-west tilted extensional sag basin above the eroded remains of the earlier Palaeozoic basin (Underdown and Redfern, 2008).

Braided river sandstones form the basal Triassic TAG-I (Triassic Argilo Gréseux Inférieur) Formation which is one of the major reservoir targets within the Ghadames basin. The Upper Triassic – Jurassic transgressive marine mudstones and interbedded carbonates and regressive evaporites form reservoir seals above the truncated older Palaeozoic reservoir rocks (Underdown and Redfern, 2008).

Two unconformities exist within the Cretaceous: one between the base of the Lower Cretaceous and the underlying Mesozoic and Palaeozoic rocks and a second separating the Lower Cretaceous succession from the Upper Cretaceous and Palaeocene rocks. The Cenomanian transgression resulted in the deposition of mudstones and evaporites, overlain by shallow-marine carbonates deposited in an

embayment of the Neothethys Sea (Underdown and Redfern, 2008). Thin Cenozoic alluvial sands occur in the western (Algerian) section of the Ghadames basin, but are largely absent from the eastern (Libyan) section. Oligocene-Quaternary rocks are separated from the partially eroded Upper Cretaceous succession by the unconformity produced by the Alpine-orogeny (Sahagian, 1988; Underdown and Redfern, 2008).

4.1.2 Field-scale Geological background

The Berkine Basin has been explored by many oil companies. Extensive study of the Northern Part of the basin was published by Anadarko, focussing on the Upper Devonian and Lower Carboniferous strata (Cochran and Petersen, 2001). In the subsurface the Berkine Basin is bounded structurally by the Damah zone to the Northeast, the Hassai Messoud Ridge to the west and northwest, and separated from the Illizi basin in the south by the Mole D'Ahara (Cochran and Petersen, 2001) (Figure 4.1). The distribution of the Lower Devonian through to the Lower Carboniferous is controlled by Hercynian-related erosion in the north and west and the Mole D'Ahara in the south (Cochran and Petersen, 2001). In the Northern part of the Berkine Basin the basal part of the Carboniferous (Tournaisian and earliest Viséan) is missing, resulting in a minor angular unconformity between the uppermost Devonian and Viséan (Cochran and Petersen, 2001), but further east the succession is more complete (Figure 4.3). This more easterly section is the location of the Study field, with the Lower Carboniferous reservoirs in this area forming the focus of this research. These reservoirs were identified as Upper Devonian until a palynology study by Hughes et al. (2003) reclassified them as Tournaisian (Lower Carboniferous) in age. These Tournaisian sandstones are the least studied of the siliclastic reservoirs within the Berkine Basin, because the Triassic TAG-I formation is the more common target.

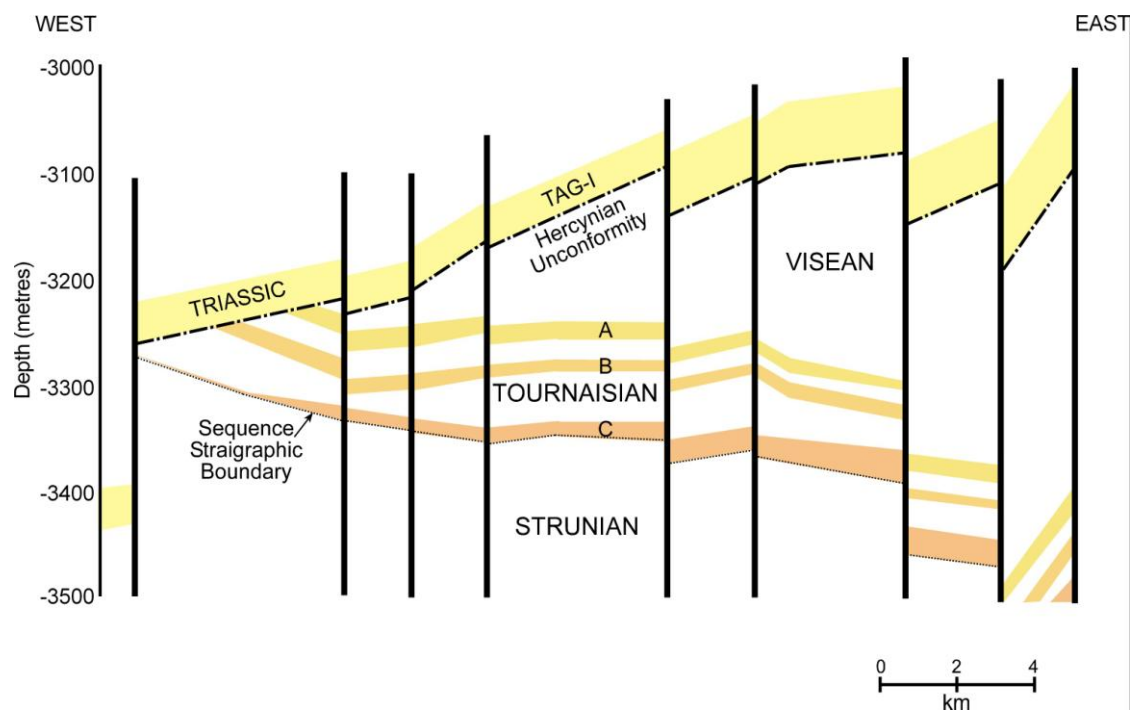


Figure 4.3: Cross-section of the Study field highlighting the Carboniferous reservoirs and the Triassic TAG-I reservoirs (Hughes et al., 2003). The Early Carboniferous sequence boundary is marked at the base of the lowermost sandstone (Fekirine and Abdallah, 1998).

The Tournaisian is interpreted to be a transgressive succession deposited during a period of sea level rise, depositing cyclical shallow-marine, deltaic sandstones and shales, through to deeper marine sediments (Fekirine and Abdallah, 1998; Hughes et al., 2003). An extensive coastal plain was established during the Upper Tournaisian and Viséan as a result of a strong southward progradation from the landmass to the north of the basin (Hughes et al., 2003). As figure 4.3 shows, the Tournaisian succession can be sub-divided into three distinct reservoirs, C, B and A. Reservoir A is the uppermost Tournaisian oil-bearing reservoir and is the main focus of this study.

4.2 Sedimentary Facies

Information provided by ConocoPhillips gives a more detailed description of the sedimentary sequences encountered within the study field. The Tournaisian reservoirs are characterised by cyclical sand and shale sequences. Focussing in on reservoir A a

succession of transgressive deposits, cut by tempestites, fluvial channels and tidal inlets can be identified.

The main sandstone bodies can be broken down into environments of lower shoreface sandstones, upper shoreface, tidal inlet channel sands and barred shoreline upper shoreface sandstones (Hughes et al., 2003). Along with the depositional environments the initial data set provided by Burlington Resources/ConocoPhillips included core data. Table 4.2 documents the available core data for the sedimentary analysis, including the initial dataset provided by ConocoPhillips and a subsequent dataset obtained during the project. The available data includes thin sections, SEM data, XRD analyses and sedimentary logs.

Well	Sample Depth (m)	ConocoPhillips Provided Data				Project Obtained Data		
		Thin Sections	SEM Images	XRD Analysis - Clay Fraction	Core Photographs	Thin Sections	SEM Images	XRD Analysis - Clay Fraction
MLNW-1	3479.3	-	-	-		X	X	-
	3481.35	-	-	-	X	X	X	-
	3577.75	-	-	-		X	X	-
MLNW-2	3458.6	-	-	-		-	-	X
	3459.09	X	-	-		-	-	-
	3459.13	-	-	X		-	-	-
	3459.6	-	-	-		X	X	X
	3460.6	-	-	-		X	X	-
	3462.5	-	-	-		X	X	-
	3463.45	-	-	-		X	X	X
	3464.13	X	-	X		-	-	-
	3464.45	-	-	-	X	X	X	-
	3468.2	-	-	-		X	X	-
	3469.7	-	-	-		X	X	-
	3472	-	X	-		-	-	-
	3493.03	X	-	-		-	-	-
	3493.07	-	X	X		-	-	-
	3497.03	X	-	-		-	-	-
3497.07	-	-	X		-	-	-	
3497.12	-	X	-		-	-	-	
MLNW-3	3571	X	X	-		-	-	-
	3567.14	X	X	-		-	-	-
	3573	X	X	-		-	-	-
MLNW-5	3509.03	X	-	-		-	-	-
	3509.08	-	-	X		-	-	-
	3509.13	-	X	-		-	-	-
	3509.15	-	-	-		X	X	-
	3510.1	-	-	-		X	X	-
	3511	X	X	X	X	-	-	-
	3511.15	-	-	-		X	X	X
	3513	-	-	-		X	X	X
	3514.54	-	-	-		X	X	-
	3515	X	X	X		-	-	-
3539.02	X	X	X		-	-	-	
MLN-5	3522.2	-	-	-	X	X	X	-
MLSE-5	3329	-	-	-		X	X	-
	3330.1	-	-	X		-	-	-
	3330.5	-	-	-		X	X	-
	3332.02	-	-	X		-	-	-
	3334.02	-	-	X		-	-	-
	3338.14	-	-	X	X	-	-	-
	3339.5	-	-	-		X	X	-
	3341.07	-	-	X		-	-	-
	3341.5	-	-	-		X	X	-
	3341.8	-	-	-		X	X	-
	3344.03	-	-	X		-	-	-
	3347.02	-	-	X		-	-	-

Table 4.2: Available core data for sedimentary analysis, and its origin

The sedimentary logs provided by ConocoPhillips identify different depositional environments but not sedimentary facies. Consequently the core photographs were used to construct sedimentary logs, focussing on identifying facies (see Appendix II) as part of this project. The detail obtained from this approach is constrained by the quality of the core photographs, however, in the absence of core it is the best approach to defining sedimentary facies. These core-photograph based sedimentary facies were then integrated with the core data and the original depositional environments defined by ConocoPhillips.

The sedimentology is determined from core data at two well sites (MLNW-5 and MLSE-5), and represents a transgression. Overall 19 small-scale facies are defined (Table 4.3), with three main sandstone facies. Each sandstone facies exhibits slightly different properties, and varies in occurrence. These defined facies can be grouped into facies associations which broadly correspond to the depositional environment interpretation provided by ConocoPhillips (Table 4.4 and Figures 4.4 and 4.5). Micaceous and pyritic mudstones facies (II and VI) correspond to the offshore depositional environment; the silty mudstone facies (XIII and XVI) correspond to the offshore transition zone, with the sand mud inter-bedded facies (XV and XIX) and sandstone facies III correlating to the lower shoreface environment. Sandstone facies VIII correlates to the upper shoreface. The tidal channel facies detailed in the provided sedimentary analysis is not distinguishable from facies VIII on the core-photographs; therefore any samples from this environment are included in the facies VIII descriptions. One occurrence of sandstone facies XII correlates to the submarine channel sandstones encountered in MLNW-5. Sandstone facies XIV is highly bioturbated and correlates tentatively with the tempestite sandstones.

Facies	Name	Description
Facies I	Pyritic mudstone with sandy-silty layers	<i>Pale grey and dark-grey mudstone with sandy silty lenses (few mm thick), finely pyritic and sub-fissile</i>
Facies II	Finely pyritic dark grey mudstone	<i>Dark grey mudstone, sub-fissile, finely pyritic, with faint pale grey laminae</i>
Facies III	Argillaceous, fine-grained sandstone with mudstone laminae	<i>Off-white sandstone, light-grey to pale grey-green, very fine to fine grained, moderately sorted, rounded, moderately cemented, argillaceous and finely micaceous sandstone, with fine pale grey laminae (mudstone), often sharp basal contact</i>
Facies IV	Off-white massive sandstone	<i>Structure-less off-white sandstone, fine-grained, highly quartzitic</i>
Facies V	Bioturbated sand-rich mudstone	<i>Mottled, pale grey pyritic mudstone with high argillaceous sand content, bioturbated</i>
Facies VI	Dark grey micaceous and pyritic mudstone	<i>Very dark grey mudstone, sub-fissile, finely pyritic & micaceous, very faint pale grey laminae, gradational base</i>
Facies VII	Bioturbated muddy sandstone	<i>Pale grey sandstone, with high mudstone content, highly bioturbated (mottled appearance). Sandstone: fine-grained, well-sorted, sub-rounded, possible dolomitic cement</i>
Facies VIII	Off-white fine-grained friable sandstone	<i>Off-white sandstone with pale red/orange surface staining, fine-grained, well-sorted, sub-rounded, friable with occasional very fine dark grey mudstone laminae. Patchy dolomitic cement, & chloritic</i>
Facies IX	Mud-rich laminated fine-grained sandstone	<i>Sandstone with dark grey mudstone layers, not clearly defined boundaries</i>
Facies X	Sandstone with gradational mud-rich layers	<i>Light-grey sandstone with orange surface staining, gradational grey mud-rich layers</i>
Facies XI	Repeating beds of mud-rich sandstone and sand-rich mudstone	<i>Repeating beds of off white-pale grey sandstone (few mm's thick) with grey sand-silt rich micaceous mudstone layers (few mm's thick) gradational boundaries</i>
Facies XII	Off-white argillaceous sandstone with dark grey irregular mudstone laminae	<i>Off-white sandstone with red surface staining, fine-grained to medium grained, rounded to sub-angular, poorly sorted, argillaceous, with occasional fine dark grey irregular laminae, sharp base</i>
Facies XIII	Dark-grey micaceous mudstone with fine silty laminae	<i>Dark grey mudstone, sub-fissile – blocky, very finely micaceous, fine pale grey (silty?) irregular laminae, gradational base</i>
Facies XIV	Sandstone dominant repeating wavy layers of sandstone and mudstone,	<i>Sandstone dominant repeating layers of sandstone and mudstone, with wavy laminae and some bioturbation. Mudstone: very finely micaceous</i>
Facies XV	Grey micaceous mudstone with sandy-silty layers	<i>Grey mudstone, sub-fissile to blocky, richly micaceous, with thin pale grey sandy-silty layers (few mm's thick)</i>
Facies XVI	Richly micaceous mudstone	<i>Grey mudstone, hard, sub-fissile to blocky, richly micaceous, with fine pale grey laminae, gradational base</i>
Facies XVII	Bioturbated sandstone with mudstone clasts	<i>Off-white sandstone, with mildly bioturbated pale grey mudstone</i>

Facies XVIII	Mud-rich bioturbated sandstone	<i>Off-white to pale gray mottled, mud-rich sandstone, possibly bioturbated, mudstone – richly micaceous, sandstone – fine-grained and heavily quartzitic</i>
Facies XIX	Alternating micaceous, chloritic and pyritic mudstone dominant and silty-sandstones,	<i>Repeating beds of pale grey micaceous & mildly pyritic, & occasionally chloritic mudstone and silty sandstone layers, few cm's thick, with clasts and burrows, mudstone dominant</i>

Table 4.3: Sedimentary facies descriptions, defined from the core-photograph sedimentary logs

Facies Associations	Group Name	ConocoPhillips equivalent Depositional Environment
I, II, VI, XIII, XVI	Mudstones	<i>Offshore</i>
V, XI, XIV, XV, XIX	Interbedded thin mudstones and sandstones	<i>Offshore transition & some lower shoreface</i>
XVII, XVIII, X, IX, VII, III	cemented sandstones	<i>Dominantly Lower shoreface</i>
VIII, IV, XII	chloritic sandstones	<i>Dominantly upper shoreface and tidal channels</i>

Table 4.4: Sedimentary facies grouped into facies associations with the equivalent depositional environment defined by ConocoPhillips

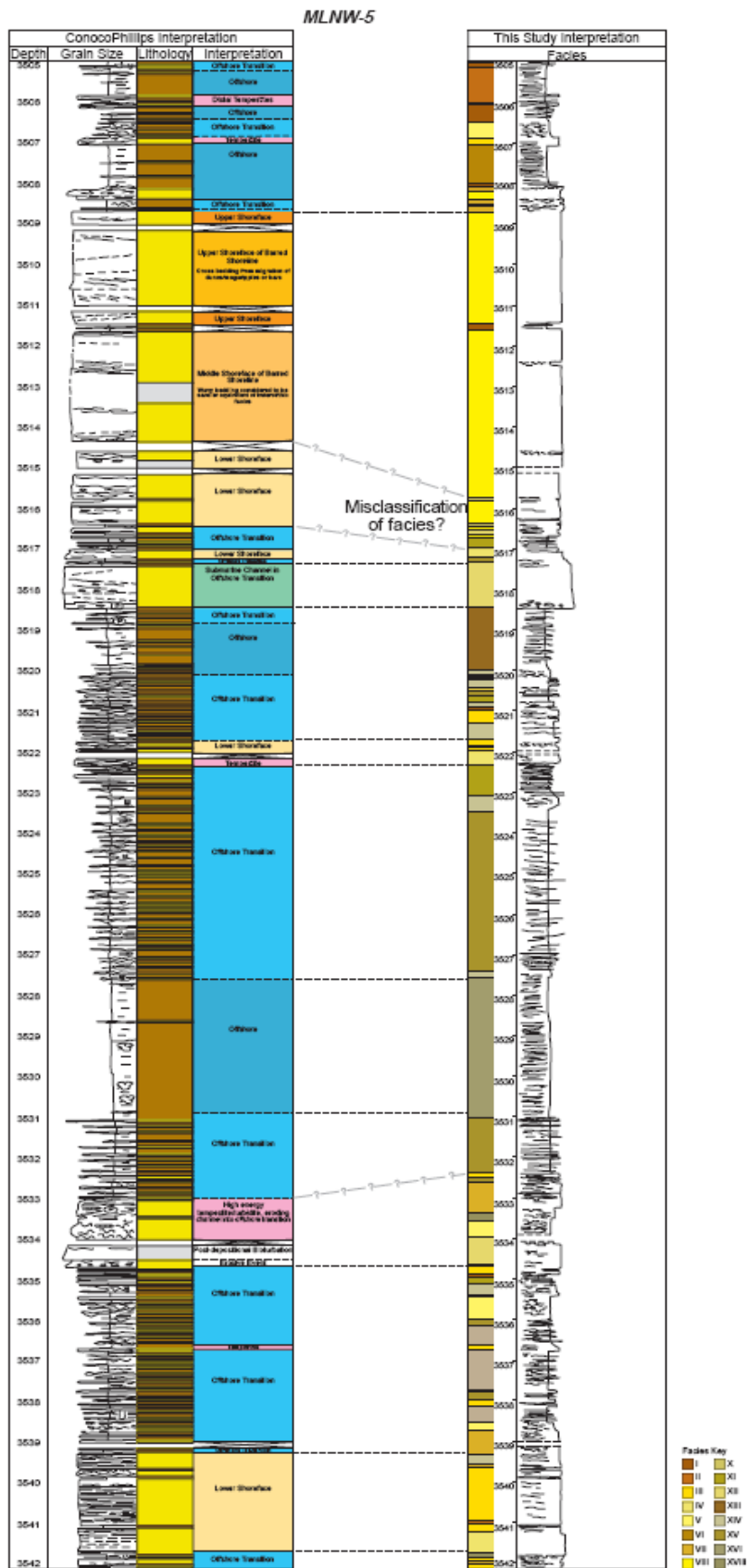


Figure 4.4: An example of the type of sedimentary succession encountered within reservoir A, from MLNW-5 with the relationship of the depositional environments defined by ConocoPhillips to the sedimentary facies defined in this study (modified from Hughes et al., 2003)

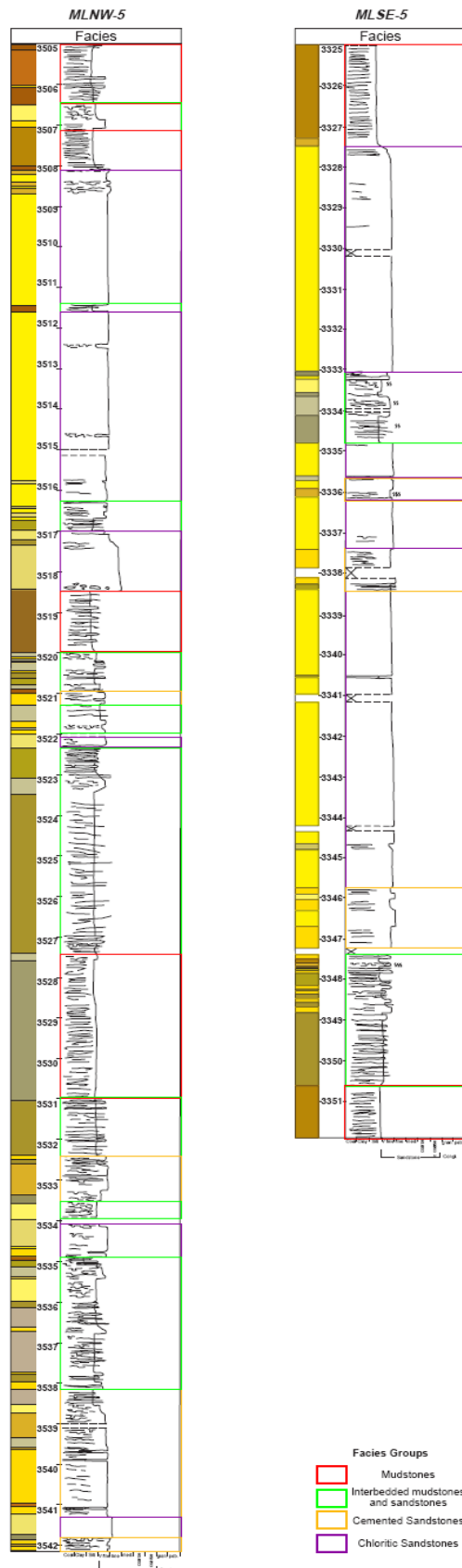


Figure 4.5: MLNW-5 (left) and MLSE-5 (right) sedimentary logs with main sandstones and sedimentary facies groupings labelled

The main sandstone facies defined in this work, described in table 4.3 above, can be linked to the occurrence of chlorite to varying degrees. The chlorite-bearing sandstones outlined in table 4.4 correlate to the upper shoreface and are dominated by facies VIII. The lower shoreface sandstones are dominated by facies III and are dominated by quartz and siderite cement, although there are minor occurrences of chlorite. As Figure 4.5 illustrates there is some overlap between the sandstone facies and ConocoPhillips depositional environments, this is most likely due to the facies being defined from the core photographs. Therefore for the purpose of this study, the chloritic facies (VIII) is related to the upper shoreface and tidal channels, while the cemented sandstones (facies III) is related to the lower shoreface. As most of the work is based on the core-defined facies, the facies III (cemented sandstones facies group) and VIII (chloritic sandstone facies group) will be the main reference in the text for the remainder of this chapter and subsequent chapters.

4.3 Sedimentary Core-Data Measurements

As the project is focussed on chlorite occurrence one of the main ways to determine its presence is through core analysis, from both thin sections and subsequent SEM analysis, or through XRD analysis. Extensive analysis of samples was performed to identify the link between the chlorite occurrence and the sedimentary facies (as defined in table 4.3).

The samples selected for thin-section and SEM analysis were chosen based on the following criteria: (1) their occurrence within the A sandstone interval, (2) depth proximity to special core analysis (SCAL) – to allow for correlations between sample properties and SCAL properties, (3) similar depth to known occurrences of chlorite, and (4) sample quality (Table 4.4). The proximity to the SCAL analysis enables the optical and SEM images to be placed in context alongside other properties (Section

4.5). Some samples were too poor quality to undergo thin section analysis. Well MLNW-2 does not have facies information available and therefore sample selection was also based on log variation. The samples were located where the gamma ray indicated a sandstone lithology, while the density-neutron separation indicated hydrocarbons (see Chapter 2 for explanation), yet the resistivity remained low. Samples were chosen to be representative of the main wells, and made into polished thin sections to allow for microscope analysis, SEM analysis and if necessary microprobe analysis. The initial facies analysis was undertaken on MLNW-5 because it provided the clearest core-photographs on which to base the description and because as a water-bearing well it would allow for clear analysis of the logging data without interference from hydrocarbons. Well MLSE-5 was sampled because this well has the most capillary pressure data, for use in S_w -height functions and has similar facies groups to those exhibited in well MLNW-5 enabling meaningful comparisons. Samples from MLNW-2 were chosen because this has the best quality core plugs which would allow other analyses, e.g. mercury porosimetry, capillary pressure, to be performed. Some of the samples from MLNW-5 were so friable that they had to be prepared as scattered sections instead of thin sections; therefore the analysis can only be done on composition as pore space had been destroyed, and intergranular relationships are not representative. There is a bias in the sampling towards the upper shoreface environment which could not be avoided due to the available core data predominately occurring within that facies.

Criteria For Selection						Analysis		
Sample	A	SCAL	Chlorite	Quality	Log Variation	Thin Section	SEM	XRD
Mlnw-5: 3509.15	X	-	X	Fair	X	X	X	-
Mlnw-5: 3510.15	X	-	X	Poor	X	X	X	-
Mlnw-5: 3511.15	X	X	X	Poor	X	X	X	X
Mlnw-5: 3513.00	X	-	-	Fair	X	X	X	X
Mlnw-5: 3514.54	X	X	X	Fair	X	X	X	-
Mlse-5: 3329.00	X	X	X	Fair	-	X	X	-
Mlse-5: 3330.50	X	X	X	Poor	-	X	X	-
Mlse-5: 3339.50	X	X	X	Fair	X	X	X	-
Mlse-5: 3341.15	X	X	-	Fair	X	X	X	-
Mlse-5: 3341.80	X	-	-	Fair	X	X	X	-
Mlnw-2: 3458.60	X	X	-	Good	-	X	X	X
Mlnw-2: 3459.60	X	X	-	Good	-	X	X	X

Table 4.5: Samples chosen for analysis, based on criteria (importance decreases to the right)

4.3.1 Polished Thin Section Analysis

Twenty one samples were made into polished thin sections and analyzed under the microscope. This was the initial step to describe the samples, and document the main characteristics, such as grain-size, sorting, mineral assemblage, and the presence of clays; as whole grains, grain coatings or filling the pore-space. Point-counting was completed to quantify the mineral abundances (Table 4.6) and the majority of the samples were found to be quartz dominated.

<i>Environment/Facies</i>	<i>Sample</i>	<i>Quartz</i>	<i>Calcite</i>	<i>Feldspar</i>	<i>Mica</i>	<i>Clay Mineral</i>	<i>Carb. Cement</i>	<i>Clay Cement</i>	<i>Space</i>	<i>Unknown</i>	<i>Zircon?</i>
Tidal Inlet/VII	MLNW-1: 3481.35	48.5	0.3	-	-	13.5	0.6	28	9	0.1	-
Lower Shoreface/III	MLNW-5: 3514.54	73.9	0.5	1.0	0.2	3.7	0	20.5	0.2	-	-
	MLNW-2: 3460.60	55.8	1.0	1.1	0.4	8.4	0.4	29.3	3.7	-	-
	MLNW-2: 3468.20	63.7	0.9	0.9	0.2	12.2	0.2	17.9	3.3	0.7	-
Upper Shoreface/VIII	MLN-5: 3522.20	72.7	1.4	0.9	2.4	0.8	3.7	15.8	2.3	-	-
	MLNW-1: 3577.75	57.3	2.7	0.1	0.8	0.6	6.8	28.2	3.4	-	0.1
	MLNW-1: 3479.30	51.0	3.0	-	0.5	3.4	3.7	23.7	14.5	0.2	-
	MLNW-2: 3459.60	56.9	3.5	0.1	1.2	3.7	3.6	29.4	1.4	0.1	0.1
	MLNW-2: 3462.50	55.7	7.8	0.7	0.3	1.5	10.1	14.8	8.7	0.4	-
	MLNW-2: 3463.45	62.9	1.6	0.2	0.1	5.1	-	19.8	10.3	-	-
	MLNW-2: 3464.45	68.6	1.3	0.3	0.7	3.9	2.5	10.9	11.7	-	0.1
	MLNW-2: 3469.70	73.1	15.6	0.7	-	2.0	7.7	0.8	0.1	-	-
	MLNW-5: 3509.15	59.5	8.8	1.5	-	1.4	22.2	4.7	1.9	-	-
	MLNW-5: 3510.10	76.1	4.5	0.9	-	3.5	3.5	3.2	8.3	-	-
	MLNW-5: 3511.15	66.6	4.8	0.2	-	1.2	11.2	16.0	-	-	-
	MLWN-5: 3513.0	59.2	3.2	0.2	-	5.4	13.3	18.0	0.7	-	-
Unknown	MLSE-5: 3329.0	66.7	1.0	-	0.1	3.5	17.3	8.4	3.0	-	-
	MLSE-5: 3330.5	74.5	0.4	-	0.1	5.8	0.3	7.3	11.6	-	-
	MLSE-5: 3339.5	69.6	1.2	-	0.1	0.9	7.7	14.9	5.6	-	-
	MLSE-5: 3341.5	59.9	-	-	0.1	3.5	1.1	30.6	4.8	-	-
	MLSE-5: 3341.8	51.3	0.4	0.1	0.4	1.3	46.5	-	-	-	-

Table 4.6: Point-counts from thin section analysis, grouped according to sedimentary facies and environments

One of the main aims of the thin section analysis was to identify the presence of grain-coating clays within the sandstone samples. Microscope analysis revealed that the majority of the samples exhibited visible porosity and had small pink individual clay grains (Figure 4.6). Several of the samples exhibit grain-coating clays which were too small to be properly resolved under the microscope but were visible as fuzzy green edges to the grains (**Error! Reference source not found.**4.7). Some samples exhibited a more well-cemented nature, with what appeared to be carbonate cement (Figure 4.6), in some samples this was extensive and cemented everything, whilst in other samples there was a split between this cement and clay cement, where the clays not only coated the grains but filled the pore-space as well (**Error! Reference source not found.**4.7). This spectrum of clay-coatings to cement-dominated samples represented the two main sandstone facies; VIII and III respectively.

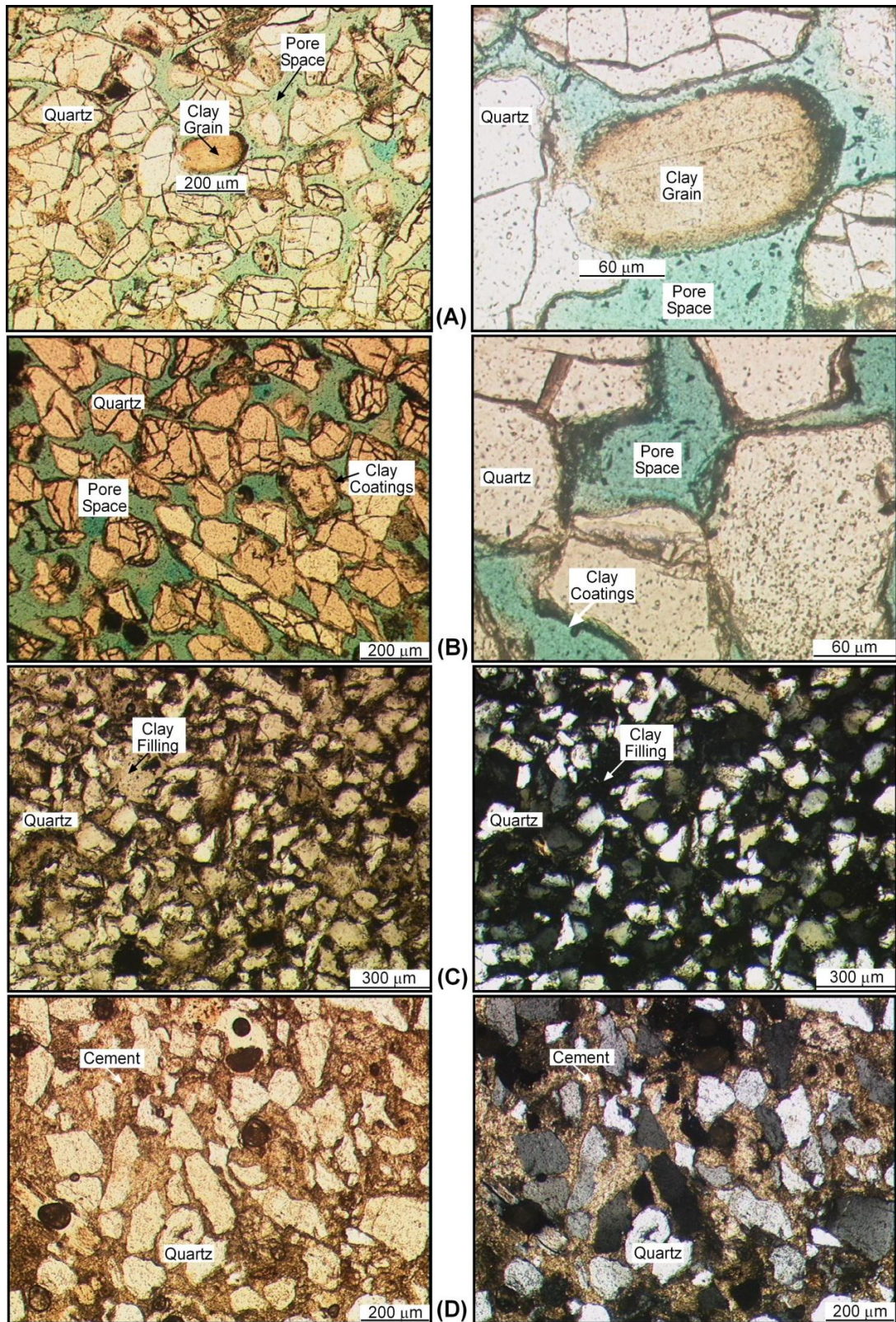


Figure 4.6: Main features observed in the thin sections, including individual clay grains (A – left plane-polarized image: right x40 magnification), grain-coating clays that appear fuzzy in thin section (B – left plane-polarized image: right x40 magnification), pore-filling clays (C – left plane-polarized image: right cross-polarized image) and calcitic/siderite cement (D – left plane-polarized image: right cross-polarized image)

4.3.2 SEM Analysis

In order to analyse the thin sections under the SEM they first had to be carbon coated; which accounts for the sharp carbon peak seen on the spectra. The SEM was used to look at the mineral assemblages at high resolution and to provide a qualitative indication of the composition of the minerals and in particular the clay rims (Figure 4.7).

Different clays form complete grains, coat the surface of other grains, and sometimes form rims around grains which have since either dissolved or been polished away (Figure 4.7). The complete clay grains occasionally show colour zoning across their length, but this does not always correspond to a variation in their spectra. The grain coating clays are so very fine-grained that their morphology cannot be resolved at the magnifications required for spectral analysis, and were imaged at a higher magnification.

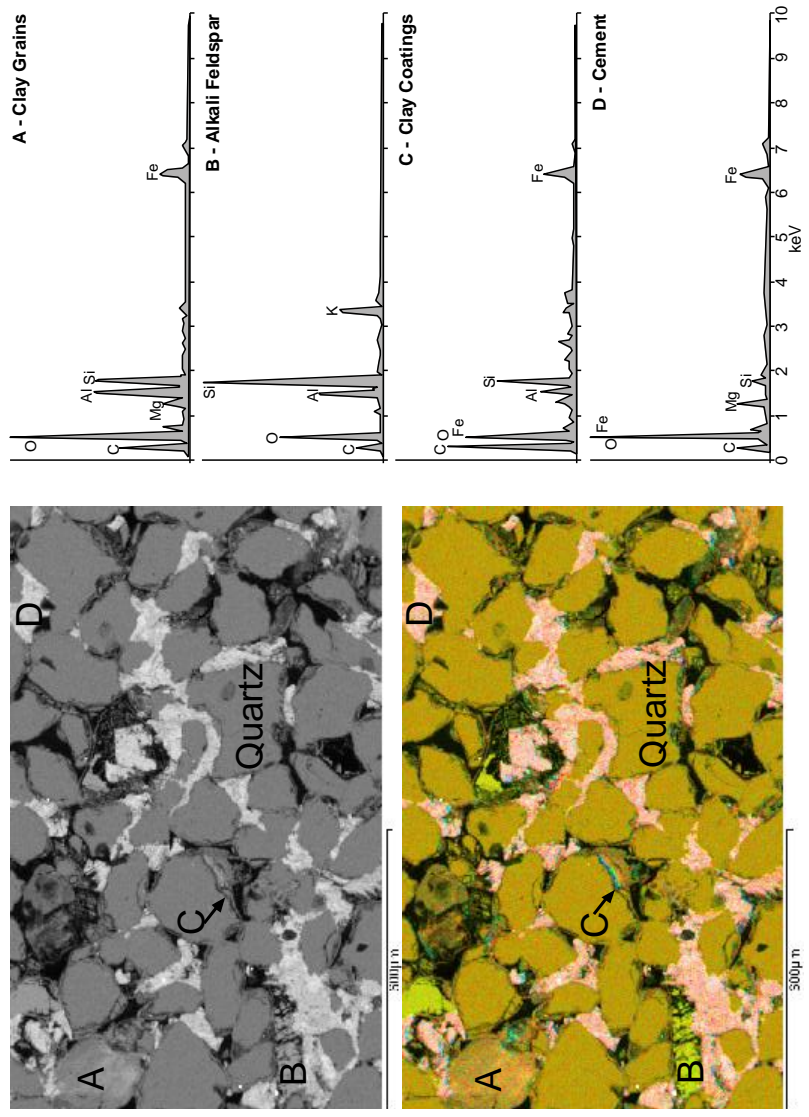


Figure 4.7: SEM images and spectra highlighting the different components: the upper image is a standard SEM image, the lower image is coloured according to composition (a “spectral map”), therefore highlighting the quartz, clay and cement proportions

The spectra seen from the clays are dominated by Fe, Mg, and Si, with occasional K, Na, or Ca. Such compositional markers unfortunately do not indicate the type of clay, because chlorites, illites and smectites can all exhibit this basic composition. However, it does rule out kaolinite as it is one clay mineral that will not contain potassium (K) under normal conditions (Deer et al., 1992; Newman, 1987; Velde, 1992).

A function of the SEM allows for spectral mapping of areas using focussed x-ray measurements (similar to XRD analysis). These maps can highlight the areas of different composition and provide a fast way of distinguishing the different matrix grains (e.g. quartz vs. feldspar) and identifying the clay cement and the carbonate cement. Point spectral analyses can provide a reference composition for the maps. An example above illustrates the dominance of quartz, occasional feldspar grains and cement with abundant clay coatings (Figure 4.7). The spectral analysis does not fully identify the clay; however it provides semi-quantitative weight-percentages of the different mineralogical components, and through investigating the relative abundances it is possible to gain an estimate of the clay type. Due to the nature of the measurement, beam width and the size of the clay grains (average $<3\mu\text{m}$) a large proportion of the spectral analyses are contaminated by quartz/silica to such an extent as to be unusable. These analyses were filtered out of the data set. The remaining analyses, while still influenced in a minor way by the surrounding quartz grains can be used to gain an estimate of the clay type present (Deer et al., 1992; Grigsby, 2001; Norry et al., 1994; Velde, 1992). Chlorite contains Fe, Mg and Al in different quantities while kaolinite contains only Al, these compositional variations mean that by plotting the normalised weight-percentage of Al, Fe, and Mg on a triangular-diagram (Figure 4.8) it is possible to separate out the clay types (Grigsby, 2001; Velde, 1985). Figure 4.8 illustrates the clays contain little Mg ($<10\%$), moderate amounts of Al (30 – 40%) and are dominated

by Fe (50 – 60%), they plot securely in the chlorite/berthierine field. Figure 4.8 highlights the absence of notable kaolinite as it would plot near 100% Al (Grigsby, 2001; Velde, 1985).

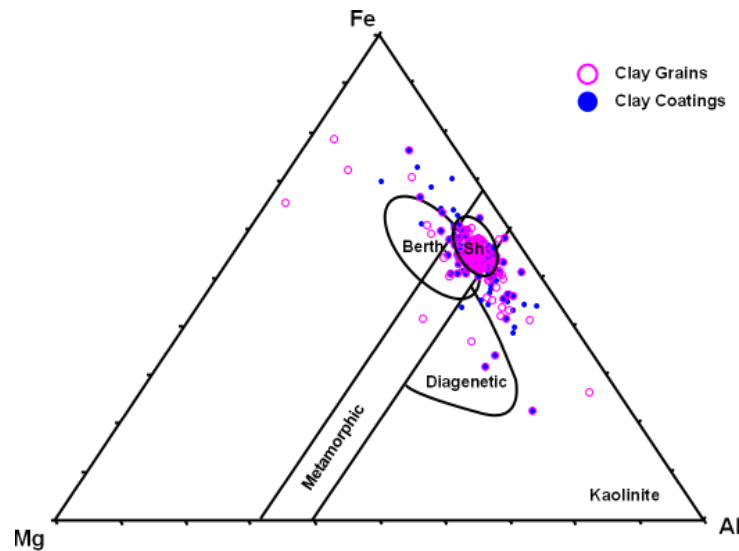


Figure 4.8: Fe-Mg-Al plot of spectral analyses to highlight clay type for clay coatings and individual clay grains, with facies zones for metamorphic, diagenetic, berthierine (Berth.) and black shale (Sh) chlorite compositions (modified from Grigsby, 2001; Velde, 1985).

If the spectral analyses of the chlorites are projected into Al/Si vs. M/Al space, where M is the combined Mg and Fe contributions, it is possible to discern the type of chlorite: e.g. Mg, Fe, or Al rich. Figure 4.9 illustrates the chlorites from this analysis plot very close to the Al-maximum, in comparison to other chlorites; these very aluminium-rich chlorites are often indicative of formation from a kaolinite precursor (Norry, 2009, Pers. Comm.).

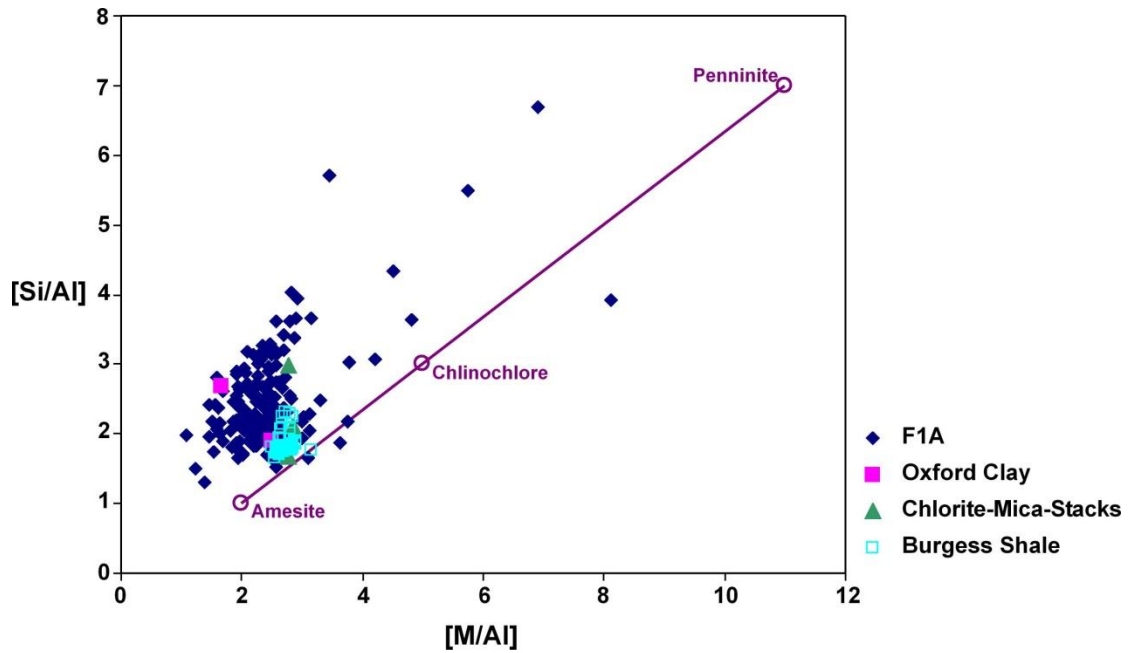


Figure 4.9: [Si/Al] vs. [M/Al] for SEM spectral analyses from reservoir A (this study) with microprobe analyses of chlorites from the Oxford Clay, Burgess Shale and Chlorite-Mica Stacks from North Wales (Milodowski and Zalasiewicz, 1991; Norry, 2009)

The spectral analysis also allows the cement to be semi-quantified. Optically it appears to be a carbonate cement, and Hughes et al. (2003) suggest it is either a ferroan dolomite or siderite. The spectra obtained on the cemented samples confirm this, as they are very iron rich (Figure 4.10).

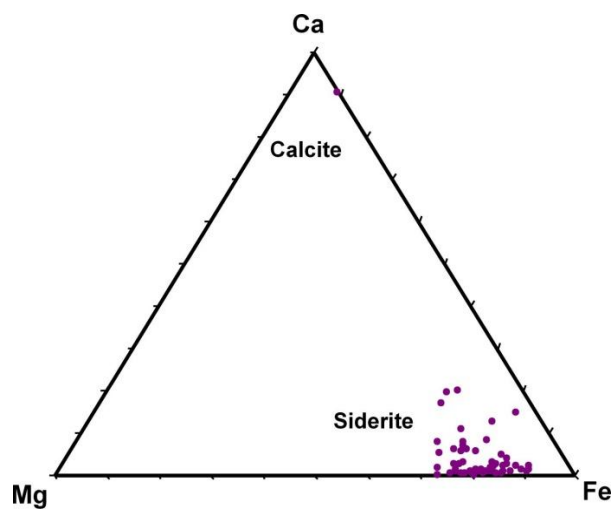


Figure 4.10: Ca-Fe-Mg plot of spectral analyses of cement, with respective percentages of iron, magnesium and calcium. The carbonate cements are very iron-rich, with only a few samples plotting close to 100% Ca.

The SEM images and analysis suggests steps exist between wholly cemented samples and clay-dominated samples, these intermediate samples exhibit both pore-lining and pore-filling clays and patches of cement (Figure 4.11). This suggests that there was an abundance of excess iron in pore waters, and that there were multiple phases of diagenesis.

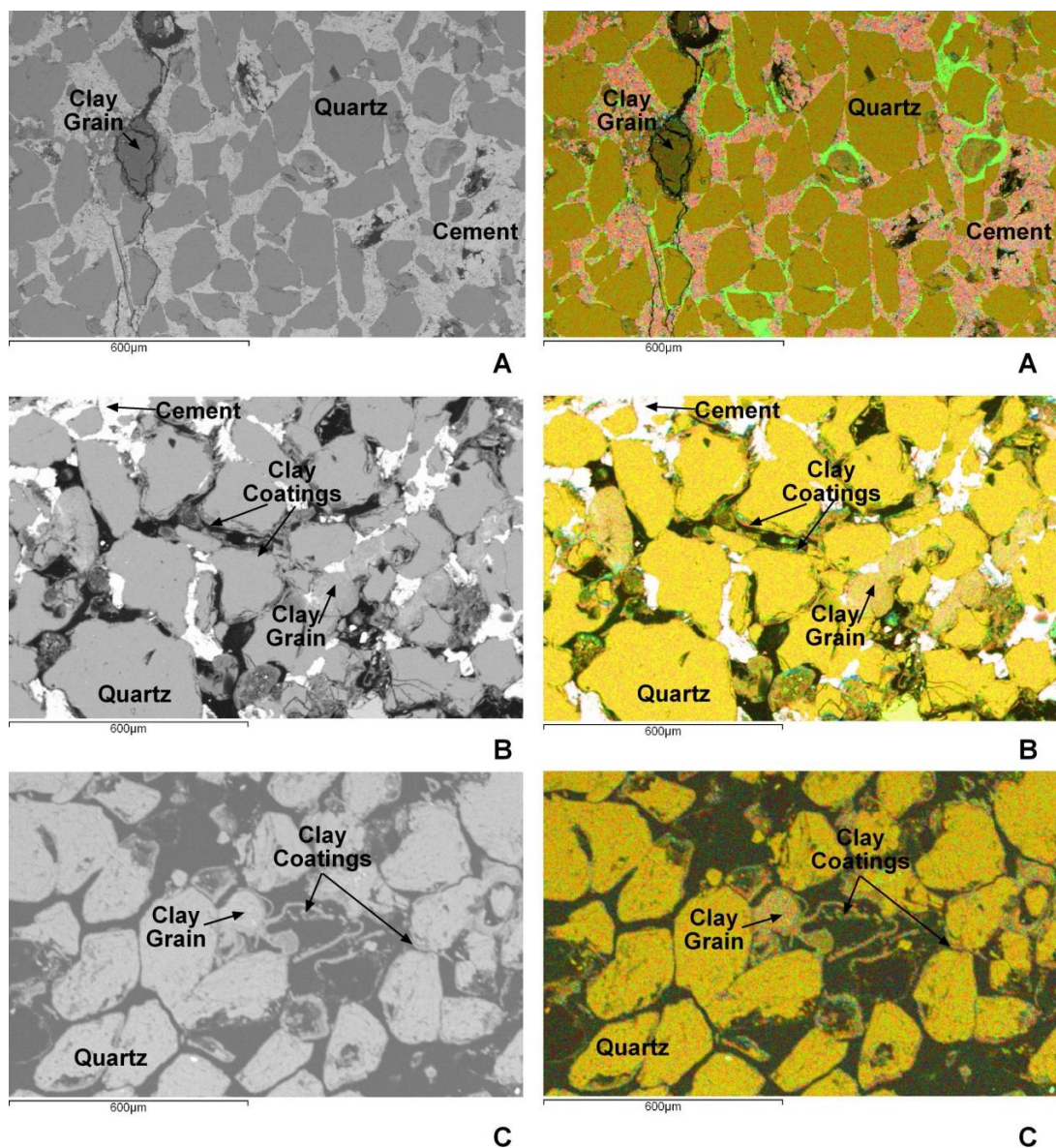


Figure 4.11: SEM images illustrating the variations between fully-cemented samples (A) through partially cemented samples (B) to clay-coating dominated samples (C). On the left are standard SEM images, on the right are SEM images coloured for the SEM spectral analysis composition.

To further support the spectral analysis of clay identification small specimens of rock were gold coated to allow for high magnification imaging of clay morphology. Different clay minerals will exhibit different morphologies; for example chlorite will often exhibit rosettes and platy morphology, which allows it to be distinguished from kaolinite which exhibits a book-like morphology (Anjos et al., 2003; Grigsby, 2001; Welton, 1984) (Figure 4.12). Illite is very fragile and can often be damaged by heating or treatment of samples (Deer et al., 1992), in these samples it is fibrous and uncommon (Figure 4.12).

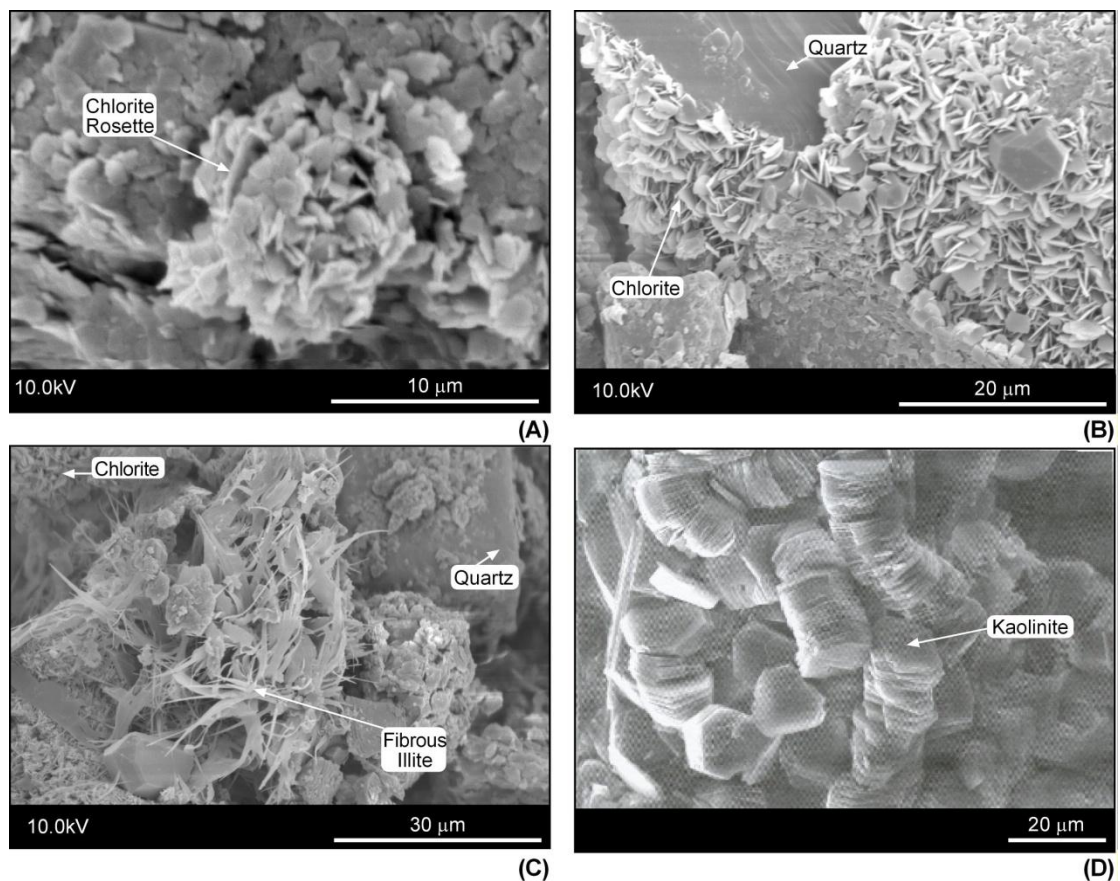


Figure 4.12: High resolution Scanning Electron images of distinct clay morphologies, examples from this study: chlorite rosette (A), typical pore-lining chlorite (B), fibrous illite (C) and an example of typical kaolinite vermicular (“bookish”) morphology (D) from Milliken (2003).

XRD Analysis

Some of the samples selected for thin section analysis were also analysed using x-ray diffraction (XRD) to determine if the clays could be identified quantitatively.

Mudstones as well as sandstones have been analysed, to determine whether the bulk mineralogical composition differed between mudstones and sandstones and between facies. If clay types were found to be identical then the wireline logs would be unlikely to detect any distributional differences between the facies. Analysis by Hughes, et al (2003) identify chlorite as the dominant clay within the clay fraction (Figure 4.13); analysis of more samples using the department facilities indicate kaolinite as the dominant clay mineral and little-to-no chlorite (Figure 4.13). Considering the samples are only from similar not exact depths (within a few 10s cm difference), then some variation may be expected; however the amount of variation indicated would mean the reservoir is intensely stratified. Further, the SEM analysis does not support the in-house analysis, as little to no kaolinite is identified in the SEM images or spectral analysis; which as stated above is dominated by chlorite. It is possible that the chlorites detected in-house are exhibiting a strong 7\AA peak instead of the more common 14\AA peak, and are therefore being mistaken for kaolinite, which has a dominant 7\AA peak (Moore and Reynolds, 1997). However, further investigation was not undertaken and the in-house analyses were discarded.

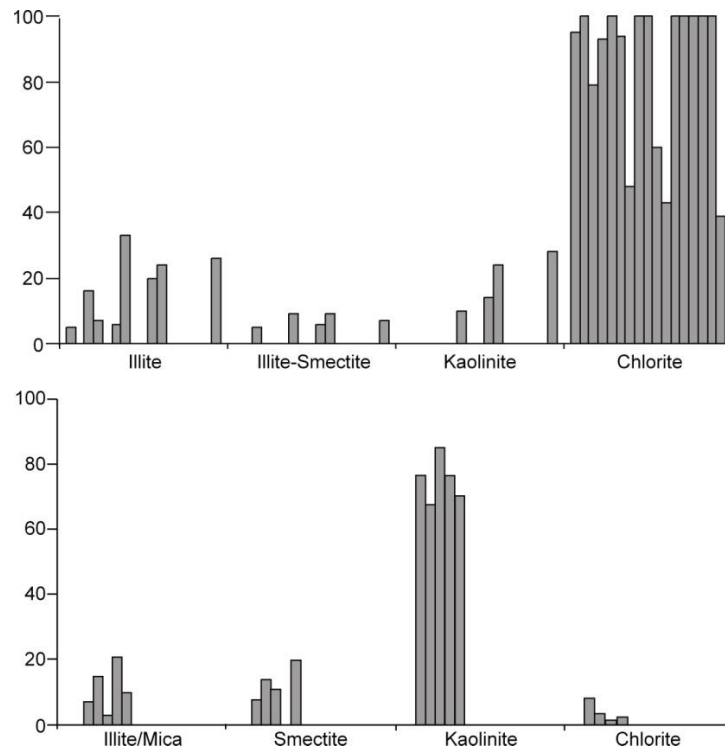


Figure 4.13: XRD analyses of clay fraction (<2μm) from ConocoPhillips (top) and obtained during the project (bottom)

4.3.4 Facies Discussion

The facies VIII, (upper shoreface), is the most abundant sandstone. In core it appears highly friable and is iron-stained. The occurrence of the chlorite is not visible on the macro-scale and must be determined through thin section and SEM analysis. The formation of chlorite is discussed in chapter 3 and hence the presence of chlorite could potentially be inferred from the friable character of these sandstones.

In thin section, the sandstones appear medium-coarse grained, are dominated by quartz grains and have visible porosity (Figure 4.14). Occasional clay grains are present as pale pink rounded grains, but the grain coating clays are visible as “fuzzy” edges to the quartz grains. When viewed under the scanning electron microscope the “fuzzy” edges are resolved as clay coatings, and exhibit morphology consistent with chlorite (Figure 4.14).

Facies III is fairly clean well-cemented sandstone, with occasional mudstone laminae. It is the lower shoreface sandstone facies, commonly interbedded with siltstones and mudstones. In thin section there is little difference between the upper shoreface (VIII) sandstones and the lower shoreface except for the increased presence of quartz overgrowths and siderite cement. The difference is more noticeable under the SEM (Figure 4.14). Due to the quartz overgrowths and compaction the quartz grain edges appear fused, and there is less visible porosity.

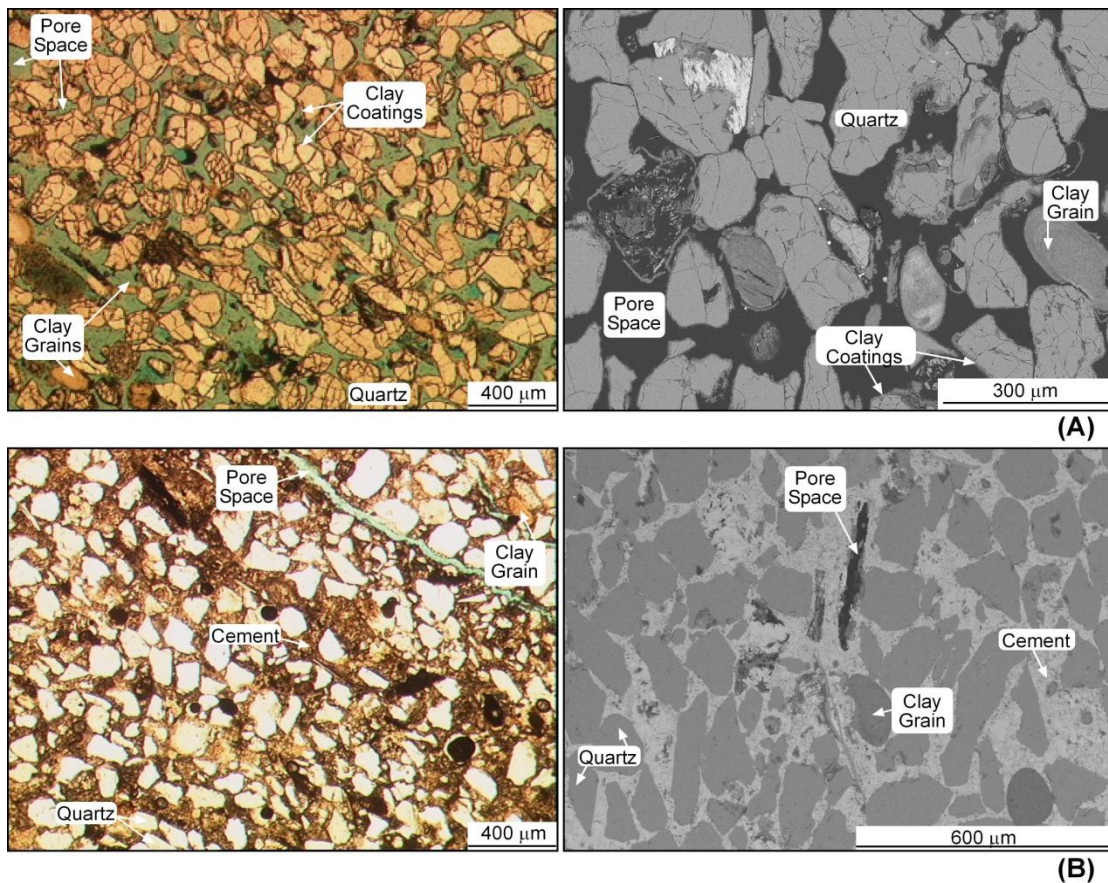


Figure 4.14: Typical thin section image and SEM image for facies VIII - upper shoreface (A) and facies III - lower shoreface (B)

The third sandstone facies (Facies XIV) is the least represented and is highly bioturbated and mud-rich, with no available thin sections.

The analysis of the available core data indicates that the cement and the chlorite formed at a similar time; there is no obvious cross-cutting relationship, and some samples exhibit both chlorite and cement. When investigated on this fine scale it appears that some of the larger sand bodies classified as e.g. facies VIII on the original core-photograph derived sedimentary logs exhibit some properties of facies III, i.e. more cemented. However, from the available data and on the scale being dealt with in the logs this internal variation is insignificant and the dominant facies from the sedimentary logs should be considered.

4.4 Porosity Distributions

Porosity distributions provide a measure of the pore throat radius variation within a sample (See chapter 2), and often there is a link between pore-throat radius and porosity. In this study porosity distributions were investigated to determine if a link existed between the porosity distributions and the presence or absence of clays and cement. The available data set was from five wells, with a total of twenty seven distributions, which when plotted up tends to exhibit either bi-modal or uni-modal distributions, with some intermediate variation (Figure 4.15).

As figure 4.15 shows the majority of the bi-modal porosity distributions occur within facies VIII. Facies III exhibits mostly uni-modal distributions, with small pore-throat radii dominating. Some uni-modal distributions do occur within facies VIII; samples K, L, P and T. When these samples are compared to their corresponding SEM image (Figure 4.16) it can be seen that they exhibit excessive clay growth, which is filling the pore space. These samples differ from the facies III distributions, as these samples exhibit less clay coatings, with quartz overgrowths and cement causing the reduction in porosity.

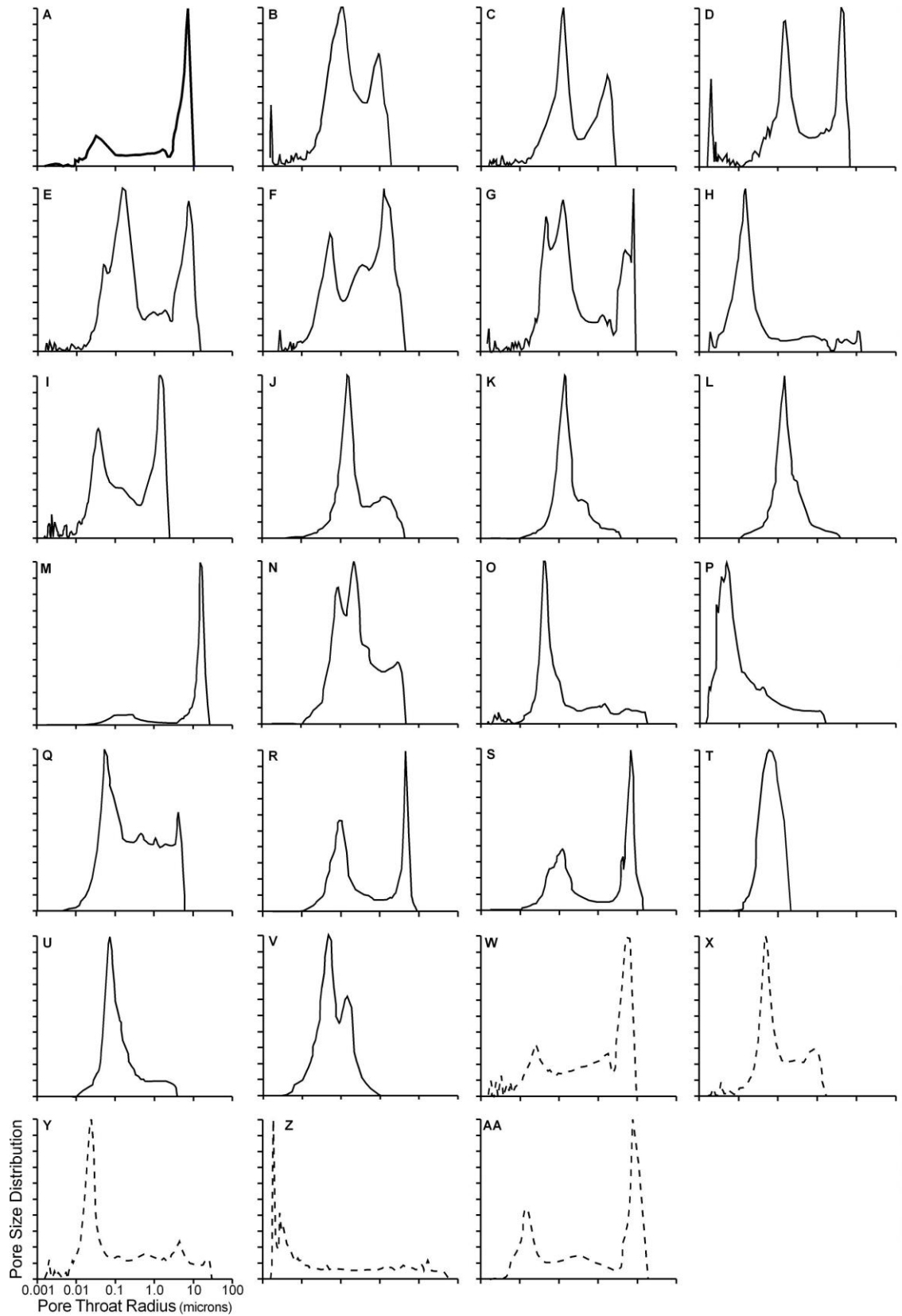


Figure 4.15: Porosity distributions for facies VIII - upper shoreface & tidal channels (A – V) and facies III - lower shoreface (W – AA). Samples P and Z are from mudstone horizons within the broader sandstone facies, hence the very low (<0.001micron) pore radii exhibited.

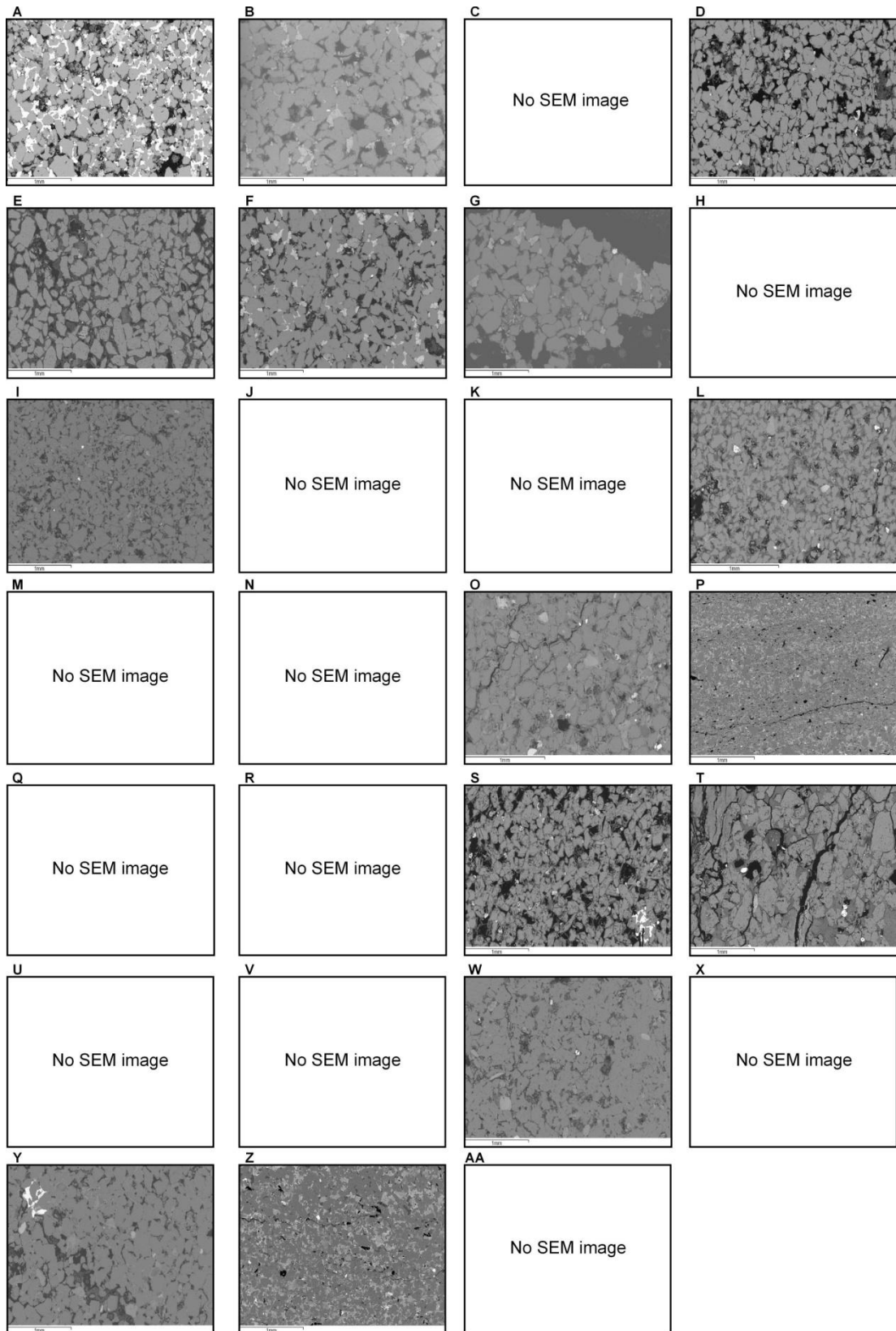


Figure 4.16: SEM images corresponding to the porosity distributions for facies VIII - upper shoreface & tidal channels (A – V) and facies III - lower shoreface (W – AA). Samples P and Z are from mudstone horizons within the broader sandstone facies, hence the finer-grained nature.

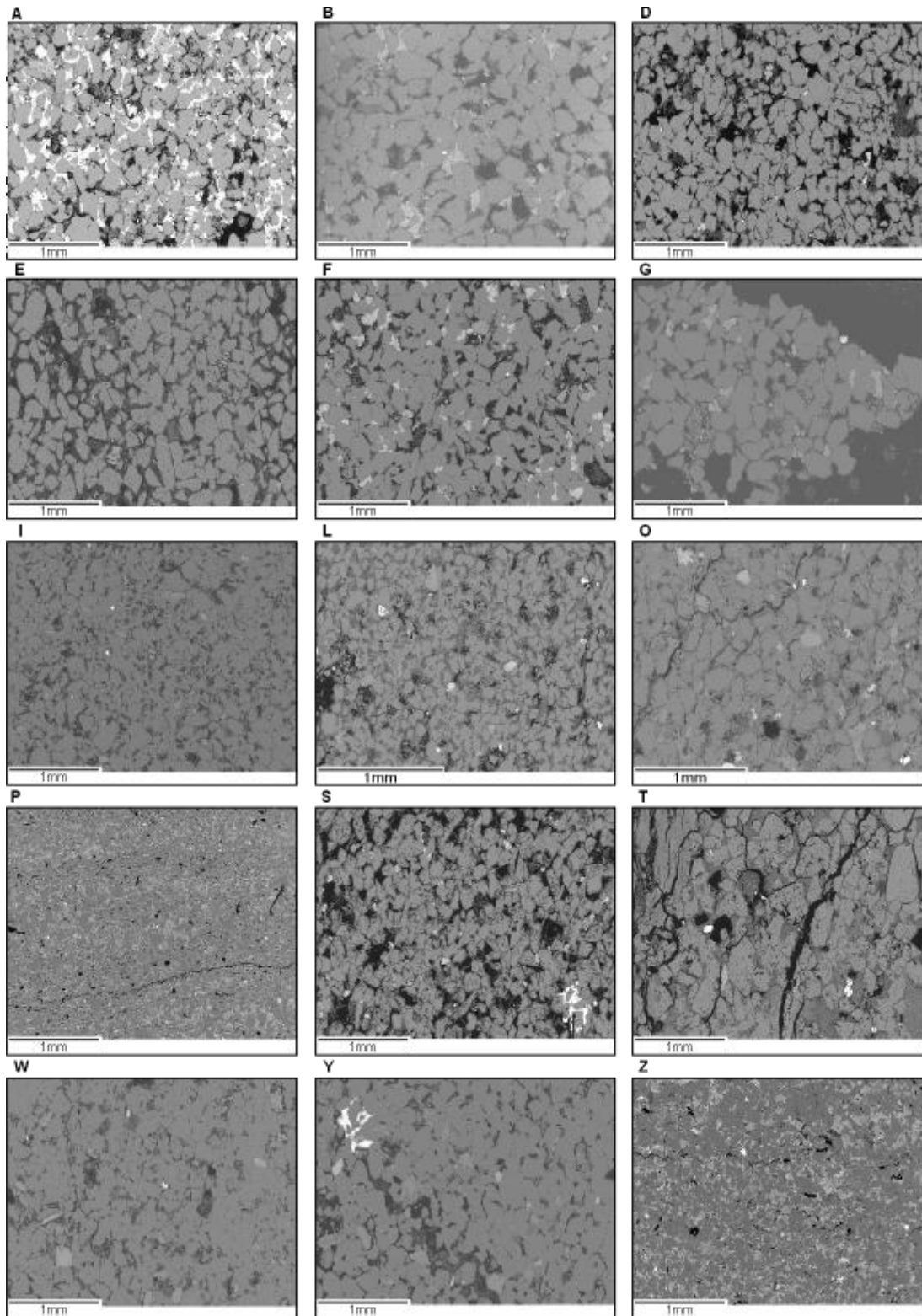


Figure 4.16a: Magnified available SEM images corresponding to the porosity distributions for facies VIII - upper shoreface & tidal channels (A, B, D – G, I, L, O, S & T) and facies III - lower shoreface (W & Y). Samples P and Z are from mudstone horizons within the broader sandstone facies, hence the finer-grained nature.

4.5 Conclusions

Sedimentological analysis of samples from reservoir A of the Berkine Basin, Algeria defines two main sandstone facies: facies III and facies VIII. These sandstone facies can be correlated to the sedimentary environments defined by Hughes et al (2003), with facies III correlating with the lower shoreface sandstones and facies VIII correlating primarily with the upper shoreface and tidal channels, as they cannot be differentiated on the core photographs, from which the facies scheme was defined. Thin section and SEM analyses indicate that facies VIII is dominated by the presence of grain-coating chlorite, which is occasionally so abundant as to occlude the porosity. Facies III exhibits a much lower proportion of clay, with an increase in quartz overgrowths and Fe-rich cement. This more cemented nature of facies III is highlighted in the dominance of uni-modal porosity distributions, while the clay-rich nature of facies VIII is highlighted in the bi-modal porosity distributions. The link between the main sedimentary facies and the occurrence/absence of chlorite and subsequent relationship to the porosity distributions provides a basis for investigating the petrophysical signature of the chlorite occurrence in the log data, which will be investigated further in chapter 5.

5. Wireline Log Analysis

Chapter 4 discussed how the chlorite related to the different sedimentary facies and environments. This chapter discusses how the chlorite can be detected from the wireline log data. Of all the available wells, those with sedimentary core information were chosen for analysis, as they provide a data set which enables comparison between core and log data (Table 5.1).

Well	Oil vs. Water-bearing?	Available Log data							Core Data
		Density	Neutron	PEF	Gamma Ray	SGR (Th, K, U)	Resistivity	Acoustic	
MLNW-1	Oil	x	x	-	x	x	x	x	x
MLNW-2	Oil	x	x	-	x	x	x	x	x
MLNW-3	Water	x	x	-	x	-	x	x	x
MLNW-4	Water	x	x	-	x	-	x	x	x
MLNW-5	Water	x	x	-	x	x	x	x	x
MLNW-6	Oil	x	x	x	x	x	x	x	-
MLN-1	Oil	x	x	-	x	x	x	x	-
MLN-2	Oil	x	x	-	x	x	x	x	-
MLN-3	Oil	x	x	-	x	x	x	x	-
MLN-4	Oil	x	x	-	x	x	x	x	-
MLN-5	Oil	x	x	-	x	x	x	x	x
MLN-6	Water	x	x	-	x	x	x	x	-
MLN-7	Oil	x	x	x	x	x	x	x	-
MLN-8	Oil	x	x	-	x	x	x	x	-
MLN-9	Water	x	x	-	x	x	x	x	-
MLSE-5	Oil	x	x	x	x	x	x	x	x

Table 5.1: Details of available wells, available logs and oil vs. water-bearing; PEF = photoelectric factor, SGR = spectral gamma ray. Core data refers to sample measurements, sedimentary logs and core photographs (see chapter 4 for a full break-down).

All the wells used in this study are assumed vertical, and were drilled with an oil-based mud.

5.1 Initial/Standard Log Analysis

5.1.1 Data Quality

The available data were provided in a corrected and processed form, with all the necessary corrections applied, outlined in table 5.2, (Theys, 1991). Some corrections are made directly with the tool response, for example, the density tool automatically corrects counting rates of the different energy readings (Theys, 1991). Temperature and pressure effects are corrected for by the logging engineer immediately following data collection, so no further information is available on these corrections.

Logging Tool	Correction	Origin
Neutron porosity	<i>Borehole size Temperature Pressure Standoff Salinity Cement/casing</i>	Experimental
Induction Resistivity	<i>Borehole conductivity Shoulder / invasion Shoulder / no invasion Bedding dip</i>	Mathematical modelling
Density	<i>Mud cake P_e on density Borehole size Pad tilt Mudcake on P_e</i>	Experimental
Spectral gamma ray	<i>Mudcake Borehole size Tilt Anisotropy</i>	Mathematical modelling
Total gamma ray		API test pit calibration (University of Texas)

Table 5.2: A brief overview of some of the main environmental corrections for the common logging tools; where P_e is the photoelectric component, and standoff refers to distance from the borehole wall (modified from Theys, 1991).

The borehole quality, and thus data quality, for the chosen wells across reservoir A was assessed using the caliper data. The quality of the borehole wall impacts on the quality of the logging tools, particularly the density tool which requires contact with the

borehole wall to get accurate readings (see chapter 2). It is not just average borehole size but also rate of change of the borehole, as a sudden increase in borehole size can affect the pad-based tools (e.g. density) even if the enlargement is small (Millar, 2008, Pers. Comm.; Theys, 1991). Well-site reports indicate a 6 inch drill bit was used, and in table 5.3 the caliper indicates very good quality holes. The exception is MLN-5 which indicates an 8.5 inch borehole. No well-site report is available for this well; but given the concentrated nature of the histogram it is assumed that it is 8.5 inches and therefore also reliable. Good quality caliper indicates a good quality borehole and therefore suggests reliable log data.

Well	Mean (Inches)	Standard Deviation
MLN-5	8.545	0.009
MLNW-1	5.948	0.025
MLNW-2	6.038	0.050
MLNW-3	6.344	0.017
MLNW-4	5.922	0.166
MLNW-5	5.852	0.036
MLSE-5	5.818	0.054

Table 5.3: Mean and standard deviation of caliper data for study wells; means of ~6in and 8.5in for MLN-5 indicate good quality boreholes

Where the PEF data was available (Table 5.1) the drilling mud was barite-rich (McNeill, 2006, Pers. Comm.), and since barite has such a heavy Z number and given the relationship of PEF to Z, (explained in chapter 2; section 2.1.2), the heaviness of the barite overrides the signal from the formation, meaning the curve is unreliable (Theys, 1991).

The logging data was obtained over several years by two different contractors (Baker Atlas and Schlumberger) so it was necessary to ensure consistency between the two data sets using a “coherence check” (Theys, 1991); this involves a comparison of logging data from different wells in the same field, based on simple stable field-wide lithologies. This is not a rigorous check as it is not possible to verify the homogeneity of the

formations, and if a log has been rated “anomalous” other quality indicators must be assessed. The sonic, neutron and density logs are good to use on these checks as they reflect parameters with limited variability within each geological unit. The test involves statistical analysis, expressed as histograms and standard deviations across the interval of interest; in this case a field wide black shale covering the A formation was chosen. The density, neutron and sonic histograms for the available wells are shown in figure 5.1. Wells MLNW-1, MLNW-2 and MLNW-4 were logged using Baker Atlas tools, and MLNW-3 and MLNW-5 using Schlumberger tools. The standard deviations for the log variables (Table 5.4) and the fact that wells are small enough and comparable enough suggests the data from both contractors and from the same contractors at different times (e.g. MLNW-3 and MLNW-5) can be used in conjunction with no modifications.

Log Measurement	Mean	Standard Deviation
<i>Density</i>	2.6413 g/cm ³	0.07342
<i>Neutron Porosity</i>	0.27792	0.05902
<i>Sonic Travel Time</i>	77.518 μs/ft	4.604

Table 5.4: The combined mean and standard deviations of the sonic, density and neutron data for MLNW-1, 2, 3, 4, & 5 wells.

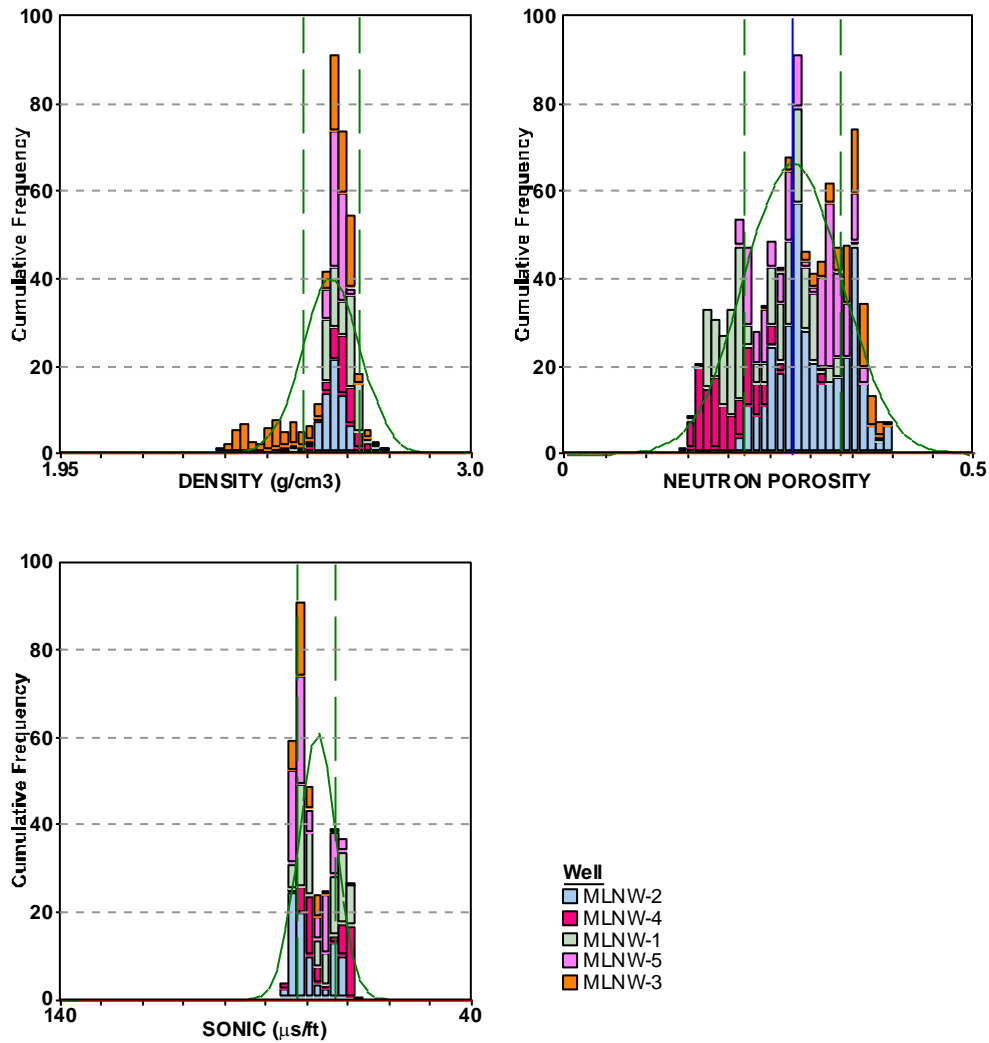


Figure 5.1: Histograms of density, sonic and neutron for the coherence checks

In order to compare the wireline log data to the core data it is necessary to make sure the cored depths and the log depths match. From the log data for all the wells studied the top of reservoir A is marked by a sharp increase in the gamma ray curve, which corresponds to a black shale identified in core. This was assumed to be the top of the sand body and the depth of the core data was shifted accordingly (Table 5.5) using a simple bulk shift, so that the top of the sand body in the core matched the drop in the log gamma ray (Parkinson, 2001). A simple bulk shift was applied because not enough information was available about core recovery and individual core section depths to determine if non-linear shifts were necessary.

Well	Log Depth (m)	Thickness (m)	Core Depth (m)	Depth-Shift (m)
MLNW-1	3476.49 – 3496.31	19.82	3374.0 – 3512.0	1.45
MLNW-2	3461.59 – 3476.30	14.71	3455.0 – 3475.0	-3.2
MLNW-3	3566.81 – 3579.58	12.77	3558.0 – 3576.0	No information
MLNW-4	3568.61 – 3584.13	15.52	3563.0 – 3583.0	-2.1
MLNW-5	3512.10 – 3526.47	14.37	3508.0 – 3514.6	-3.63
MLN-5	3515.67 – 3530.41	14.74	3515.0 – 3543.00	+3.33
MLSE-5	3328.65 – 3348.29	19.64	3337.0 – 3352.0	0.0

Table 5.5: Reservoir A depths in each of the wells chosen for analysis, and the linear depth-shift necessary to shift the log data to match the core data

5.1.2 Log-based lithology analysis

There are many standard interpretation methods available for log-based lithology determination; in this study a first-pass visual interpretation was performed to become familiar with the data, a more detailed computer-based lithology model was developed (discussed in more detail below), and finally cross-plots allow the relationship of the log variables to each other to be investigated. The aim of the log-based lithological assessment is to identify the sedimentary facies (see chapter 4), or the chlorite-bearing sandstones, from the log data. Before any interpretation can be discussed, the discrepancy between the industry standard term “shale”, and the sedimentological definition needs to be dealt with, to provide clear terminology. For the purpose of this study what would commonly be referred to as shale by the industry is the equivalent of the mudstones defined in the sedimentary analysis (chapter 4), and shall be referred to here as mudstones. The term clay refers to clay minerals (defined in chapter 3); in this study clay refers to the grain-coating chlorites, individual clay grains, and other clay minerals that may be present in the sandstone formations.

Visual Interpretation Method

In each of the selected wells reservoir A’s main sandstone formation occurs at a different depth, and exhibits variable thickness (Table 5.2). In the selected wells it is

possible to do a visual interpretation of the log data for reservoir A formations, as each of the different measurements respond to different properties, e.g. the gamma ray responds primarily to shale (mudstone) content and therefore is a proxy for lithology (See chapter 2 where this is discussed in more detail). In a visual assessment high gamma ray values are taken to represent mudstones, with the maximum value often taken as representative of ‘100% shale’. Low gamma ray values are taken to be sandstones in this case, as no limestone formations are present, and the lowest consistent gamma ray value is taken to represent “clean sandstone”, i.e. with no clay or mudstone contamination. The resultant interpretation is not robust, but is essentially a first pass, and so a more detailed lithological interpretation was done using in-built functions of Interactive Petrophysics™ (IP™), the log analysis software used in this project.

Computer-based Lithological Interpretation Method

The ‘Clay Volume Analysis’ module of Interactive Petrophysics™ allows the user to select log data curves to be used to determine the volume of clay and mudstone material present in a formation. Either ‘Single Clay Indicators’, using only one log curve, or ‘Double Clay Indicators’, two log curves can be used. For this analysis the gamma ray curve (*Gr*) was chosen as the ‘Single Clay Indicator’, and was calculated with a linear relationship (equation 5.1). The gamma ray input parameters (*GrClay* and *GrClean*) were taken as the ‘100% Shale’ and ‘clean sandstone’ values determined in the visual analysis of each well.

$$V_{clGr} = \frac{Gr - Gr_{Clean}}{Gr_{Clay} - Gr_{Clean}} \quad (5.1)$$

For the ‘Double Clay Indicators’ the density-neutron relationship was chosen, because the density and neutron responses are linked to lithology (discussed in Chapter 2). This method works from the density-neutron cross-plot (discussed in more detail below), by

defining a ‘clean sandstone’ line, and a ‘100% shale’ point (Figure 5.2). The volume of clay and mudstone material (V_{clND}) is then determined using equation 5.2: where notations Cl_1 and Cl_2 relate to the ends of the ‘clean sandstone’ line, and $NeuClay$ and $DenClay$ relate to ‘100% clay point’ neutron and density values.

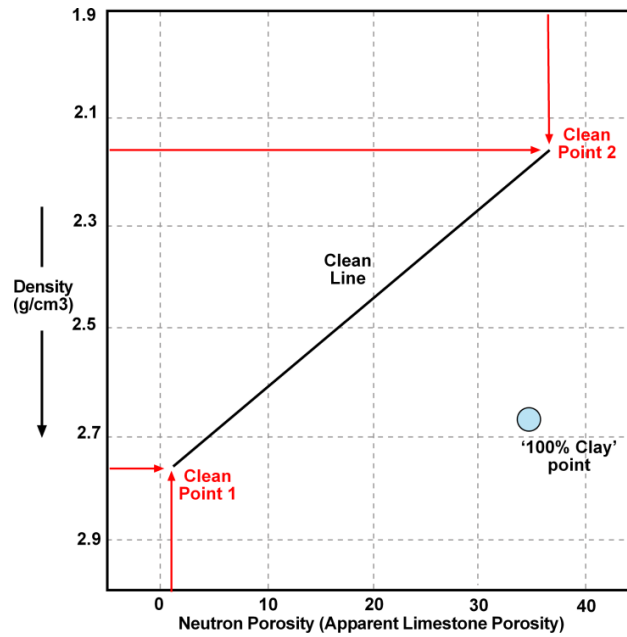


Figure 5.2: Density-Neutron cross-plot indicator of parameters used in clay and mudstone volume calculations within Interactive Petrophysics™

$$V_{clND} = \frac{(DenCl_2 - DenCl_1) \times (Neu - NeuCl_1) - (Den - DenCl_1) \times (NeuCl_2 - NeuCl_1)}{(DenCl_2 - DenCl_1) \times (NeuClay - NeuCl_1) - (DenClay - DenCl_1) \times (NeuCl_2 - NeuCl_1)} \quad (5.2)$$

When both ‘Single’ and ‘Double Clay Indicators’ are used to estimate clay and mudstone volume the absolute clay and mudstone volume (V_{cl}) displayed in the lithology interpretation is calculated from the minimum volume estimate of all chosen ‘Single’ and ‘Double Clay Indicators’. The results from this interpretation are referred to as the log-based lithological assessment or model throughout the remainder of this thesis.

Cross-plot Interpretation Method

Cross-plots are a simple way of expressing the relationship of one parameter to another. They are commonly used in wireline log evaluation and one of the most popular is the relationship between the bulk density and the neutron porosity curve which can help to distinguish different lithologies. In this density-neutron cross-plot the density, on the y-axis, has an inverted scale, with the lower densities towards the top, while the neutron tool is plotted along the x-axis with values increasing from left to right (Figure 5.3).

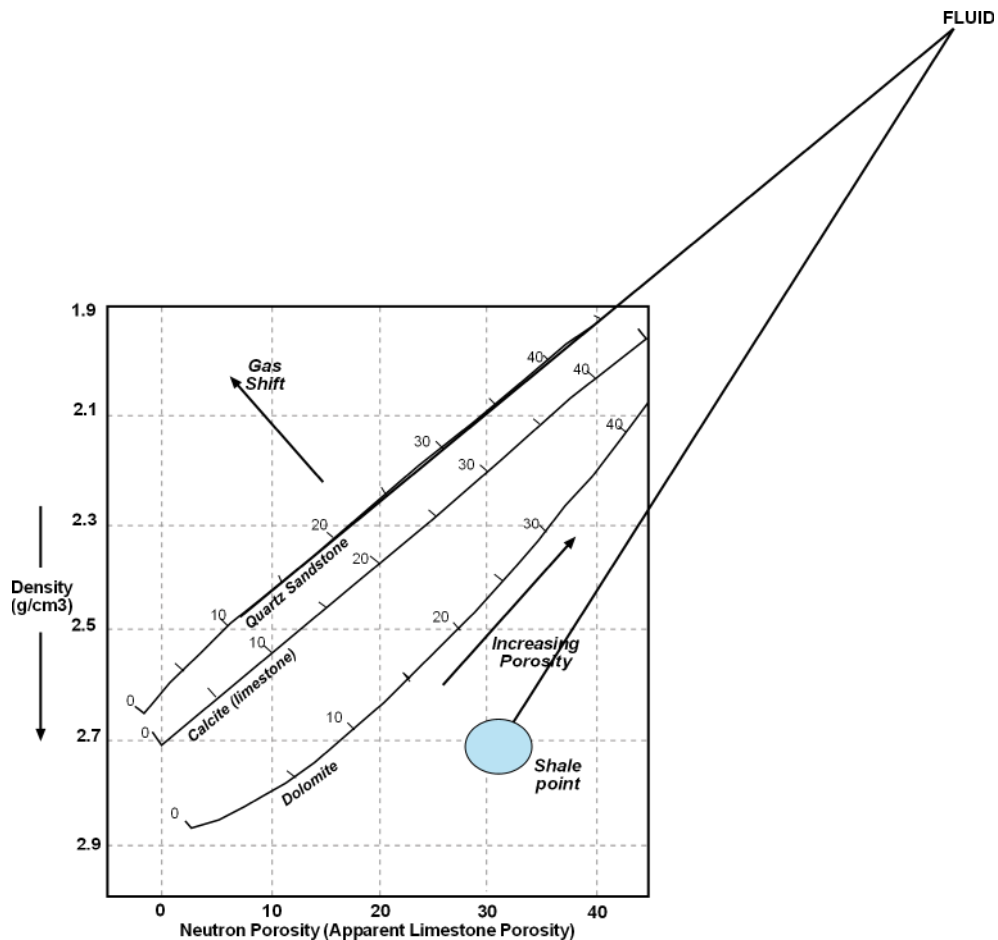


Figure 5.3: A blank density-neutron cross-plot, with the lithology lines indicated, and the end-point water saturation shown. Also shown is the general area shale may expect to plot. Note the neutron axis plots to negative numbers; this is an artefact of calibration of the tool to limestone porosity of 0% at the approximate density of limestone (2.71 g/cm^3) (modified from Rider, 2004).

The density-neutron plot enables lithology determination based on known relationships between the densities of main lithologies at different porosities for a water-filled formation, represented by the lines. For example, a rock sample with 20% actual

porosity, with a saturating fluid density of 1.0g/cm^3 , will have a density of 2.34g/cm^3 if it is a clean quartz sandstone, or 2.38g/cm^3 if a limestone. The apparent neutron porosity will be slightly lower than the actual porosity in sandstones because the neutron porosity is primarily related to the amount of hydrogen in the fluids in the pore space (see chapter 2 for detailed explanation), but also detects a small matrix effect (see fluid point of figure 5.3). If dealing with a water-bearing well then the plot can be used for lithology in a straight forward manner, however, if light hydrocarbons are introduced into the pore space then more care must be taken. The density-neutron plot uses the assumption that the electron density is equal to the bulk density (see Chapter 2), but in the presence of hydrocarbons this is not strictly true, and a correction must be applied to the data (Ellis, 2004; Ellis, 1987). Additionally the low density of the fluid hydrocarbons mean caution must be applied when calculating porosity from the density tool. Since light hydrocarbons fill the same amount of pore space in a rock with fewer hydrogen atoms the response from the neutron tool will be lower, indicating lower porosities, but the density response will continue to decrease as fewer atoms are present for Compton scattering interaction: therefore the cross-plot values will move to lower neutron (apparent) porosities at lower densities (Figure 5.3). This effect is more pronounced with 'light' hydrocarbons (density >40 deg API) where the porosity is higher ($>25\%$). The effect is reduced if deeper invasion of drilling fluid occurs, which can be caused by higher differential pressure between drilling mud weight and the formation, or low porosity formations.

Shales can plot over a range of density and porosity values, depending on composition and mineralogy. They will often exhibit higher densities ($\sim 2.7\text{g/cm}^3 \pm 0.01\text{g/cm}^3$) due to the tight packing of grains (see Chapter 2 for explanation), but the high content of water within the structure of the minerals (i.e. clays) and the bound water in the small

pores can result in shales exhibiting a high apparent neutron porosity (Figure 5.3). When interpreting the density-neutron cross-plot for lithology it is necessary to take care that the effect of light hydrocarbons or shale within the rock is taken into consideration, with each effect opposing the other.

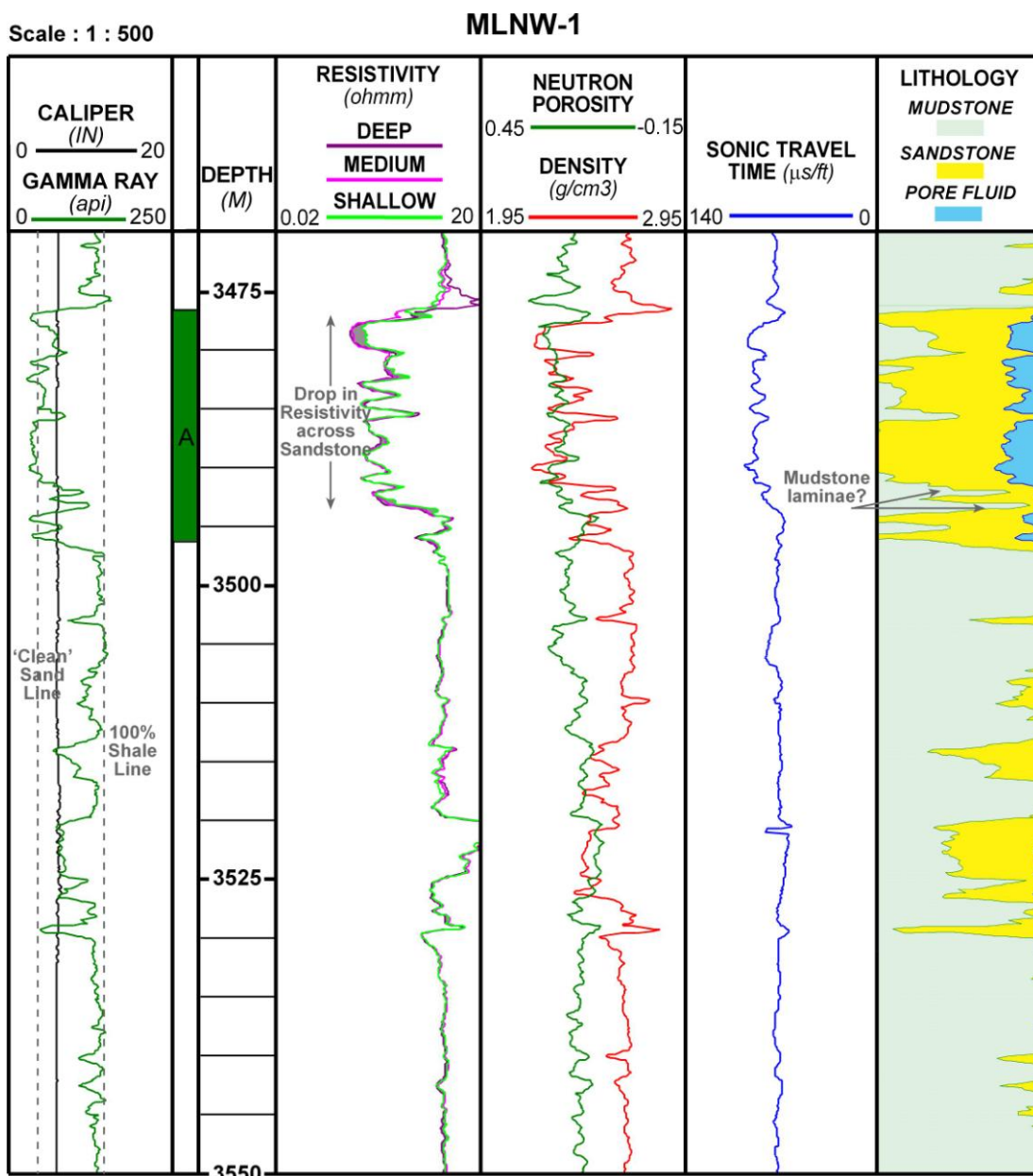
Visual descriptions of the log variations and cross-plots, beginning with the density-neutron, were investigated to determine if the sedimentary facies and therefore the chlorite occurrence (described in chapter 4) could be easily resolved from the log data for the chosen wells. Clean quartz-rich sandstones, calibrated on a limestone matrix, would exhibit approximately a 4 pu (porosity units) separation between the density and neutron tracks without fluid effects. The presence of chlorite, an iron-rich mineral, would increase the bulk density and reduce this separation effect; while a light or low-density fluid would increase this effect. The uranium response from the spectral gamma ray (SGR) would give a more reliable estimate of the overlying shales compared to the shales within the sandstone formation; however 100% shale was determined using the total gamma ray to ensure consistency between wells where SGR was unavailable.

Log-based Lithological Assessment Results

MLNW-1

From the broad scale (Figure 5.4a) ‘clean sandstone’ and ‘100% shale’ values can be defined based on the gamma ray variation (Figure 5.4a); the ‘100% shale’ is based on the widespread mudstone interval directly overlying reservoir A, with a value of ~150api. The ‘clean sandstone’ is taken as the average gamma ray value for all the sandstone bodies within the well; ~30api. These are the end-member values defined from visual analysis and incorporated into the log-based lithological model run within Interactive Petrophysics (described previously). On this scale (1: 500) reservoir A is characterised by a distinct drop in the gamma ray, indicative of sands, with a

gradational base and a sharp top. Reservoir A appears as a single, large sandstone body. However, on a more detailed scale (1:100) the log responses indicate some internal variation, and in particular the gamma ray and density-neutron separation indicate a variation in the proportion of clean sandstone to mudstone and clay (Figure 5.4b). Further, despite being hydrocarbon-bearing and producing dry oil, the resistivity response is low, with an average value of $\sim 0.4\Omega\text{m}$, in contrast to the surrounding formations ($\sim 2\Omega\text{m}$) (Figure 5.5).



Figures 5.4a: Scale 1:500, with main features highlighted

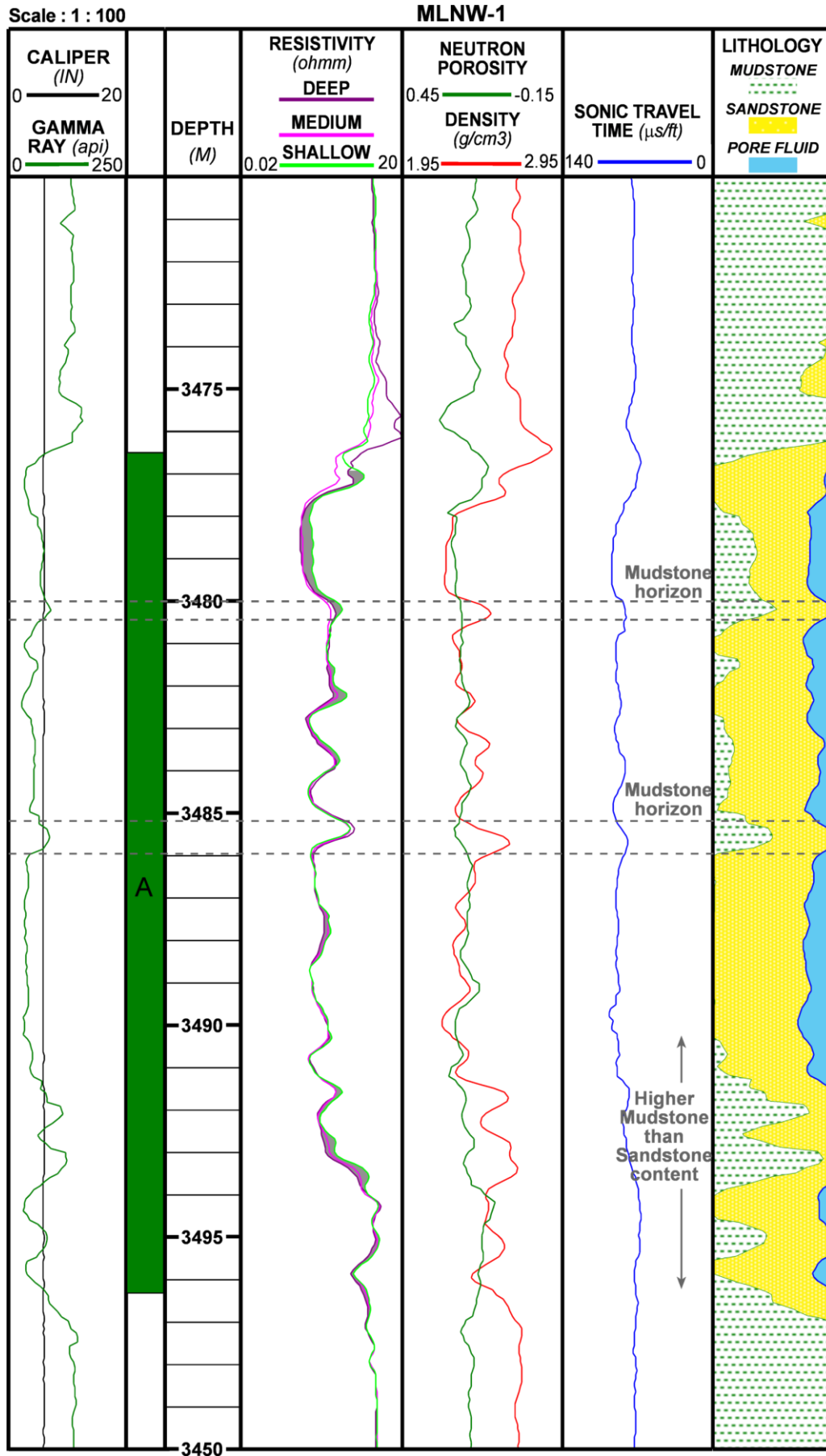


Figure 5.4b: Scale 1:100

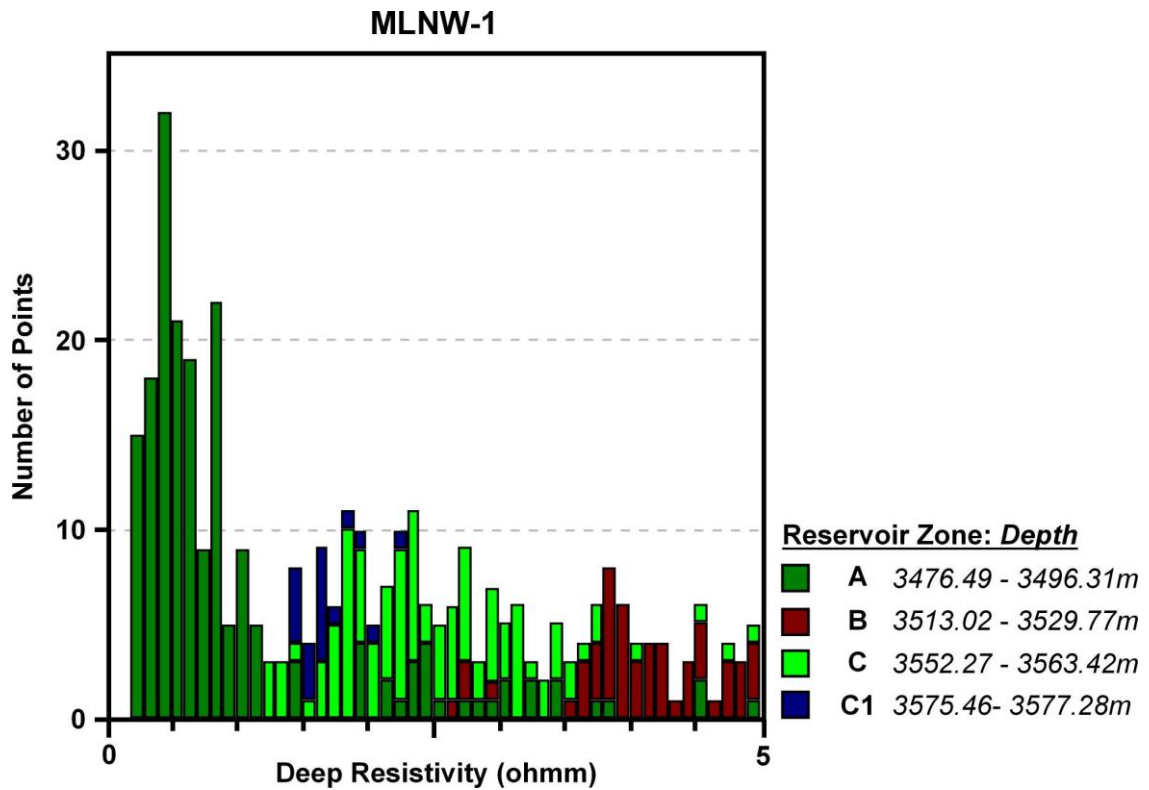


Figure 5.5: Histogram of resistivity values illustrating the difference in resistivity between reservoir sandstone formations in MLNW-1; note that reservoir A formation exhibits the lowest values.

MLNW-2

The mudstone interval directly overlying the main reservoir A sandstone (Figure 5.6a) provides the ‘100% shale’ gamma ray value (~140api) with the ‘clean sandstone’ gamma ray value (~56api) defined as the well average. These values were used in the log-based lithological model, which as shown in figure 5.6a indicates reservoir A is clean sandstone, with minor clay content and no mudstone. When viewed on a more detailed scale (1:100) reservoir A appears as two separate sandstone bodies based on the gamma ray. The lower sandstone has a distinct channel-like signature (Chow et al., 2005) with a sharp top and base (Figure 5.6b). The upper sandstone body has a sharp base with a gradational top, which suggests a transitional nature, and increase in either clay content or a decrease in grain size; reflected in the lithology estimation.

The density-neutron separation suggests the presence of hydrocarbons within reservoir A, and production data supports this (McNeill, 2006, Pers. Comm.). Therefore a distinct contrast in resistivity between the sandstones and the shale would be expected. As figure 5.6a shows the contrast is low, indicating that this well (MLNW-2) is an example of the low resistivity pay problem; the low resistivity response is not indicative of the well being water-bearing.

Scale : 1 : 500

MLNW-2

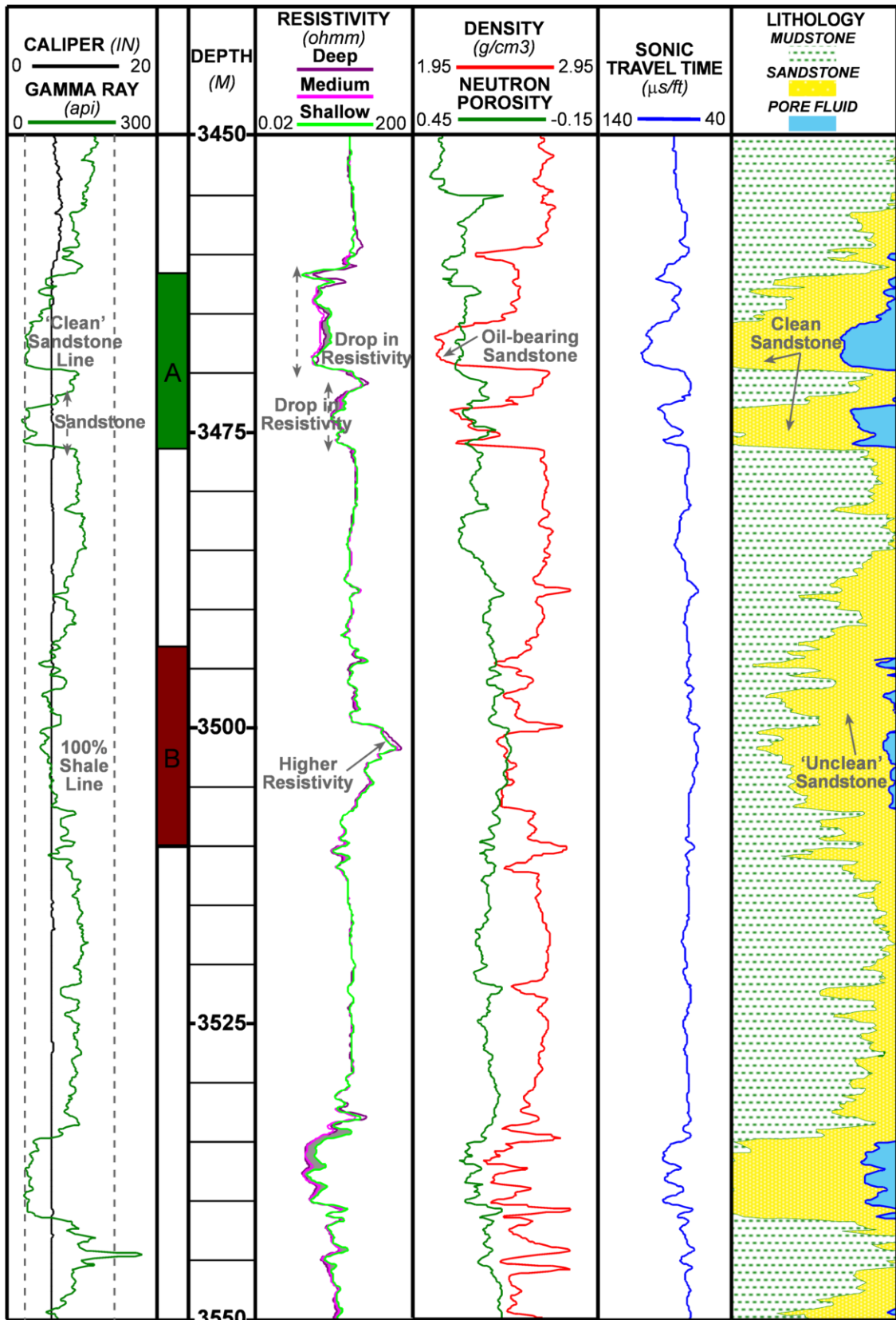


Figure 5.6a: Scale 1:500, with main features highlighted

Scale : 1 : 100

MLNW-2

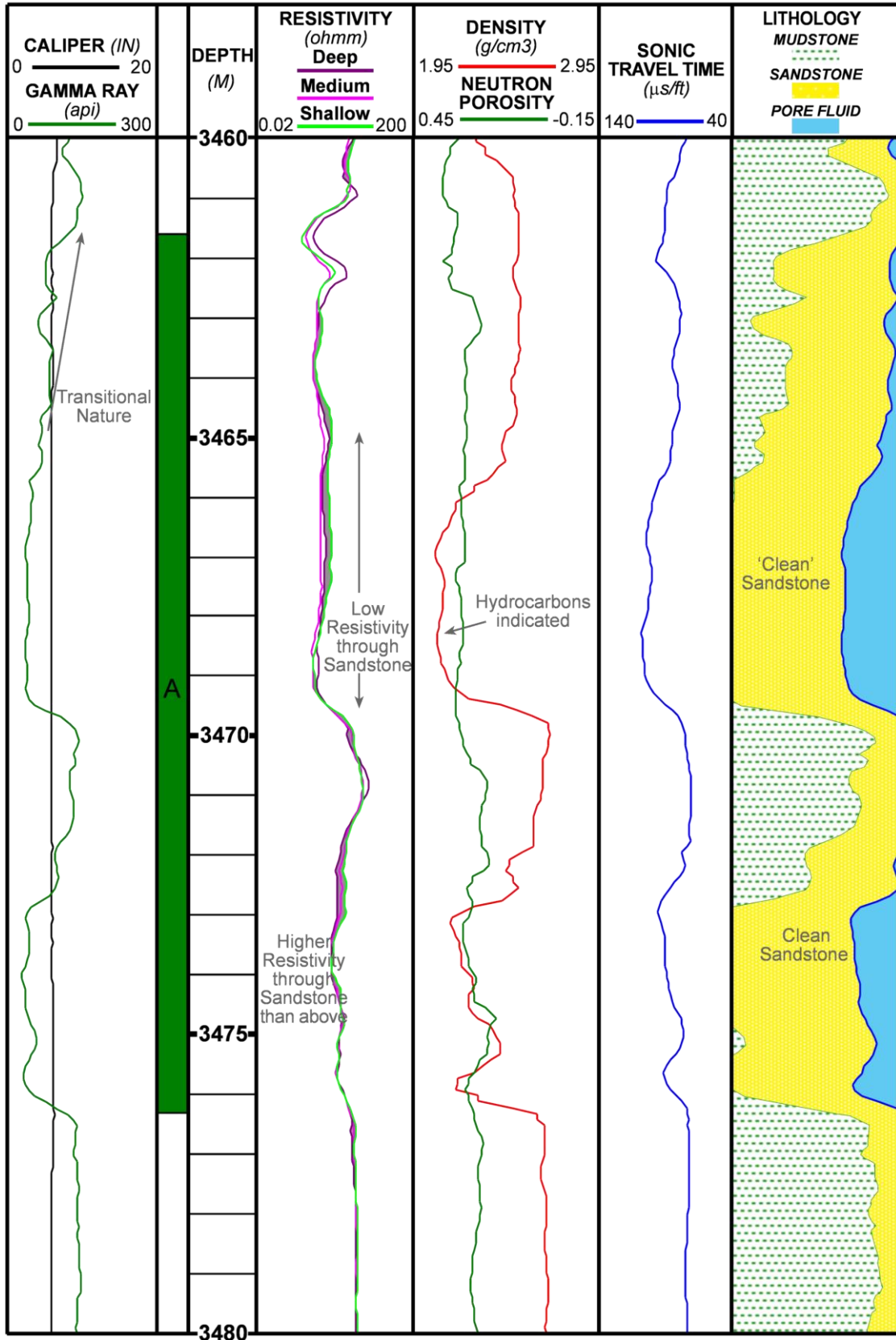


Figure 5.6b: Scale 1:100 with much more detailed features highlighted, and the log-based lithology track shown

MLNW-3

The gamma ray profile for reservoir A in this well suggests a very thin horizon, with a sharp base and top (Figure 5.7a & b) indicative of a channel deposit (Chow et al., 2005). The field-wide overlying mudstone provided the '100% shale' value (~200api), with the 'clean sandstone' taken as a well average (~40api) for the log-based lithological model. The results suggest varying proportions of clay and mudstone present throughout reservoir A sandstone.

This reservoir is known to be water-bearing, and the low resistivity (<1Ωm) and low contrast with the overlying mudstone is consistent with this. The separation of the deep and shallow suggests invasion of the formation, indicating moderate/high permeability.

Scale 1:500

MLNW-3

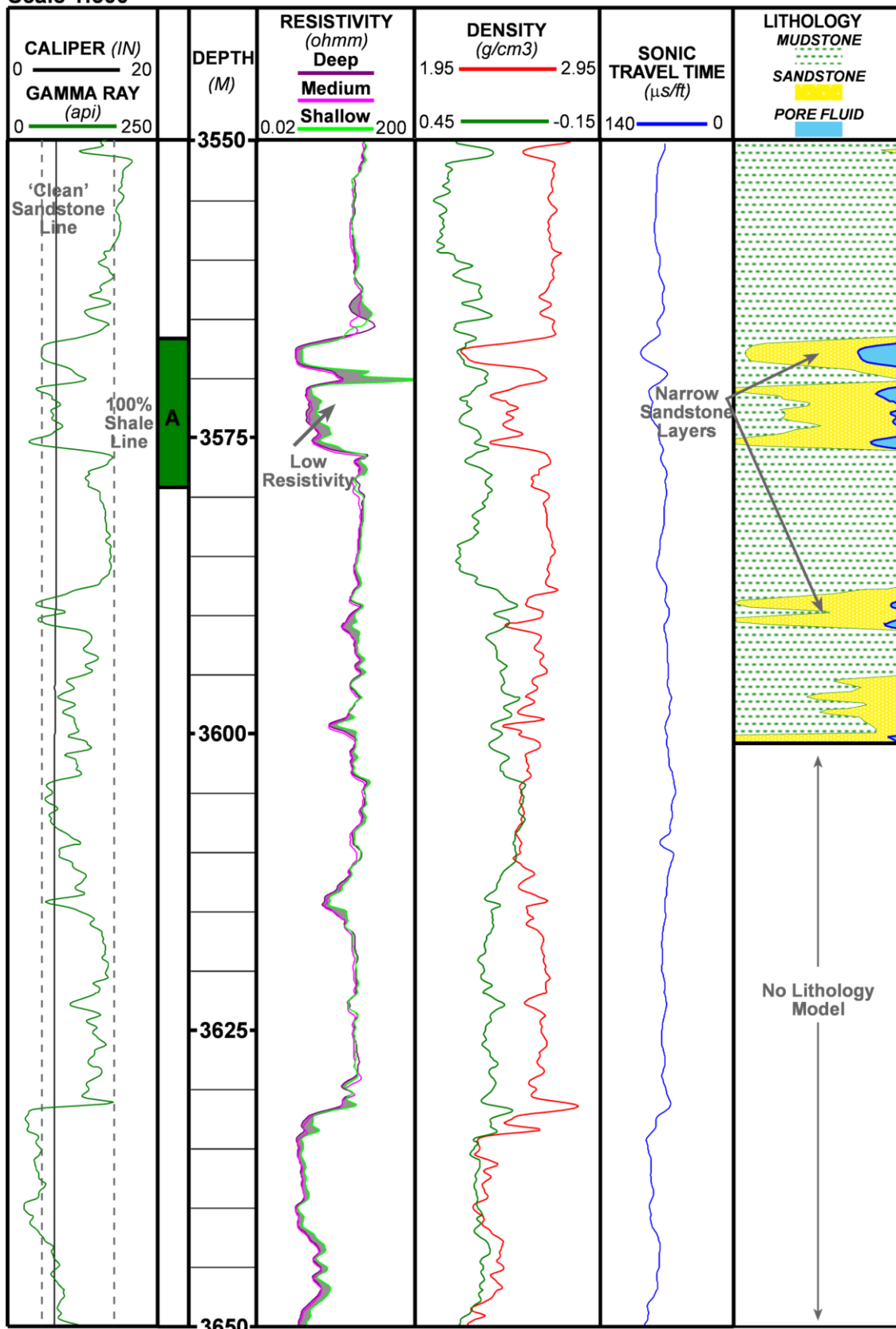


Figure 5.7a: Scale 1:500, with main features highlighted, but not any calculation results.

Scale : 1 : 100

MLNW-3

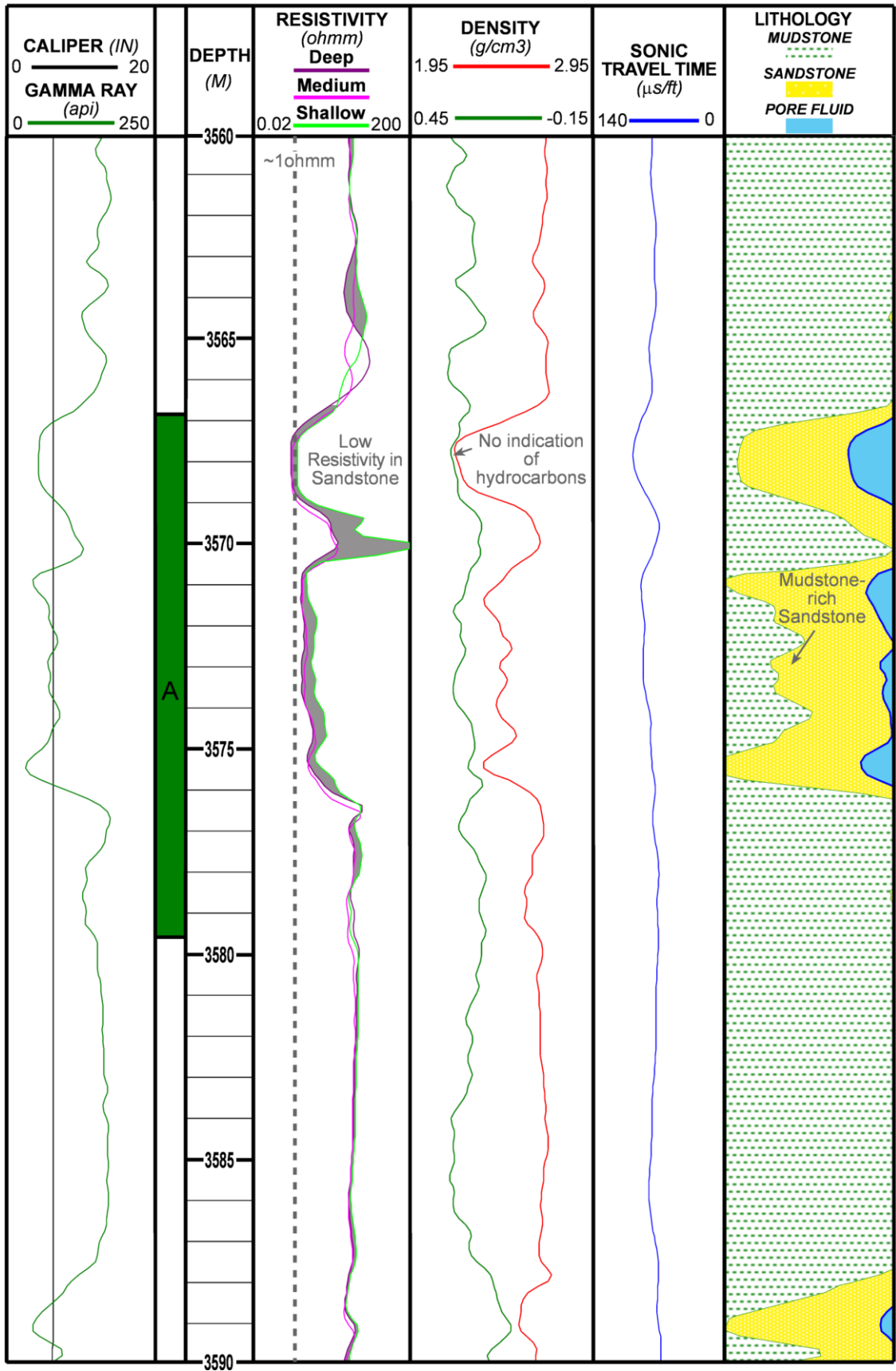


Figure 5.7b: Scale 1:100 with much more detailed features highlighted, and the log-based lithology track shown.

MLNW-4

The gamma ray profile suggests one thick sandstone body with a sharp base and top (Figure 5.8a & b). In detail, minor mudstone horizons are implied based on gamma ray spikes. For the log-based lithological estimation the '100% shale' value is again from the overlying black shale (~150api), and the 'clean sandstone' is a well average (~36api). The log-based lithological model suggests some clay content within the sandstone.

The resistivity across reservoir A sandstone exhibits a low value ($<0.7\Omega\text{m}$) with little contrast to the surrounding formations. This indicates a water-bearing well, which is supported by the production data (McNeill, 2006, Pers. Comm.).

Scale : 1 : 500

MLNW-4

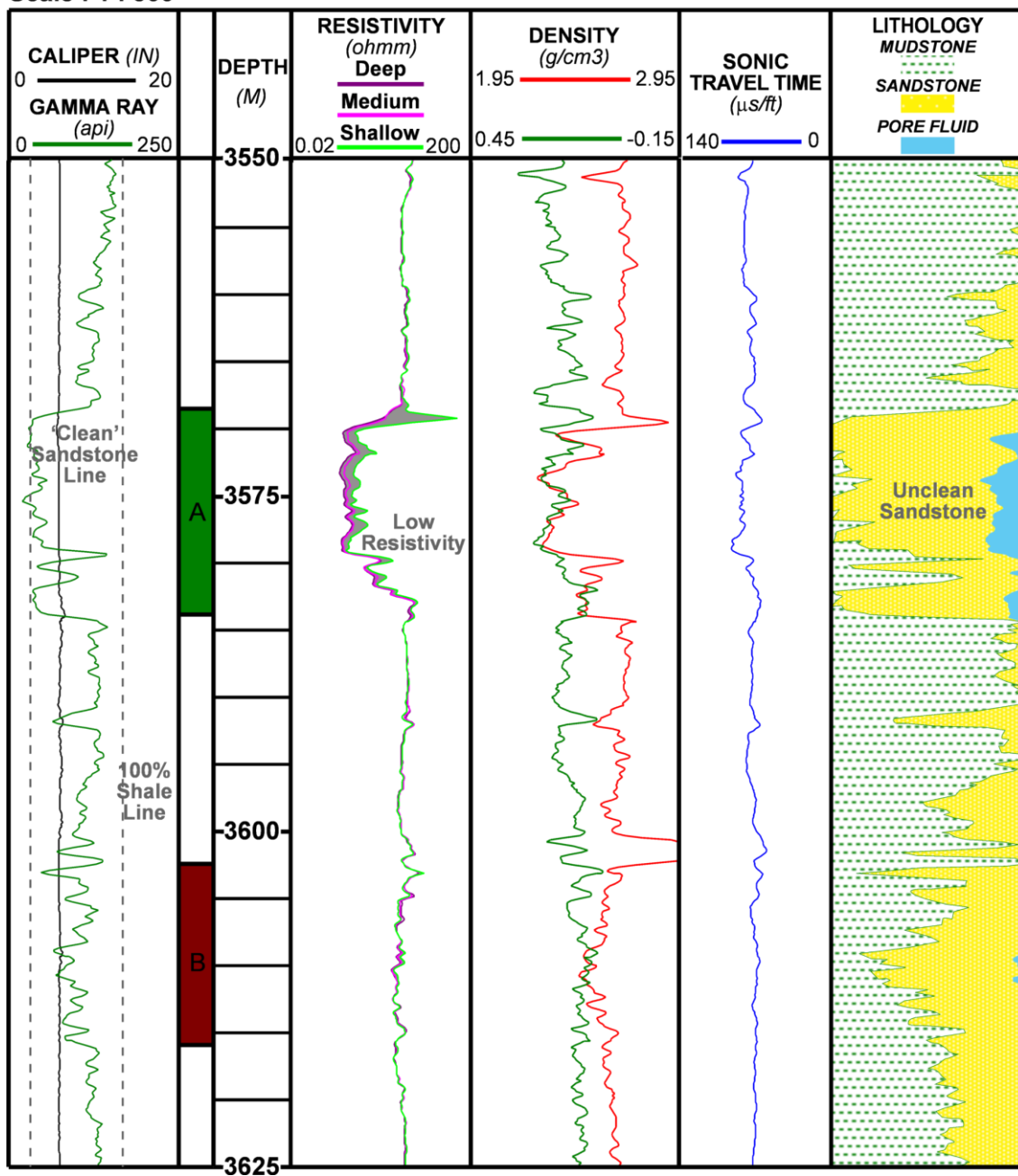


Figure 5.8a: Scale 1:500, with main features highlighted.

Scale : 1 : 100

MLNW-4

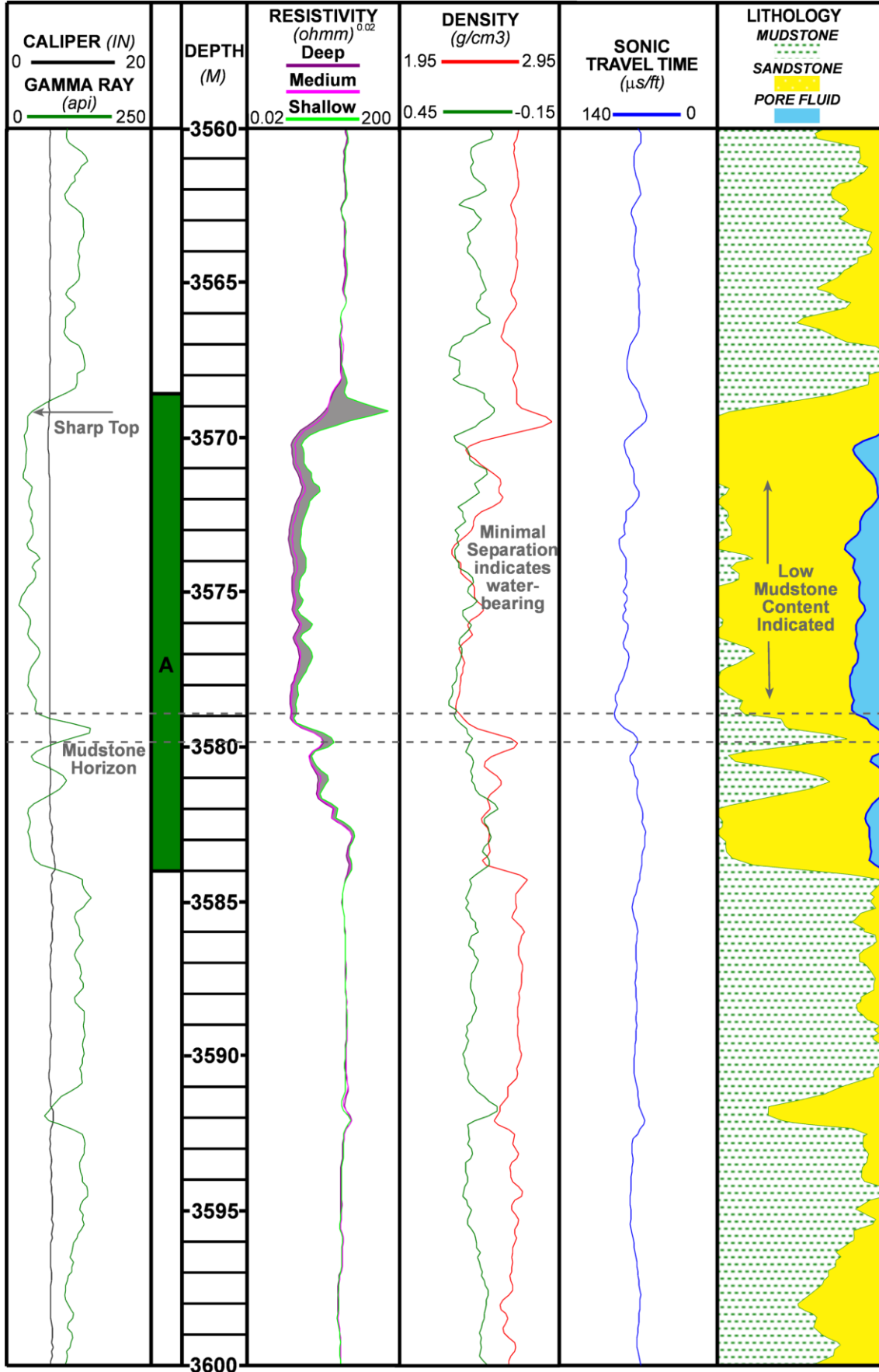


Figure 5.8b: Scale 1:100 with much more detailed features highlighted, and the log-based lithology track shown.

MLNW-5

Based on the gamma-ray profile reservoir A comprises multiple sandstones with inter-layer mudstone horizons (Figure 5.9b). The log-based lithological assessment is based on a '100% shale' value of 150api, determined from the overlying mudstone formation, and 'clean sandstone' of 30api (a well average). The resulting lithology (Figure 5.9a & b) indicates some clay and mudstone content throughout the sandstones.

The resistivity across reservoir A varies little from the surrounding formations, with a mean value of 0.5Ωm indicating a water-bearing formation. The separation of the deep and shallow resistivities suggests moderate permeability.

Scale : 1 : 500

MLNW-5

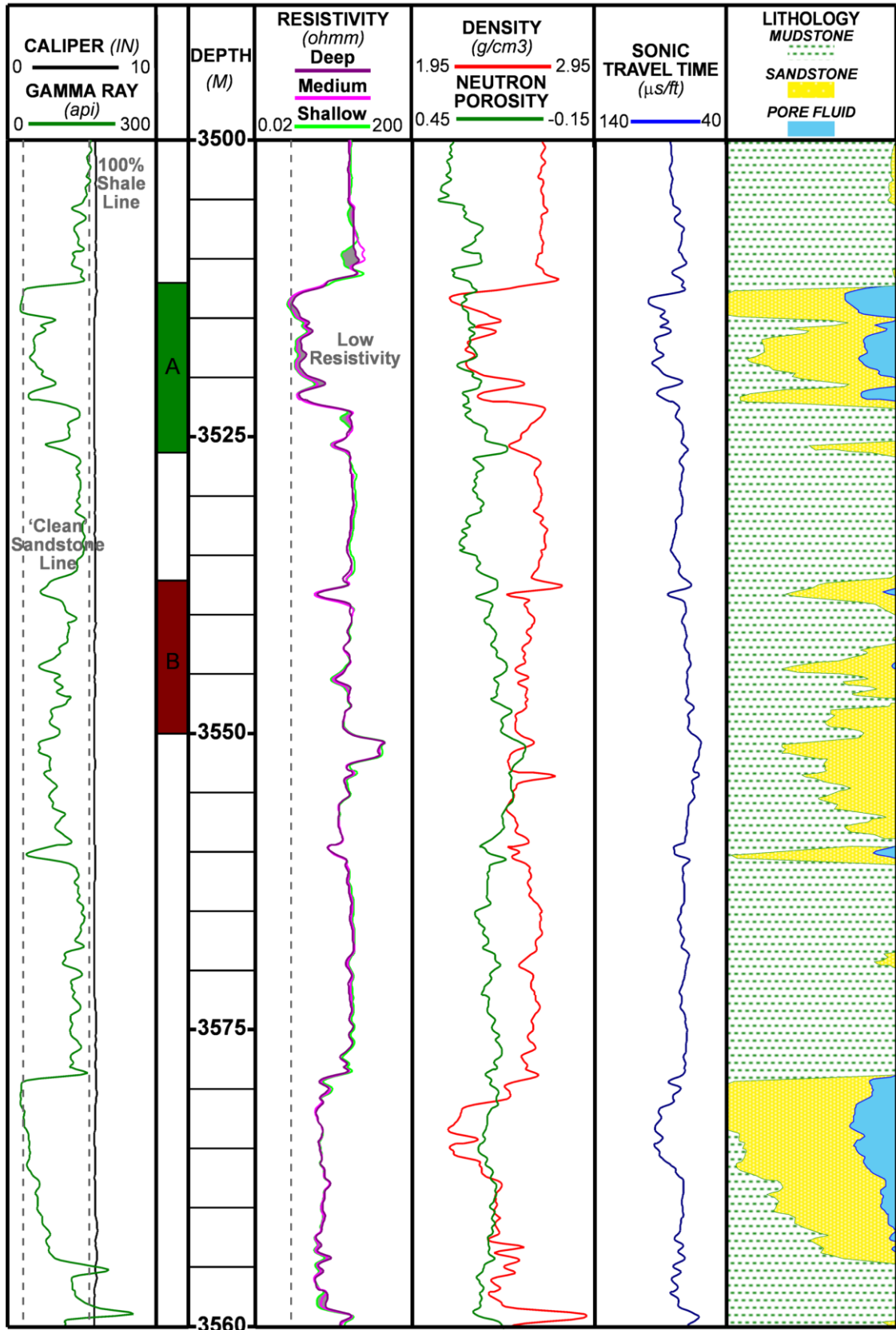


Figure 5.9a: Scale 1:500, with main features highlighted

Scale : 1 : 100

MLNW-5

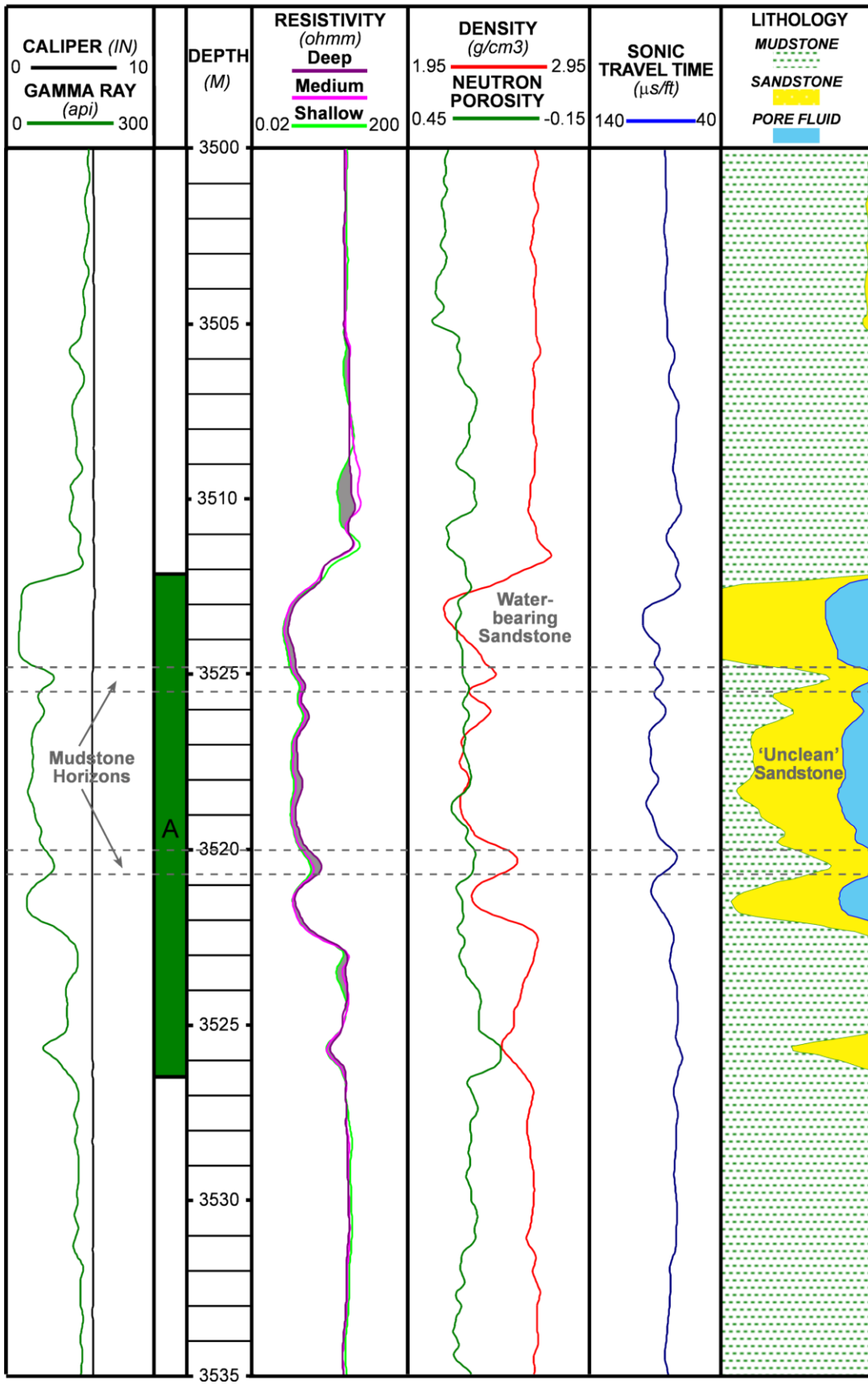


Figure 5.9b: Scale 1:100 with much more detailed features highlighted, and the log-based lithology track shown.

MLN-5

From a different area (MLN) of the study field the gamma ray profile and reservoir A signature is slightly different to that seen in the MLNW section (wells described above). The gamma ray does not indicate a sharp base to reservoir A, but exhibits a gradual upward decrease, suggesting a gradual increase in sand content. The log-based lithological estimation also indicates an increase in sand content up through reservoir A. The 'clean sandstone' and '100% shale' gamma ray values used in the model are ~45api and ~165api respectively (Figure 5.10a & b).

The density-neutron separation is not obviously indicative of hydrocarbon presence, having only a small separation. The resistivity also exhibits low contrast between the sandstones and shale, with a value of ~1Ωm across reservoir A. However, the well produces oil (McNeill, 2006, Pers. Comm.), and is another example of the low resistivity contrast problem under investigation in this project.

Scale : 1 : 500

MLN-5

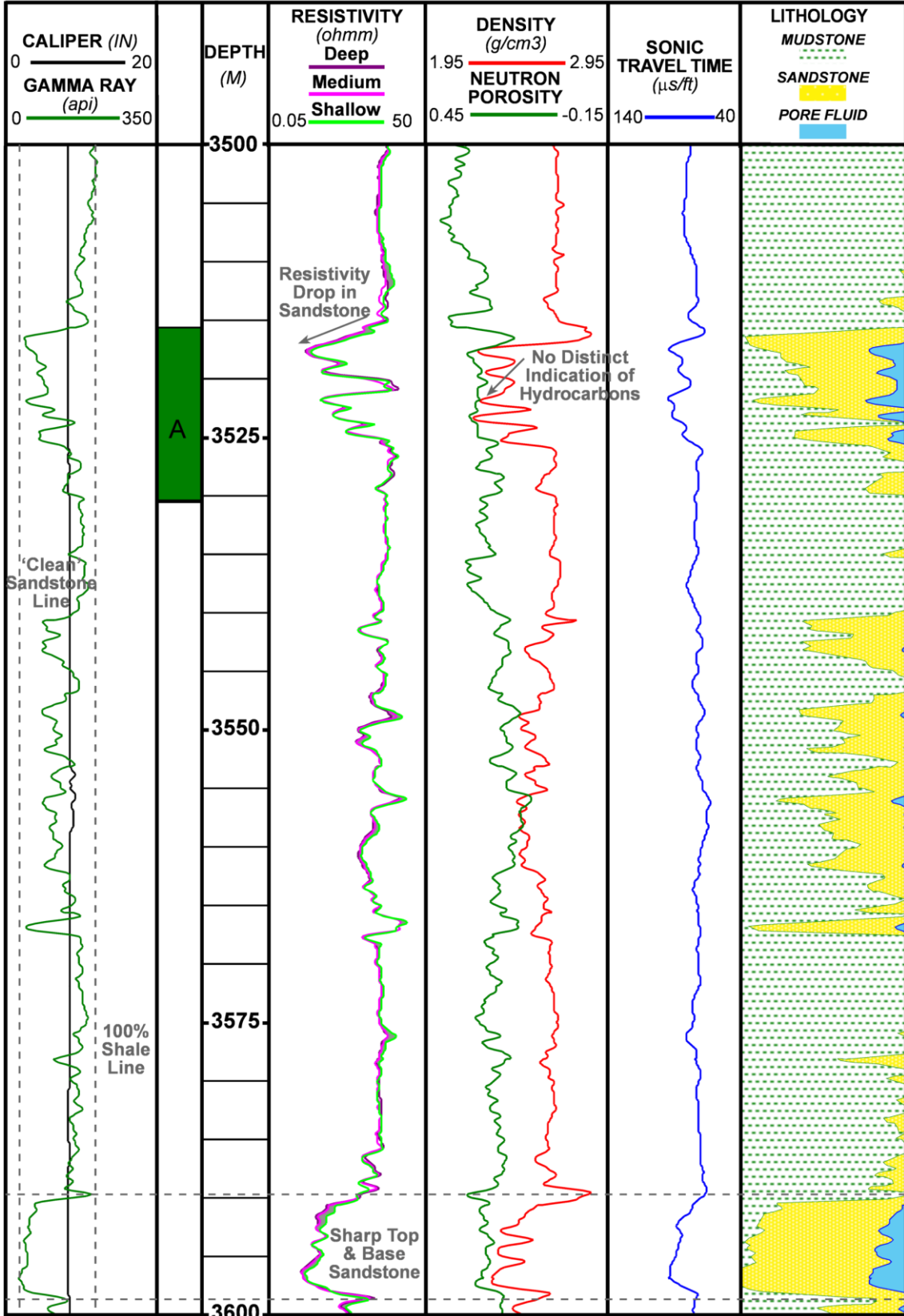


Figure 5.10a: Scale 1:500, with main features highlighted

Scale : 1 : 100

MLN-5

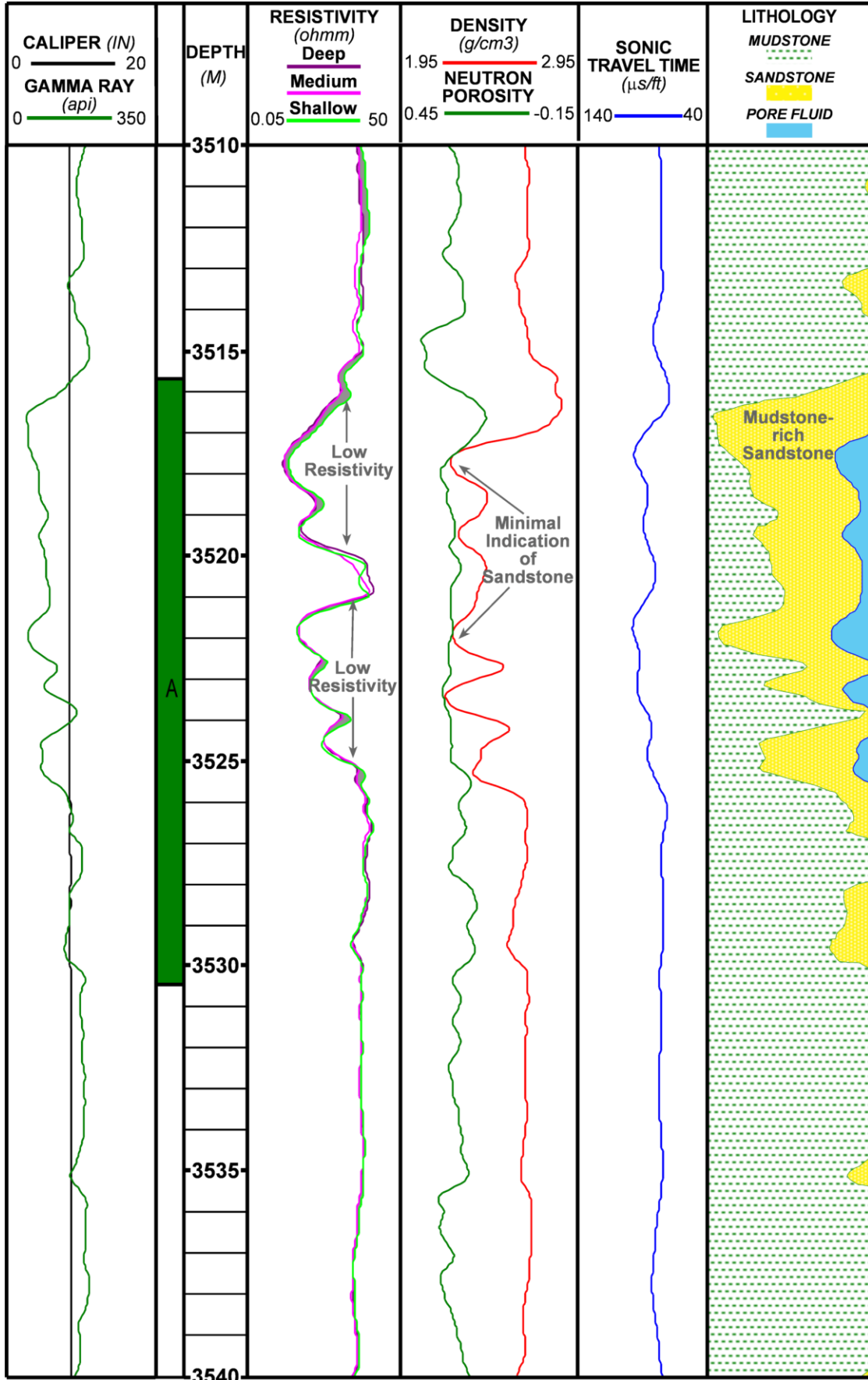


Figure 5.10b: Scale 1:100 with much more detailed features highlighted, and the log-based lithology track shown.

MLSE-5

In a separate area of the study field well MLSE-5 exhibits a similar gamma ray profile across reservoir A to wells from the MLNW area (Figure 5.11). Reservoir A has a sharp base and top, with a more mud-rich horizon (Figure 5.12b) separating two distinct sand bodies. The log-based lithological assessment suggests the upper sandstone is ‘cleaner’ i.e. with a lower mudstone and clay content than the lower sandstone. The gamma ray values used in the computer model were ~155api and ~50api for ‘100% shale’ and ‘clean sandstone’ respectively.

As shown on figure 5.12a, the density-neutron separation clearly indicates the presence of hydrocarbons, in this case, gas (McNeill, 2006, Pers. Comm.). However the resistivity across this interval is the lowest (~1.4Ωm) exhibited through this section of well (Figure 5.12a). Therefore this well is a very good example of low resistivity pay.

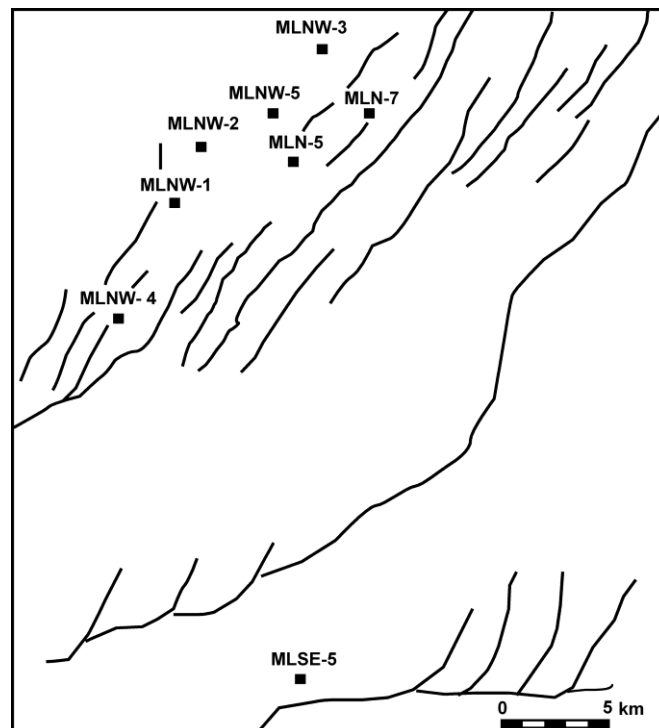


Figure 5.11: Map showing proximity of wells, lines represent main fault barriers

Scale : 1 : 500

MLSE-5

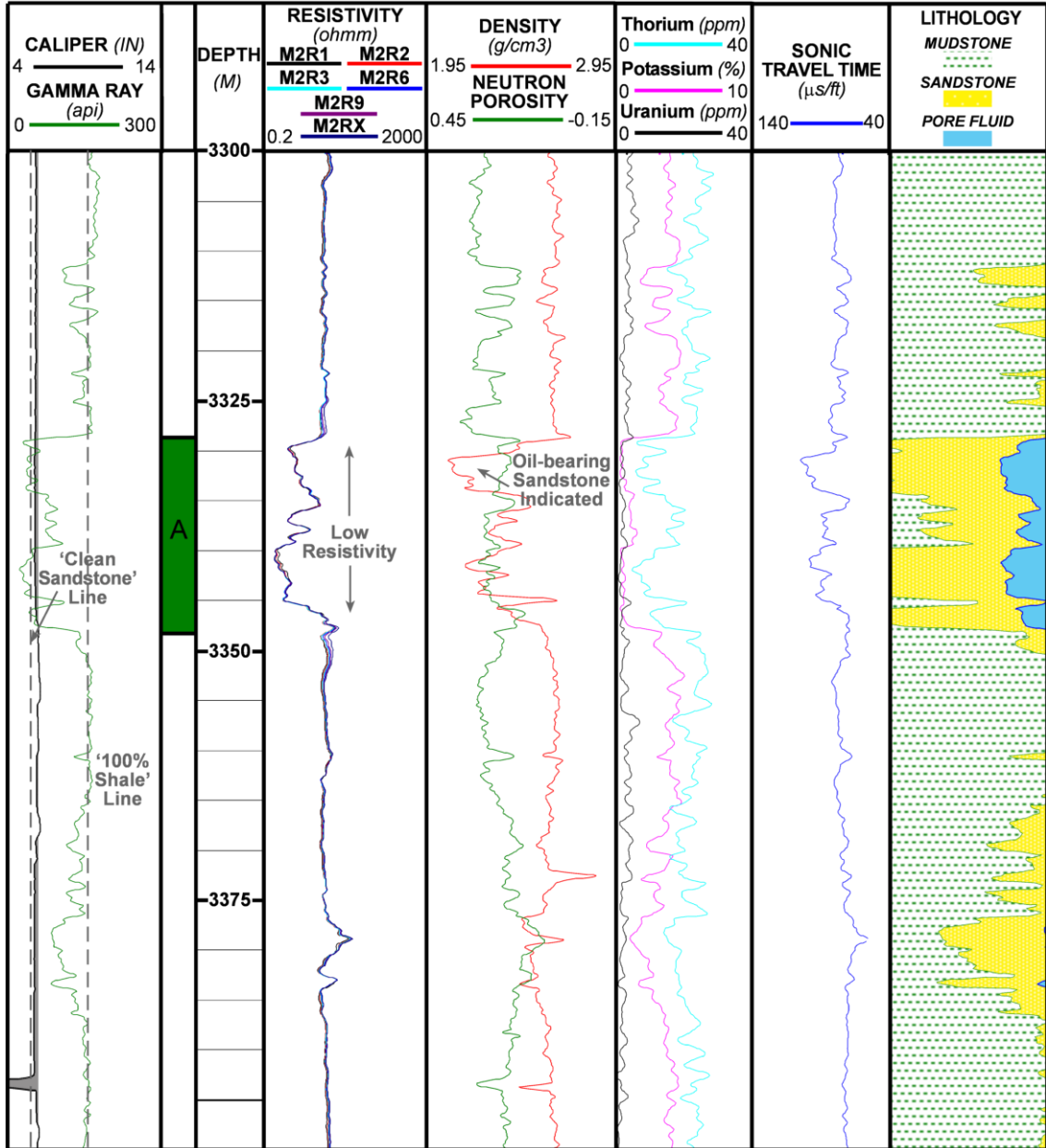


Figure5.12a: Scale 1:500, with main features highlighted

Scale : 1 : 100

MLSE-5

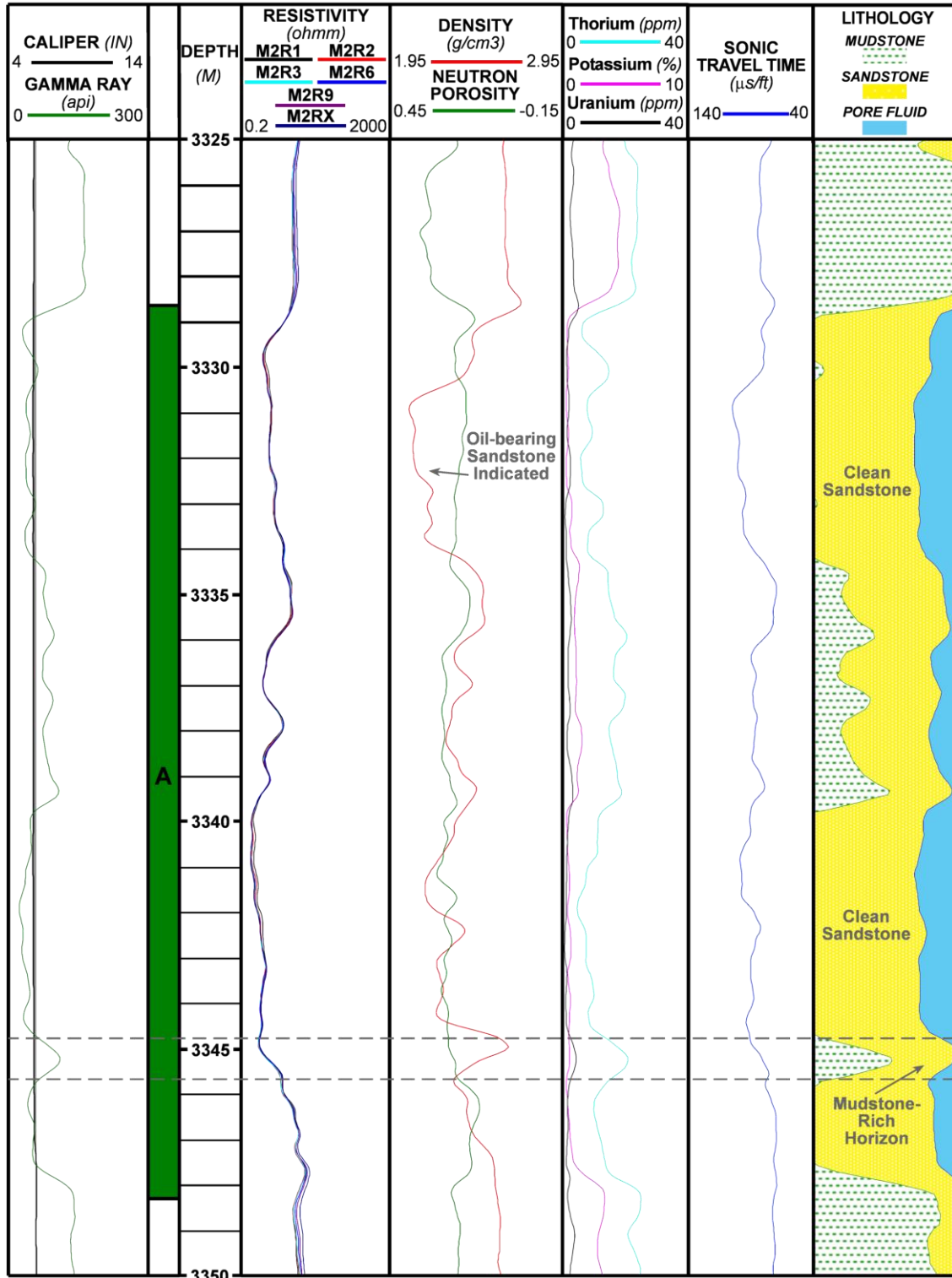


Figure 5.12b: Scale 1:100 with much more detailed features highlighted, and the log-based lithology track shown.

The lithological analysis of the described wells, based on the gamma ray log indicates that although in most cases the sandstones can be resolved; these intervals contain varying amounts of clay material (“clay”) and mudstones (“shale”). The above log-

based lithological models do not, however, provide a good match with the core-derived sedimentological model (discussed in chapter 4), as no distinction is made between the dispersal of the mudstone and clay content within the sandstones. This is important as not only does it link to the sedimentary facies, how the clay is distributed within the sandstone can have a strong impact on the properties and therefore the log responses. In order to determine how best to deal with the log responses, and future saturation calculations (See chapter 6) it is necessary to understand how the mudstone and clay (“shale”) are distributed within the sandstones. One approach to this is through Thomas-Stieber analysis.

5.1.3 Thomas-Stieber Analysis

The problem of terminology arises because in the Thomas-Stieber analysis, what is normally termed “shale” encompasses both mudstone and clay (see section 5.1.2 introduction). This section discusses the Thomas-Stieber analysis and highlights the misuse of the term “shale”. The principle underlying Thomas-Stieber analysis is that “shale” abundance (clay minerals and mudstones) within a sandstone is not the only important control on log responses, but also the way in which the “shale” is distributed can affect the log responses (Ellis, 1987; Thomas and Stieber, 1975). It is possible to define three end-members of “shale” distribution within sandstones; ‘*dispersed*’, ‘*laminated*’ and ‘*structural*’ (Figure 5.13) and each are considered to affect porosity in a different way (Poupon et al., 1970).

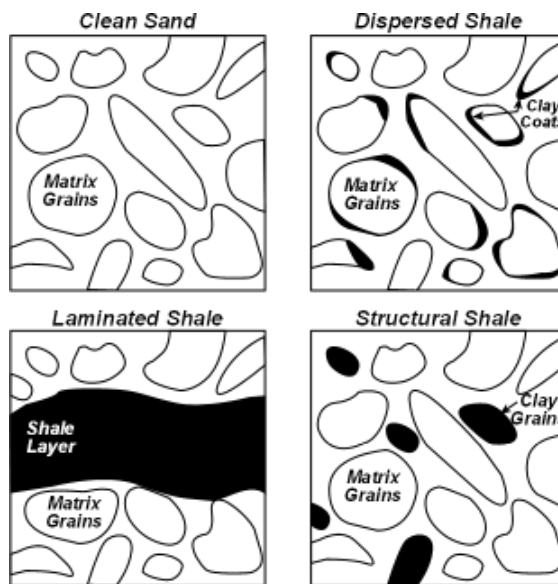


Figure 5.13: Classification of shale by distribution (modified from Ellis, 1987)

'Dispersed shale' is considered to be present throughout the pore space; essentially representing the diagenetic growth of clay minerals around grain edges. This growth clearly reduces the original porosity, particularly if it occurs early in the burial history as it can prevent further porosity loss (see chapter 3). *'Structural shale'* is defined as individual clay grains that occur alongside the sand-sized grains (such as quartz, feldspar, lithic fragments) and are present from time of deposition. As detrital grains, they do not significantly affect the original porosity, especially in compacted formations. *'Laminated shale'* represents discrete horizons of “shale” mudstone layers, lenses or laminae, in otherwise clean sandstone and are present from the time of deposition. Since these different distributions of “shale” will affect the porosity and log responses in a different manner it is common to try and determine which type of “shale” distribution end-member is dominant within a reservoir.

For this study, all three end-member distributions can be identified in the core sedimentological analysis (see chapter 4); *'dispersed'* relates to the grain coating chlorites, *'structural'* relates to the minor individual clay grains, and *'laminated'* refers to the mudstone laminae, and all these occurrences would be considered “shale” in the

industry (Table 5.6). However, the grain coating chlorite and the individual clay grains are clay minerals, whereas the mudstone laminae are a separate lithology likely composed of silt-sized grains (potentially quartz, feldspar, mica and a range of clay minerals – see Appendix II). Despite the difference in classification terminology, applying this classification scheme could provide an alternative method for distinguishing between the chlorite, grain-coating sandstones (Facies VIII) and the more cemented sandstones (Facies III).

<i>Original Classification</i>	<i>Main Feature</i>	<i>Sedimentological Term</i>
<i>Dispersed</i>	Grain-coating chlorite	Grain-coating clay minerals
<i>Structural</i>	Individual sand-sized clay grains	Clay minerals
<i>Laminated</i>	Thin mudstone laminae	Mudstone lithology

Table 5.6: “Shale distribution” classification and the suggested link to sedimentological features, and new classification

Using the Thomas-Stieber method of a cross-plot of porosity against sandstone fraction, determined from the gamma-ray log, the different “shale” classification distributions separate (Thomas and Stieber, 1975). Given the minor occurrence of the ‘*structural*’ component a lack of separation of that class is to be expected. Given the strong correlation between the ‘*dispersed*’ class with facies VIII, and facies III with the ‘*laminated*’ class a clear separation would be expected. However, figure 5.14 illustrates that for this whole study the clay mineral and mudstone distribution within the different sandstone facies are indistinguishable. However, this is not an entirely unexpected result. The Thomas-Stieber plot focuses on end-member conditions of ‘*laminated*’ or ‘*dispersed*’ but in reality there exists a spectrum, and while one sandstone may be dominated by ‘*dispersed*’ for instance there will still be some occurrence of ‘*laminated*’.

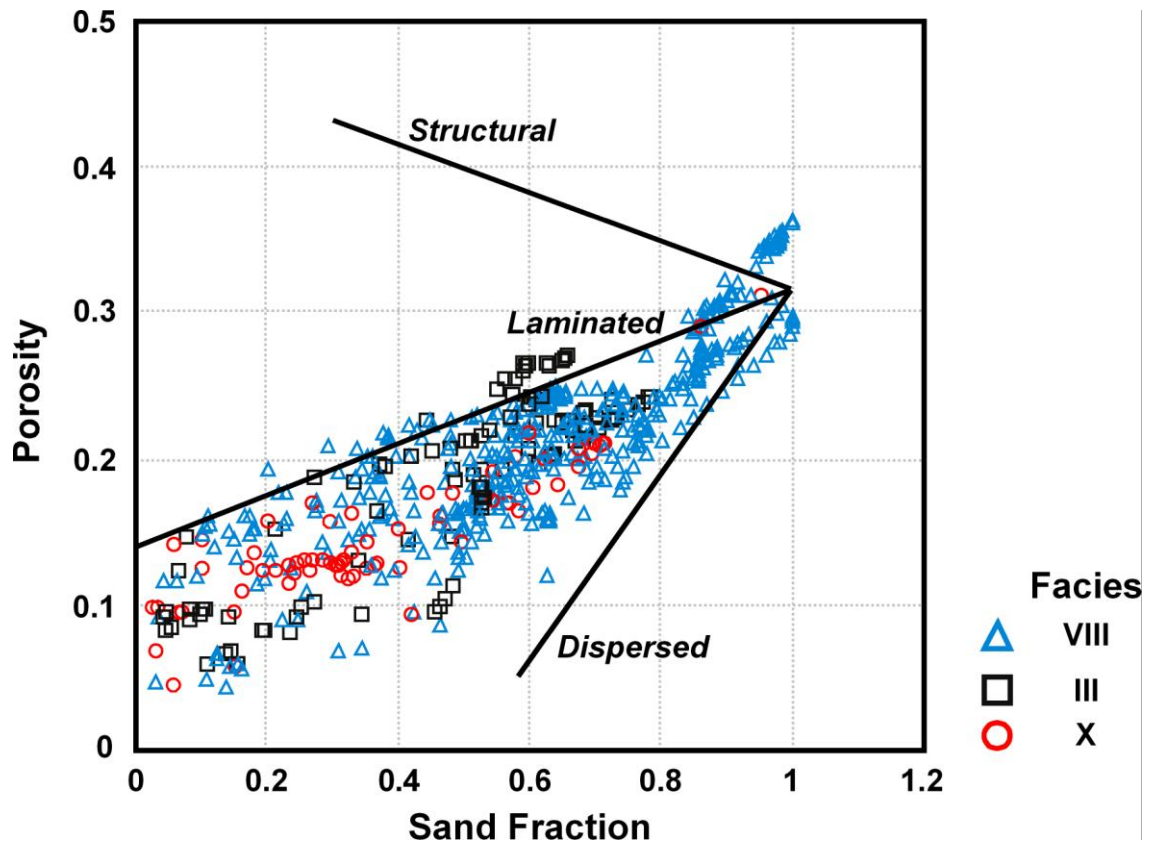


Figure 5.14: Thomas-Stieber cross-plot for sandstone facies from four wells in this study (mlnw-1, mlnw-4, mlnw-5, and mlse-5). The sandstones all exhibit a shale distribution between dispersed and laminated, plot modified from Thomas and Stieber (1975).

This therefore is not a suitable method for differentiating the main sandstone facies, and is inappropriate for interpreting the presence of chlorite. Alternative methods for identifying the chloritic sandstones facies or presence of grain-coating chlorite from log responses are required. It also suggests that the industry standard of employing a broad “shale” term should be reconsidered.

5.2 Log-analysis relationship to chlorite occurrence

The problem of chlorite in hydrocarbon-bearing reservoirs is not a new one, and multiple techniques exist for the analysis of such reservoirs. However, in this case the drilling conditions used render these standard techniques unusable. For example, cross-plots of thorium vs. potassium ratios and also thorium/potassium vs. PEF can be used to identify the presence of chlorite (methodology discussed in Chapter 2). However, the

use of heavy drilling mud (barite-rich) results in an unreliable PEF curve in the majority of the wells. In the few wells where the PEF is useable, (MLSE-5, MLNW-6, MLN-7, MLN-8) it does not provide a reliable means of identifying where the chlorite occurs within the sediments, particularly within the sandstones (Figure 5.15). When the data from MLSE-5 are investigated using this plot in relation to the defined sedimentary facies and known chlorite occurrences it is clear that no predictive capability is possible. The main sandstone facies (VIII) known to contain chlorite does plot towards the chlorite field, suggesting the tool response is detecting the chlorite presence (Figure 5.15); however, there is a lot of overlap with the other sedimentary facies.

These plots (Figure 5.15) illustrate the ineffective use of the standard cross-plots for the identification of clay-type. The same data set plotted on two different plots indicate different clays; figure 5.15a indicates the presence of glauconite, as well as some chlorite but figure 5.15b indicates a complete absence of glauconite.

There is, however, a broad correlation between the two lithology types, for example on figure 5.15a, the area that appears to be glauconite-rich broadly corresponds to the mudstones above and below reservoir A, while the area that most closely corresponds to the chlorite “field” coincides broadly with the main sandstone bodies of reservoir A. However, despite this broad-correlation it cannot be used to accurately determine where the chlorite is present within the sandstones, and furthermore this method is of little predictive use for wells where the PEF curve is unavailable. In such cases a plot of Th vs. K can often be used to identify clay type.

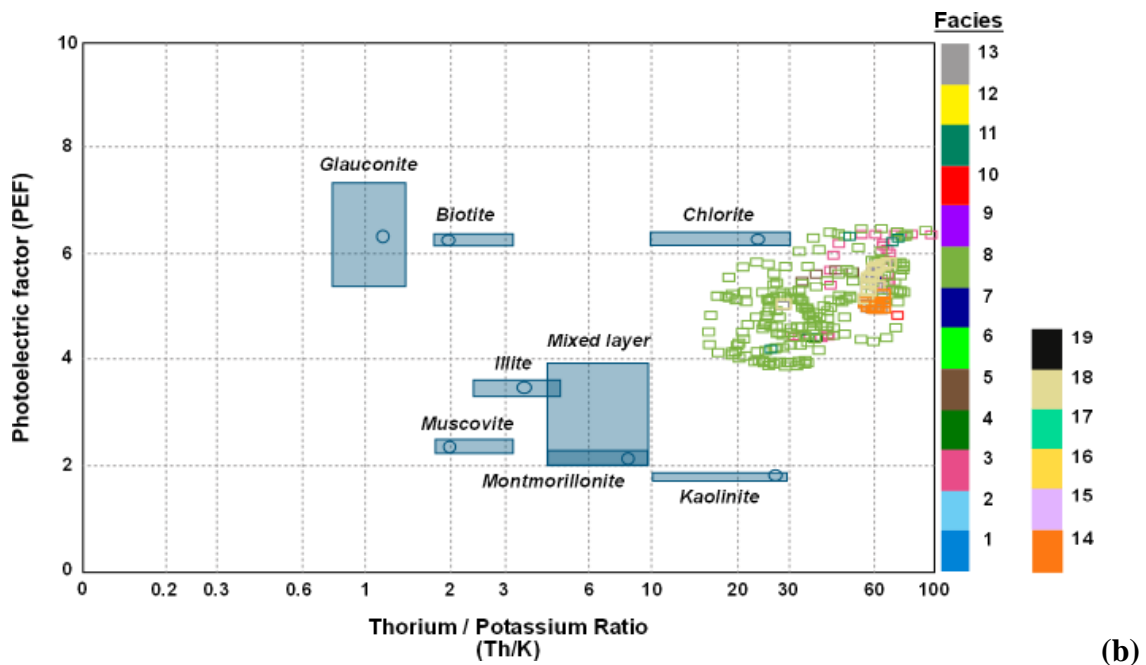
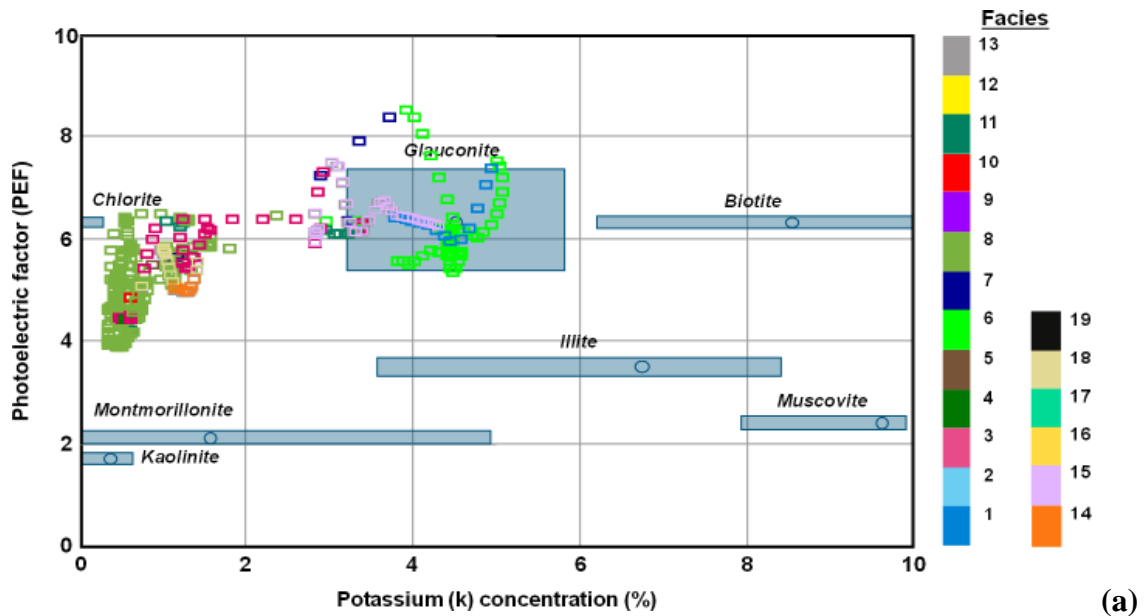


Figure 5.15: PEF vs. Potassium (top), and PEF vs. K/Th ratio (bottom) for MLSE-5, separated for the sedimentary facies

As discussed in Chapter 2, there are two main cross-plots for thorium vs. potassium used to determine clay type, each with different scales and slightly differing areas for clay classification. For the two focus wells (MLNW-5 and MLSE-5) both Th vs. K plots exhibit a spread of clay types, with some close to the chlorite field (Figure 5.16), but neither plot clearly identifies the mineralogical variation observed in the core. There is

however, a degree of overlap between the different sandstone and mudstone facies on both plots, and therefore as a predictive method for defining unequivocally chlorite occurrence within the uncored wells it is not useable.

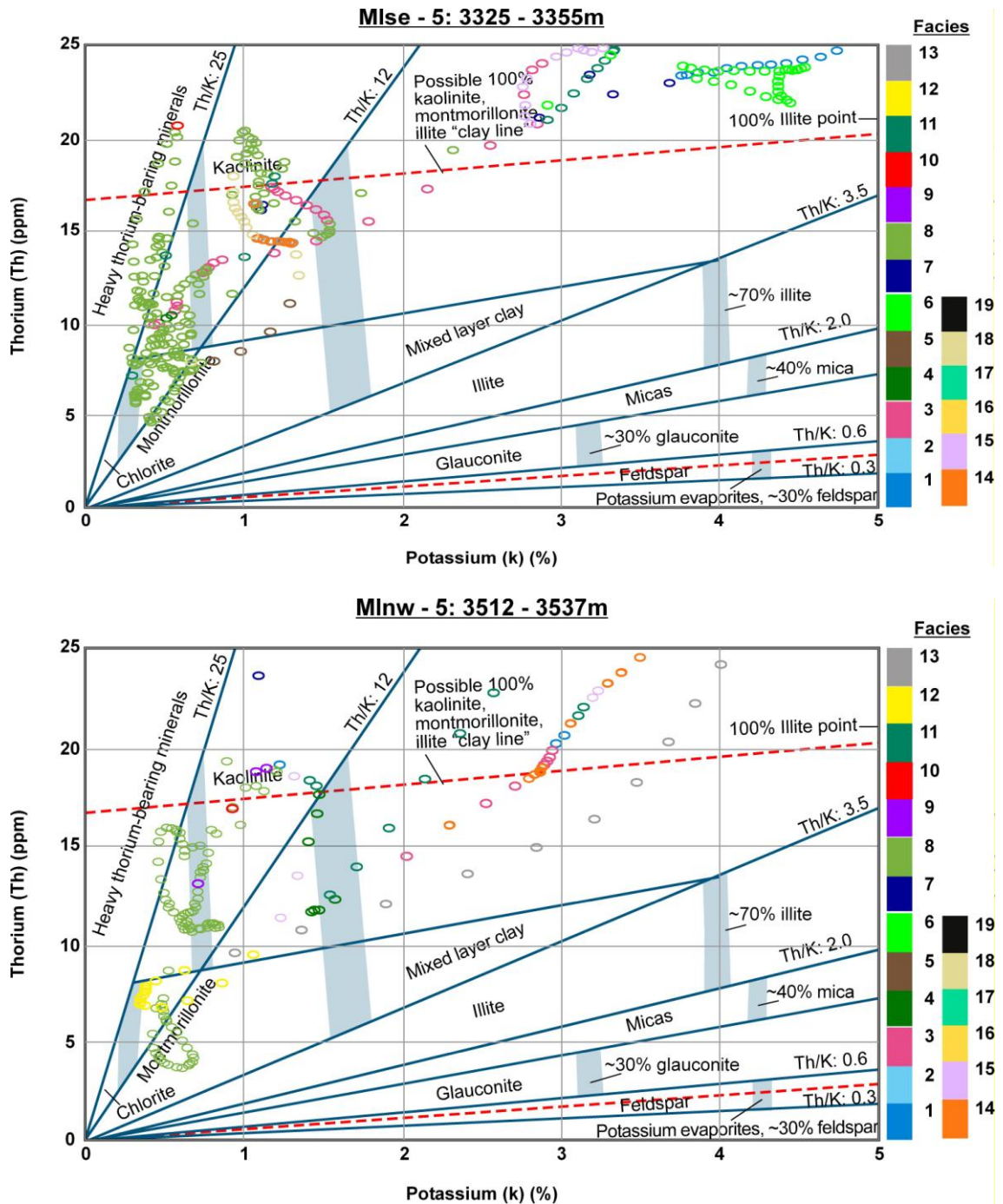


Figure 5.16a: Thorium vs. Potassium, Schlumberger clay fields, for MLSE-5 (top) and MLNW-5 (bottom) separated for the sedimentary facies

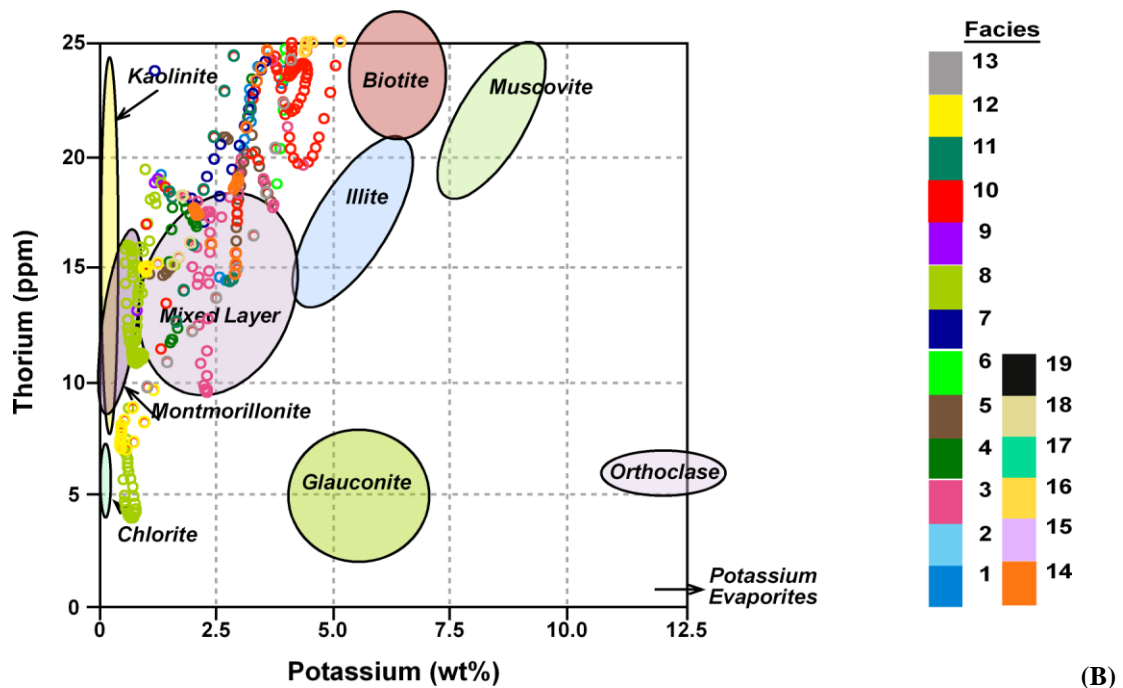
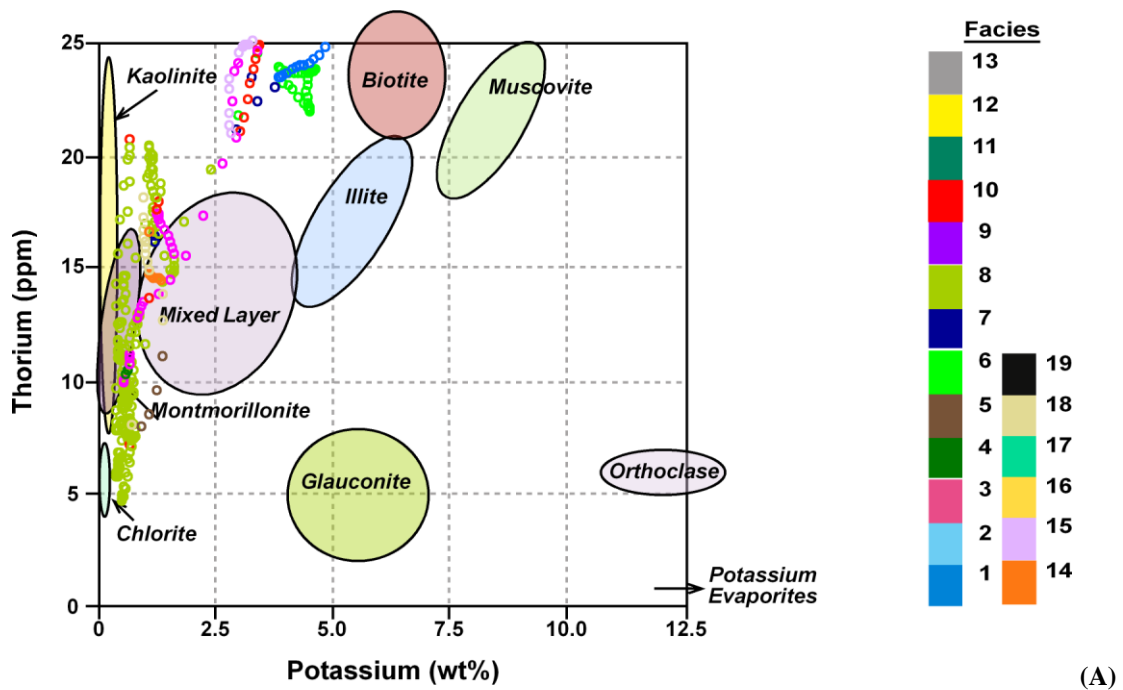


Figure 5.16b: Thorium vs. Potassium, Serra clay fields for MLSE-5 (A) and MLNW-5 (B) separated for the sedimentary facies

Analysis of both of the above cross-plot types (PEF vs. Th/K and Th vs. K) indicates that conventional analysis to determine the presence of chlorite on the detailed scale is not possible with this data set. Therefore alternative methods are investigated.

5.3 Log-analysis relationship to sedimentary facies

The visual log analysis including the gamma ray variation and computer-based lithological analysis provides a good basis for the prediction of overall lithology; however this does not provide a link to the sedimentary facies. A link between the log data and the detailed sedimentary facies is required because the facies variations provide a direct link to the presence/absence and abundance of chlorite in the sandstones (Facies VIII = chlorite-rich; Facies III = cemented, low chlorite content). The facies are the focus of the log analysis, as the chlorite itself exhibits no obvious log response, and the usual cross-plot methods from the PEF and spectral gamma ray (described in Chapter 2) do not provide a definitive means of discrimination; as discussed in Section 5.2. Initial log analysis focussed on wells MLNW-5 and MLSE-5; where a detailed sedimentology analysis was completed (see Chapter 4). MLNW-5, as a water-bearing well, formed the basis for the log analysis, with MLSE-5, an oil-bearing well, providing the data to test the log analysis accuracy.

5.3.1 Density – Neutron cross-plot for Facies

As discussed (section 5.1.2) the density-neutron cross-plot can provide information on lithology, therefore the first step was to see if the dominant sedimentary facies could be resolved. Due to the resolution of the logging tools, only beds <~60cm will be fully resolved, therefore any facies occurring in thinner beds than this were filtered from the data prior to plotting, to avoid excessive scatter on the plots. Several facies are clearly resolved for MLNW-5: VIII, III, XIX, XV and VI (Figure 5.17).

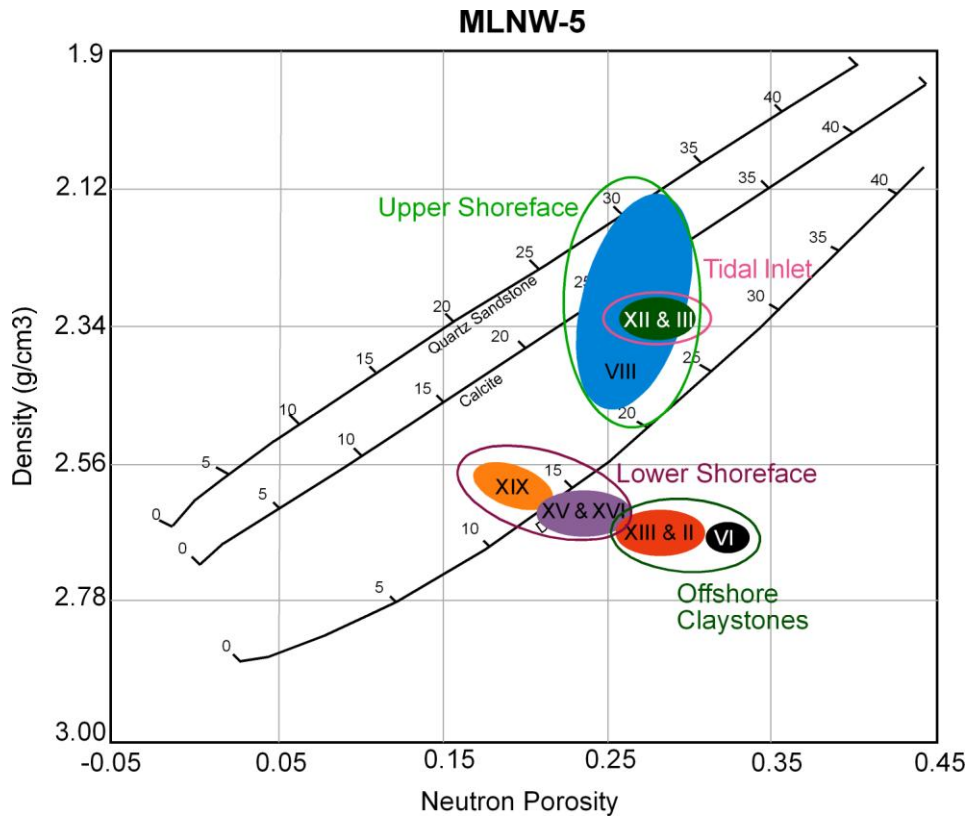


Figure 5.17: Density – neutron cross-plot for the main sedimentary facies from MLNW-5

The cross-plot is successful in separating the main sandstone facies (III, VIII and XII) from the mudstone facies. Therefore the sedimentary environment; upper shoreface, lower shoreface and offshore environments, can also be resolved (Figure 5.17, and see chapter 4 for facies relationship to depositional environment). The mudstone separation shows a distinct trend from left to right, with decreasing sandstone content, consistent with moving to more offshore environments. A further aspect of the mudstone trend could be related to mineralogy, when the facies are examined in detail, from micaceous silty mudstones (XIX), through micaceous mudstones (XV and XVI) to pyritic and micaceous mudstones (XIII and VI) (Figure 5.17).

This relationship between sedimentological facies type and wireline log data is supported when compared to the data and facies from well MLSE-5. Again beds <60cm thick were removed to prevent excess scatter, and the same separation between sandstones and mudstones is seen on the plot (Figure 5.18).

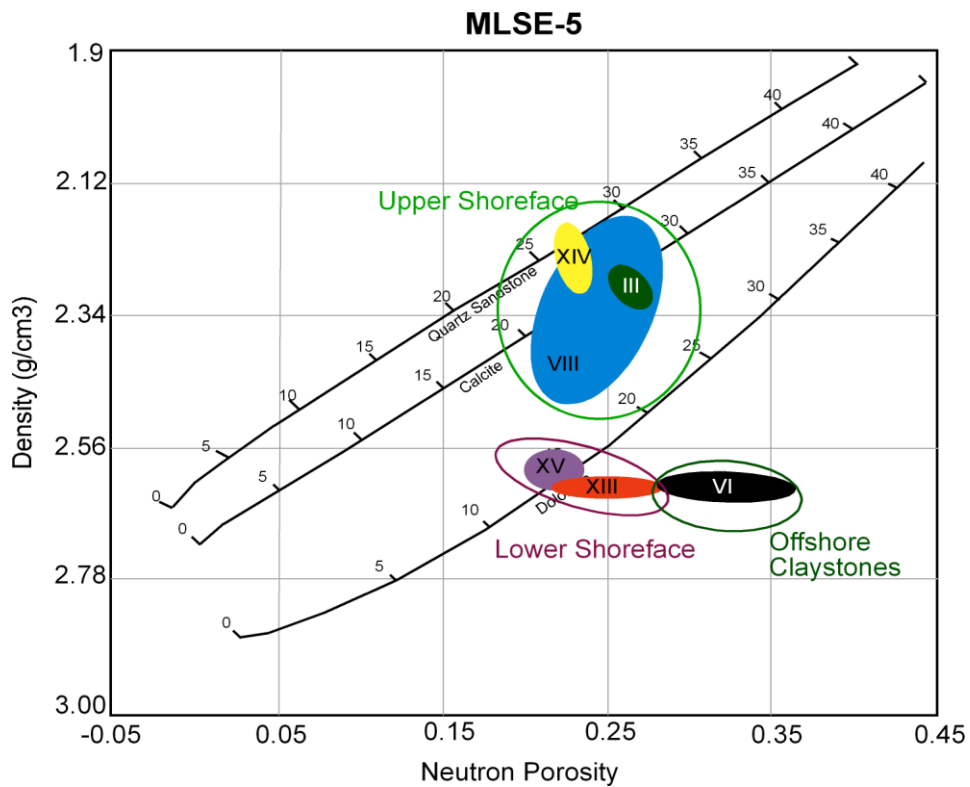


Figure 5.18: Density – neutron cross-plot for the main sedimentary facies from MLSE-5

However, with both wells the two main sandstone facies (VIII & III) overlap on the plot; within the sandstone field. This suggests that whilst individual sandstone facies cannot necessarily be defined from the wireline logs it is possible to distinguish the sandstones from the mudstones and, to some extent, determine broad mineralogical variations within the mudstones.

5.3.2 Gamma-ray – Sonic cross-plot relationship to facies

The core data suggest the main difference between the two main sandstone facies (III and VIII) is the degree of cementation. Therefore, other log responses may be more susceptible to distinguishing the two facies. The sonic travel time (inverse of velocity), for instance, is more susceptible to the structure and porosity of a formation; indirectly it is responding to textural variations, as it is affected by changes in the porosity and

permeability changes caused by varying degrees of grain-coating clay minerals or cement (Braaksma et al., 2003; Serra and Serra, 2003). The clay content, related to the chlorite, is also variable between the two sandstones, with facies III, the more cemented sandstone, having lower clay content. Based on this knowledge of the sedimentology it would be logical to assume that on a cross-plot of sonic travel time vs. gamma ray the more cemented sandstone facies (III) would plot at higher velocities and lower gamma ray values than the more porous, chloritic facies (VIII).

On a gamma-ray vs. sonic travel time cross-plot, for well MLNW-5 the two sandstone facies partly separate out and the mudstone facies plot at much higher gamma ray values (Figure 5.19). This separation is also clearly seen for MLSE-5 (Figure 5.19). However, while it does provide a broad indicator of sedimentary facies it is not accurate enough to allow for the discrimination of these two sandstone facies in a well where the sedimentology and particularly the bed thickness is unknown.

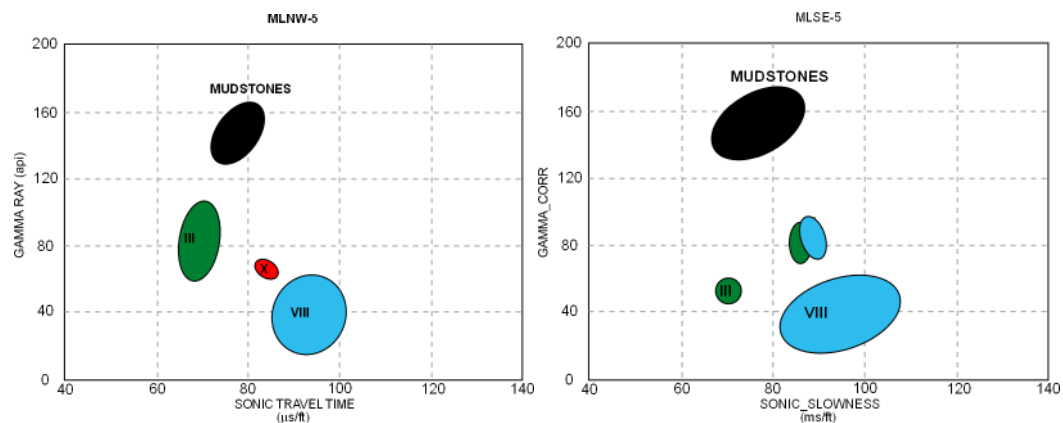


Figure 5.19: Gamma-ray vs. Sonic travel time cross-plot for the main sedimentary facies from MLNW-5 (left) and MLSE-5 (right)

5.4 Statistical Analysis

The use of statistical analysis of logging data is common practice, and goes beyond simple cross-plots, previously discussed. One of the most common uses of statistics is

the derivation of electrofacies from the logging data. Electrofacies is a term introduced by Doveton (1994) to describe the “*set of log responses which characterise a bed and permits it to be distinguished from others*”. More commonly it is used to characterise collective associations of log responses linked to geological attributes, be it physical properties e.g. flow zones (Amaefule et al., 1993), or lithological variations e.g. lithofacies (Pelling et al., 1991; Yang et al., 2006). The advantage of statistical analysis of log data is that natural variability of measurements is accounted for (Yang et al., 2006). Multiple methods are available for determining the electrofacies; including principle component analysis (PCA), *k*-means cluster analysis, and discriminant analysis as the three most common methods, all with varying degrees of success in accurately predicting lithologies in uncored wells (e.g. Gupta and Johnson, 2001; Nashawi and Malallah, 2009; Yang et al., 2006).

The available methods are all a form of multivariate data analysis (see Davis, 2002 for more details), and can either be “*supervised*” or “*unsupervised*”, depending on whether prior information is available. “*Supervised*” methods, for example discriminant analysis, depend on prior knowledge of the different categories or groups to be sought, and searches for the best function to distinguish the categories based on the data characteristics. The results of these “*supervised*” methods can be used to classify unknown observations on the basis of probable membership of each group (Davis, 2002; Doveton, 1994). “*Unsupervised*” methods, for example *k*-means clustering, use no prior knowledge of categories or group membership, and are designed to analyse the intrinsic structure of the data. Results are most commonly expressed as clouds of points in hyper-dimensional space of multivariate log measurements. These resultant clusters and trends are then critically examined for geological meaning, either by general

principles or in relation to data from other observations, e.g. core or previous studies (Davis, 2002; Doveton, 1994).

Multivariate data sets can be either parametric, which exhibit a normal distribution (Figure 5.20) or nonparametric, which have a fixed small sample size whose underlying population is distinctly non-normal (Davis, 2002). The majority of logging data is assumed to be parametric, or if not then any non-normal variables are transformed appropriately, for example, core permeability is often non-normal, however log-permeability transforms the data to a more normal distribution (Doveton, 1994). Log data can be considered effectively normal if two-thirds of the data fall within one standard deviation of the mean (Davis, 2002; Doveton, 1994). The mean (\bar{X}) of a group of variables (X) is the arithmetic average of n samples, given by equation 5.3, where X_i is the i^{th} observation of variable X :

$$\bar{X} = \frac{\sum X_i}{n} \quad (5.3)$$

The spread or distribution of data around the mean can be represented by the *variance* (s^2), the square root of which gives the standard deviation (s).

$$s^2 = \frac{\sum (X_i - \bar{X})^2}{n-1} \quad (5.4)$$

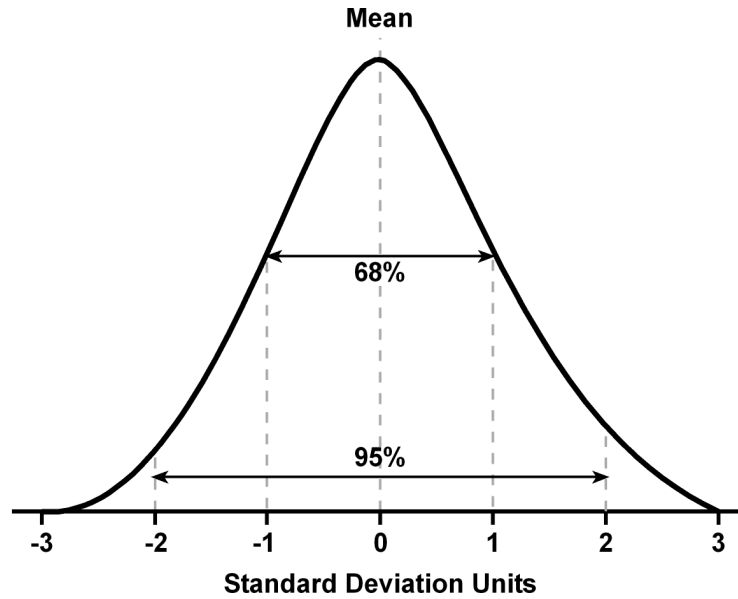


Figure 5.20: A schematic normal (Gaussian) distribution, with mean and standard deviations marked, and the percentage of data points which would fall within 1 and 2 standard deviations (modified from Doveton, 1994)

The log data used in this study can be considered to exhibit a normal distribution, based on their standard deviations, means and variance (Table 5.7), although some of the parameters have a higher variance than others.

Log Data Variable	Arithmetic Mean	Standard Deviation	Variance
<i>Caliper</i>	5.9401	0.1589	0.025249
<i>Total Gamma Ray</i>	73.137	36.83	1356.4489
<i>Density</i>	2.411	0.1603	0.026569
<i>Neutron Porosity</i>	0.23554	0.04457	0.001986
<i>Deep Resistivity</i>	1.1806	3.264	10.6537
<i>Th</i>	13.76	5.978	35.7364
<i>K</i>	0.80261	2.523	6.3655
<i>U</i>	1.9268	1.076	1.15778
<i>Sonic Travel Time</i>	83.372	9.375	87.8906

Table 5.7: The arithmetic mean, the standard deviation and variance for each of the variables for the combined log data from the wells used in this study

Since log data variables are often related to each other through underlying properties, another term is necessary to describe their dispersion; covariance (COV). This allows the variance of the data across each variable pair to be determined (Davis, 2002; Doveton, 1994):

$$COV_{xy} = \frac{\sum (X_i - \bar{X})(Y_i - \bar{Y})}{n - 1} \quad (5.5)$$

In a simple case of two variables, the normal distribution is expressed as elliptical isocontours centred about the bivariate mean, where the contours reflect the percentage of points within (Davis, 2002). The shape of the ellipse is controlled by the correlation coefficient (equation below), and for variables with no correlation ($R^2 = 0$) expressed as a circle and a perfect correlation ($R^2 = 1$) a straight line. This relationship is the main principle behind the cross-plot correlations discussed previously.

$$r_{xy} = \frac{COV_{xy}}{s_x s_y} \quad (5.6)$$

The above statistical analysis methods will be used with the aim of determining where the chlorite-bearing sandstones occur in uncored wells, from the available log data.

5.4.1 Iterative Non-hierarchical Cluster Analysis (INCA)

One of the most common statistical methods for determining electrofacies is *k*-means cluster analysis (Davis, 2002). This method can be *unsupervised* or *supervised*, depending on whether the user defines the number of clusters or not. In this project we employ the *unsupervised* method, and use a variation on the *k*-means principle: Iterative Non-hierarchical Cluster Analysis (INCA), which is a method and computer program developed at the University of Leicester by Prof. Peter Harvey.

“Classic” *k*-means cluster analysis separates a multivariate data set into *k* number of clusters based on the internal variation of the data. The initial seed points, the data points around which the clusters will form, are chosen either arbitrarily or by the user. Centroids for the each initial *k* cluster are calculated and a matrix of similarities between the *k* seeds and the *n* observations is calculated, based on Euclidian distances. The process iterates with the initial centroid shifting toward the true centre of the

growing cluster, as the real data observations overwhelm the arbitrary seed points (Figure 5.21). One main disadvantage of this method is that sub-optimal clustering may result if the initial arbitrary seed points do not fall within divergent clusters, resulting in the premature merger of the centroids and failure to detect outlying clusters (Davis, 2002).

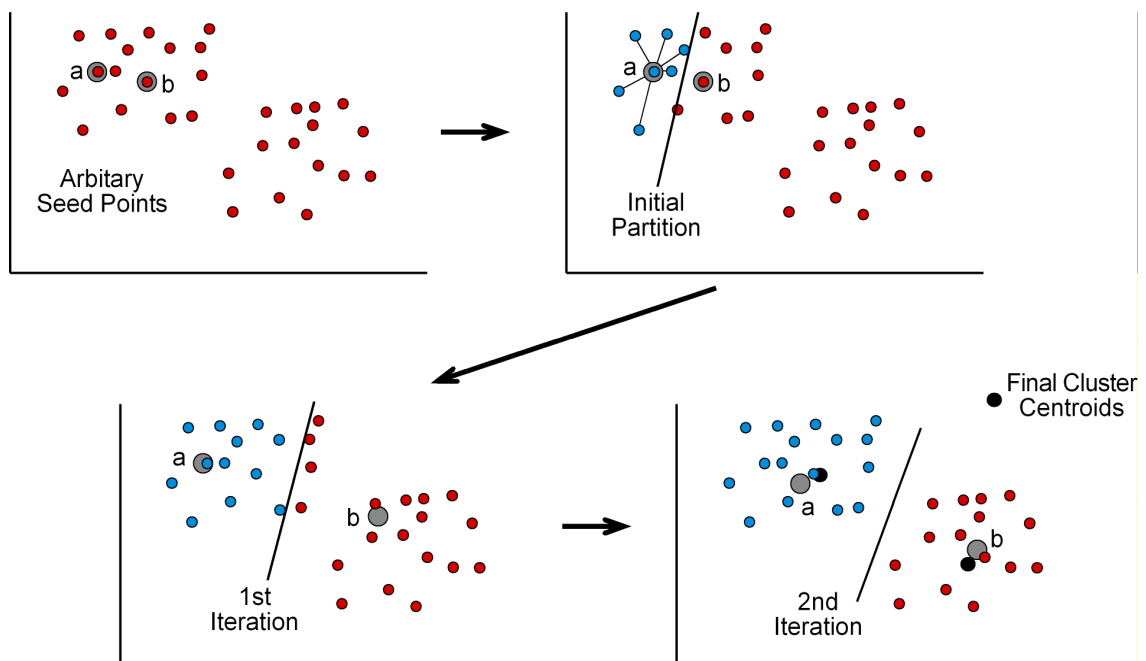


Figure 5.21: Schematic diagram of how the clusters are grouped, for a simple model of two clusters

“Classic” k means cluster analysis assumes there is no correlation between the variables used in the analysis. However, log variables are intrinsically related and this needs to be taken into consideration. On this point INCA has the advantage over “classic” k means as it uses a variance-covariance matrix to account for this relationship between the variables.

INCA is initially run to determine the optimum number of clusters, dictated by the data itself. The iterative calculation of centroids works the same as for “classic” k means except multiple cluster results are compared by looking at the variation within and between cluster sets. The variation within and between clusters is based on both

Euclidian and Mahalanobis distances (Figure 5.22), which allows for the relationship of the variables to be considered (covariance).

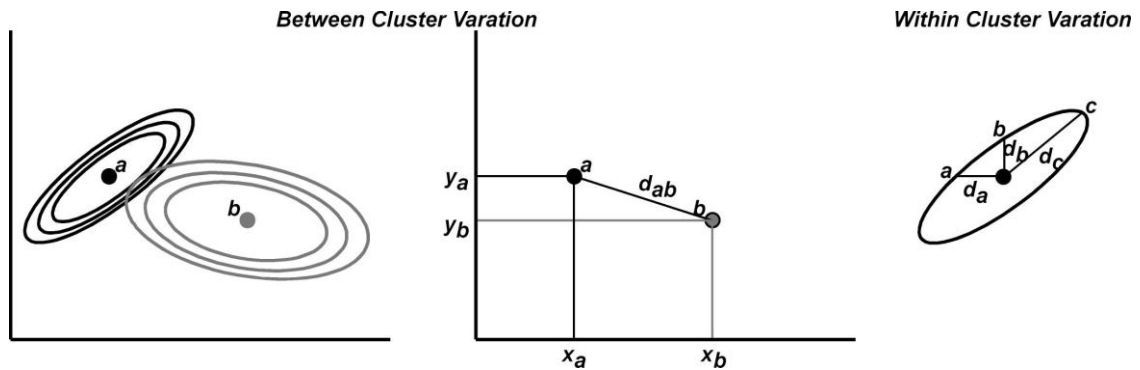


Figure 5.22: Euclidean distances (between cluster variation) and Mahalanobis distances (within cluster variation) for clusters & how they are calculated

Once the optimum number of clusters for a data set is determined, the program is run to group the data into the selected number of clusters e.g. 5 (k). Each cluster has an arbitrarily selected seed point and, by calculating a matrix of similarities between the number of seed points (k) and the number of observations (n), the data points are clustered with the nearest seed point, as per “classic” k means cluster analysis. Centroids are then calculated for each initial cluster and the process repeats iteratively until the variation within clusters is minimised while the variation between clusters is maximised (Davis, 2002; www.statsoft.com/textbook).

INCA has been used to characterise sediments and geochemical variations from logging data acquired through scientific ocean drilling (ODP and IODP) (e.g. Pelling et al., 1991; Tudge et al., 2009). In these cases it has been applied to divide a multivariate data set (logging data) into groups with similar characteristics.

In this study the gamma ray, thorium, potassium, and uranium concentrations along with the sonic travel time from reservoir A intervals were used in the analysis of the water-bearing well (MLNW-5) that was also used to determine the sedimentary facies.

These data are believed to be most susceptible to chlorite and mineralogical composition while not being affected by changes in the pore fluid. Chlorite contains more thorium than potassium, but only in relatively low amounts and contains no uranium. As discussed in chapter 4, if cement is absent where chlorite coatings resulting a distinct textural variation, a signature in the sonic log would be expected. The gamma ray vs. sonic travel time cross-plots (section 5.3.2) also indicates they are the most susceptible variables.

A depth range from 3506 – 3570m was chosen for the INCA analysis, to ensure full coverage of the cored interval. The optimum number of clusters was determined, by INCA, to be four. When the results are then plotted against the log and core data there is a correlation between clusters 3 and 4 with the sandstones (Figure 5.23). When the individual log variables, used in the study, are analysed (Figure 5.24) the gamma ray, thorium and potassium values for clusters 3 and 4 are significantly lower than those of clusters 1 and 2. This is to be expected considering their correlation with the sandstones. For the sonic travel time the clusters 1 and 2, representing the mudstones, exhibit very similar values. The two sandstone clusters exhibit the two velocity extremes; cluster 3 has low travel time/high velocities and cluster 4 has high travel time/low velocities (Figure 5.24). This suggests that cluster 4 represents more porous sandstones than cluster 3. However, this correlation between the clusters and the broad lithologies does not give a good indication of the presence or absence of chlorite.

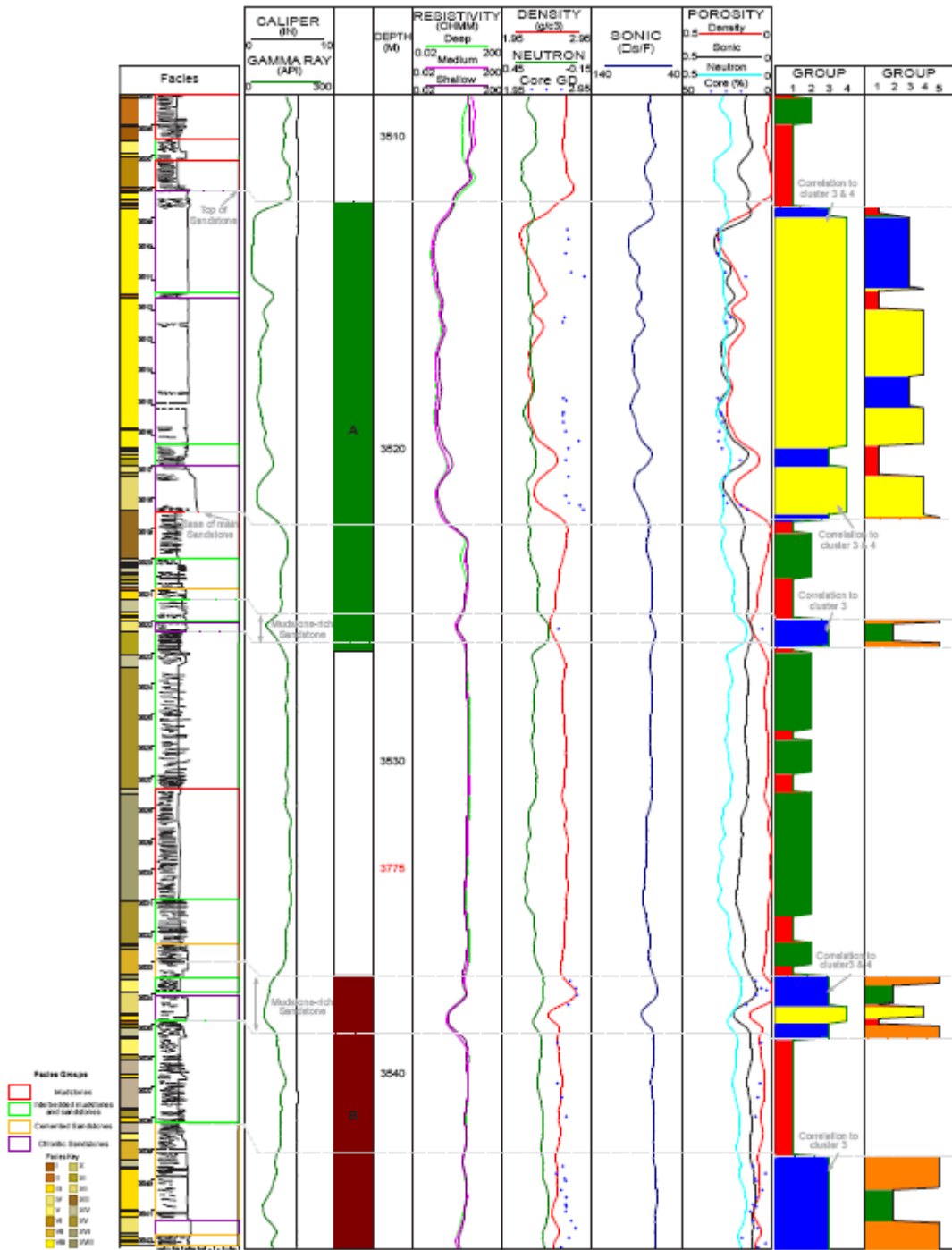


Figure 5.23: plot of log and core data with both full and sandstone clusters plotted, with correlations highlighted.

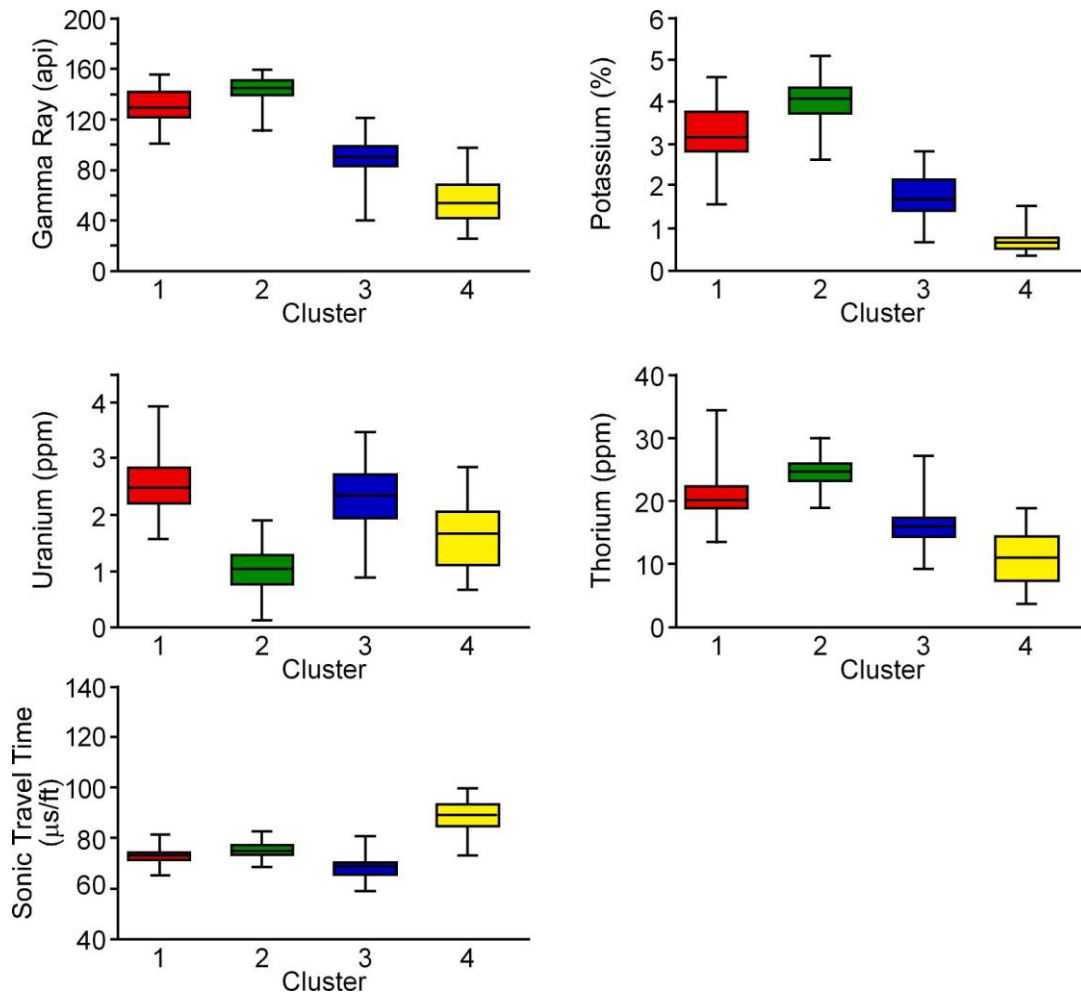


Figure 5.24: Box and whisker plots of whole interval clusters (4) of variables used in the study

The sandstones were then separated out of the data set, and on these data alone the INCA analysis was re-run, with the intention of highlighting the different sedimentary sandstone facies. Using the same five variables (gamma ray, sonic, thorium potassium and uranium concentrations) INCA determined five clusters to be optimum. When plotted against core (Figure 5.23) the clusters exhibit a tentative relationship with the sedimentary environments. For example cluster 1 and cluster 5 relate quite well to the more shale-rich horizons, as reflected in the relatively high gamma ray values exhibited (Figure 5.25). The other clusters do not bear any relationship to the chlorite facies described in chapter 4. Therefore the cluster analysis was deemed not suitable for

determining the presence or absence of chlorite in the sandstones, and thus other analysis was pursued.

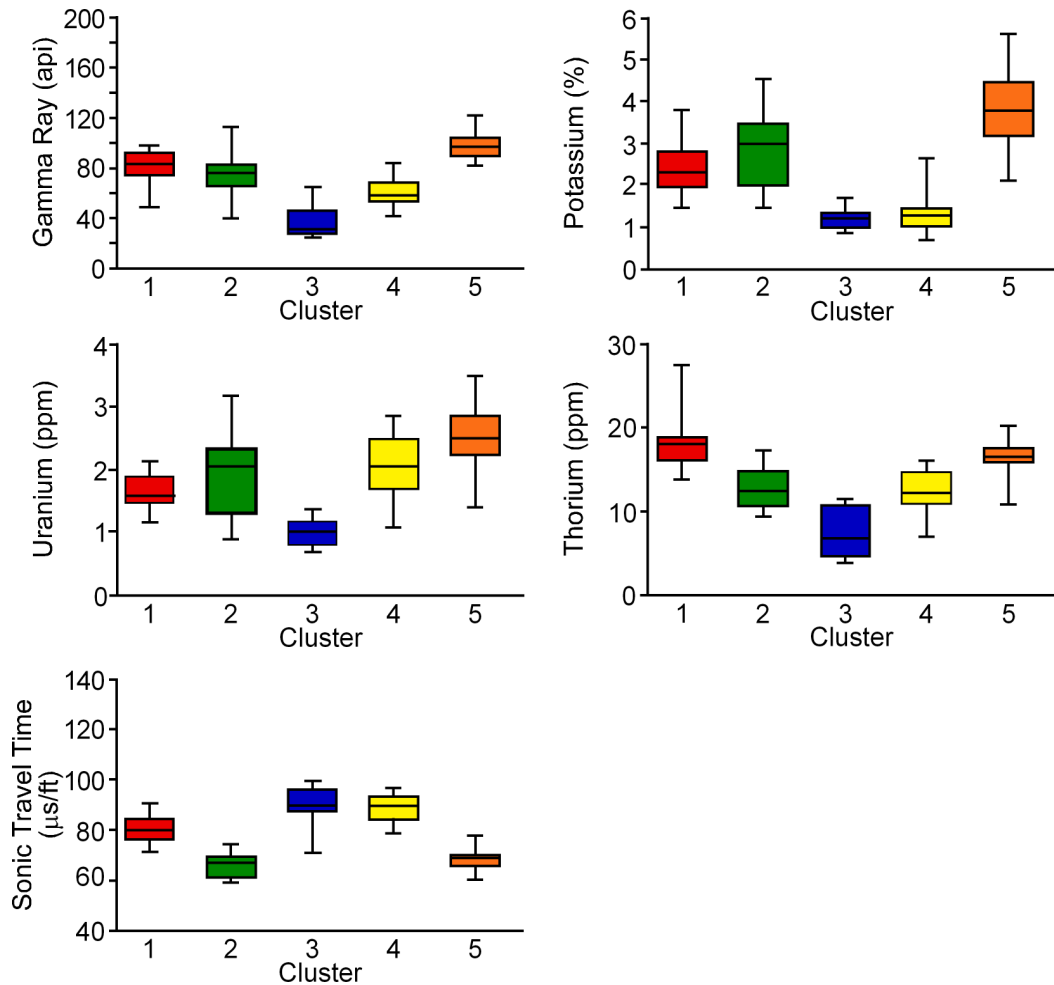


Figure 5.25: box and whisker plots of sandstone interval clusters (5) of variables used in the study

5.4.2 Discriminant Analysis

An alternative method for statistical analysis is discriminant analysis, which is a supervised analysis technique, which requires training data with a minimum of two known populations (i.e. a known model). Assuming a simple two variable model, the aim of discriminant function analysis is to develop “a transform which gives the maximum ratio of difference between the two group multivariate means to the multivariate variance within the two groups” (Davis, 2002). In simple terms, this refers

to the orientation along which the two clusters have the greatest separation with the least inflation within each cluster. The underlying principle to discriminant analysis is the Multivariate Analysis of Variance (MANOVA), which utilizes a matrix of variances and covariances, with a matrix of within-group variances and covariances. The advantage of this form of analysis is its use in classifying unknown variables into groups based on those defined in the model.

In this study the model was built from the sedimentary facies analysis of well MLNW-5. The detailed facies descriptions (detailed in Chapter 4: Table 4.3) were combined into four main groups based on the dominant facies, supplemented with the thin section descriptions and the environmental setting (Table 5.8).

Group	Dominant Facies	Minor Facies
Cemented sandstones (1)	<i>III</i>	<i>VII, XI, X, XVII, XVIII</i>
Chloritic sandstones (2)	<i>VIII</i>	<i>IV, XII</i>
Mudstones (3)	<i>XIII</i>	<i>I, II, VI, XVI</i>
Sandy-mudstones (4)	<i>XVIII</i>	<i>V, XI, XIV, XV, XIX</i>

Table 5.8: Main facies groups for the MLNW-5 model, which are the same as the sedimentary facies associations outlined in table 4.4

The log data used in the model were the gamma ray, thorium, potassium, uranium and sonic travel time. This selection was used for the same reasons as stated in the INCA analysis section (above), and also because the resistivity log, density and neutron logs are affected by the presence of hydrocarbons and would affect the future predictive capability of the model.

When preparing the data for inclusion in the discriminant analysis the vertical resolution of the tools was taken into consideration; to remove the shoulder effects and effects of thin beds on the data scatter. The vertical resolution of the sonic tool, (~60cm), is the largest of the variables under consideration and thus any bed thinner than 60cm was eliminated from the study.

Discriminant Analysis Results

Discriminant analysis will always produce one less function than the number of groups: in this case three functions result from the four groups input (Table 5.7). The significance of the functions needs to be investigated, and can be done through various parameters (Table 5.9). For example, Wilks' lambda is a direct measure of the proportion of variance in the combination of dependant variables that is unaccounted for in the independent variable. The value of Wilks' lambda will range from zero to one; a small value of Wilks' lambda indicates a significant effect from the independent variable, and thus a better function result (Hinton, 2004). The partial Lambda is the Wilks' Lambda for the unique contribution of the variable to the discriminatory power of the model. The tolerance is a measure of the variable's redundancy, i.e. it indicates the proportion of variance that is unique to the variable. The smaller the tolerance the less its contribution to the final classification result, with the classification declared void if the tolerance of any variable equals zero. For example, a tolerance value of 0.10 means the variable is 90% redundant with the other variables in the model. The lowest acceptable tolerance value in this case is 0.01 and as table 5.9 shows all the variables in this case indicate a tolerance well within limits. It can also be seen that the model is mostly influenced by the Sonic variable with the highest tolerance value (0.89) and is least influenced by the gamma ray (GR) which exhibits a tolerance value of only 0.15.

<i>Variable</i>	<i>Wilks' Lambda</i>	<i>Partial Lambda</i>	<i>Tolerance</i>
<i>GR</i>	0.039354	0.861116	0.150403
<i>K</i>	0.038097	0.889528	0.350503
<i>Sonic</i>	0.093157	0.363772	0.893131
<i>Th</i>	0.038767	0.874144	0.258929
<i>U</i>	0.036461	0.929438	0.515274

Table 5.9: Discriminant function analysis summary values

The squared Mahalanobis distances provide a measure of the difference between the groups, and the F-values (Tables 5.10 & 5.11) indicate multivariate equality, with a larger number indicating better variation between the groups (www.statsoft.com/textbook). As tables 5.9 and 5.10 below illustrate the groups have significant enough variation to judge the function reliable.

	<i>Group 1</i>	<i>Group 2</i>	<i>Group 3</i>	<i>Group 4</i>
<i>Group 1</i>	-	46.24383	11.53450	7.74400
<i>Group 2</i>	46.24383	-	58.73338	66.09987
<i>Group 3</i>	11.53450	58.73338	-	1.53576
<i>Group 4</i>	7.74400	66.09987	1.53576	-

Table 5.10: Squared Mahalanobis distances

	<i>Group 1</i>	<i>Group 2</i>	<i>Group 3</i>	<i>Group 4</i>
<i>Group 1</i>	-	380.5997	82.2724	57.9374
<i>Group 2</i>	380.5997	-	529.8281	634.6976
<i>Group 3</i>	82.2724	529.8281	-	12.4845
<i>Group 4</i>	57.9374	634.6976	12.4845	-

Table 5.11: F-values

To interpret the discriminant functions the standardized beta (*b*) coefficients for each variable in each function can be assessed. The higher the standardized coefficient the greater the contribution of the respective variable to the discrimination between groups. Table 5.12 indicates that all the variables contribute to the discrimination. It is possible to identify the nature of discrimination for each discriminant function by looking at the means for the functions across the groups (www.statsoft.com/textbook).

	<i>Function 1</i>	<i>Function 2</i>	<i>Function 3</i>
<i>GR</i>	-0.86900	-0.350059	-2.31499
<i>K</i>	-0.53260	0.061387	1.30444
<i>Sonic</i>	0.66210	-0.760270	0.00879
<i>Th</i>	0.62226	-0.333086	1.52093
<i>U</i>	0.23134	0.308370	1.11475
<i>Eigenvalue</i>	12.44470	1.129548	0.03066

Table 5.12: Standardized beta (*b*) coefficients for the three functions and each variable

An easier way of interpreting the discriminant function is through a plot of the discriminant functions against each other (Figure 5.26). It is clear on both plots (function 1 vs. 2 and function 1 vs. 3) that group 2, representing the chloritic sandstones, are clearly separated from the other groups. Groups 1, 3 and 4 are very similar within function 3, but with function 2 a vertical separation between group 1 and groups 3 and 4 is seen (Figure 5.26). This indicates that the chloritic sandstones (group 2) exhibit distinct properties to the other groups, as would be expected. The close correspondence of groups 3 and 4 indicate that these two groups exhibit similar properties, which is expected given their sedimentology; both groups are dominated by mudstone facies.

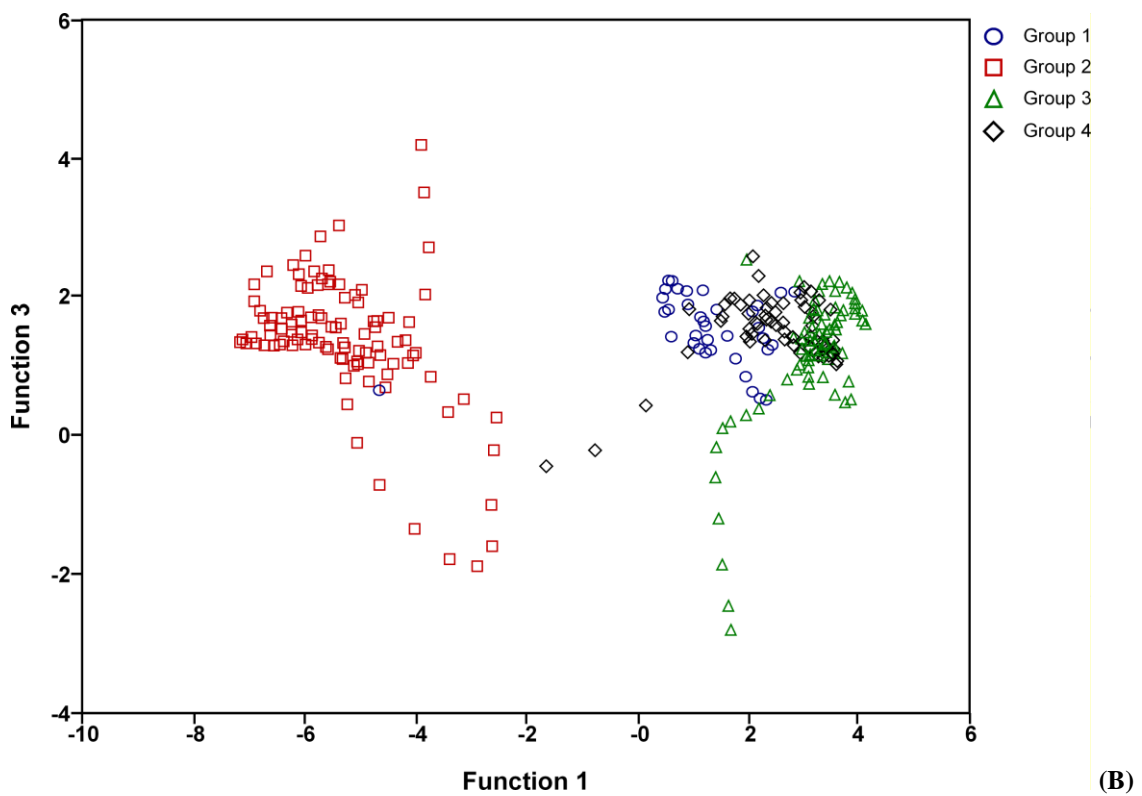
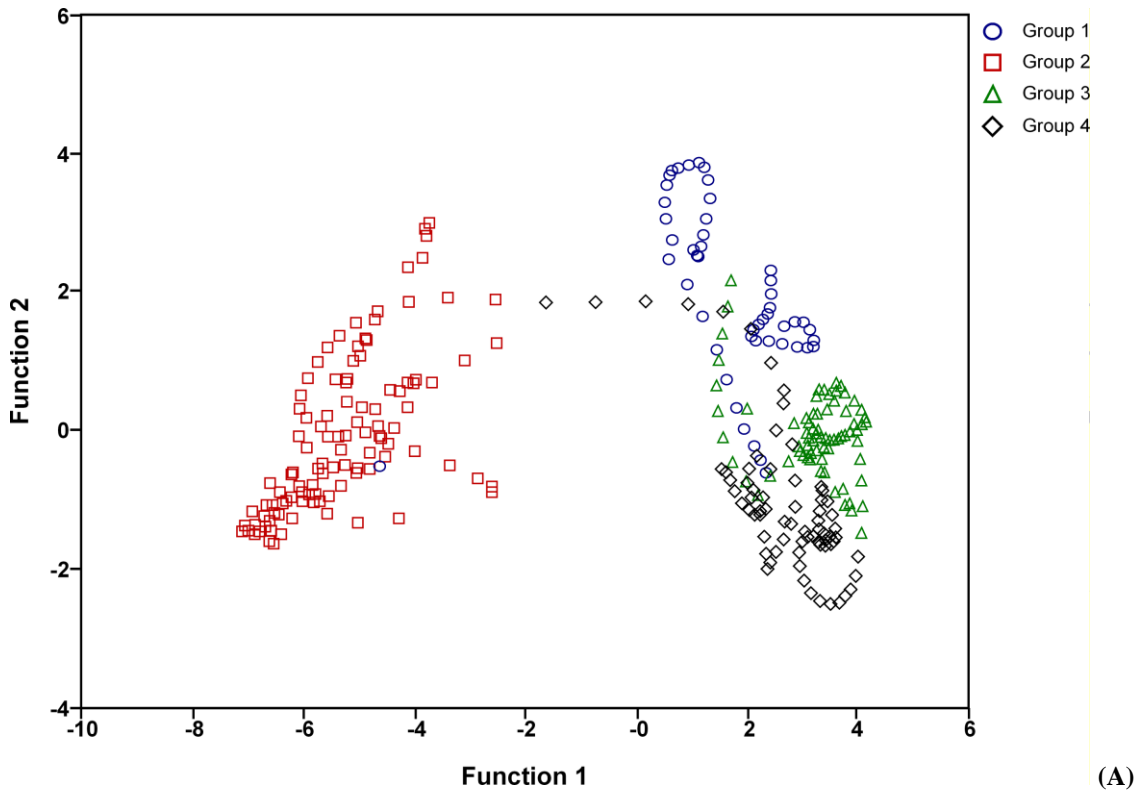


Figure 5.26: (A) Discriminant function 1 vs. 2. (B) Discriminant function 1 vs. 3

This model was then tested on the other wells with sedimentary facies known: MLSE-5 and MLNW-1. The resultant classification matrices for the two wells indicate that the

predictive capabilities are excellent (Table 5.13). For both MLSE-5 and MLNW-1 the correct classification of group 2 (dominantly facies VIII) exceeds 90%.

<i>MLNW-1</i>	<i>Group 1</i>	<i>Group 2</i>	<i>Group 3</i>	<i>Group 4</i>	<i>Percent correct</i>
<i>Group 1</i>	2	88	0	0	2.222
<i>Group 2</i>	4	66	0	0	94.286
<i>Group 3</i>	5	1	0	0	0.00
<i>Group 4</i>	20	21	0	0	0.00

<i>MLSE-5</i>	<i>Group 1</i>	<i>Group 2</i>	<i>Group 3</i>	<i>Group 4</i>	<i>Percent correct</i>
<i>Group 1</i>	13	24	0	6	30.233
<i>Group 2</i>	10	190	0	0	95.0
<i>Group 3</i>	1	0	44	7	84.615
<i>Group 4</i>	27	5	0	27	45.763

Table 5.13: Classification matrices for MLNW-1 & MLSE-5: Rows = initial observed classifications, columns = discriminant analysis predicted classification

It appears that the main misclassification is between groups 1 and 2 (the two main sandstone facies). For MLNW-1 only 2% of the original group 1 samples were correctly identified by the discriminant analysis as group 1, with the remainder classified as group 2. As such of all the samples classified as group 2 by the discriminant analysis only 37.5% were originally observed to be group 2. But in MLSE-5 this increases to 87%, suggesting that the prediction of group 2 from discriminant analysis is in MLSE-5 is better than for MLNW-1. This difference in correct prediction from discriminant analysis could be due to the internal variation of the wells, since MLNW-1 contains only two of the four defined groups. Alternatively the prediction of group 1 as group 2 in MLNW-1 could be related to the misidentification of the original sedimentary facies considering they were defined from core photographs. Despite this, overall the discriminant analysis functions and classifications are deemed successful.

5.5 Conclusions

The log analysis results discussed in this chapter investigate the variation in the log data through visual analysis, computer-based lithological interpretation, cross-plots and

statistical analysis. The aim of this log analysis has been to develop a method for identifying the zones of chlorite occurrence, or distinguishing the chlorite-bearing sandstone facies from the cemented sandstone facies. Five main wells, with a range of oil-bearing and water-bearing formations, were analysed in this chapter: MLNW-1, MLNW-2, MLNW-3, MLNW-5, MLN-5, and MLSE-5.

The log-based lithological analysis constructed using the computer software program Interactive Petrophysics (see section 5.1.2 for details), identifies the sandstones and the mudstones of reservoir A formations. However, it does not distinguish the chlorite-rich sandstones from the cemented sandstones and, when compared to the core-based sedimentological model (chapter 4), overestimates the mudstone and clay content. This overestimation of mudstone and clay content propagates errors into the petrophysical analysis and saturation estimates (discussed further in chapter 6).

Analysis of the Thomas-Stieber “shale distribution” classification suggests a link between the different classes (end-member distributions) and sedimentological features (Table 5.6). All three end-members of “shale” distribution (Thomas and Stieber, 1975) can be recognised in samples and core from these wells, and there is an association between the end-members and the sedimentary facies. However, the Thomas-Stieber cross-plots fails to separate the “*dispersed*” grain coating chlorite (Facies VIII), from the “*laminated*” mudstone laminated sandstones (Facies III).

Other standard cross-plots for determining clay mineralogy from log data, specifically the relationship between photoelectric factor (PEF) data and spectral gamma ray data (K, Th, U) provide conflicting interpretations. For example, in MLSE-5 chlorite and glauconite are identified when using a PEF vs. potassium (K) cross-plot, yet when the same data set is plotted on a PEF vs. thorium-potassium (Th/K) ratio neither mineral is

identified. This contradiction within the same data set, coupled with a lack of available PEF data from other wells, discount this as a method of chlorite prediction in this study. Investigation of the density-neutron cross-plot in a water-bearing well (MLNW-5), to negate the effect of hydrocarbons, provides a clear separation between the sandstone and mudstone lithologies. It does not, however, differentiate the chlorite-rich sandstones (Facies VIII) from the low-chlorite, cemented sandstones (Facies III). Separately it does identify a mineralogical variation in the mudstones, which reflects the transition from lower shoreface to offshore depositional environments.

Standard log analysis techniques fail to provide a method for distinguishing the chlorite-rich sandstones from the cemented sandstones therefore statistical analysis methods were investigated. Sonic travel time, gamma ray and spectral gamma ray components (thorium, potassium, and uranium) were used because of their sensitivity to mineralogy and textural variations.

Iterative non-hierarchical cluster analysis (INCA) is a form of *k*-means cluster analysis, which searches for the optimum number of clusters within the data. In this study it was able to distinguish the sandstones from the mudstones but unsuccessful in identifying the different sedimentary facies.

Using the core-based sedimentological analysis as a model discriminant analysis was investigated, to separate the chlorite-bearing sandstones from the cemented sandstones and the mudstones. Discriminant analysis relies on a training data set to determine the characteristics of each group, in this case each facies, and then employs the classification on a data set of unknown groupings. The sedimentary model used was from the water-bearing well MLNW-5, and the discriminate analysis was successful in distinguishing the chlorite-rich sandstone facies from the cemented sandstone facies and the mudstone facies. This classification was then applied to wells MLSE-5 and MLNW-

1, where the sedimentology was known, to allow for the verification of the discriminant analysis classification results. A success rate of +90% correct classifications for the observed chlorite facies association (group 2) was achieved, which provides a method for determining the distribution of chlorite-bearing sandstones in un-cored wells. However, there is some misclassification of the cemented sandstones (group 1) as group 2, potentially leading to an overestimation of the presence of chloritic sandstones.

Overall the analysis of the available log data proves that standard techniques for lithology determination do not identify the chlorite-bearing sandstones, nor do they distinguish the chlorite-bearing sandstones from the cemented sandstones. Discriminant statistical analysis does provide a method for distinguishing between the chlorite-bearing sandstones (Facies VIII) from the cemented sandstones (Facies III) and the mudstones. This method of statistical analysis for facies associations is an alternative method for wireline log investigation, where standard chlorite identification doesn't work, and could be applied to other sandstone reservoirs.

6. Petrophysical Interpretation

6.1 Introduction

Being able to identify where the chlorite occurs within the reservoir (as discussed in Chapter 5), is an important step in assessing the occurrence of low resistivity pay sections. The next step is to calculate the hydrocarbon saturation within the affected areas, and hence determine if the resistivity is truly a problem. It is also possible to investigate if there is an alternative method for assessing the saturation or a method to develop a correction factor which could be applied to the resistivity. In order to determine the effect on resistivity it is necessary to calculate water saturation using standard resistivity-based methods initially and then investigate alternatives; in this case using saturation height functions. As discussed in chapter 2 to calculate saturation various parameters are required: porosity, formation factor, and porosity and saturation exponents. These can be determined from both core and log properties.

6.2 Petrophysical Core Data

Some of the necessary petrophysical parameters required to calculate saturation can be measured directly from core (outlined in table 6.1 below) and others can be calculated. This section discusses the calculation of the parameters, including the porosity (m) and saturation (n) exponents at both the field-scale and the sedimentary facies scale.

Well	Porosity	Perm	Grain Density	Brine Resistivity	Resistivity Index	FF	Co/Cw	Dean-Stark	Cap. Pressure
MLNW-1	X	X	X	-	-	-	-	-	X
MLNW-2	X	X	X	X	X	X	X	-	X
MLNW-3	X	X	X	-	-	-	-	-	-
MLNW-4	X	X	X	-	-	-	X	-	-
MLNW-5	X	X	X	X	X	X	X	X	X
MLSE-5	X	X	X	X	X	X	-	-	X
MLN-5	X	X	X	X	X	X	-	-	X

Table 6.1: The available petrophysical core data per well (SCAL & CCA); each well is marked as either oil-bearing or water-bearing

6.2.1 Archie Petrophysical Parameters

Field-scale Calculations

Field-scale parameters were initially considered based on the core data provided by ConocoPhillips. The formation factor (FF) values were grouped per field used (MLNW, MLN and MLSE) and then used to calculate the field-average porosity exponents (m & a). Pressurized porosity and formation factor measurements were also available, and given the depth of the reservoir a pressure of 4000psi was assumed representative.

To estimate the porosity exponent, the porosity is plotted against formation factor; the resulting m and a values are dependent on the mudstone (“shale”) content of the formation. A higher a coupled with a lower m indicates increasing mudstone content, while an a of 1 with a high m value (steep gradient) suggests a clean sandstone.

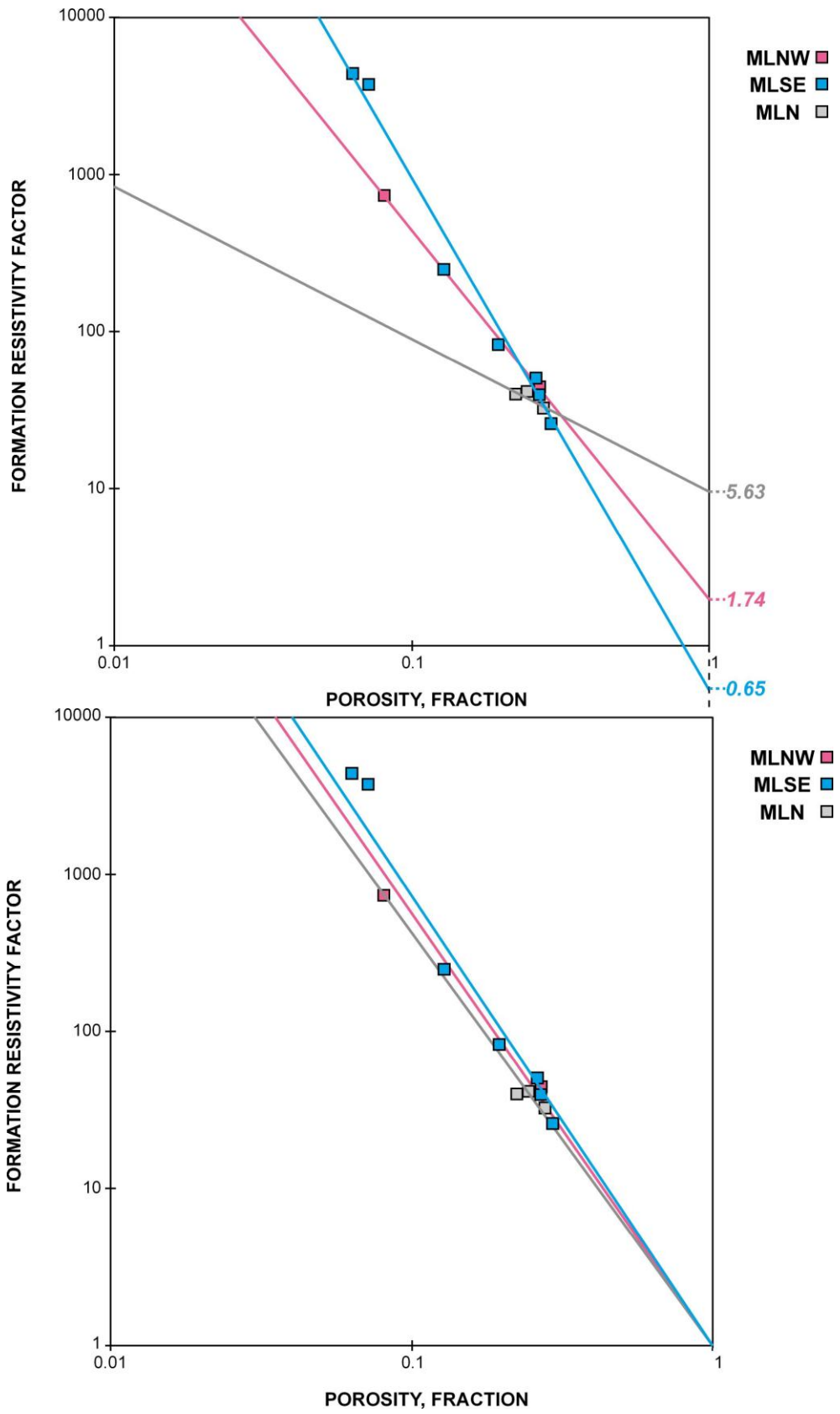


Figure 6.1: Core-derived formation factor and porosity values per well. Top: free-fitting lines for each field, with a values marked. Bottom: force-fitted ($a=1$) regression line.

Figure 6.1 illustrates the relationship between the formation factor and 4000psi porosity values for each of the field areas (MLNW, MLSE and MLN), both free-fitting and forced through the (1, 1) origin. On the free-fitting plot the MLNW field average exhibits a steep gradient (m) and a small a value suggesting some mudstone content but not excessive amounts, consistent with the lithology interpretation of chapter 5 (section 5.1.2). The MLSE field, from well MLSE-5 only, exhibits an a value lower than 1, which is unusual but not unheard of, as in the Humble equation (Rider, 2004). The data from MLN, on the free-fitting plot, indicates unusual behaviour as the gradient is very shallow (m) suggesting a higher mudstone content than MLNW field, but this is not reflected in the log-lithology interpretation (chapter 5 section 5.1.2). Therefore in order to obtain a reliable porosity exponent (m) it is necessary to force the fit line through the (1, 1) origin. The resultant porosity exponents (m) and a values are outlined in table 6.2.

Field-area	Free-fitting:		Force-fitted	
	m	a	m	a
<i>MLNW</i>	1.76	1.74	2.02	1
<i>MLN</i>	0.72	5.63	1.97	1
<i>MLSE</i>	2.43	0.65	2.21	1

Table 6.2: Table of free-fitting m and a values and force-fitted m and a values for the field groups

Facies-based porosity exponents

Given the distinct sedimentary sandstone facies (discussed in chapter 4), and the relationship between facies and chlorite occurrence (discussed in chapter 5) it is possible that the different facies have different reservoir qualities. The variation of porosity exponents (m) with facies is therefore important in any discussion of reservoir quality. Assuming the facies variation is independent of field then all available samples can be pooled and split according to the main sedimentary facies. These samples

formation factor and porosity values, still at 4000psi, can then be used to derive facies-based porosity exponents (Table 6.3).

Facies	Free-fitting:		Force-fitted	
	<i>m</i>	<i>a</i>	<i>m</i>	<i>a</i>
<i>iii</i>	2.64	0.35	2.06	1
<i>viii</i>	1.82	0.18	2.18	1

Table 6.3: Facies-based porosity exponents

6.2.2 Saturation exponents (*n*)

Another important parameter for Archie water calculation saturations is the saturation exponent (*n*) and this is calculated from core samples, measured at ambient conditions. A plot of resistivity index vs. core saturation will yield a best-fit plot with slope *n*. As the resistivity index (i.e. the rock to water resistivity) will be equal to 1 at 100% water saturation, this (1, 1) origin is the starting point in the experiment and must be included in the best-fit relationship. Each plot contains values from a single sample, and they can be grouped to provide both field-scale and sedimentary facies averages (see Appendix III for individual graphs).

Field-scale saturation exponents

A field-scale saturation exponent (*n*) can be calculated for each of the fields (MLNW, MLN, and MLSE). Available data points could then be averaged for each of the fields (Table 6.4). The resulting saturation exponents (*n*) are all slightly higher than a value of 2, routinely taken as the average when otherwise unknown.

Well	Sample Depth	Sample n	Field Average
MLNW-5	3509.08	1.9361	2.15
MLNW-2	3459.13 3497.07	1.9303 2.5735	
MLSE-5	3330.1	2.0344	2.06
	3338.14	2.1559	
	3341.07 3347.02	1.9137 2.1449	
MLN-5	3521.1	2.4562	2.18
	3521.2	1.7788	
	3523.13	2.3009	

Table 6.4: Core-derived water saturation exponents (n) from resistivity index vs. water saturation data, grouped per field, with resultant average saturation exponents (n) (for original graphs see appendix).

Facies-scale saturation exponents

Sedimentary facies, presence or absence of cement and the occurrence of clays control reservoir quality. Rock resistivity will vary with the different sedimentary facies and therefore so will the resistivity index (RI) when dealing with hydrocarbon-bearing sections. It is therefore necessary to derive facies-based saturation exponents (n). Assuming the facies variation is independent of field then all available samples can be pooled and split according to their sedimentary facies. The available data was plotted on a log-log RI vs. S_w plot per plug sample (Appendix III). These n values were then grouped according to sedimentary facies and an average saturation exponent (n) for each facies group was then derived (Table 6.5).

Facies	Well	Sample Depth	Sample n	Facies average
III	<i>MLNW-2</i>	<i>3497.07</i>	<i>2.5735</i>	2.24
	<i>MLSE-5</i>	<i>3338.14</i>	<i>2.1559</i>	
	<i>MLSE-5</i>	<i>3347.02</i>	<i>2.1449</i>	
	<i>MLN-5</i>	<i>3521.1</i>	<i>2.4562</i>	
	<i>MLN-5</i>	<i>3521.2</i>	<i>1.7788</i>	
	<i>MLN-5</i>	<i>3523.13</i>	<i>2.3009</i>	
VIII	<i>MLNW-5</i>	<i>3509.08</i>	<i>1.9361</i>	1.95
	<i>MLNW-2</i>	<i>3459.13</i>	<i>1.9303</i>	
	<i>MLSE-5</i>	<i>3330.1</i>	<i>2.0344</i>	
	<i>MLSE-5</i>	<i>3341.07</i>	<i>1.9137</i>	

Table 6.5: Each sample saturation exponent grouped according to facies, and averaged

6.2.3 Clay-corrected Parameters

The porosity and saturation exponents calculated in section 6.2 are for sandstones that are assumed to be mudstone and clay (“shale”) free; “clean sandstones”. In cases where mudstone and clays might be present within the sandstones then the exponents can be corrected for shale effect on the electrical conductivity; known as intrinsic exponents (m^* n^*) (Worthington, 2004). The relationship between the core-derived shale conductivity (BQ_v) and the formation water resistivity (R_w) can be used to assess whether the modified shaly-sand models are applicable (Worthington, 2000). To determine the shale conductivity (BQ_v) the reservoir rock conductivity, when fully saturated (C_w) is plotted against the saturating brine conductivity (C_o); this plot also separates “clean sandstones” from “shaly sandstones” (Figure 6.2).

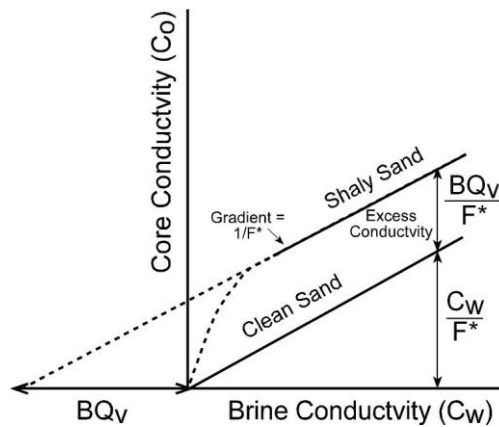


Figure 6.2: Schematic relationship between the conductivity of the reservoir rock (C_w) vs. the conductivity of the saturating brine (C_o), with the separation of the shaly sand from the clean sand

Using values for a single sample on the C_o/C_w plot (Figure 6.2) it is possible to determine a shale-corrected formation factor (FF^*), and therefore porosity exponent (m^*) (see Chapter 2 for detailed equations) by determining the slope of the line. A select range of samples were available with the necessary conductivity values (C_o , C_w & BQ_v) (Table 6.6). These values could be plotted and a correlation line fitted; either forced through the origin or allowed to over-shoot the origin and yield an excess

conductivity (BQv) and thus an intrinsic formation factor (FF*). This excess conductivity is necessary for the Waxman-Smiths shaly sand saturation equation to allow the excess conductivity associated with the clays to be taken into consideration (Waxman and Smits, 1968). In this format, B is the equivalent conductance of sodium clay exchange cations, Qv is the cation exchange capacity per unit pore volume, and FF* is the formation factor for a shaly sand (Waxman and Smits, 1968; Worthington, 1985).

<i>Sample</i>	Mlnw-5: 3509.5m	Mlnw-2: 3459.13m	Mlw-3: 3503.03m	Mlnw-4: 3573.02m
<i>BQv</i>	1.262	0.393	0.247	0.737
<i>FF*</i>	81.3	9.89	12.28	38.46
<i>m*</i>	-1.83	-1.81	-1.53	-1.63

Table 6.6: Calculated BQv, FF* and m* values for available samples

The intrinsic formation factor (FF*) values for the available samples when plotted against the porosity values allowed intrinsic porosity exponents (m^*) to be determined (see Chapter 2 for calculations). The excess conductivity values for the samples are very low when coupled with the low resistivity saturating brine values of reservoir A the projected decrease in water saturation from the Waxman-Smiths equation should not be very high; discussed in section 6.4.2 (Table 6.6).

A relationship between excess conductivity (BQv) and formation brine resistivity can provide an indication of whether Archie or non-Archie saturation models should be used (Worthington, 2000). Figure 6.3 below illustrates, that for this study, Archie parameters should be valid and shaly-sand models should not need to be applied. However, given the proximity to the shaly-sand model field of the graph both Archie and selected shaly-sand models will be used to calculate water saturations for comparison.

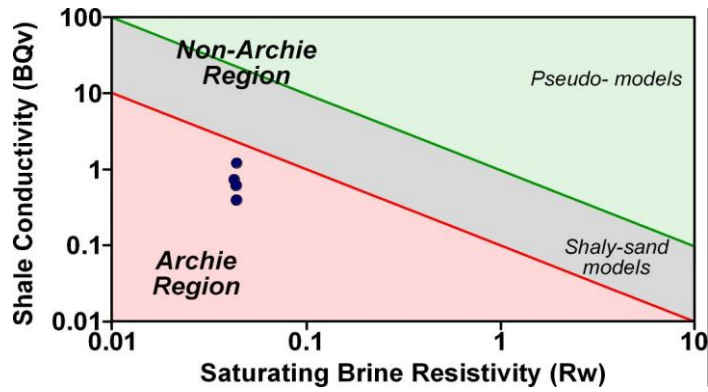


Figure 6.3: Resistivity of the formation water vs. excess conductivity subdivides regions based on Archie or Non-Archie rocks, the samples for this study plot clearly in the Archie region (modified from Worthington, 2000)

6.2.4 Core Sw Values and Sw_{irr} analysis

Core-based water saturations are most commonly derived from the Dean-Stark method when drilled with oil-based mud (McPhee, 2009; Ringen et al., 2001). In this project only two wells (MLNW-5 and MLW-3) provide any Dean-Stark core-derived water saturations (Table 6.7), providing a total of 3 data points (Craig, 2003). This lack of data provides a very poor basis for comparison to any log-based saturation calculations.

Well	Sample Depth	Water saturation
<i>MLNW-5</i>	3509.13	0.345
<i>MLW-3</i>	3491.90	0.560
<i>MLW-3</i>	3494.03	0.264

Table 6.7: Dean-stark water saturation values & sample depths, note that only one of the values comes from a well explored in this study (MLNW-5)

An alternative core-based method for assessing water saturation is to determine irreducible water saturations (Sw_{irr}) from core capillary pressure measurements (see Appendix IV) (Tiab and Donaldson, 1996). The determined irreducible water saturation values provide a greater range of data points than the Dean-Stark saturations and by plotting against core porosity a “best-fit” relationship can be determined (Figure 6.4). This relationship allows irreducible water saturation (Sw_{irr}) curves to be generated based on the log-based porosity, in this case density porosity.

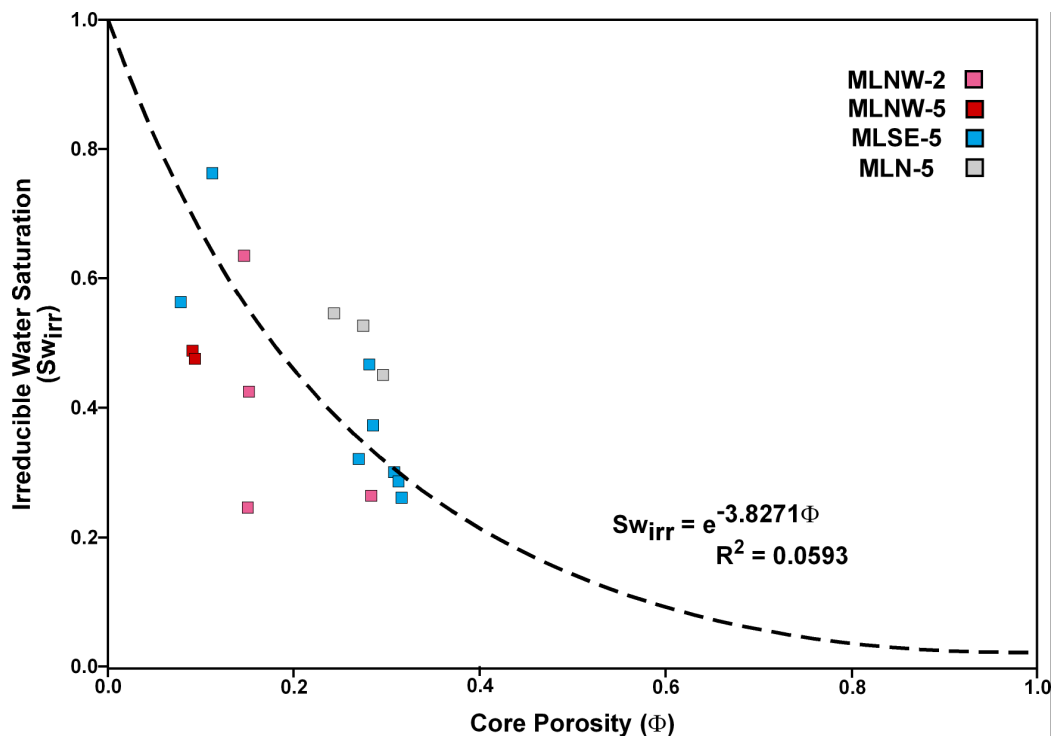


Figure 6.4: Core-derived porosity values plotted against the core irreducible water saturation values determined from capillary pressure curves for each of the field areas

For well MLNW-5 the calculated irreducible water saturation curve fits very well with the sole available Dean-Stark water saturation value (Figure 6.5), and therefore will allow a good basis for comparison of the log-based saturation calculations.

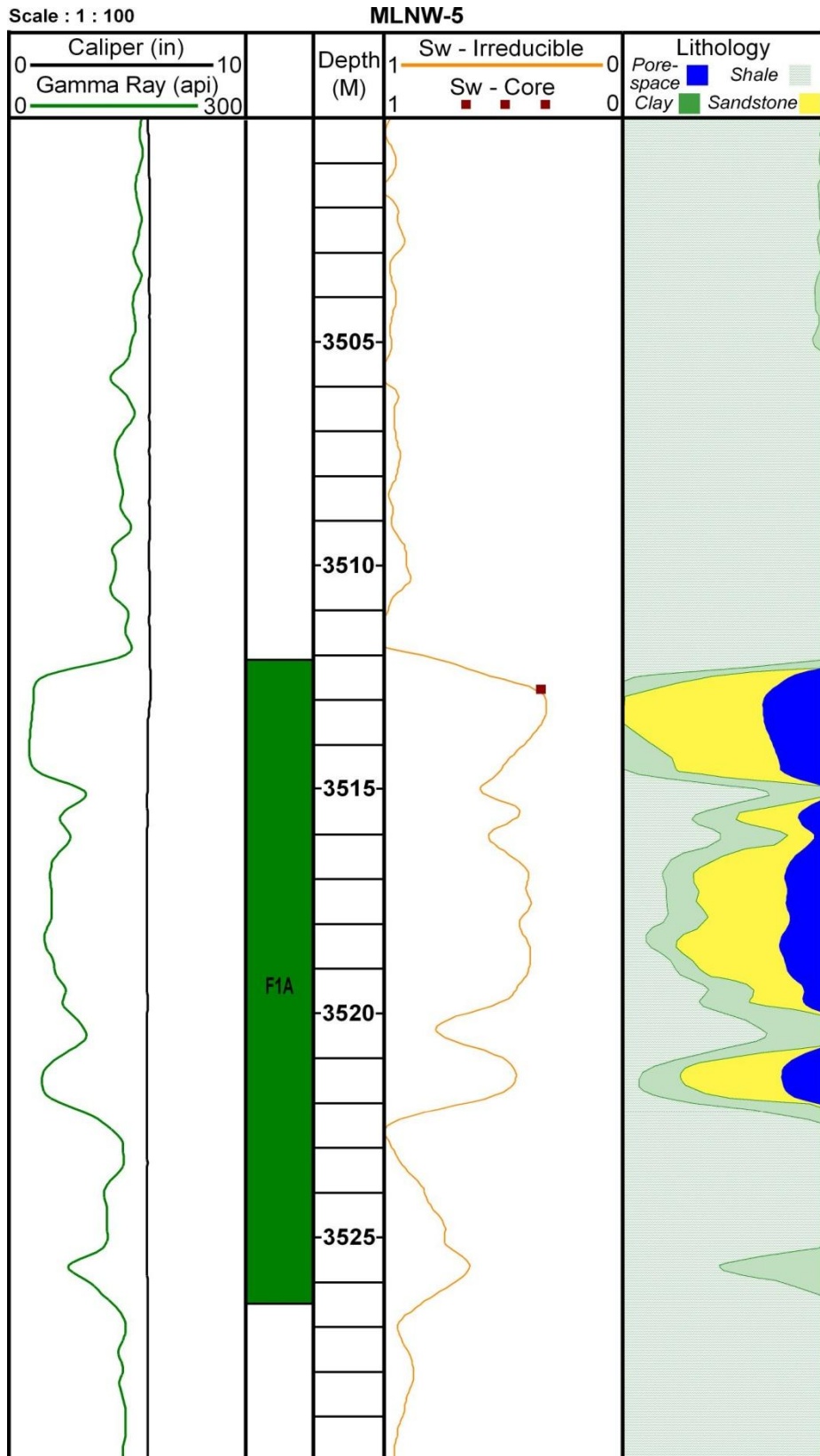


Figure 6.5: MLNW-5 plot of Dean Stark water saturations and the calculated irreducible water saturation curve.

6.3 Petrophysical Log Data

Many of the core-derived variables described above need to be available on the scale of the borehole, not just as discrete sample points. Therefore petrophysical parameters need to be investigated from the log data, and can then be compared to the core-derived values for a reliability check. The main log-derived parameters are porosity and saturation, with permeability and porosity exponent (m) obtained from core.

6.3.1 Porosity Calculations

To calculate saturation from resistivity the porosity is calculated from the log data. Unlike porosity measurements on core data which generally measure the connected pore-space, the log-derived porosity is more often a measurement of the total pore-space, including any isolated pores and clay-bound water. However, if core porosity is derived from the helium porosity method, on cleaned and oven-dried samples, the damage to the clays from the temperatures used can result in a core porosity closer to total porosity (McPhee, 2009). For saturation estimation *effective* porosity is commonly used; this describes the volume of the rock which has the potential to store hydrocarbons (Hook, 2003). A simplified breakdown of the different porosity types is outlined in figure 6.6. Logging tools do not directly measure porosity, although the neutron response provides a close approximation in water-filled formations and under limited circumstances. Instead porosity can be calculated from either the density or sonic data based on variations of the weighted-average relationship of the formation density (X) (Hook, 2003):

$$\begin{aligned} X_{\log} &= X_{ma} \cdot V_{ma} + X_{cl} \cdot V_{cl} + X_w \cdot V_w + X_{hyd} \cdot V_{hyd} \\ &= X_{ma} \cdot V_{ma} + X_{cl} \cdot V_{cl} + X_w \cdot \phi \cdot S_w + X_{hyd} \cdot \phi \cdot (1 - S_w) \end{aligned} \quad (6.1)$$

Where V_{ma} = volume of matrix grains

V_{cl} = volume of clay

V_w = volume of water

V_{hyd} = volume of hydrocarbons

S_w = water saturation

ϕ = porosity

This allows *total* porosity (ϕ_t) to be calculated from:

$$\phi_t = \frac{V_{pt}}{V_b} \quad (6.2)$$

The exclusion of clay-bound water allow for calculation of the *effective* porosity (ϕ_e) from:

$$\phi_e = \frac{V_{pe}}{V_b} = \frac{(V_{pt} - V_{cbw})}{V_b} \quad (6.3)$$

Where V_{pe} = effective pore volume

V_b = bulk volume of rock

V_{pt} = total pore volume

V_{cbw} = volume of clay bound water

The aim of this interpretation is to determine which log-based porosity model most closely reflects the core-derived porosity and can therefore be used in the saturation estimates.

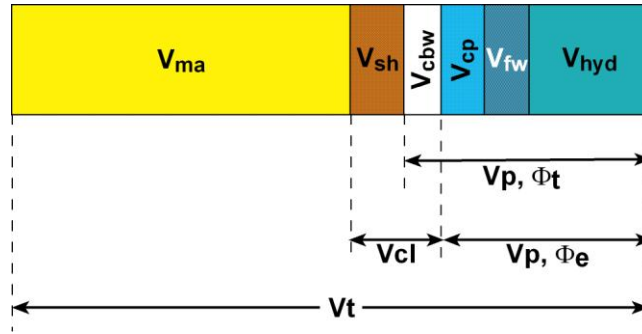


Figure 6.6: Breakdown of a rock's proportions into effective (Φ_e) and total porosity (Φ_t), where V_{ma} is matrix volume, V_{sh} is shale volume, V_{cbw} is volume clay bound water, V_{cp} is capillary bound water, V_{fw} is volume free water, V_{hyd} is volume of hydrocarbons, V_p is pore volume, V_t is total volume and V_{cl} is clay volume (modified from Hook, 2003)

Density-derived Porosity

Based on this weighted-average relationship (above) a simple relationship exists between the density (ρ) and porosity (ϕ), for a measurement of the *total* porosity:

$$\rho_b = \rho_{ma}(1 - \phi) + \rho_f \phi \quad (6.4)$$

Which relates the measured density (ρ_b) to the proportions of the rock components (solid: ρ_{ma} and fluid: ρ_f). To calculate the total porosity (ϕ_t) from the bulk density then the re-arranged equation (below) is used:

$$\phi_t = \frac{\rho_b - \rho_{ma}}{\rho_f - \rho_{ma}} \quad (6.5)$$

To calculate the *effective* porosity (ϕ_e) then the clay fraction (ρ_{cl}) must be taken into consideration, to compensate for the clay-bound component of the rock:

$$\phi_e = \left(\frac{\rho_b - \rho_{ma}}{\rho_f - \rho_{ma}} \right) - V_{cl} \left(\frac{\rho_{cl} - \rho_{ma}}{\rho_f - \rho_{ma}} \right) \quad (6.6)$$

Unfortunately it is not possible to distinguish the connected from the unconnected pore space with the density tool, and therefore a slight over-estimation of the porosity may be expected when compared to core data (Hook, 2003).

For specific calculations of the porosity the various input parameters can be determined from either core data or from a sensible estimate following experience and density tables. In this instance the fluid density (ρ_f) was assumed to be the drilling mud filtrate, given the shallow depth of investigation of the tool, and the matrix/solid density (ρ_{ma} and ρ_{cl}) was obtained from core density measurements (Table 6.8).

	<i>MLNW-1</i>	<i>MLNW-2</i>	<i>MLNW-5</i>	<i>MLSE-5</i>	<i>MLN-5</i>	<i>Average</i>
ρ_{ma}	2.70	2.66	2.68	2.72	2.69	2.69
ρ_f	0.9	0.9	0.9	0.9	0.9	0.9
ρ_{cl}	3.0	3.0	3.0	3.0	3.0	3.0

Table 6.8: Outline of the density input parameters used in the calculations: the fluid density and clay density are averages determined from available tables (Rider, 2004; Serra and Serra, 2003)

For this study both the *total* and *effective* porosities were calculated, with both used in subsequent saturation calculations to assess the impact of the two values on the results.

Sonic-derived Porosity

The calculation of porosity from the sonic data also relies on the volume-weighted average relationship outlined above (equation 6.1), but relates to the velocity of an acoustic wave as it propagates through the rock (Hook, 2003). However, the nature of the sonic measurement is such that this volume-weighted relationship is too simple for the signal received from a propagating wave, and is not often reliable in unconsolidated material (Raymer et al., 1980; Rider, 2004). There have been many studies into improving this relationship between the sonic measurement and porosity (e.g. Hoffman and Tobin, 2004; Raymer et al., 1980; Wyllie et al., 1956), often resulting in very environment specific equations. One of the more frequently used and a reliable equation for most consolidated reservoirs is the Wyllie time-average equation (Wyllie et al., 1956):

$$\frac{1}{V_p} = \frac{\phi}{V_f} + \frac{(1-\phi)}{V_{ma}} \quad (6.7)$$

Where V_p = p-wave velocity

V_{ma} = velocity through the rock matrix (solid component)

V_f = velocity through the fluid component

This original Wyllie time-average equation relates P-wave velocity to porosity, but the sonic tool measures the travel time (Δt_{\log}) of the wave. Given the inverse relationship between the velocity and travel time of a P-wave the Wyllie time-average equation is more commonly used in terms of travel time:

$$\phi = \frac{\Delta t_{\log} - \Delta t_{ma}}{\Delta t_f - \Delta t_{ma}} \quad (6.8)$$

Where Δt_{\log} = measured travel time

Δt_{ma} = travel time through the rock matrix (solid component)

Δt_f = travel time through the fluid component

It is often assumed that the sonic wave bypasses the random, unconnected pore-space and is therefore assumed to be closer to the measurement of connected porosity (Φ_c) than total porosity. While the sonic-derived porosity can be corrected for shale content in a similar way to the density-porosity it is not common to do this, as the connected porosity is often good enough.

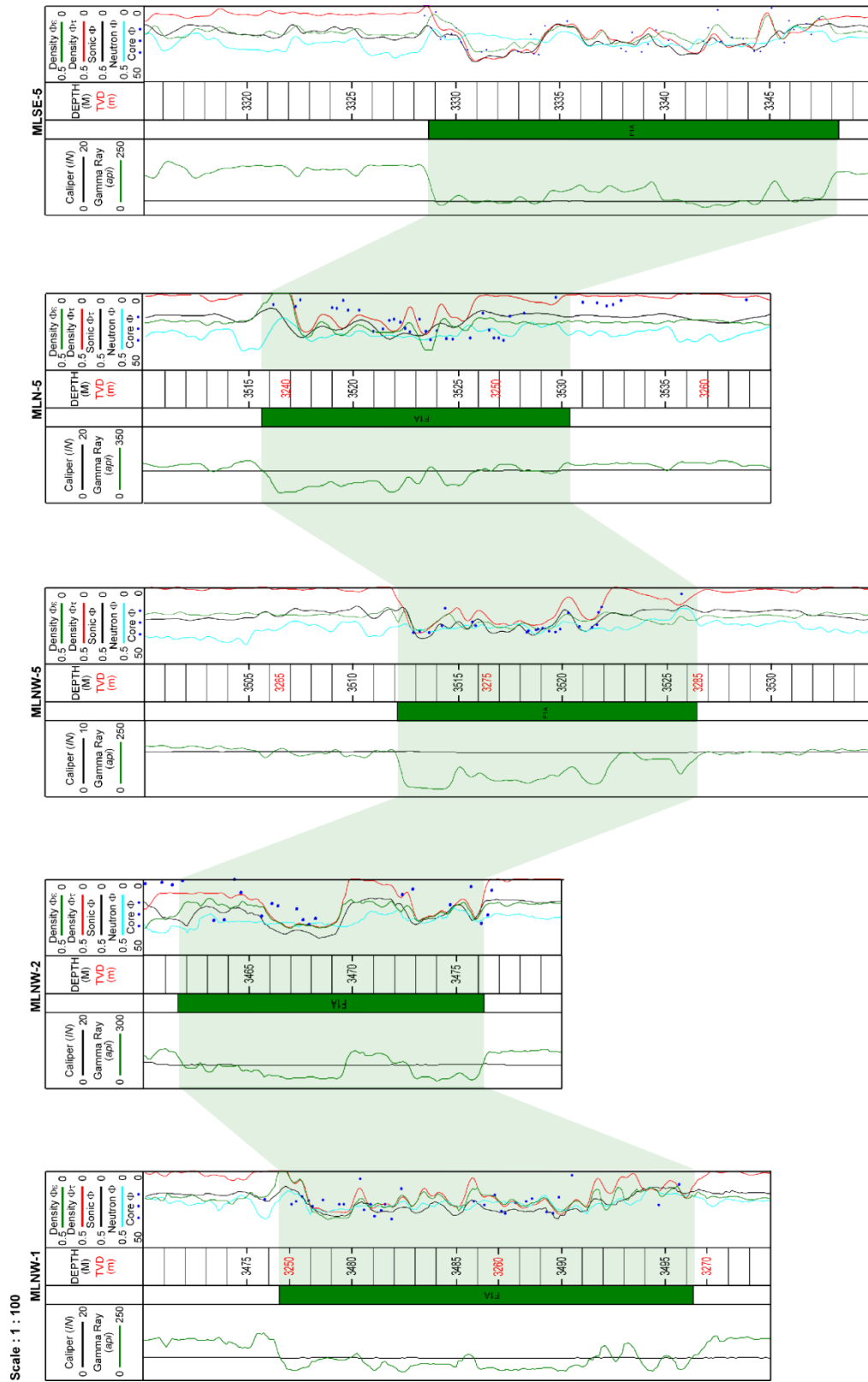
	<i>Average</i>
Δt_{ma}	52.5
Δt_f	195

Table 6.9: Outline of the sonic input parameters used in the calculations: averages determined from available tables (Schlumberger, 2000)

For this study the Wyllie time-average equation was used with average parameters for matrix and fluid travel times obtained from reference material (Rider, 2004). The matrix value is representative of consolidated sandstone approximately equivalent to the density matrix, and the fluid value is consistent with an oil-based mud filtrate (Table 6.9).

Porosity comparison

To assess which log-based porosity estimation provides the most reliable results, calculated values (estimations) were compared to the core-based porosity measurements. Figure 6.7 illustrates the various log-derived porosity estimations from the five main wells of the study. The neutron porosity curve is also included as this is an approximation of the porosity and can occasionally be the most closely correlated to core. Of the log-based porosity estimates in this study the density-derived *total* porosity provided the closest match to the core porosity, thus this will be the log-porosity measurement used in subsequent saturation calculations.



Scale : 1 : 100

Figure 6.7: Total porosity (Φ_t) logs calculated from sonic (black curve), density (red curve) and neutron (aqua curve), and the effective porosity (Φ_e) from density (green curve) compared against core porosity values (blue dots) for MLNW-1, MLNW-2, MLNW-5, MLN-5 and MLSE-5

6.3.2 Pickett Plots

The porosity exponent (m) used in saturation calculations can also be derived from log data, in the absence of suitable core, using a Pickett Plot (Pickett, 1966). Based on the principle of Archie's equation relating porosity to resistivity values on a log-log plot of porosity against resistivity zones with constant water saturation will plot along the same lines (Figure 6.8). If data from water-bearing sandstones, either assumed clean or with minimal clay content, are plotted with enough spread to fit a line through it is possible to determine the 100% water saturation line; the gradient of which will be equivalent to the porosity exponent (m):

$$\log_{10} R_o = \log_{10}(a.R_w) - m.\log_{10} \phi \quad (6.9)$$

Using the same slope lines of other water saturations can be inferred (Pickett, 1966).

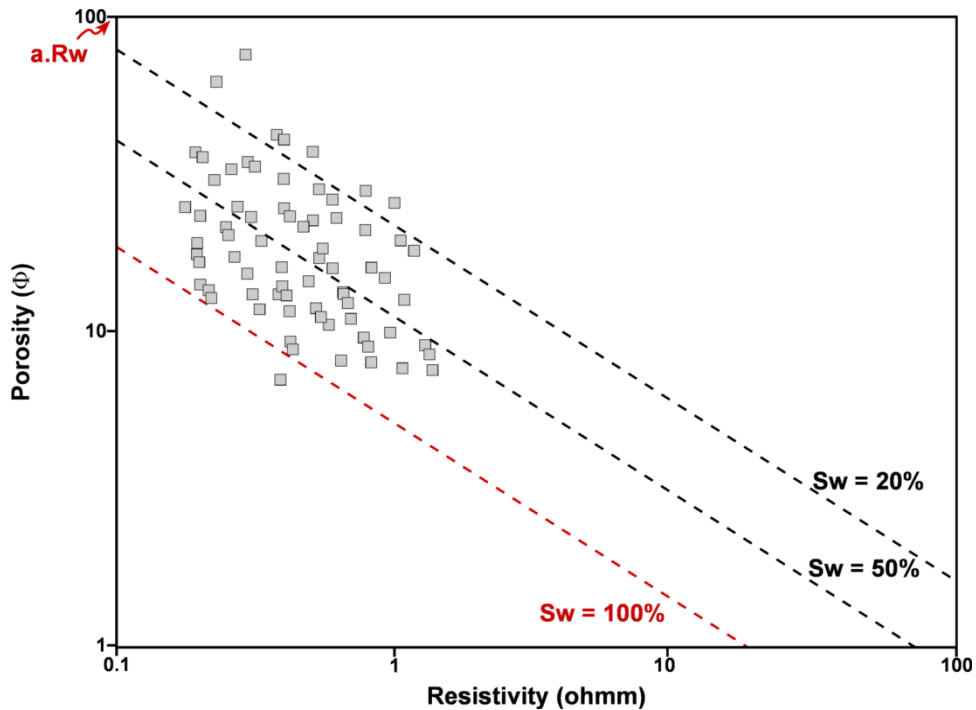


Figure 6.8: Schematic Pickett plot with relevant features marked

In this study the porosity data used in the plot was the density porosity (discussed above), and using these Pickett plots for the water-bearing wells the porosity exponent (m) value was obtained (Figure 6.9).

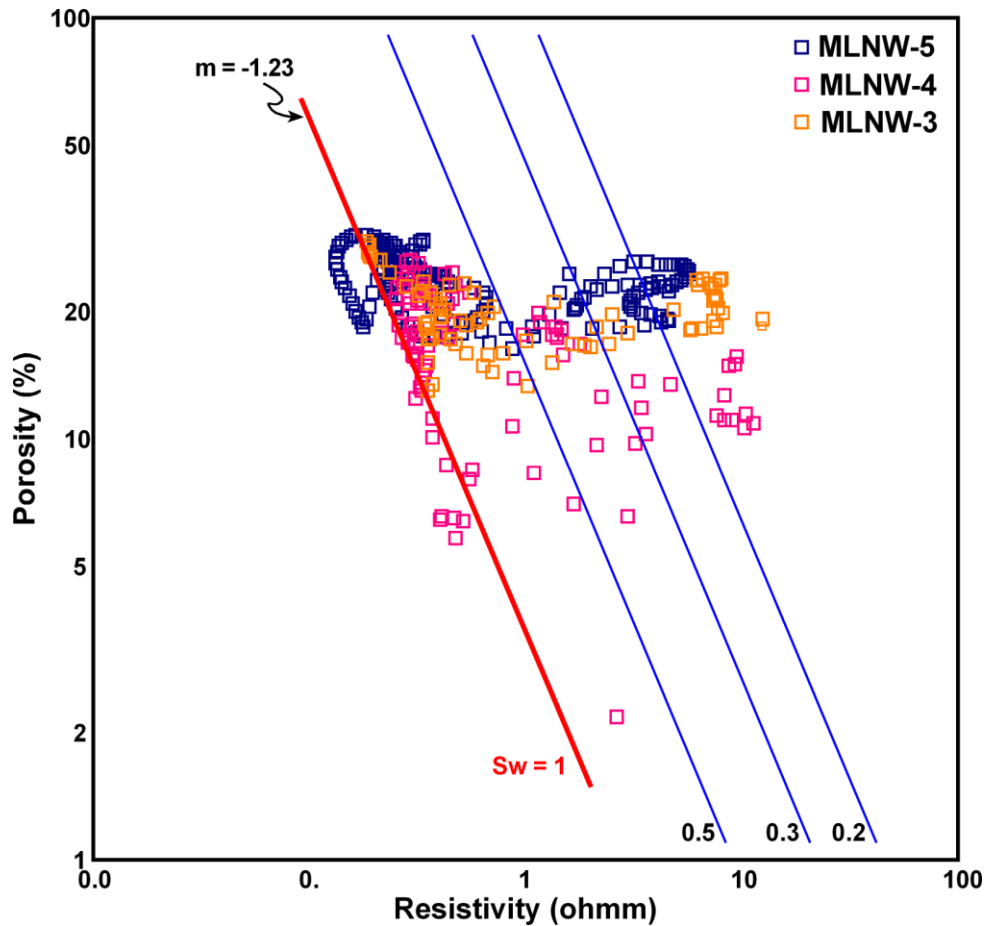


Figure 6.9: Pickett-plot of water-bearing wells, to derive porosity exponent (m) value

The log-derived porosity exponent, when compared to the core-derived values indicated a much lower value, suggesting more shale present than indicated from the core data (Table 6.10).

<i>Parameter</i>	<i>Value</i>
m	1.23
a	1.74
R_w	1.96
n	2.15

Table 6.10: Pickett plot log-based parameters

6.3.3 Permeability

Two ways were chosen to determine log permeability. One of the most common ways is through the porosity vs. permeability relationship (e.g. Tiab and Donaldson, 1996). A regression equation between the core-derived porosity and logarithmic permeability data is determined (Figure 6.10). This allows a log-based permeability curve to be calculated using the log-based porosity data: in this case density porosity.

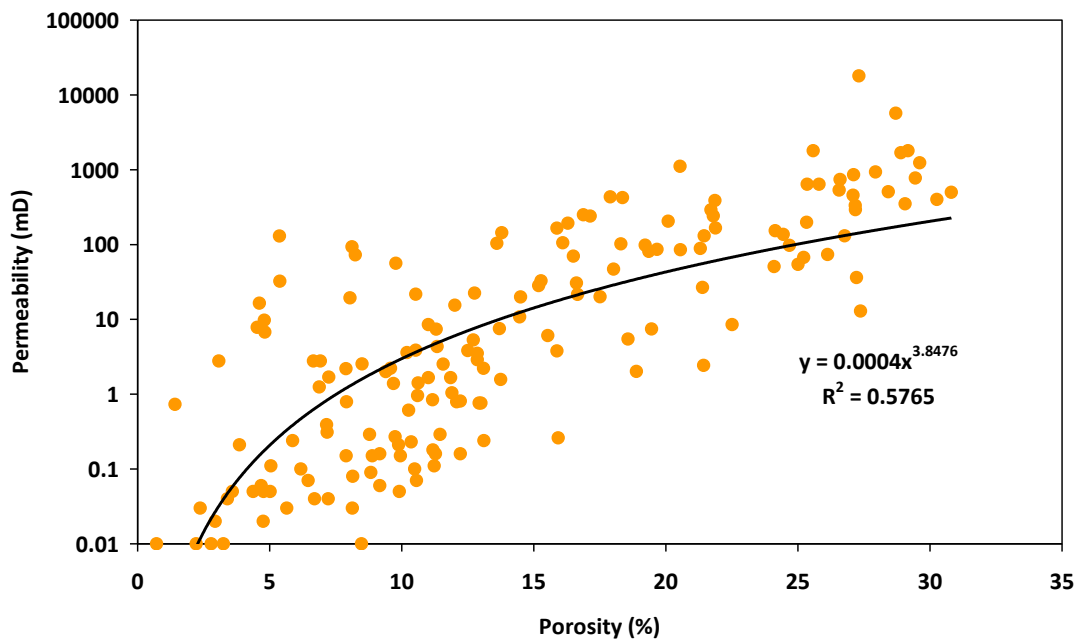


Figure 6.10: Porosity-permeability plot, with transform shown

When converted to log permeability, the resultant curve gives a relatively good match to the core permeability data (Figure 6.12). An alternative method of calculating permeability is through the relationship between core permeability and irreducible water saturations estimated from capillary pressure curves (Tiab and Donaldson, 1996). The determined mathematical relationship (Figure 6.11) can then be converted to a complete permeability curve using the log-based irreducible water saturation curve (discussed in Section 6.2.4). As figure 6.11 shows a poor correlation exists, but this could be due to the irreducible water saturations derived from porous plate capillary pressure not being fully desaturated (McPhee, 2009, Pers. Comm.; Millar, 2008).

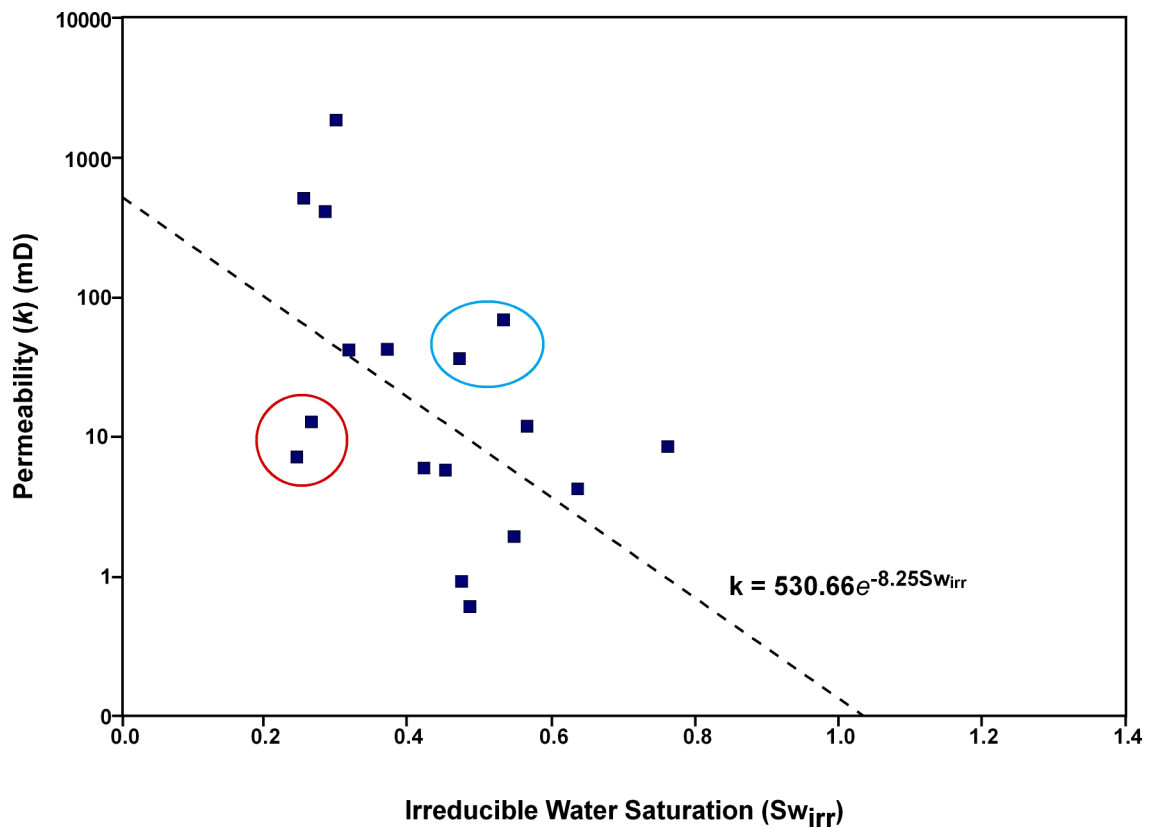


Figure 6.11: End-point saturation values vs. permeability, to assess data for outliers, blue circled points already known data quality problems, red circled points are from well MLNW-2. The equation refers to the relationship between permeability and water saturation: with the poor quality data points (blue circle) removed

The two permeability estimates when compared to core (Figure 6.12), exhibit similar variability to each other and the core values through the sandstones. However, the porosity-based permeability is lower than the irreducible water saturation permeability through the shales, suggesting the porosity-based value is a better estimate.

MLNW-5

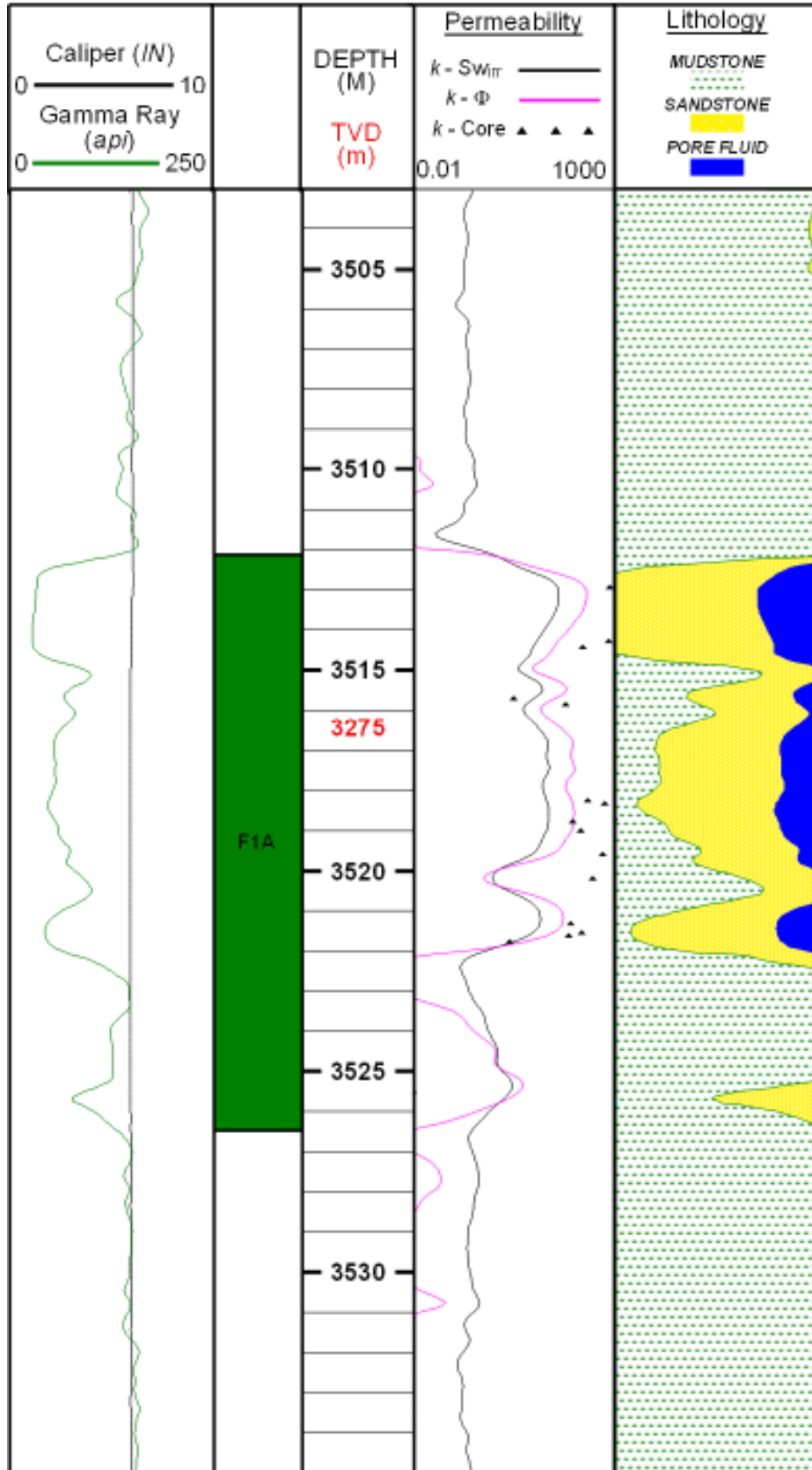


Figure 6.12: Log-plot of permeability vs. core permeability for example well: MLNW-5. With both the porosity-permeability relationship and the $S_{w_{irr}}$ derived permeability.

6.4 Log-derived Saturation Estimation

Both the standard Archie water-saturation model and the Waxman-Smiths and Juhász water-saturation for the shaly-sand models are investigated. These results can then be compared to indicate if the low resistivity is a problem. Unfortunately information on which specific intervals, of the known hydrocarbon-bearing wells, are producing is not available. Consequently only a brief assessment of the accuracy of the saturation profiles was possible.

6.4.1 Archie-derived Saturation Calculation

The main determination of log-based saturation estimation in clean sandstones is from Archie's equation (Archie, 1942):

$$S_w^n = \left(\frac{a}{\phi^m} \right) \left(\frac{R_w}{R_t} \right) \quad (6.10)$$

Of the above, R_t is measurable from the deep resistivity log, porosity is calculable from the density, neutron or sonic logs, R_w is calculable from Archie's equation in a full water saturated zone (explained in Chapter 2) or can be obtained from pore-water chemistry measurements, and the porosity exponents (m and a) are derived from the formation factor (section 6.2) or from Pickett plots (section 6.3.2). It should be noted that if a deviates from 1 there is a direct effect of changing the slope of the fit (m). The saturation exponent (n) is often taken to be 2; however it can be determined from core data using a plot of resistivity index (RI) vs. water saturation (S_w) (discussed in section 6.2.2).

In this study the core-derived parameters are taken as the field-average calculations (section 6.2.1), with the formation water resistivity (R_w) values observed to be

~0.043ohmm at 25°C (Craig, 2003). The values used in the equations are documented in table 6.11.

Field	<i>m</i> @ ambient	<i>a</i> @ ambient	<i>m</i> @4000 psi	<i>a</i> @ 4000 psi	<i>n</i>	R_w @ 25°C
<i>MLNW</i>	1.64	1.71	1.77	2.32	1.93	0.043
<i>MLSE</i>	2.09	0.801	2.43	0.65	2.03	0.043
<i>MLN</i>	1.31	2.40	0.72	5.63	2.11	0.042

Table 6.11: Available Archie parameters (*m*, *a*, *n*) and **R_w as obtained from core (Hughes et al 2003)**

Since **R_w** is affected by variations in temperature (Edmundson, 1988) and because temperature increases with depth a continuous curve of **R_w** with depth (i.e. variable temperature) was generated using the equation:

$$R_2 = R_1 \left[\frac{(T_1 + 21.5)}{(T_2 + 21.5)} \right] \quad (6.11)$$

Where **R₁** is the known formation water resistivity (**R_w**) at 25°C, **T₁** is the initial temperature (25°C) and **T₂** is the log temperature (Schlumberger, 2000). Where temperature logs were not already part of the data suite, they were calculated based on the maximum temperature reached at the bottom of the borehole, taken from the well-header information, and the depth reached.

The calculated temperature-dependant water resistivity and the density-porosity were used to calculate the Archie-based water saturations, with the hydrocarbon saturation then calculated (1 – **S_w**) and plotted (Figure 6.14) for the necessary wells.

6.4.2 Waxman-Smits Saturation Calculation

Waxman and Smits (1968) developed a modification to Archie’s main resistivity to water-saturation empirical relationship taking into consideration the excess conductivity associated with shale content (Worthington, 2000). It was one of the first shaly-sand models developed and is widely used; the main modified equation is below:

$$C_t = \left(\frac{S_{wt}^{n^*}}{F^*} \right) \left(C_w + \frac{BQ_v}{S_{wt}} \right) \quad (6.12)$$

The excess conductivity term is defined as BQv (see section 6.2.3), and can be determined from the C_o vs. C_w plots. A continuous BQv log curve is required to produce a continuous water-saturation profile in the log-analysis program (Interactive Petrophysics). This can be done by relating the Qv term to inverse porosity on the core samples, and producing a relationship that can then be extrapolated for estimation of Qv from log-porosity.

Initially the $B_{max}Q_v$ is determined through the extrapolation of the C_o vs. C_w trend line to a point where the rock conductivity is zero ($C_o = 0$). Since B is affected by temperature B_{max} can be calculated easily, using equation 6.13, as it is the equivalent of B when $R_w = 0$ (Eq. 6.14).

$$B = \frac{-1.28 + 0.225t - 0.0004059t^2}{1 + R_w^{1.23}(0.045t - 0.27)} \quad (6.13)$$

$$B_{max} = -1.28 + 0.225t - 0.0004059t^2 \quad (6.14)$$

Qv can therefore be calculated using:

$$Q_v = \frac{B_{max} Q_v}{B_{max}} \quad (6.15)$$

Where $B_{max}Q_v$ is a single value obtained from the C_o vs. C_w plot, and B_{max} is calculated from equation 6.14.

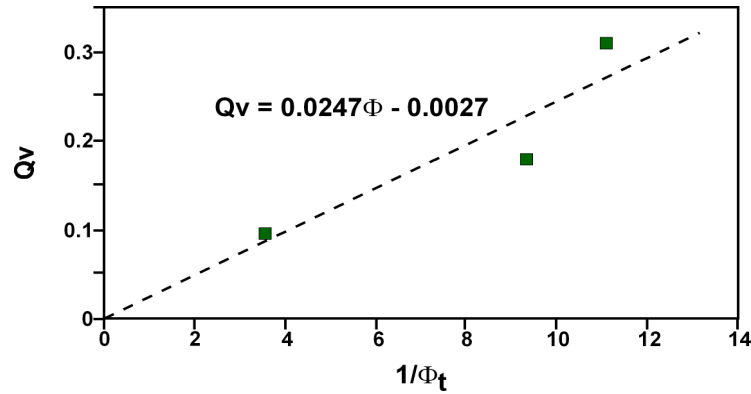


Figure 6.13: Excess conductivity vs. $1/\Phi_t$, based on the Waxman-Smiths model for shaly sands

This allows for specific values of Q_v to be determined for each sample, which can then be plotted against the inverse porosity of the core samples (Figure 6.13) to determine the relationship of Q_v to porosity, of the form $Q_v = c/\Phi_t - d$. Only three data points were available for use so the relationship is tentative at best. However it could still be used to generate a continuous Q_v curve using the log-based density porosity curve for Φ_t . The continuous Q_v curve was then used in the in-built Waxman-Smiths function of Interactive Petrophysics to calculate water saturations. Within Interactive Petrophysics the Waxman-Smiths equation used is in the form:

$$\frac{1}{R_t} = \left(\frac{\phi T^{m^*} \cdot S_w T^*}{a \cdot R_w} \right) \left(1 + \frac{B Q_v \cdot R_w}{S_w \cdot T} \right) \quad (6.16)$$

The calculated clay corrected porosity and saturation exponents (m^* and n^*) were used in the saturation calculation and the used values are summarized in table 6.12.

Field	m^*	n^*	$R_w @ 25^\circ\text{C}$
<i>MLNW</i>	1.66	1.96	0.043
<i>MLW</i>	1.53	No RI Data	0.043
<i>MLSE</i>	No Cw/Co	2.07	0.043
<i>MLN</i>	No Cw/Co	2.17	0.042

Table 6.12: Shaly-sand Archie parameters per field area and the core-derived water resistivity, measurements are at ambient conditions

The resultant saturations were plotted for the used wells, for comparison to the Archie-derived and core-derived saturations (Figure 6.14).

6.4.3 Juhász (Waxman-Smits) Saturation Calculation

One down-side of the Waxman-Smits estimation is its dependence on core-derived parameters (e.g. excess conductivity); Juhász (1979) developed an alternative log-based version:

$$\frac{1}{R_t} = \left(\frac{\phi_T^{m^*} \cdot S_w T^*}{a \cdot R_w} \right) \left(1 + Bn \cdot Qvn \frac{R_w}{S_w T} \right) \quad (6.17)$$

The main parameters are the same as those used in the Waxman-Smits calculation but include the normalized cation exchange capacity per unit total volume (Qvn) and normalised equivalent conductance of clay cations (Bn). The in-built functions within Interactive Petrophysics allow the Bn and Qvn terms to be calculated from the log data rather than relying on core data, using the following equations then normalising:

$$Qvn = \frac{a}{\phi_t} + b \quad (6.18)$$

$$Bn = \frac{-1.28 + 0.225t - 00004059t^2}{1 + R_w^{1.23}(0.045t - 0.27)} \quad (6.19)$$

The ‘a’ and ‘b’ terms in the Qv equation can be selected from a $1/\phi_t$ vs. Qv_{app} cross-plot, and in this study resulted as $a = 0.0247$, $b = -0.0027$. This log-based shaly-sand model was run, using the in-built function of Interactive Petrophysics, and the results were compared. In particular the comparison to the Waxman-Smits saturation model was of interest to assess the core-based vs. log-based excess conductivity assessment. The results of these calculations are not dissimilar to the Waxman-Smits estimations,

suggesting that the core data although sparse is accurate. Both Waxman-Smits and Juhász saturation profiles are compared to the Archie obtained estimates (Figure 6.14).

6.4.4 Log-derived Water Saturation Estimates Comparison

The Archie, Waxman-Smits and Juhász saturation estimations were plotted together with the core-derived irreducible water saturations and core measurements (where available). The five main wells focussed on provided a range of water-bearing and known hydrocarbon-bearing examples (Figure 6.14). The Archie-derived saturation estimates show more accuracy than the Waxman-Smits and Juhász models; in the known water-bearing wells the Archie results exhibit a water saturation of 100%, as would be expected. The Waxman-Smits and Juhász models, which are near identical in all the wells, indicate the presence of hydrocarbons even in the water-bearing wells e.g. MLNW-1. The core-based irreducible water saturation curve provides an estimate of the minimum water saturation, and in all cases the Waxman-Smits and Juhász models exceed this, suggesting lower water saturations, as low as 0% in places (Figure 6.14). The Archie estimations, however, do not often exceed this lower limit, but neither do they provide a very high estimation of potential hydrocarbon saturations. The available Dean-Stark water saturations are much lower than any of the log-derived estimates of saturation, but with so few data points this is not a reliable indicator of saturation model quality.

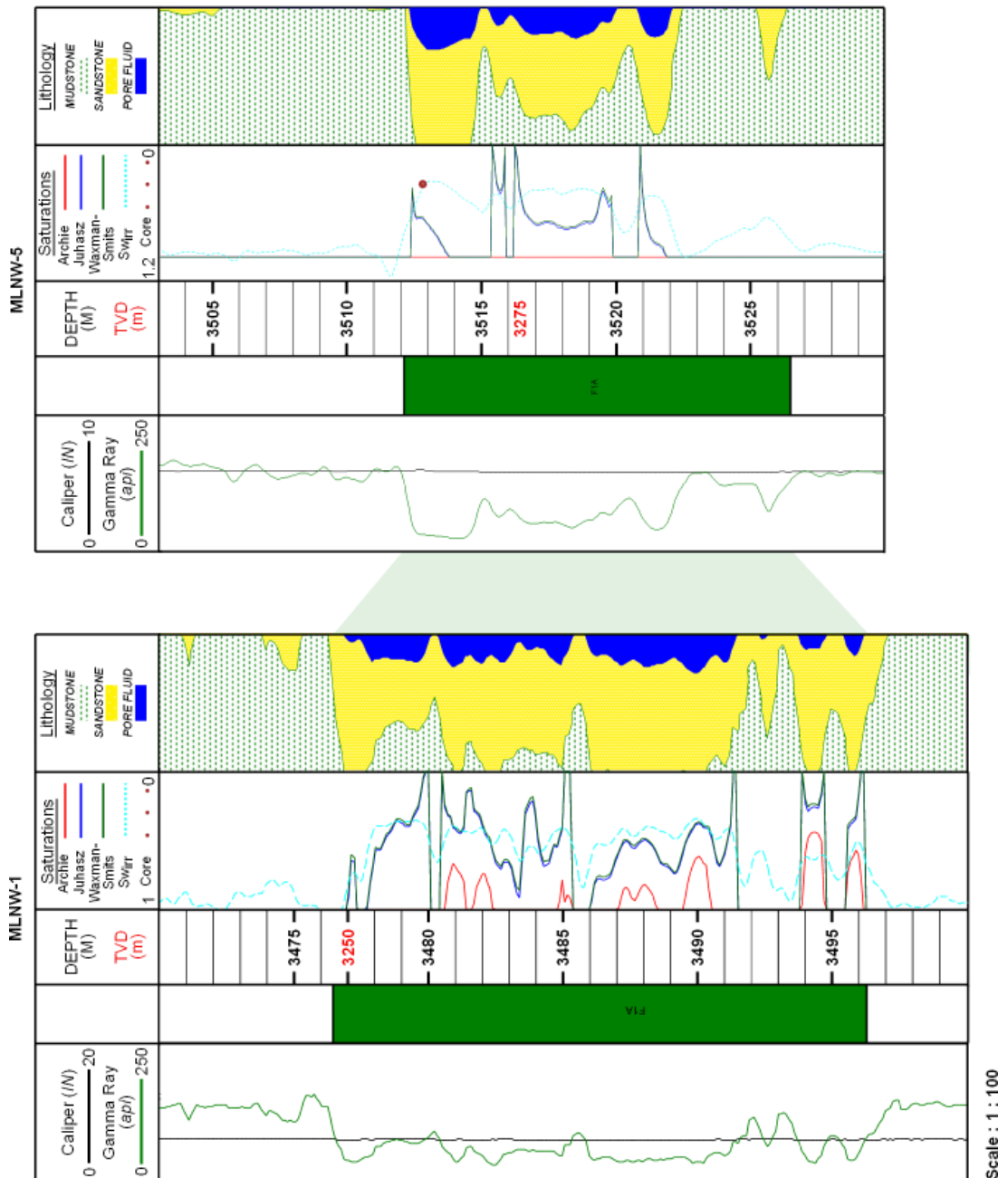


Figure 6.14: Water saturation profiles for different methods of log-based calculation; Left in the water-bearing well (MLNW-5). Right: Hydrocarbon-bearing well (MLNW-1).

Overall, there is not enough consistency between the models and the irreducible water saturations, or known about the producing intervals to determine the reliability of the saturation estimates. However, it is clear that the shaly-sand models do not apply in this reservoir (A) study, and so alternative estimations for saturation may be viable.

6.5 Saturation Height Functions

Saturation height functions provide a way to calculate saturation without relying on resistivity measurements, and are based on the height above the free water level (FWL). Many varieties of saturation height functions are available; Skelt-Harrison, Leverett J-functions, FOIL functions to name a few (discussed in Chapter 2). The Leverett J-function is based on core data but can also be used on log-data and therefore provides a good calibration between the two and the basis for the saturation height models.

Core capillary pressure curves can be used to calculate the Leverett J-functions, as described in chapter 2 (section 2.2.3). This allows the determination of a transform relating water saturations to the J-function parameter, which is directly related to the capillary pressure and thus height above the free water level in a well (Leverett, 1941) (equations below). One draw-back of this method is the data points need to be from rock types or facies with the same properties i.e. the Leverett J-function is “*inappropriate where there is a diversity of rock types within a reservoir*” (Stiles, 1998).

$$h = \frac{2.309 P_{c_{res}}}{(\rho_w - \rho_o)} \quad (6.20)$$

$$J = \left[\frac{0.217 P_{c_{res}}}{(\sigma \cos \theta)} \right] \left[\sqrt{\frac{k}{\phi}} \right] \quad (6.21)$$

6.5.1 Work-flow for Sw-height analysis:

Prior to calculating the Leverett J-functions, the data quality of the underlying capillary pressure curves must be investigated. In this project the capillary pressure curves were

determined through both the centrifuge and porous plate methods (see chapter 2 for details and Appendix IV). To determine if the results from the two methods were comparable samples from each method at similar depths were transformed into J-functions and compared (Table 6.13).

Sample	Porosity	Permeability	Ratio	Correlation
<i>MLNW-5: 3509.08m</i>	0.09	0.59	0.15	0.7646
<i>MLNW-5: 3509.03m</i>	0.091	0.92	0.099	
<i>MLSE-5: 3341.13m</i>	0.269	42	0.0064	0.877
<i>MLSE-5: 3341.07m</i>	0.283	42	0.0067	
<i>MLSE-5: 3330.1m</i>	0.31	395	0.00078	0.8656
<i>MLSE-5: 3330.05m</i>	0.309	1913	0.00016	
<i>MLNW-2: 3459.13m</i>	0.282	13	0.022	0.2433
<i>MLNW-2: 3459.09m</i>	0.145	4	0.036	
<i>MLNW-2: 3497.07m</i>	0.151	5.9	0.026	0.4027
<i>MLNW-2: 3497.03m</i>	0.151	7.1	0.021	

Table 6.13: J-function values for correlation between porous plate and centrifuge methods: sample pairs from similar depths analysed by different methods: with respective correlation values (R^2), porosity values, permeability values and porosity-permeability ratios.

For wells MLNW-5 and MLSE-5 good correlations are observed, but for MLNW-2 the correlations for both sample sets are very poor. The underlying data quality of these samples is good suggesting another reason for this mismatch. One explanation could be that the porosity/permeability relationship for these samples varies, and could directly (due to use in derivation of the J-function) account for the difference. Indeed the two samples in both sets exhibit very different porosity-permeability relationships. However, when the samples from the other wells respective porosity-permeability relationships are investigated, they also exhibit different values (Table 6.13), and therefore there must be another reason to account for this mismatch in the samples from MLNW-2.

A plot of end-point saturations plotted against core permeability is a standard way of assessing saturation data quality; a good data set would exhibit a negative trend, with any outliers indicating either data quality problems or other data discrepancies. The data set does show a negative trend with four outliers (Figure 6.11). The two on the right of

the slope exhibit initial loss on the capillary pressure measurements (samples: MLN-5-3521.1m; MLSE-5-3347.02m), so can be discounted from further analysis. The other two outliers on the other side of the slope are from MLNW-2: at depths 3459.13m and 3497.03m. It is possible that the cause of these two MLNW-2 samples outliers could explain the discrepancy with the MLNW-2 samples fitting in with the rest of the J-function profiles. It is conceivable that an error in the labelling of the capillary-pressure curves could be responsible for this discrepancy, but there would be no way to correct for this.

Overall, the remaining samples are of good quality and the two methods can be compared. When the data are converted to J-functions and plotted together, the resultant correlation indicates multiple rock types are present (Figure 6.15). The samples were then grouped for various rock properties, e.g. porosity, permeability, sedimentary facies, to determine the control on the J-function variation (Table 6.14).

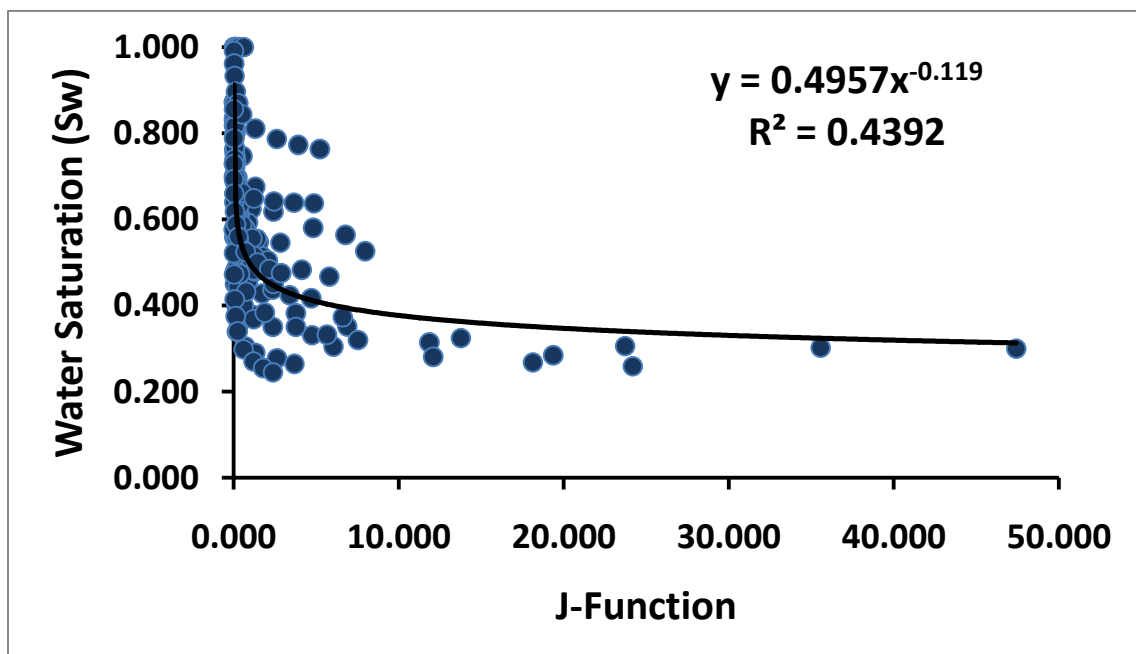


Figure 6.15: Plot J-values against brine saturations from capillary pressure curves

From table 6.14 the facies groupings appear to provide the overall best correlations. Not all the samples have the relevant data to allow this relationship to be tested, but for the possible samples there is a moderately good correlation (Figure 6.16). The majority of the samples are from facies VIII and when plotted all together give a good correlation ($R^2 = 0.8103$). The other obvious facies is XIV but there is only one sample of this facies and it does not have a good correlation with any of the other samples (Figure 6.16). The other facies group (III) has two known samples, although one is of dubious quality, so no direct correlation can be seen. However, when two of the samples with unknown facies associations are plotted with the good facies III sample, the correlation is excellent ($R^2 = 0.9181$). This implies that the two unknown samples from MLN-5 are likely to exhibit similar properties to that of Facies III.

Parameter	Group	Samples	Correlation
<i>Porosity</i>	1 (0.05 – 0.10)	Mlnw-5: 3509.08m Mlnw-5: 3509.03m	$R^2 = 0.7646$
	2 (0.1 – 0.2)	Mlse-5: 3334.06m Mlnw-2: 3459.09m Mlnw-2: 3497.07m Mlnw-2: 3497.03m	$R^2 = 0.0973$
	3 (0.2 – 0.3)	Mlse-5: 3341.13m Mln-5: 3523.13m Mlse-5: 3338.14m Mlnw-2: 3459.13m Mlse-5: 3341.07m Mln-5: 3521.2m	$R^2 = 0.549$
	4 (+0.3)	Mlse-5: 3330.05m Mlse-5: 3330.1m Mlse-5: 3332.06m	$R^2 = 0.7548$
<i>Permeability</i>	1 (0.1 – 1.9mD)	Mlnw-5: 3509.08m Mlnw-5: 3509.03m	$R^2 = 0.7646$
	2 (2.0 – 9.9mD)	Mln-5: 3521.2m Mlnw-2: 3497.07m Mlse-5: 3334.06m Mlnw-2: 3459.09m Mlnw-2: 3497.03m	$R^2 = 0.1396$
	3 (9.9 – 19.9mD)	Mlnw-2: 3459.13m	$R^2 = 0.9423$
	4 (20.0 – 99.9mD)	Mln-5: 3523.13m Mlse-5: 3338.14m Mlse-5: 3341.07m Mlse-5: 3341.13m	$R^2 = 0.7229$
	5 (100+mD)	Mlse-5: 3330.1m Mlse-5: 3330.05m Mlse-5: 3332.06m	$R^2 = 0.7548$
<i>(Φ/k) Ratio</i>	1 (0.0001 – 0.001)	Mlse-5: 3330.05m Mlse-5: 3332.06m Mlse-5: 3330.1m	$R^2 = 0.7548$
	2 (0.001 – 0.01)	Mln-5: 3523.13m Mlse-5: 3338.14m Mlse-5: 3341.13m Mlse-5: 3341.07m	$R^2 = 0.7229$
	3 (0.01 – 0.05)	Mlse-5: 3334.06m Mlnw-2: 3459.09m Mln-5: 3521.2m Mlnw-2: 3497.03m Mlnw-2: 3459.13m Mlnw-2: 3497.07m	$R^2 = 0.1823$
	4 (0.05+)	Mlnw-5: 3509.03m Mlnw-5: 3509.08m Mln-5: 3521.2m Mlse-5: 3334.06m	$R^2 = 0.7646$
<i>Facies</i>	iii	Mlse-5:3338.14 Mlse-5: 3347.02	$R^2 = 0.5425$
	viii	Mlnw-5: 3509.08 Mlnw-5: 3509.03 Mlse-5: 3330.1 Mlse-5: 3332.06 Mlse-5: 3341.13 Mlse-5: 3341.07	$R^2 = 0.8103$
	xiv	Mlse-5:3334.06	$R^2 = 0.9933$
	iii with additional 'unknown' samples	Mlse-5: 3338.14 Mlse-5: 3347.02 Mln-5: 3521.2 Mln-5: 3523.13	$R^2 = 0.9181$

Table 6.14: Groupings according to various parameters and their respective correlations, with the initial known facies providing the consistent good correlations

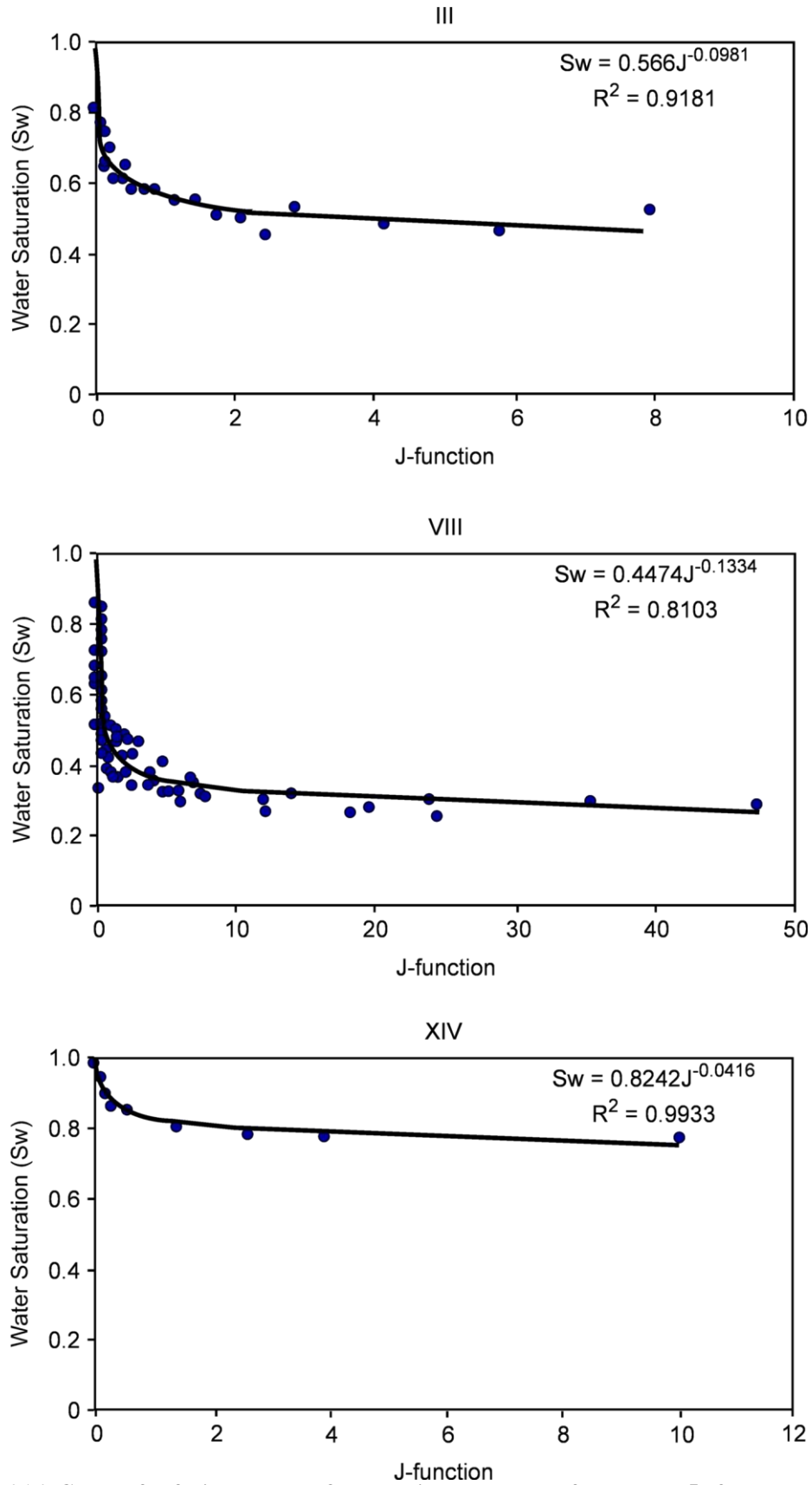


Figure 6.16: Groups for facies VIII, III & XIV, with the samples from MLN-5 of unknown facies association added to the facies III J-function plot

6.5.2 Composite J-function derived water saturation profile

Demonstrating that sedimentary facies control the J-function variation enables a composite saturation profile to be created based on the relevant J-function for the sedimentary facies as defined from the core. This can be achieved by calculating the log-equivalent capillary pressure ($P_{c_{res}}$), based on the height above the free water level (h):

$$h = \frac{2.309 P_{c_{res}}}{(\rho_w - \rho_o)} \quad (6.22)$$

Which when re-arranged to give $P_{c_{res}}$, is a function of the height (in metres) in the reservoir above the free water level (h);

$$P_{c_{res}} = \frac{(\rho_w - \rho_o)h}{2.309} \quad (6.23)$$

Where the reservoir-fluid density (ρ_w) = 1.19 g/cm³, and saturation oil density (ρ_o) = 0.796g/cm³. The oil density is derived from well test data, converted from API to specific gravity, which is approximate to density (see Appendix V for calculations.) To calculate the height above the free water level, the depth of the free water level (FWL) must be known. Each field is structurally separate, thus each has a different free water level (Table 6.15). The surface topography affects the reservoir depths, and so the comparison of the free water level must be done against true-vertical depth (TVD) relative to a datum. Where a TVD was not part of the original data set it was calculated from the elevation data documented on the well-headers. The free water level for the MLN field the free water level was determined from well MLN-10 RFT data, while the MLNW field FWL was determined from the oil-down-to (ODT) in MLNW-1 and the water-up-to (WUT) in MLNW-2 (Malick, 2009, Pers. Comm.).

Field	FWL (in TVDss m)
<i>MLNW</i>	~3270m TVDss
<i>MLN</i>	~3298m TVDss
<i>MLSE</i>	Unknown

Table 6.15: Provided FWL data per field, (Malick, 2009, Pers. Comm.)

In addition to the capillary pressure, based on the height above FWL, a log-based porosity and permeability are needed to generate a continuous log-based J-function:

$$J = \left[\frac{0.217 P_{c_{res}}}{(\sigma \cos \theta)} \right] \left[\sqrt{\frac{k}{\phi}} \right] \quad (6.24)$$

The log-based porosity is the density porosity, (section 6.3.1). One thing to note is that if using log data to calculate J-function, and using log-based porosity to calculate permeability (k), there will be a reduction in variability from the (\emptyset/k) function of the equation. This is because the permeability is being divided by the porosity log used in the original permeability calculation (Millar, 2008, Pers. Comm.). However, when the two permeability measurements (Section 6.3.4) are converted to J-functions (equation above), the porosity-based permeability gives the most variation and more realistic estimate through the mudstones (Figure 6.17). Therefore the log-based permeability used in further calculations is the porosity-based permeability.

MLNW-5

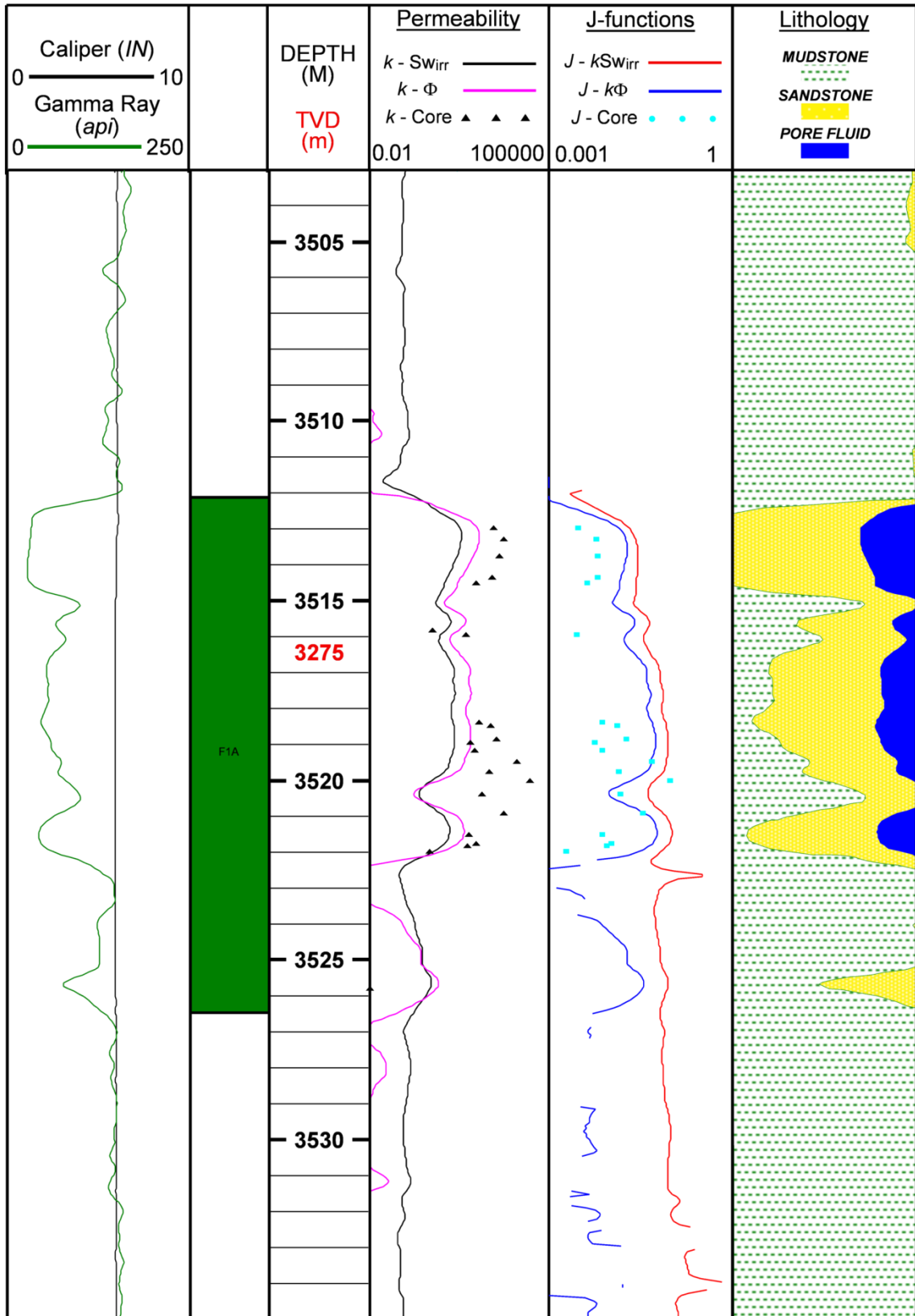


Figure 6.17: Example of the J-function calculated on both permeability estimates: porosity based gives the most variation

Using the J-function to saturation (S_w) relationships determined per facies (Table 6.16) individual water saturation profiles were calculated. To check the results, water saturations were calculated in the same way using core data. The core-derived water saturations were compared to the log values, and show a good match (Figure 6.18).

Facies	J-function
VIII	$S_w = 0.447.J^{-0.13}$
III	$S_w = 0.566.J^{-0.09}$
XIV	$S_w = 0.820.J^{-0.04}$

Table 6.16: Main sandstone facies and the S_w vs. J relationship

The resultant curves calculated using the $S_{w_{irr}}$ based permeability have low variability, and closely follow the variation of the irreducible water saturation curve. In contrast, despite the ‘double dipping’ effect mentioned above, the S_w curves based on the porosity-based permeability exhibits higher variation (Figure 6.18).

A composite S_w profile can be determined, from splices of each facies-based curve. The discriminate analysis, discussed in chapter 5, provides a method for predicting where each of the main sandstone facies occurs. Across each known interval the relevant J-function can be applied, and a composite profile built up. Figure 6.19 shows an example from well MLNW-1.

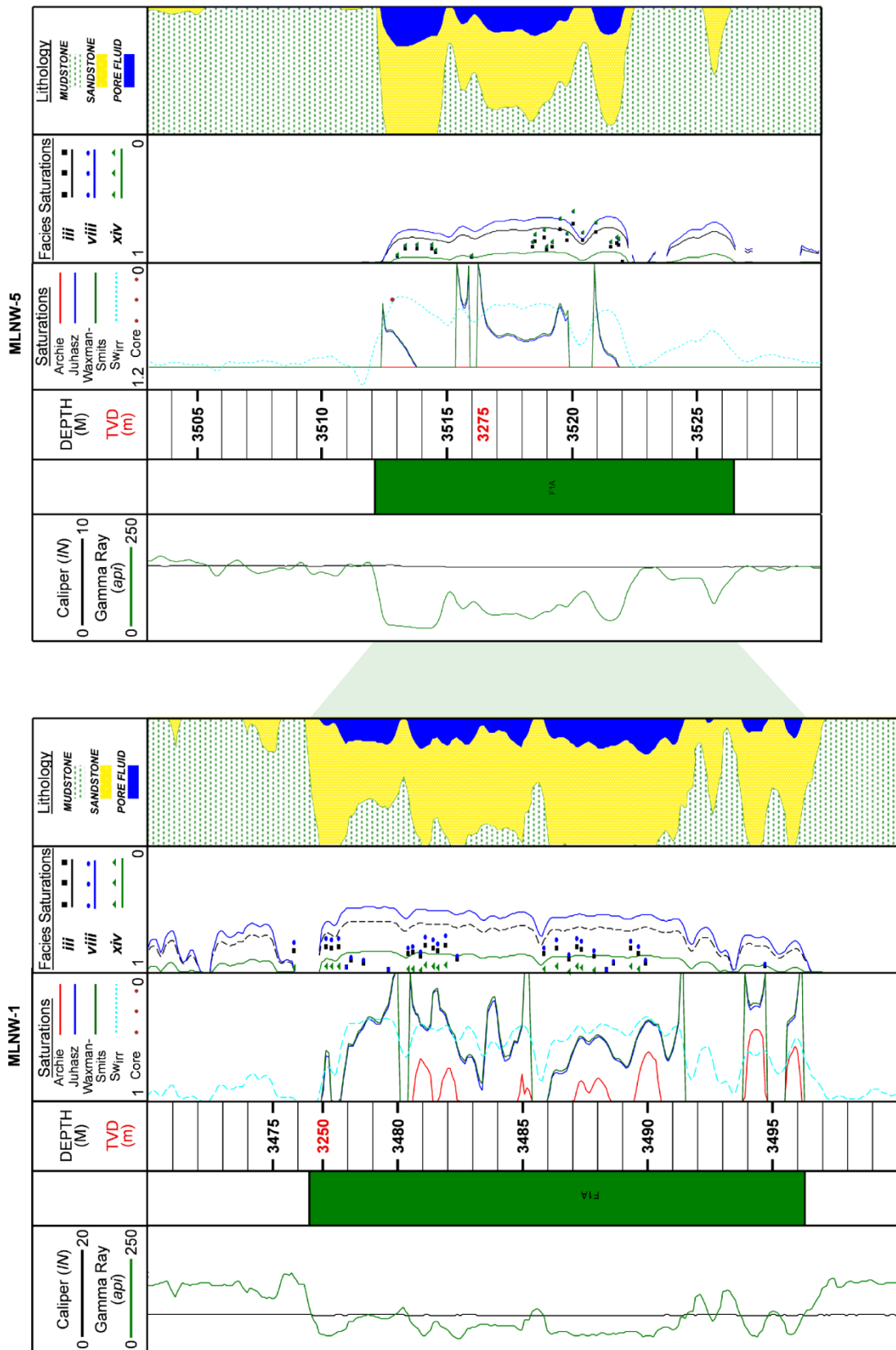
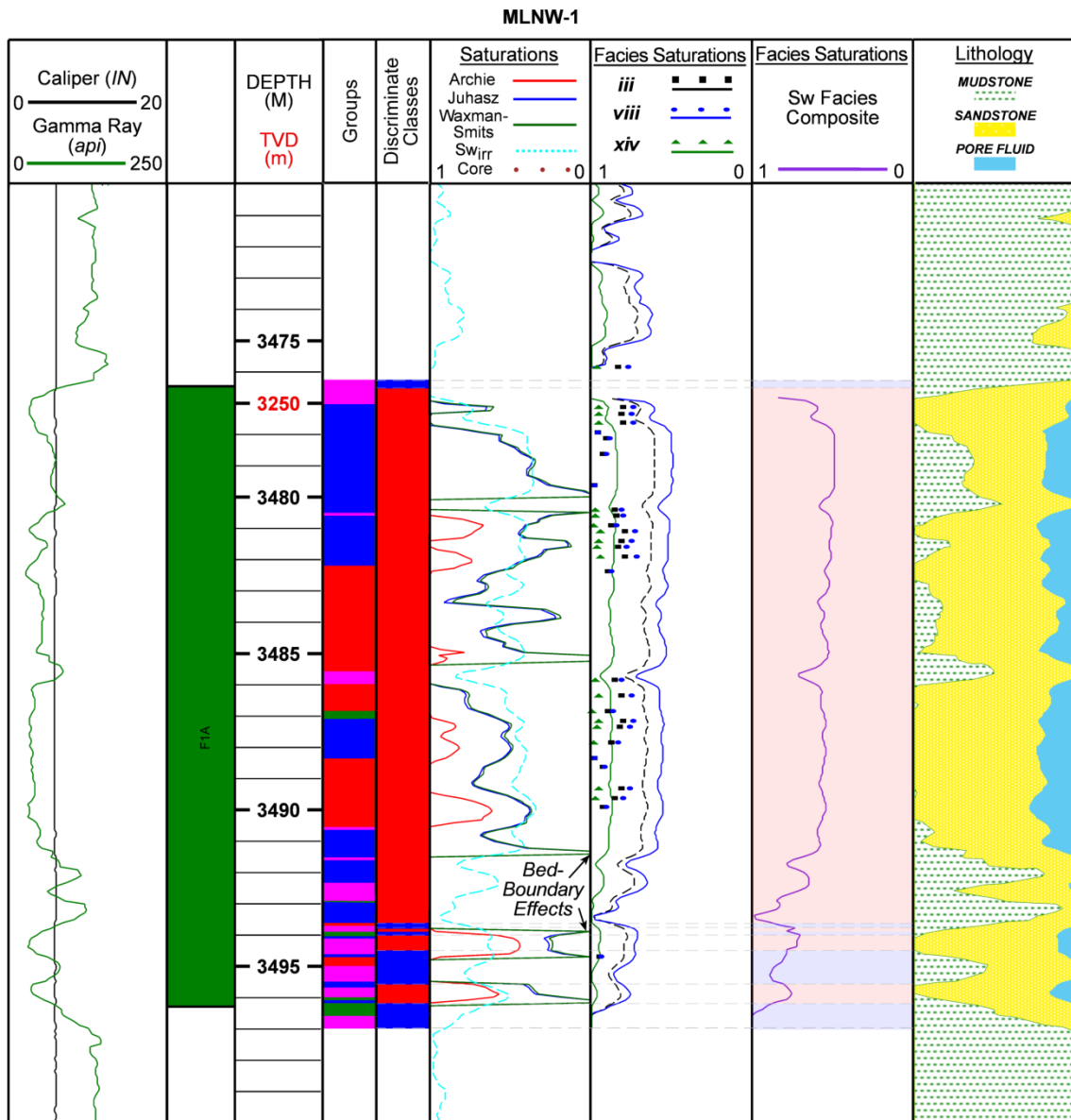


Figure 6.18: Each facies Sw curve, and the Sw_{irr} curve, for examples of water-bearing (MLNW-5) and oil-bearing (MLNW-1) wells



Scale : 1 : 100

Figure 6.19: MLNW-1 composite profile with discriminate analysis results shown & each individual facies profile, to document where the splice has occurred

6.6 Comparison of Saturation Results

In an oil-bearing well (e.g. MLNW-1) the various saturation estimates give different responses (Figure 6.19). Assuming the irreducible water saturation curve to be the most reliable and the minimum water saturation value possible, the other saturation estimates can be considered in relation to it. The Waxman-Smits and Juhász estimations consistently overestimate the minimum water saturation, and are affected by bed

boundary effects (Figure 6.19). Therefore the shaly sand models are discounted as reliable estimates. The Archie estimates are mostly below the irreducible water saturation estimates, and within the large sandstones produce low estimates of water saturation. However, it does indicate some saturation where there is minimal sandstone (Figure 6.19). The J-function based saturation estimates are very similar to the irreducible water saturation, and the composite profile is also a reasonable estimate.

Assessing the accuracy of the estimates further is not possible given the absence of any data relating to the producing intervals within each well. But it is possible to say that the Archie estimates are not completely unreliable, and the J-function based composite saturations are reasonable given the facies variation.

6.7 Conclusions

Log-based saturation estimations use Archie's equation (Archie, 1942) in clean, mudstone and clay free, sandstones. For sandstones that contain significant amounts of mudstone and clay shaly-sand models exist. This study focused on the Waxman-Smits and Juhász models, which are based on the addition of a clay conductivity term to Archie's original equation (Juhász, 1979; Waxman and Smits, 1968). A log-based porosity is necessary for all three of the saturation calculations used in this study. The *total* density porosity provided the closest match to core porosity data, and was therefore used in the saturation estimations.

A simple plot of excess conductivity vs. saturating brine resistivity (Figure 6.3), derived from core sample data, suggests that this reservoir should fit Archie's equation, i.e. shaly-sand models should not apply. The resulting saturation estimates, from Archie, Waxman-Smits and Juhász, do not provide accurate estimates of hydrocarbon presence. The Waxman-Smits and Juhász saturation estimates consistently overestimate the minimum water saturation, and are affected by bed boundary effects. The Archie

estimate fits closer to the known hydrocarbon occurrences, but does overestimate the water saturation in some of the sandstones. Therefore an alternative, core-based saturation estimate was investigated, using the Leverett-J saturation height function (Leverett, 1941).

A strong link between the main sedimentary sandstone facies (facies VIII, III and XIV) and Leverett J-function saturation height profiles was established (Figure 6.16 and Table 6.16). Therefore a saturation profile was constructed using the different facies-based Leverett J-functions. Where each of facies VIII, facies III and facies XIV was known to occur, based on the discriminant statistical analysis (Chapter 5, section 5.4.2), the corresponding J-function equation was applied. The resulting composite facies-based saturation profile provides a method for estimating saturation in the chlorite-rich zones, based on the link between facies VIII and chlorite occurrence (see Chapter 4). However, without further knowledge of specific producing intervals within the hydrocarbon-bearing wells, it is not possible to further test the accuracy of the saturation estimates.

Overall this chapter outlines a new method for estimating saturations in sandstone reservoirs where normal Archie-based calculations are affected by low resistivity contrast. A core-based saturation height profile is a common alternative, however, specific facies based profiles targeting the cause of the low resistivity can be developed, creating a more detailed saturation estimation.

7. Conclusions

The main aim of this project is to refine the saturation estimations in the Carboniferous A hydrocarbon reservoir which are affected by the effects of low resistivity pay. The two main objectives, outlined in chapter 1, have been discussed in detail in previous chapters:

Objective 1: “*understanding the occurrence and distribution of the grain-coating chlorite*” was addressed through detailed sedimentary analysis of available core data and was assessed in connection with a review of published literature. Objective 1 was broken down into the following questions and answered in chapters 3 and 4:

i) How do grain-coating chlorites form? The chlorites in this study are iron-rich, as demonstrated from SEM spectral analysis and XRD data. Iron-rich chlorites are known to form in specific depositional environments, specifically shallow marine deltaic environments, where iron and magnesium cations can mix with anions in saline waters. Chlorite formation can occur from the alteration of various precursor minerals; berthierine, kaolinite or amorphous iron-rich clays, and often occurs early in the burial history.

ii) Is the chlorite in reservoir A diagenetic or authigenic? The high aluminium content of the chlorites suggests the formation of the chlorites from the alteration of kaolinite. This indicates a diagenetic origin of the chlorite. The grain-coating nature of the chlorite and the lack of quartz overgrowths indicate formation early in the burial history, which helps preserve the porosity with depth.

iii) Is there a depositional environmental or facies control on the chlorite distribution within reservoir A? The link between depositional environment and chlorite formation is discussed above (i), and reservoir A depositional environments are consistent with a

deltaic shallow marine setting. Through detailed analysis of core photographs, thin sections and SEM analysis (chapter 4) three main sandstone facies were identified. The different characteristics of these facies indicate a link between chlorite abundance and sedimentary facies. The most abundant sandstone facies, VIII, is off-white friable sandstone, with abundant chlorite clay coatings and minimal cement. Facies III is characterised by the occasional mudstone laminae, the presence of siderite cement, and only minor grain-coating chlorite. The facies VIII is linked to the upper shoreface depositional environment, while facies III is linked with the lower shoreface.

iv) Does the presence of the grain-coating chlorite affect the porosity distributions (i.e. porosity) of the sediment? Analysis of porosity distributions in relation to the sandstone facies indicates a link to chlorite occurrence. Facies VIII, which contains abundant grain-coating chlorite, exhibits a bi-modal porosity distribution indicative of the micro-porosity known to be exhibited by chlorite coatings. In contrast the pore-size distributions for facies III are consistently uni-modal, exhibiting narrow pore throats consistent with the more cemented nature of this sandstone facies.

Objective 2: “development of a saturation model which accounts for the low resistivity pay zones” is addressed in chapters 5 and 6 of the thesis. Objective 2 breakdowns into two questions (below) which can be addressed through detailed wireline log analysis (v) and the subsequent integration of the wireline analysis results with the sedimentary model developed from objective 1.

v) Can the presence of chlorite be predicted from the wireline log data, either with or without input from core data? Using the sedimentary facies model developed in response to objective 1, the wireline log data was assessed for its ability to distinguish the chlorite-bearing facies from the cemented facies. Standard cross-plots of density vs. neutron do not separate the different sandstones, but do separate the sandstones from the

mudstones. More detailed statistical analysis successfully provides a method for distinguishing between the main sandstone and mudstone facies. Discriminant analysis, a form of supervised statistical analysis, used the sedimentary facies model derived from core data, as the training model. The discriminant analysis successfully identified the chlorite-bearing sandstone facies from the cemented facies and the mudstone facies. This was then used as a classification scheme on other wells to predict the sedimentary facies, and when tested on data from other wells with known sedimentary facies (MLNW-1 and MLSE-5) proved to be reliable. In particular, with regard to the chlorite-bearing facies (VIII), there is a >90% success rate at predicting the occurrence of the facies. The variation between the observed classification and predicted group classification could be due to the limited interpretation of facies from core photographs, and thus the predictive capability is within acceptable limits.

vi) Does a saturation-height model provide a more realistic estimate of water saturation than the resistivity measurement estimation? To answer this question standard methods for water saturation were applied and compared to a facies based saturation height model (chapter 6). The saturation-height function chosen was the Leverett-J, and a link was determined between different J-functions and the main sandstone facies (III and VIII), which resulted in a composite water saturation profile. When the J-function based water saturation estimates are compared to the Archie and shaly-sand saturation estimates, it is clear that Archie estimates give a patchy estimation of water-saturation, whereas the shaly-sand estimates overestimate water saturation in apparent shaly-rich zones. This indicates that the computer-based shale-estimation (chapter 5), is inaccurate and overestimated. As such the composite J-function based water saturation estimate most closely matches the core-based irreducible water saturations. However, in the

absence of more detailed information about the specific producing intervals within wells it is not possible to further assess the accuracy or reliability of any of the models.

Through the thesis the above questions were addressed and answered, demonstrating that the Carboniferous reservoir A, of the study field of Algeria is another example of a low resistivity pay reservoir. Through detailed analysis of core data a link between the abundance of pore-lining chlorite and sedimentary facies was determined. Discriminant analysis of the log data, with the classification scheme built from the core-based sedimentary facies, provided a method for determining the distribution of the chlorite-bearing sandstone facies in the uncored wells. Using the Leverett-J saturation height function, determined for each main sandstone facies, a composite water-saturation estimate was produced. The resultant facies-based J-function water saturation estimates closely matched the variation in the core-derived irreducible water saturation curve. However, without more detailed knowledge of which intervals within reservoir A produce and which don't it is not possible to assess the robustness of the Leverett-J function facies based saturations further.

Ultimately what has been developed through this thesis is another methodology for dealing with a low resistivity pay reservoir where chlorite is believed to be the cause of the low resistivity. The methodology is based on using the core data to build a saturation height model, and then translating the model to the log scale, thus allowing for the estimation of saturation without resorting to the resistivity measurement. In addition a discriminant analysis classification has been developed, specifically for this study reservoir, to identify and separate chlorite-rich sandstones from mudstone-rich sandstones and mudstones. This could be tested and applied on other chlorite-rich sandstone reservoirs to test its versatility. Alternatively the discriminant analysis method could be employed based on the individual reservoirs sedimentary model.

Appendix I. Glossary

PEF – Photoelectric factor

NGR - Natural Gamma Ray

SGR - Spectral Gamma Ray

Φ - Porosity

ρ - Density

ρ_b - Bulk density

ρ_e - electron density

ρ_f - fluid density

ρ_{ma} - matrix density

R_w – formation water resistivity

R_{mf} – mud-filtrate resistivity

S_w – water saturation

S_{xo} – invaded zone saturation

R_t - measured total resistivity

R_o – resistivity of fully brine saturated rock

n – saturation exponent

m – cementation exponent

V_b – measured bulk velocity

V_f – pore fluid velocity

V_{ma} – rock matrix velocity

FF – formation factor

$S_{w_{irr}}$ - irreducible water saturation

Δt - total travel-time (inverse of velocity)

Δt_f - fluid travel-time

Δt_{ma} - matrix travel-time

C_o - Total conductivity (measured)

C_w - Water/brine conductivity

RI - Resistivity Index

FF - Intrinsic Formation factor – shale corrected*

m^ - Intrinsic porosity exponent – shale corrected*

n^ - Intrinsic saturation exponent – shale corrected*

BQ_v – Excess conductivity

P_c – capillary pressure

P_{c_{res}} – Capillary pressure at reservoir conditions

P_{c_{lab}} – Capillary pressure at laboratory conditions

h – height above free water level

θ – contact angle (wettability) (degrees)

σ – interfacial tension (dynes/cm)

k – permeability (mD)

r – pore throat radius (μm)

Z – atomic number

SEM – scanning electron microscope

CEC – cation exchange capacity

FWL – Free water level

OWC – Oil-water contact

SCAL – special core analysis

XRD – x-ray diffraction

Appendix II. Sedimentary Facies Analysis

For the detailed sedimentary analysis discussed in Chapter 4 sedimentary logs from core photographs, thin sections and SEM analysis were used. This appendix outlines the supplementary data that was used in construction of the sedimentary facies. Table IIa outlines the samples used, grouped for previously defined (by Conoco-Phillips) depositional environments, and the interpreted sedimentary facies.

For each of the 5 wells (MLNW-1; MLNW-2; MLNW-5; MLN-5; MLSE-5) the overall sedimentary interpretations and sedimentary logs are presented, including those provided by ConocoPhillips, with the sample locations marked. Then per well each sample is presented with a short description accompanying a 1mm scale SEM image and a thin section example. More detailed thin section images, SEM images and the full SEM spectral analysis per sample is on the accompanying data CD, due to space constraints.

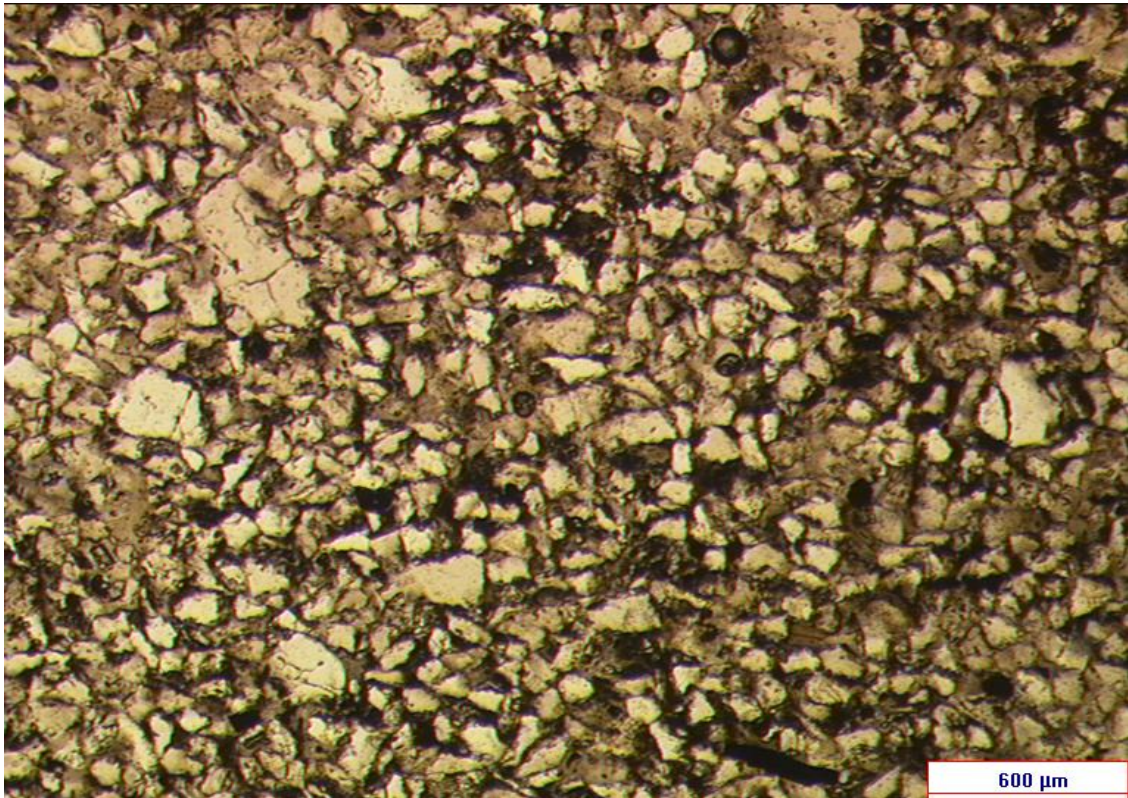
<i>Sample</i>	<i>ConocoPhillips Environment</i>	<i>Interpreted Facies</i>
<i>MLNW-1: 3481.35</i>	Tidal Inlet	viii
<i>MLNW-5: 3514.54</i>	Lower Shoreface	iii
<i>MLNW-2: 3460.60</i>		?
<i>MLNW-2: 3468.20</i>		?
<i>MLN-5: 3522.20</i>	Upper Shoreface	viii
<i>MLNW-1: 3577.75</i>		viii
<i>MLNW-1: 3479.30</i>		viii
<i>MLNW-2: 3459.60</i>		?
<i>MLNW-2: 3462.50</i>		?
<i>MLNW-2: 3463.45</i>		?
<i>MLNW-2: 3464.45</i>		?
<i>MLNW-2: 3469.70</i>		?
<i>MLNW-5: 3509.15</i>		viii
<i>MLNW-5: 3510.10</i>		viii
<i>MLNW-5: 3511.15</i>		viii
<i>MLWN-5: 3513.0</i>	viii	
<i>MLSE-5: 3329.0</i>	Unknown	viii
<i>MLSE-5: 3330.5</i>		viii
<i>MLSE-5: 3339.5</i>		viii
<i>MLSE-5: 3341.5</i>		viii
<i>MLSE-5: 3341.8</i>		viii

Table IIa: Sample used in the study and the interpreted sedimentary facies, as well as the ConocoPhillips defined depositional environment

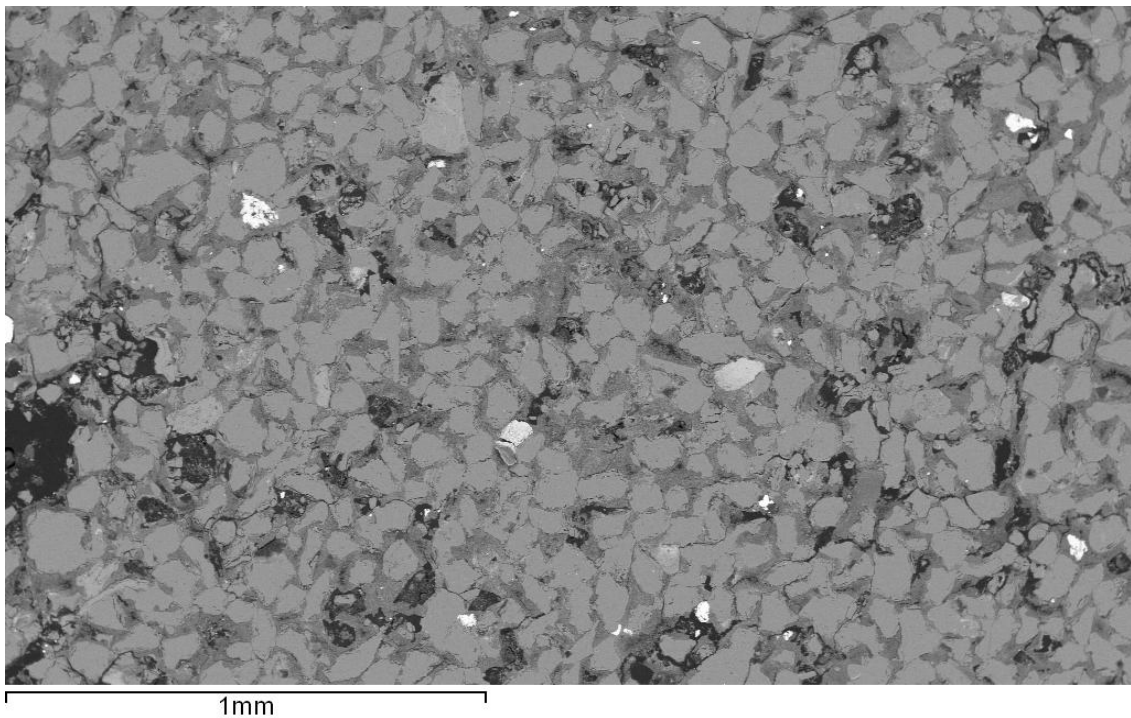
MLNW-1

ConocoPhillips Interpretation				This Study Interpretation (Core Photograph-based)			
Depth	Grain Size	Lithology	Interpretation	Facies	Core Photograph	Descriptions	Samples
3474			Offshore	3474		Claystone: dark grey, hard, sub-fissile to fissile, siltstone, micaeous	
3475			Major Tidal Inlet	3475		Sandstone: light to medium grey, fine - medium grained, poorly - moderately sorted, sub-angular - sub-rounded, slightly argillaceous, chloritic, micaeous, poor intergranular porosity	
3476			Upper Shoreface	3476		Sandstone: light grey, fine-grained, moderately to well-sorted, sub-angular to sub-rounded, argillaceous, micaeous, chloritic, poor - moderate intergranular porosity	
3477			Upper Shoreface	3477		Sandstone: medium brown, fine - medium grained, moderately sorted, sub-rounded, friable, good - very good intergranular porosity	MLNW-1: 3477.75m
3478			Tidal? Channel or Upper Shoreface	3478		Sandstone: light grey, very fine - fine grained, moderately sorted, sub-rounded to sub-angular, argillaceous, micaeous, poor intergranular porosity	
3479			Minor Tidal Inlet	3479		Sandstone: light grey, very fine - fine grained, moderately sorted, sub-rounded to sub-angular, argillaceous, micaeous, poor intergranular porosity	MLNW-1: 3479.30m
3480			Minor Tidal Inlet	3480		Sandstone: medium grey, fine-medium grained, moderately sorted, sub-rounded to sub-angular, very friable, argillaceous, micaeous, pyritic, poor - moderate intergranular porosity with fine laminae of dark grey, pyritic, micaeous claystone	
3481			Minor Tidal Inlet	3481		Sandstone: medium grey, fine-medium grained, moderately sorted, sub-rounded to sub-angular, very friable, argillaceous, micaeous, pyritic, poor - moderate intergranular porosity with fine laminae of dark grey, pyritic, micaeous claystone	MLNW-1: 3481.35m
3482			Shallow Channel or Spit Bar	3482		Claystone: dark grey, hard, sub-fissile, micaeous, sandy in part	
3483			Upper Shoreface	3483		Sandstone: light grey, very fine - fine grained, sub-angular - sub-rounded, well-cemented, quartz overgrowths, micaeous, chloritic, no visible porosity	
3484			Lower Shoreface	3484		Sandstone: medium brown, fine - medium grained, moderately sorted, sub-rounded, friable, good - very good intergranular porosity	
3485			Upper Shoreface	3485		Sandstone: medium brown, fine - medium grained, moderately sorted, sub-rounded, friable, good - very good intergranular porosity	
3486			Upper Shoreface	3486		Sandstone: light grey, very fine - fine grained, moderately sorted, argillaceous, sub-angular - sub-rounded, micaeous, moderate intergranular porosity	
3487			Upper Shoreface	3487		Sandstone: light grey, very fine - fine grained, moderately sorted, argillaceous, sub-angular - sub-rounded, micaeous, moderate intergranular porosity	
3488			Upper Shoreface	3488		Sandstone: light grey to grey brown, fine-grained, moderately sorted, sub-rounded to sub-angular, very friable, very fine argillaceous laminae, moderate - good intergranular porosity	
3489			Minor Tidal Inlet (shallow channel)	3489		Sandstone: light grey, very fine - fine-grained, moderately sorted, sub-angular - sub-rounded, argillaceous, no visible porosity, interbedded with	
3490			Lower Shoreface	3490		Claystone: dark grey, hard, sub-fissile, micaeous, sandy in part	
3491			Minor Tidal Inlet	3491		Sandstone: light grey, fine-grained, moderately sorted, sub-angular to sub-rounded, argillaceous grain coating, chloritic, micaeous, moderate intergranular porosity	
3492			Minor Tidal Inlet	3492		Sandstone: light grey, very fine - fine-grained, sub-angular - sub-rounded, very hard, well-cemented, quartz overgrowths, micaeous, chloritic, no visible porosity	
3493			Middle Shoreface (tempestite)	3493		Sandstone: dark grey, fine-grained, sub-angular to sub-rounded, moderately sorted, argillaceous, poor to no visible porosity	
3494			Minor Tidal Inlet	3494		Claystone: dark grey, hard, sub-fissile, micaeous, silty in part	
3495			Minor Tidal Inlet	3495		Claystone: dark grey, hard, sub-fissile, micaeous, silty in part	

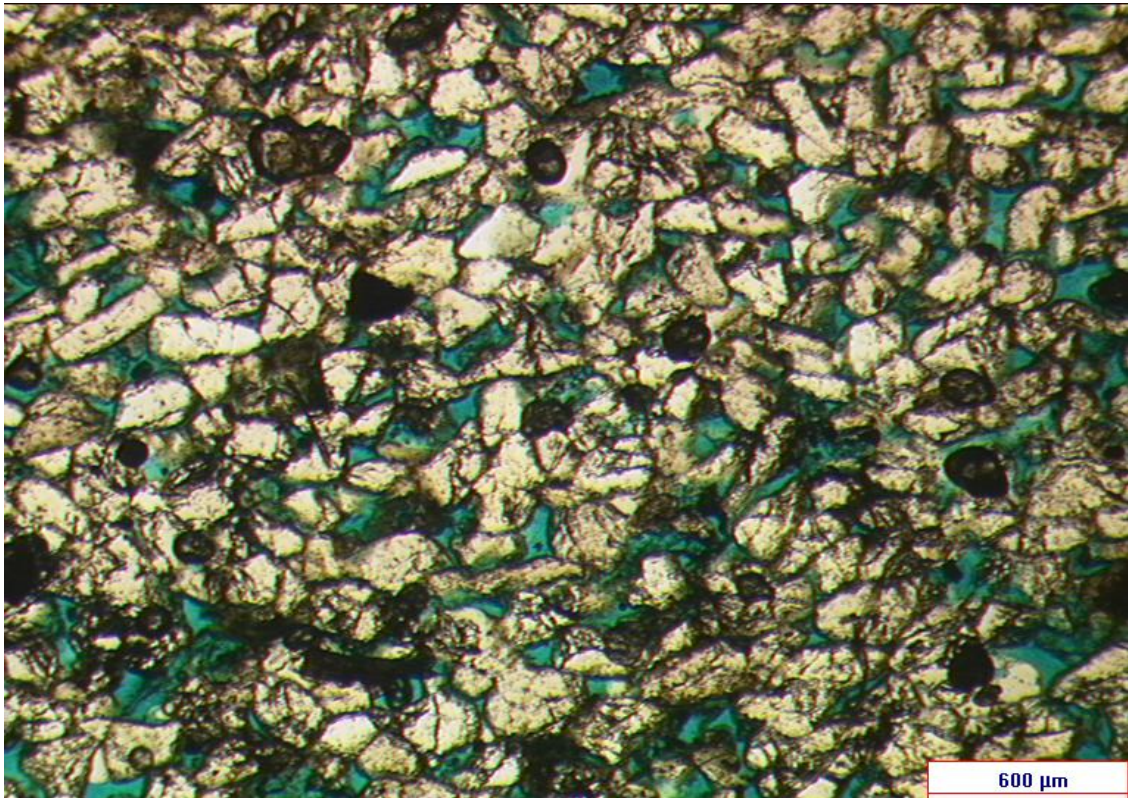
MLNW-1: 3477.75m



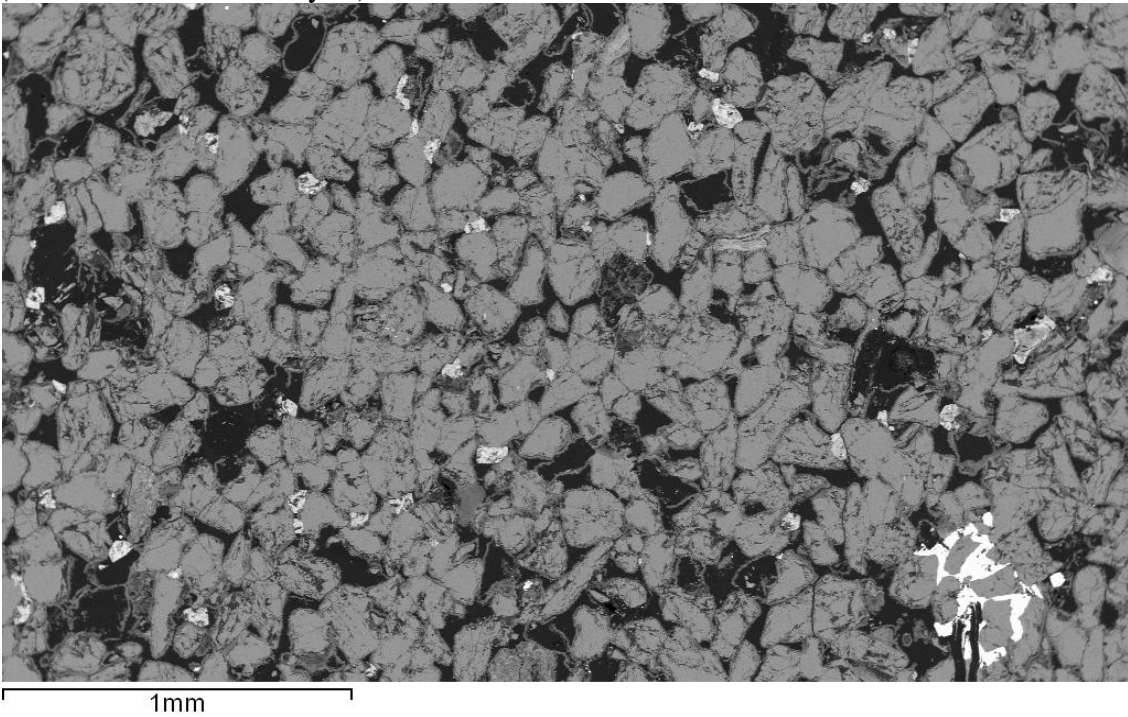
Quartz-rich, fine grained sandstone sample, little-to-no visible porosity, sub-angular to sub-rounded grains, poorly sorted. Sample is well-cemented, with clay grains, both grain-coating and pore-filling clays, (confirmed in SEM analysis) with minor occurrences of individual well-rounded clay grains, and some mica and feldspar grains.



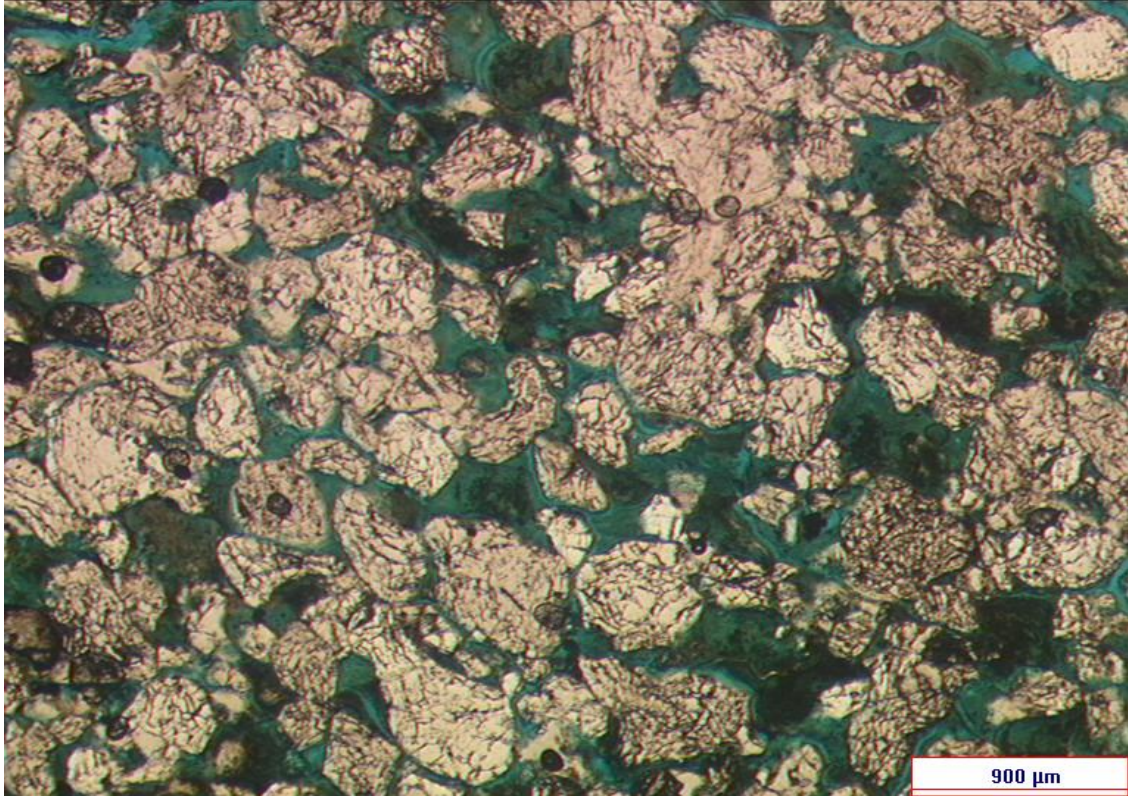
MLNW-1: 3479.30m



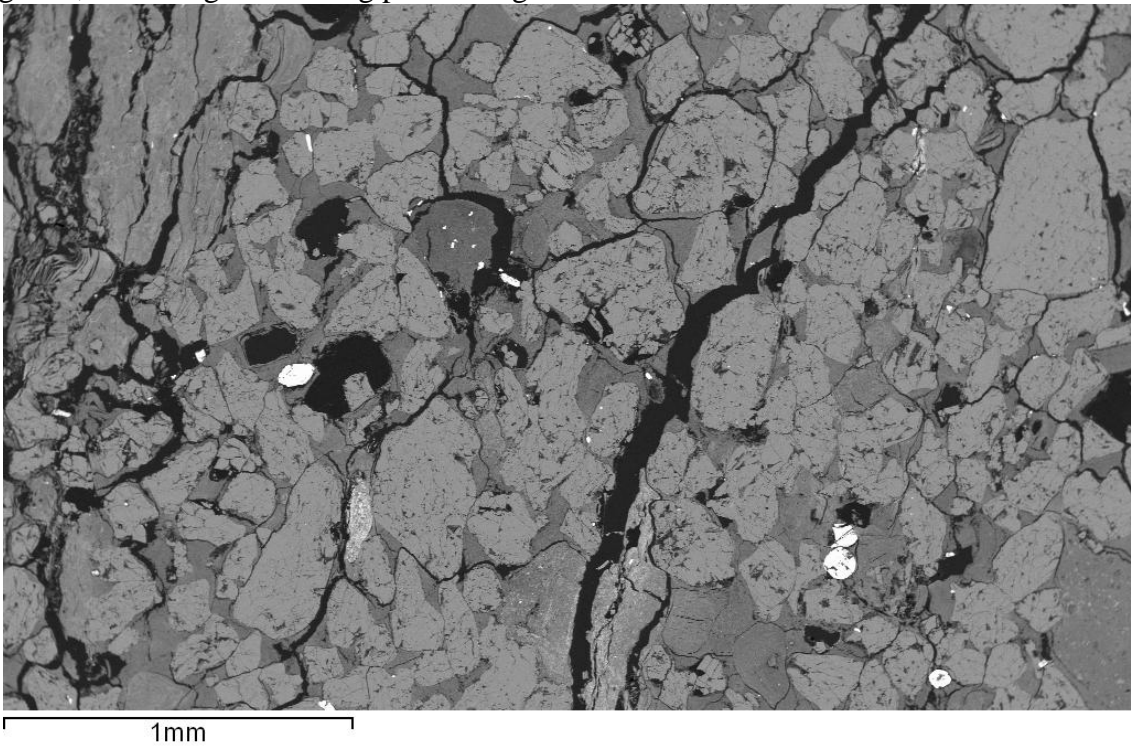
Quartz rich medium – fine-grained sandstone sample, with moderate to high porosity (visible pore-space), is moderately well-sorted, with sub-angular to sub-rounded grains. The sample is poorly cemented by clay-cement; pale pink in colour and grain-coating (confirmed in SEM analysis)



MLNW-1: 3481.35m



Quartz-rich, moderately coarse-grained sandstone sample, with moderate visible pore-space, rounded – sub-rounded grains and abundant clays, both individual well-rounded grains, and as a grain-coating pore-filling cement

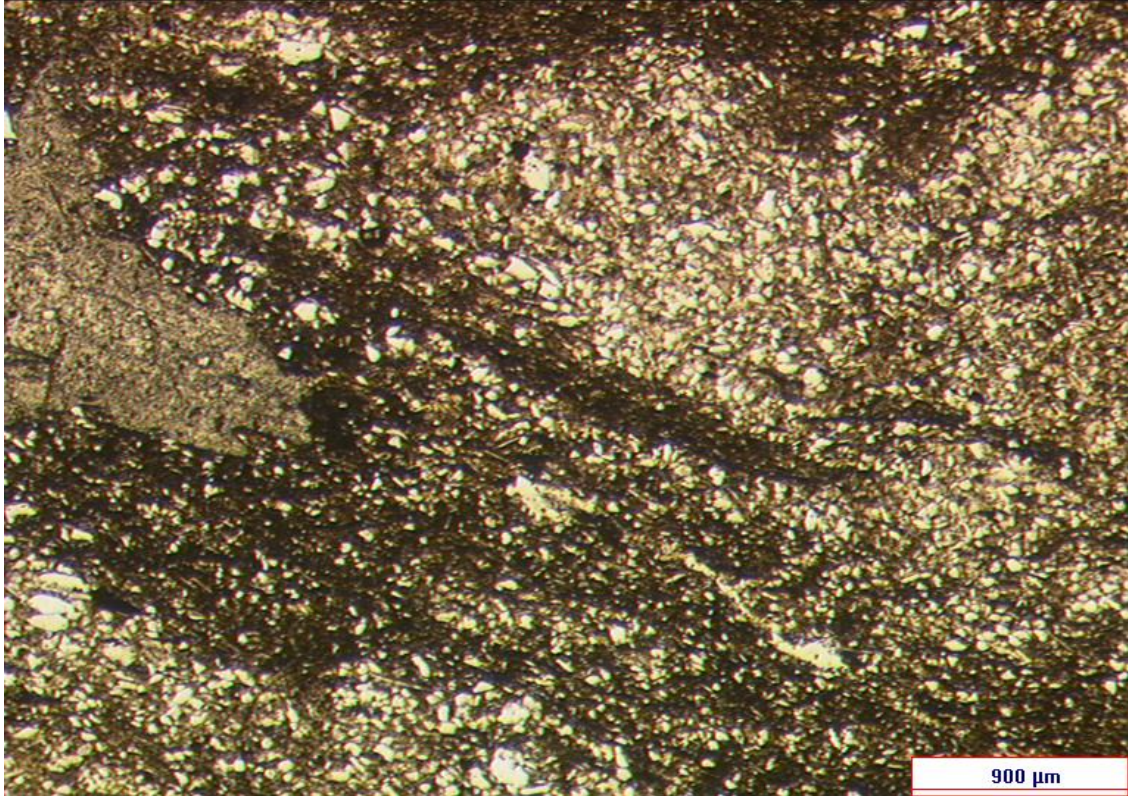


MLNW-2

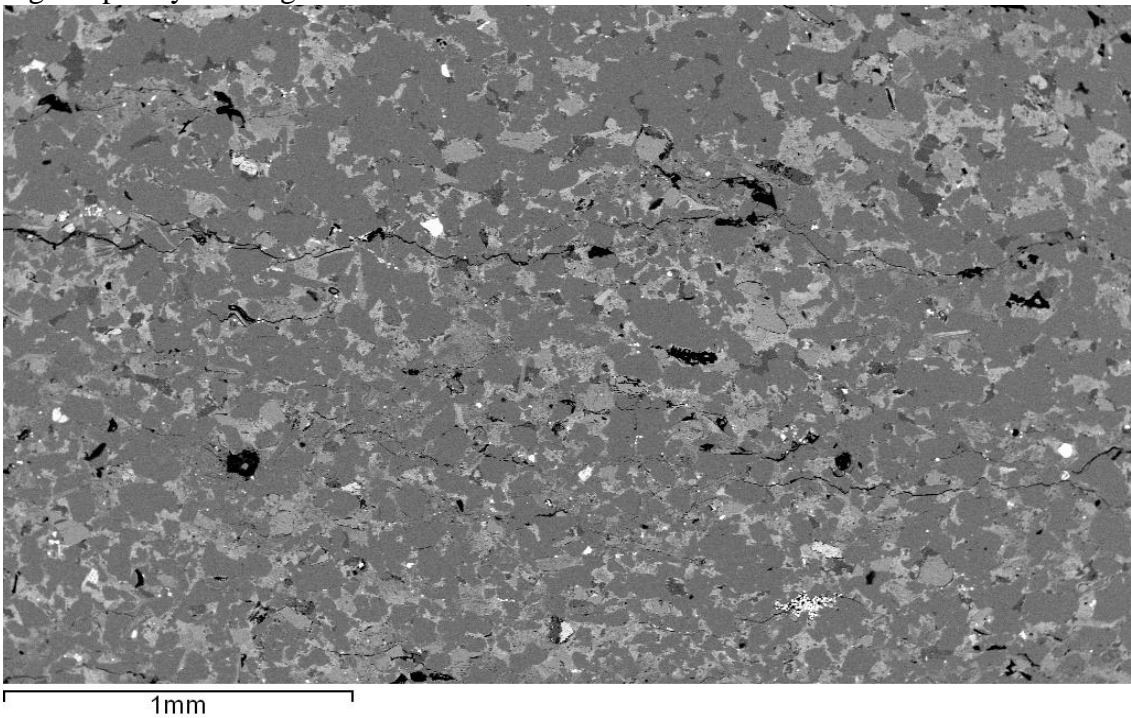
ConocoPhillips Interpretation				This Study Interpretation (Core Photograph-based)		
Depth	Grain Size	Lithology	Interpretation	Facies	Descriptions	Samples
3455			Lower Shoreface		Claystone: dark grey, hard, sub-fsille, finely micaceous	
3456			Offshore		Claystone: dark grey, hard, sub-fsille, silty, richly micaceous with fine flasers and interbeds of sandstone; off white, very fine grained, micaceous, well-cemented, no visible porosity	MLNW-2: 3457.05m
3457			Lower Shoreface		Claystone: dark grey, hard, sub-fsille, finely micaceous	
3458			Offshore		Claystone: dark grey, hard, sub-fsille, finely micaceous	
3459			Upper Shoreface		Claystone: dark grey, hard, sub-fsille, finely micaceous	MLNW-2: 3458.60m
3460			Lower Shoreface		Sandstone: medium grey, grey brown, fine grained, sub-rounded, moderately sorted, soft & friable, micaceous, slightly argillaceous, poor intergranular porosity	MLNW-2: 3459.60m
3461			Succession of tidal inlets or fluvial (?) channels		Sandstone: medium grey, grey-brown, fine grained, sub-rounded, hard, well-cemented, siliceous with quartz overgrowths, very micaceous, poor intergranular porosity	MLNW-2: 3460.60m
3462			Lower Shoreface		Sandstone: medium grey, grey-brown, fine-grained, sub-rounded, rounded, locally siliceous, hard, micaceous, loosely cemented, poor - moderate intergranular porosity	MLNW-2: 3462.50m
3463			Upper Shoreface		Sandstone: medium grey brown, fine - medium grained, rounded, thin grain coating, poor - moderate intergranular porosity	MLNW-2: 3463.45m
3464			Upper Shoreface		Sandstone: medium grey brown, fine - medium grained, rounded, soft, friable, loosely cemented, moderate-good intergranular porosity	
3465			Upper Shoreface		Sandstone: medium grey brown, fine - medium grained, rounded, soft, friable, loosely cemented, moderate-good intergranular porosity	
3466			Lower Shoreface		Claystone: dark grey, hard, sub-fsille, silty, richly micaceous	MLNW-2: 3466.25m
3467			Lower Shoreface		Claystone: dark grey, hard, sub-fsille, silty, richly micaceous	
3468			Lower Shoreface		Sandstone: off white - light grey, fine to very fine grained, hard, well-cemented, siliceous, no visible porosity	MLNW-2: 3468.20m
3469			Upper Shoreface		Sandstone: medium grey brown, fine - very fine grained, well-sorted, rounded, soft, friable, poorly cemented, moderate intergranular porosity	MLNW-2: 3469.70m
3470			Upper Shoreface		Sandstone: medium grey brown, fine - very fine grained, well-sorted, rounded, soft, friable, poorly cemented, moderate intergranular porosity	
3471			Upper Shoreface		Sandstone: medium grey brown, fine - very fine grained, well-sorted, rounded, soft, friable, poorly cemented, moderate intergranular porosity	
3472			Lower Shoreface		Claystone: dark grey, hard, sub-fsille, richly micaceous	
3473			Lower Shoreface		Claystone: dark grey, hard, sub-fsille, richly micaceous	MLNW-2: 3472.70m
3474			Lower Shoreface		Claystone: dark grey, hard, sub-fsille, richly micaceous	MLNW-2: 3473.45m
3475			Lower Shoreface		Claystone: dark grey, hard, sub-fsille, silty & sandy, richly micaceous	
3476			Lower Shoreface		Claystone: dark grey, hard, sub-fsille, silty, richly micaceous	
3477			Lower Shoreface		Claystone: dark grey, hard, sub-fsille, silty, richly micaceous	
3478			Offshore		Claystone: dark grey, hard, sub-fsille, silty, richly micaceous	
3479			Offshore		Claystone: dark grey, hard, sub-fsille, silty, richly micaceous	
3480			Offshore		Claystone: dark grey, hard, sub-fsille, silty, richly micaceous	
3481			Offshore		Claystone: dark grey, hard, sub-fsille, silty, richly micaceous	
3482			Lower Shoreface		Claystone: dark grey, hard, sub-fsille, silty, very micaceous, with very fine sandy partings	
3483			Lower Shoreface		Claystone: dark grey, hard, sub-fsille, silty, very micaceous, with micro flasers and partings	
3484			Lower Shoreface		Claystone: dark grey, hard, sub-fsille, silty, very micaceous	
3485			Lower Shoreface		Claystone: dark grey, hard, sub-fsille, silty, very micaceous, carbonaceous	
3486			Lower Shoreface		Claystone: dark grey, hard, sub-fsille, silty, richly micaceous	
3487			Lower Shoreface		Claystone: dark grey, hard, sub-fsille, silty, richly micaceous, very fine flasers and laminae	
3488			Lower Shoreface		Sandstone: light grey, very fine - fine grained, hard, well-cemented, siliceous, micaceous, no visible porosity	
3489			Lower Shoreface		Claystone: dark grey, hard, sub-fsille to sub-blocky, silty, very sandy, micaceous	
3490			Lower Shoreface		Sandstone: medium grey, very fine-grained, well-cemented, siliceous, well-sorted, finely micaceous, trace chlorite, poor intergranular porosity	
3491			Lower Shoreface		Claystone: dark grey, hard, sub-fsille, silty, very sandy, micaceous	
3492			Lower Shoreface		Claystone: dark grey, hard, sub-fsille, silty, very sandy, micaceous	
3493			Lower Shoreface		Sandstone: medium grey, fine-grained, hard, well-cemented, siliceous, common chlorite, occasional fine pyrite nodules, poor - no visible porosity	
3494			Lower Shoreface		Sandstone: light grey, very fine-grained, well-cemented, chloritic, micaceous, no visible porosity, very finely banded & bedded with claystone; dark grey, hard, silty, micaceous	
3495			Lower Shoreface		Sandstone: light - medium grey, finely banded, very fine - fine grained, micaceous, finely pyritic, very poor - no visible porosity	
3496			Middle Shoreface		Sandstone: light - medium grey, finely banded, very fine - fine grained, micaceous, finely pyritic, very poor - no visible porosity	
3497			Middle Shoreface		Sandstone: medium grey brown, oil stained, fine-grained, moderately-well cemented, quartz overgrowths, very poor intergranular porosity	
3498			Middle Shoreface		Claystone: dark grey, hard, very sandy & silty, micaceous	
3499			Middle Shoreface		Claystone: dark grey, hard, very sandy & silty, micaceous, grading to argillaceous sandstone	
3500			Middle Shoreface		Sandstone: dark grey, fine - very fine grained, very argillaceous, micaceous, no visible porosity, with microstructure field with quartz & pyrite crystals	
3501			Middle Shoreface		Claystone: dark grey, hard, very sandy & silty, micaceous, grading to argillaceous sandstone	
3502			Upper Shoreface		Sandstone: medium grey-brown, oil-stained, fine-grained, moderately - well cemented, quartz overgrowths, very poor intergranular porosity	
3503			Lower Shoreface		Claystone: dark grey, hard, sub-fsille, silty, richly micaceous with very fine flasers and laminae	
3504			Lower Shoreface		Sandstone: light grey, fine - very fine grained, siliceous, well-cemented, finely pyritic, no visible porosity	
3505			Lower Shoreface		Claystone: dark grey, hard, sub-fsille, silty, finely micaceous, with very fine sandy partings	
3506			Rip Channel?		Sandstone: medium grey, grey-green, fine-coarse grained, rounded - sub-rounded, poorly sorted, patchy argillaceous matrix, well-cemented, chloritic, no visible porosity, with	
3507			Lower Shoreface		Sandstone: dark grey brown, medium grained, occasionally coarse, rounded to sub-rounded, soft & friable, poorly sorted, good intergranular porosity	
3508			Lower Shoreface			

Not Applicable:
No core
photographs
available

MLNW-2: 3457.05m



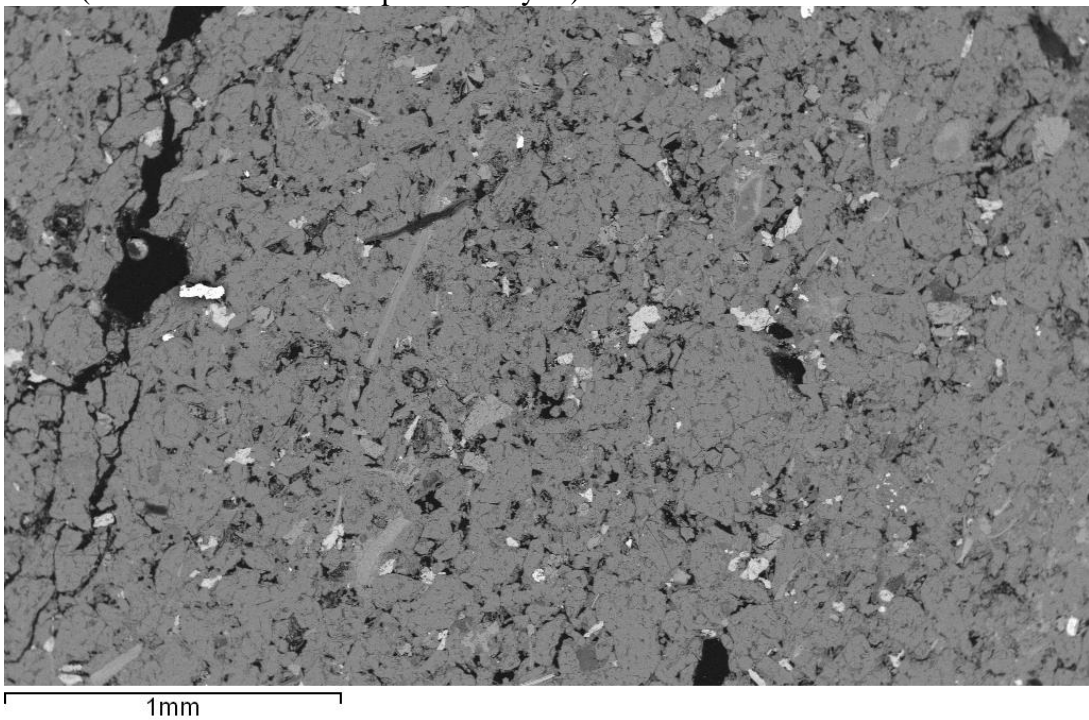
Finely-banded mudstone sample, exhibiting a mixture of fine and coarser bands and patches, dark brown matrix is dominant and dominated by clays and mica grains, the visible quartz grains are more abundant in the coarser horizons, with angular to sub-angular poorly sorted grains.



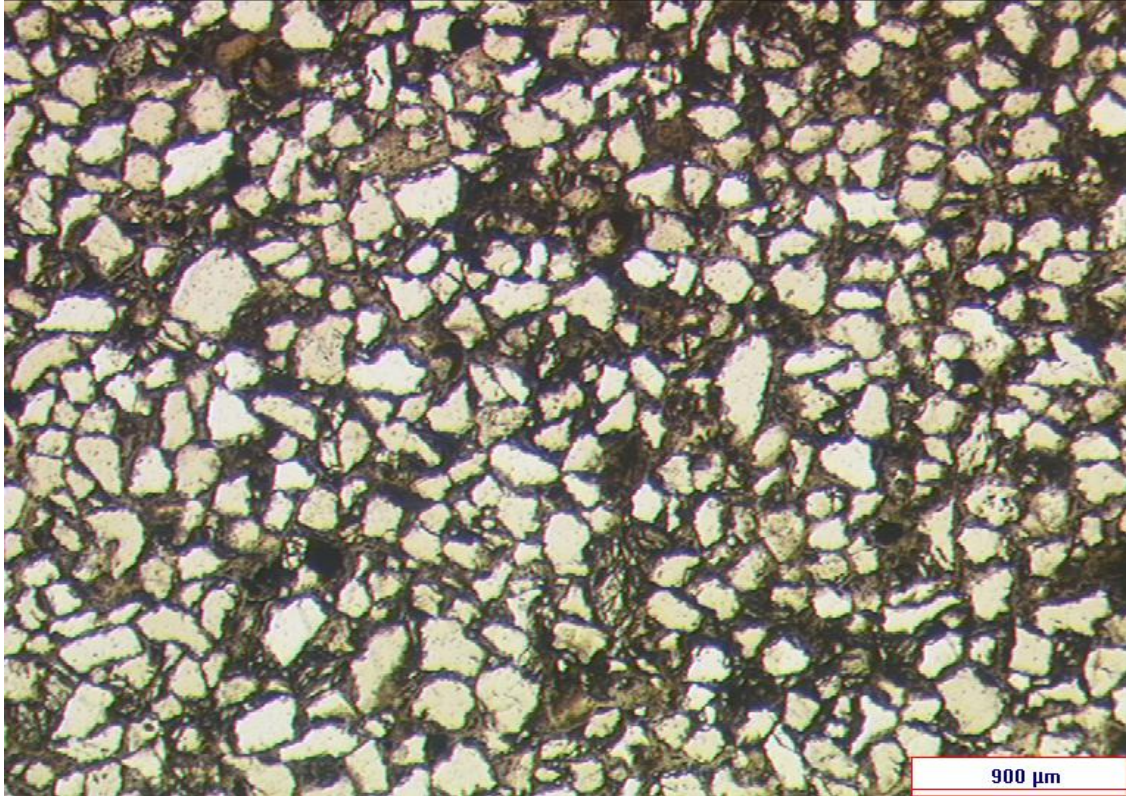
MLNW-2: 3459.60m



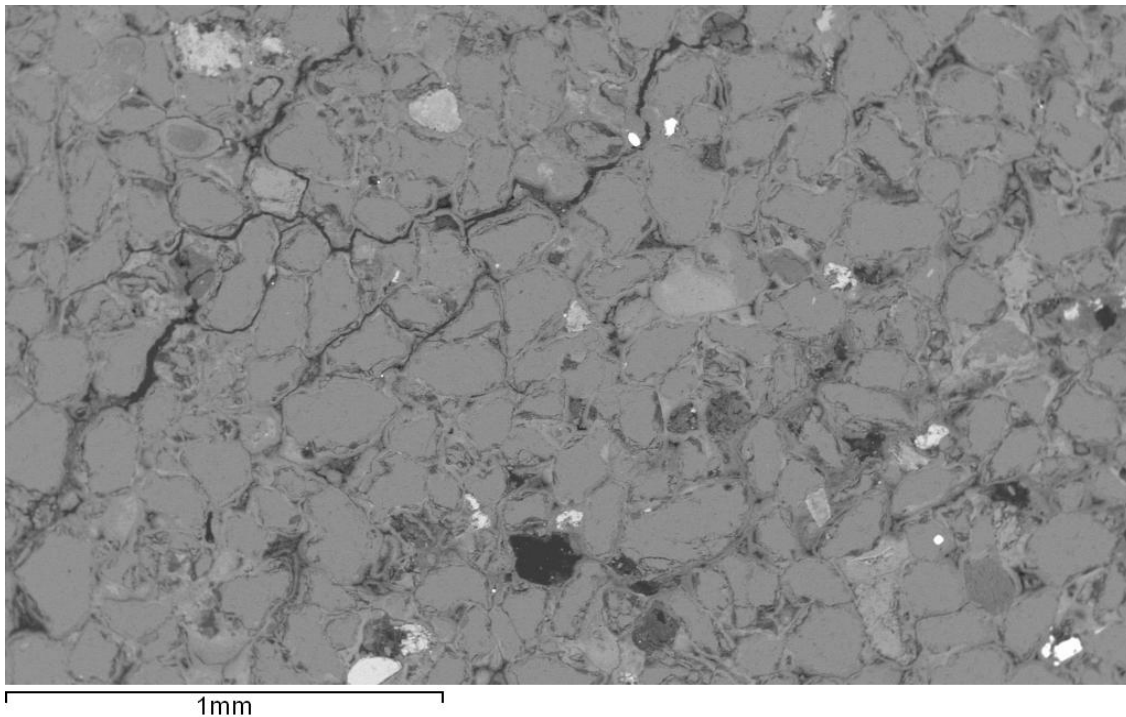
A very fine-grained, well-cemented sandstone sample, dominated by quartz grains and quartz overgrowths, the sample also exhibits some grain-coating clays (visible on the SEM image), with some mica and feldspar grains, and occasional patches of siderite cement (confirmed with SEM spectra analysis).



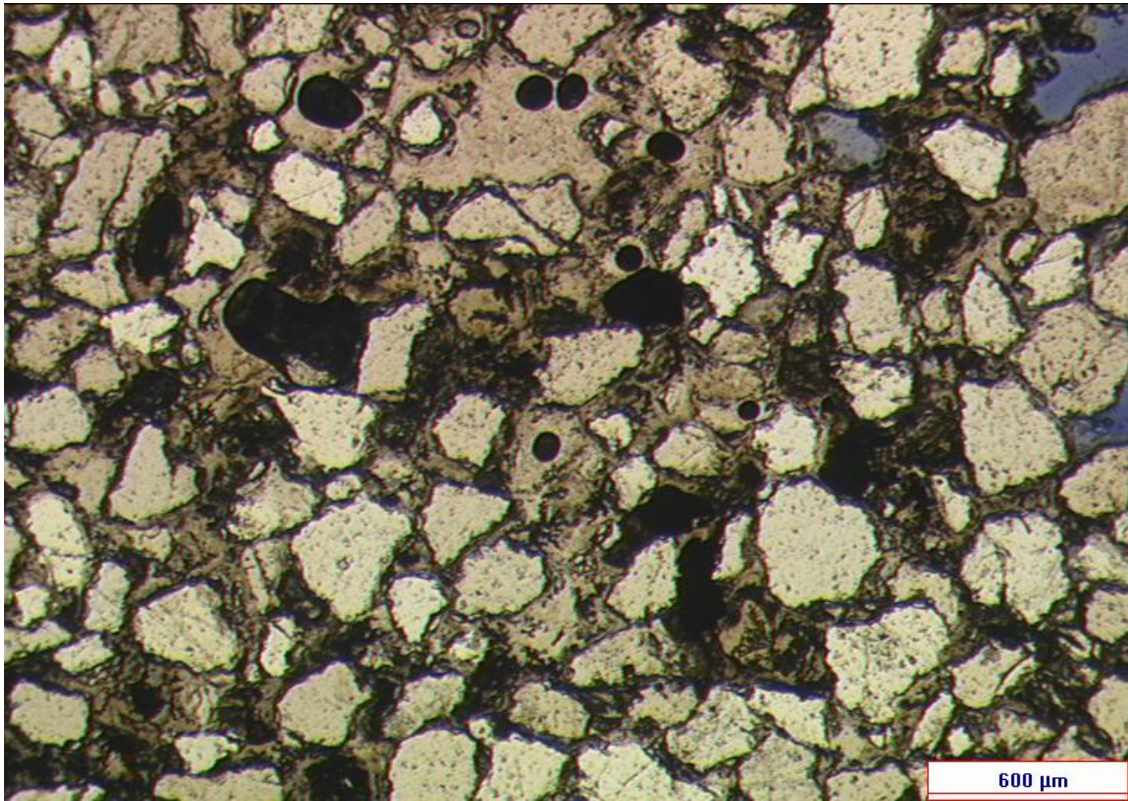
MLNW-2: 3460.60m



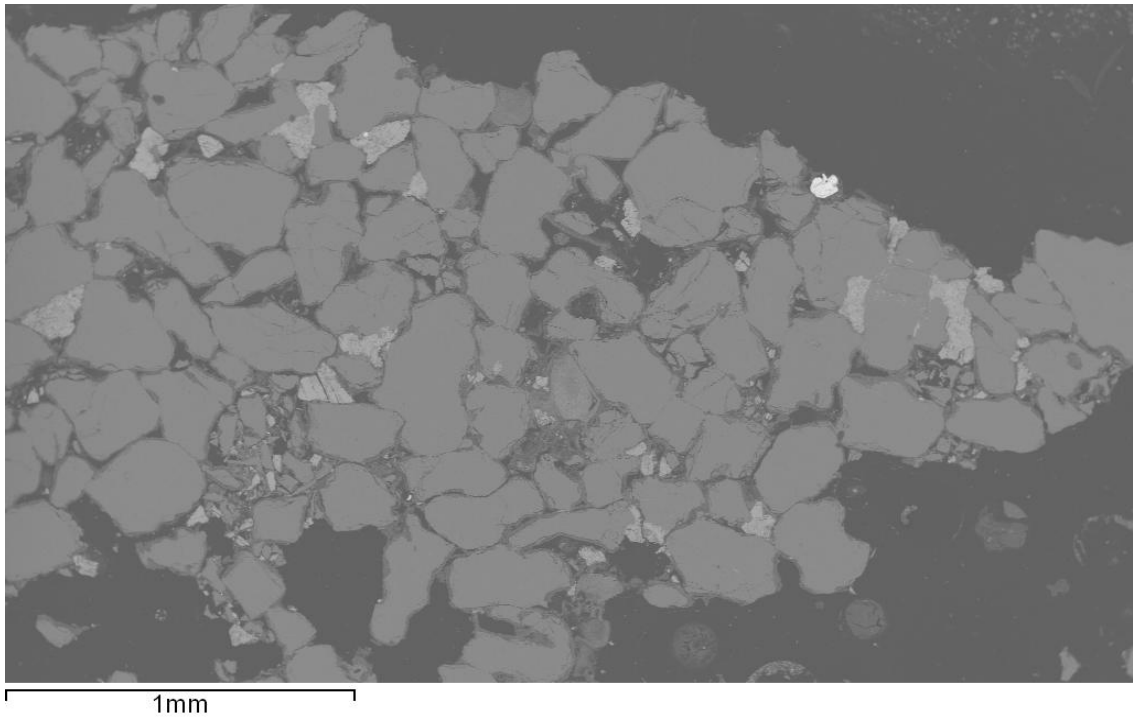
Quartz-rich fine-grained sandstone sample with sub-angular, moderately well-sorted grains, and little-to-no visible porosity. The sample is well cemented with clay coatings around the grains, clearly visible on the SEM image, and pore-filling clays as well as individual clay grains.



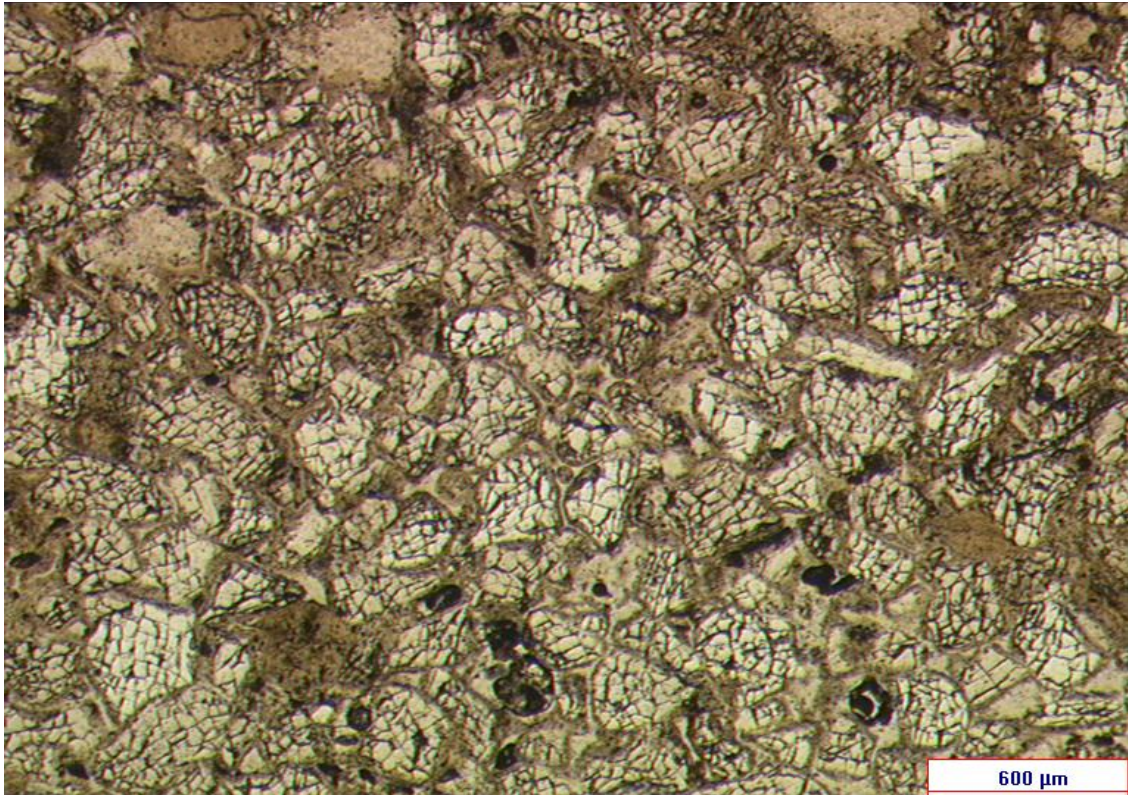
MLNW-2: 3462.50m



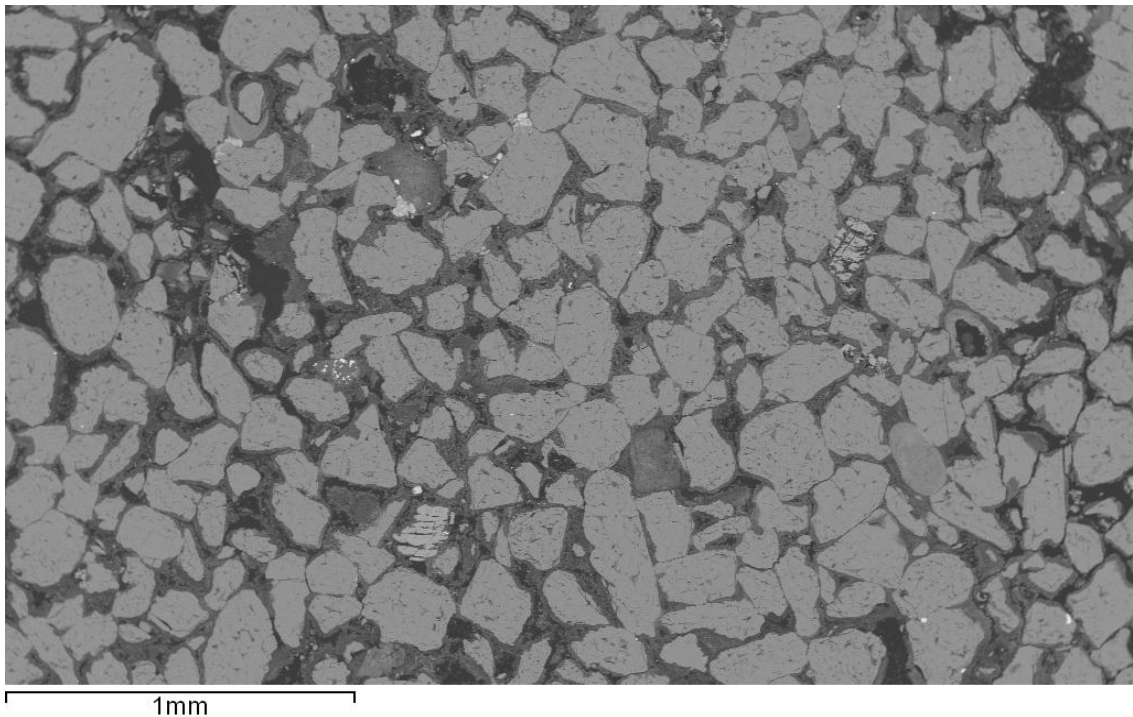
Quartz-rich, medium – fine-grained sandstone sample, with some visible porosity, poorly sorted, with sub-angular to sub-rounded quartz grains. The sample exhibits both grain-coating clays, and siderite cement, which appears dark brown in thin section and is pale in SEM, (see SEM spectra data on accompanying CD)



MLNW-2: 3463.45m



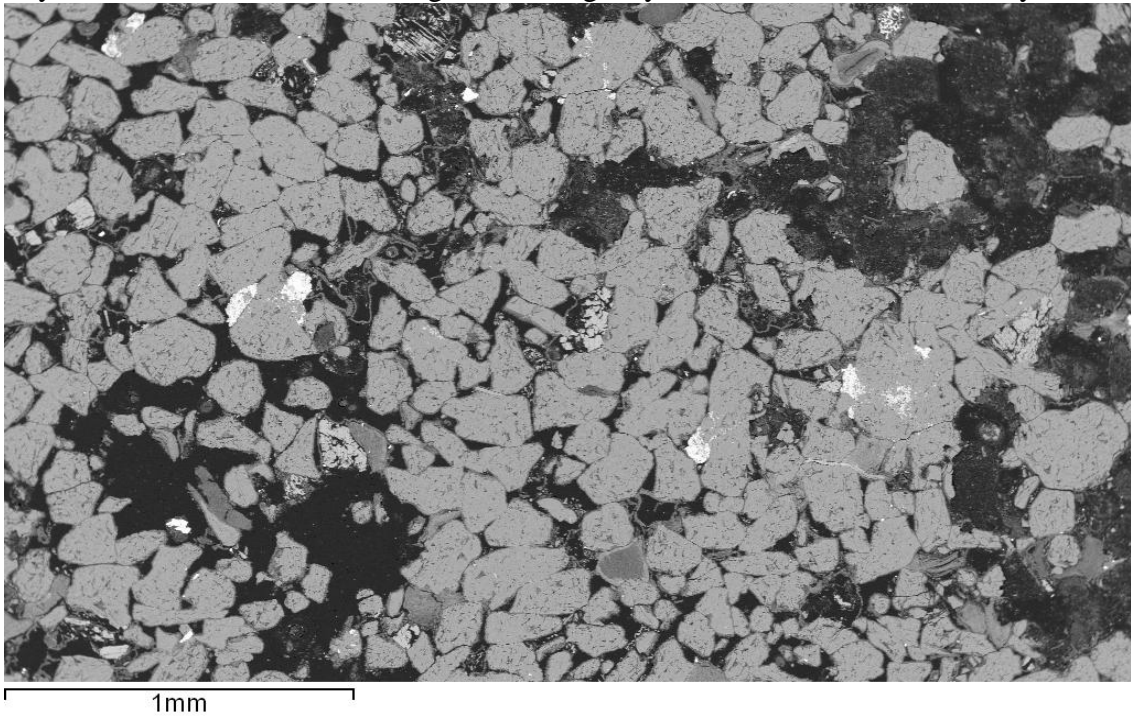
Medium – coarse grained sandstone sample, quartz grains exhibit fracturing (possibly an effect of polishing), grains are moderately well-rounded, with visible porosity and abundant clay coatings. Individual clay grains are common, and the pore-space is often occluded by the clay grain coatings, most visible on the SEM image.



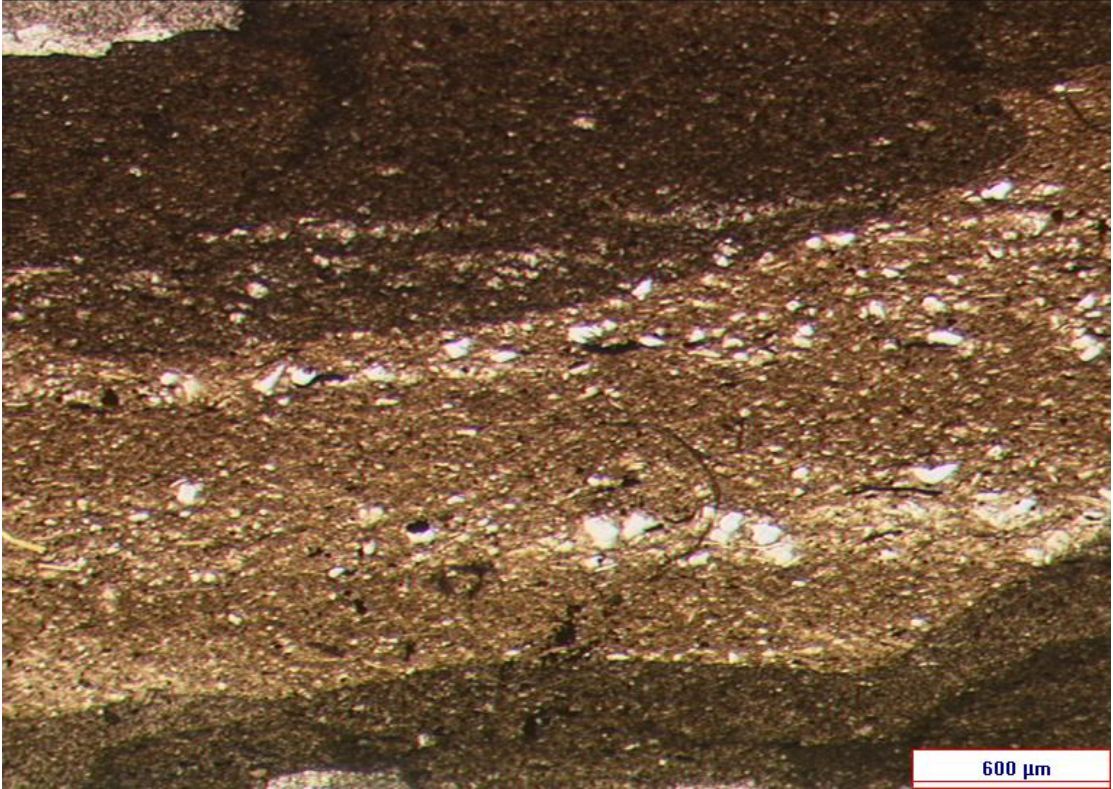
MLNW-2: 3464.45m



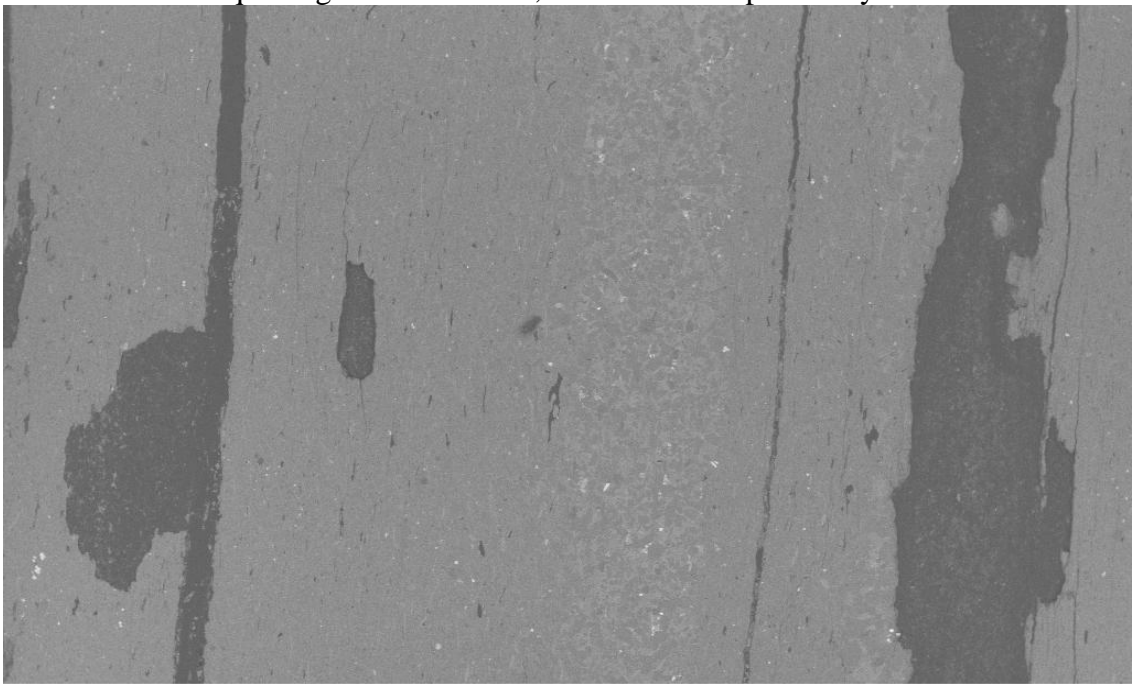
Quartz-rich, medium – fine-grained sandstone sample, highly fractured quartz grains (potentially an effect of polishing), rounded to sub-round grains, little visible porosity in thin section, more obvious in SEM image. Pale brown-pink clay grains, some patchy clay-rich cement, and occasional grain-coating clays, observed in the SEM analysis.



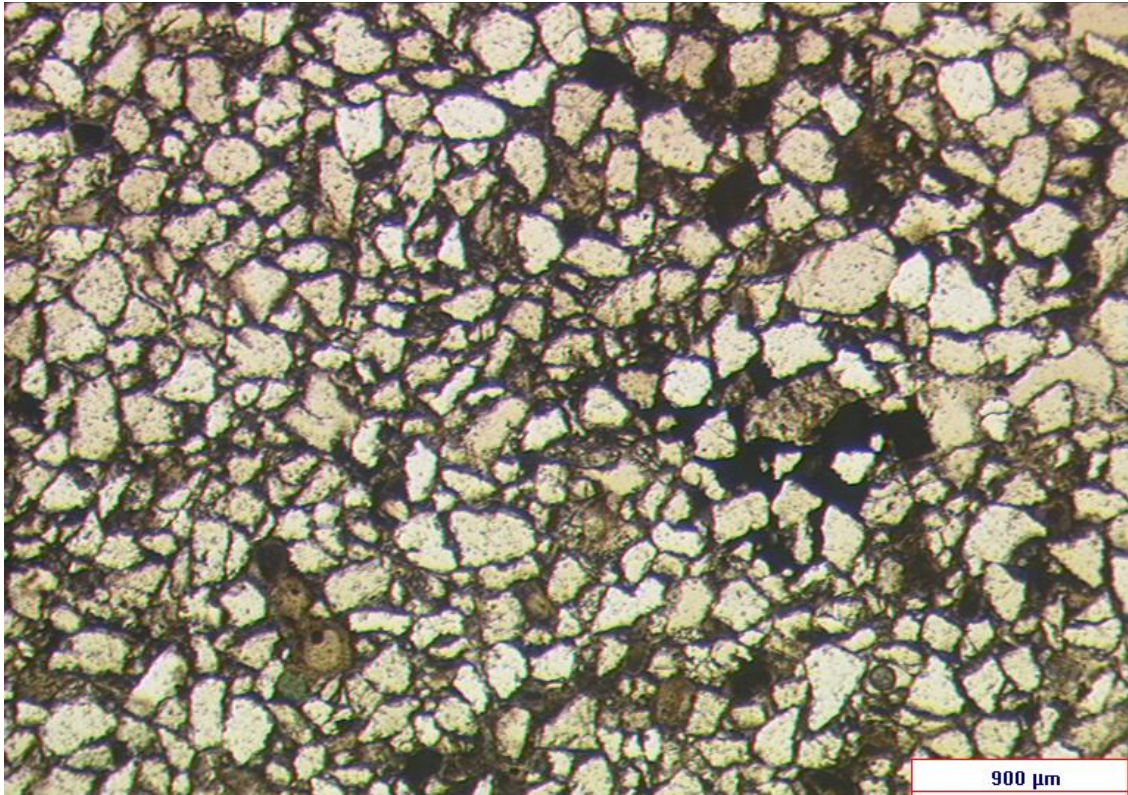
MLNW-2: 3466.25m



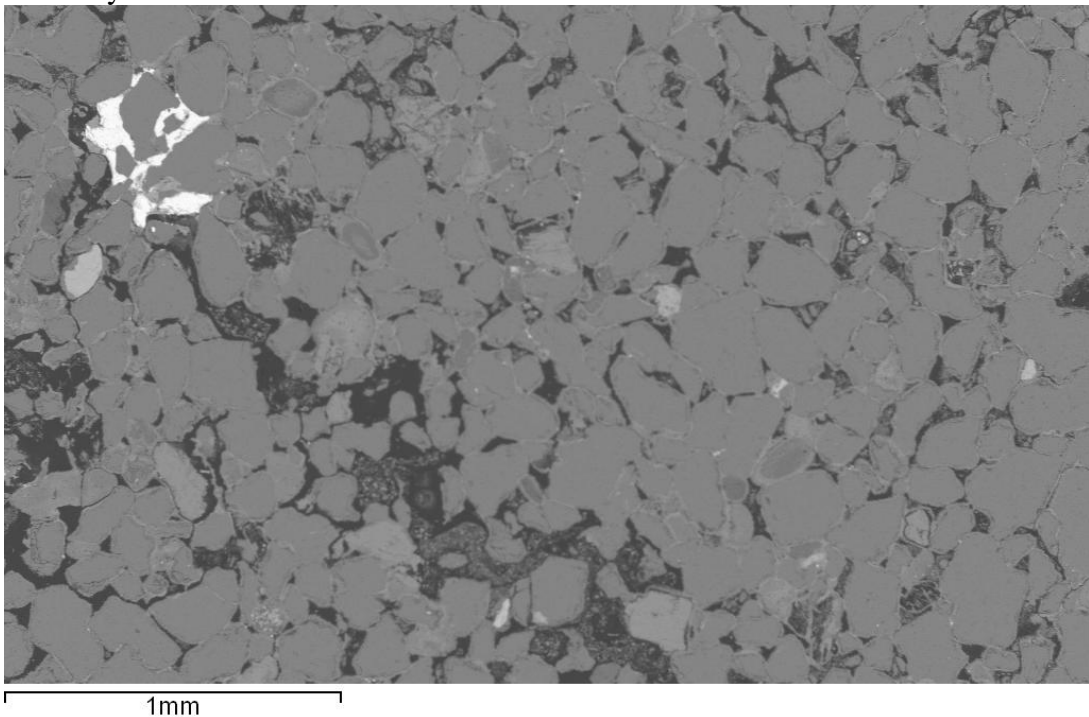
Extremely fine-grained mudstone sample, with occasional bands of coarser material where occasional quartz grains are visible, overall the sample is clay and mica rich.



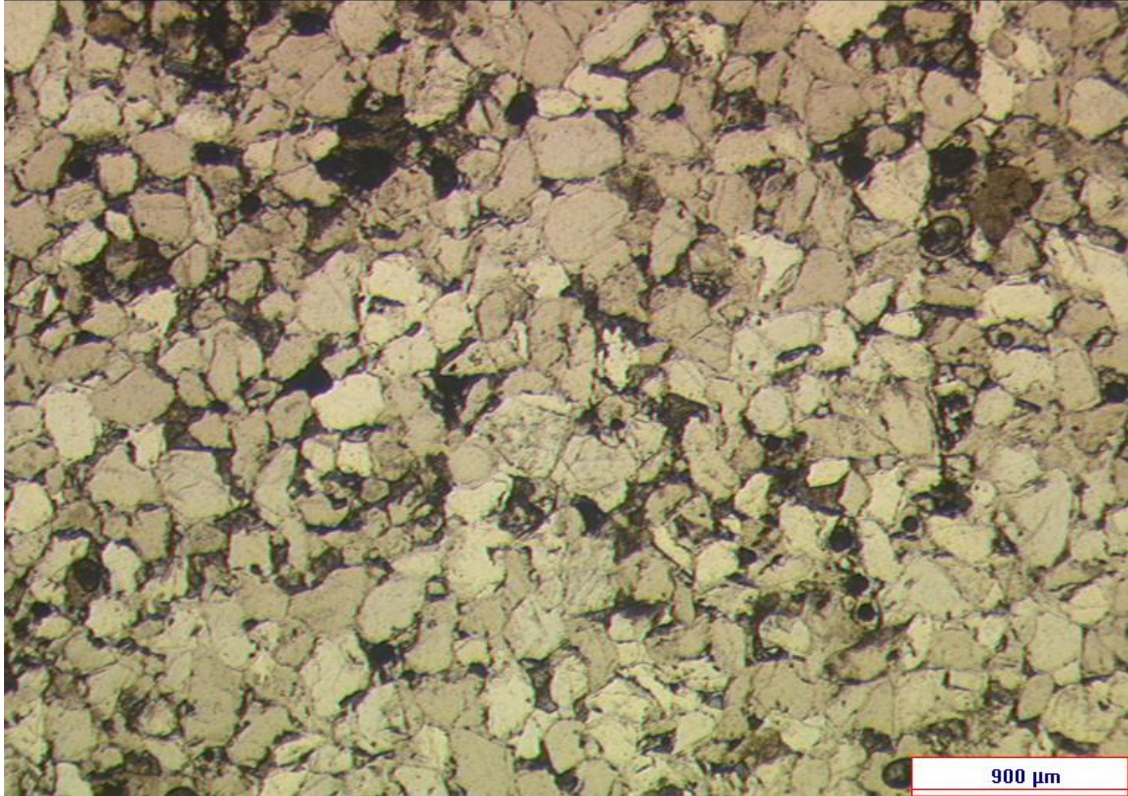
MLNW-2: 3468.20m



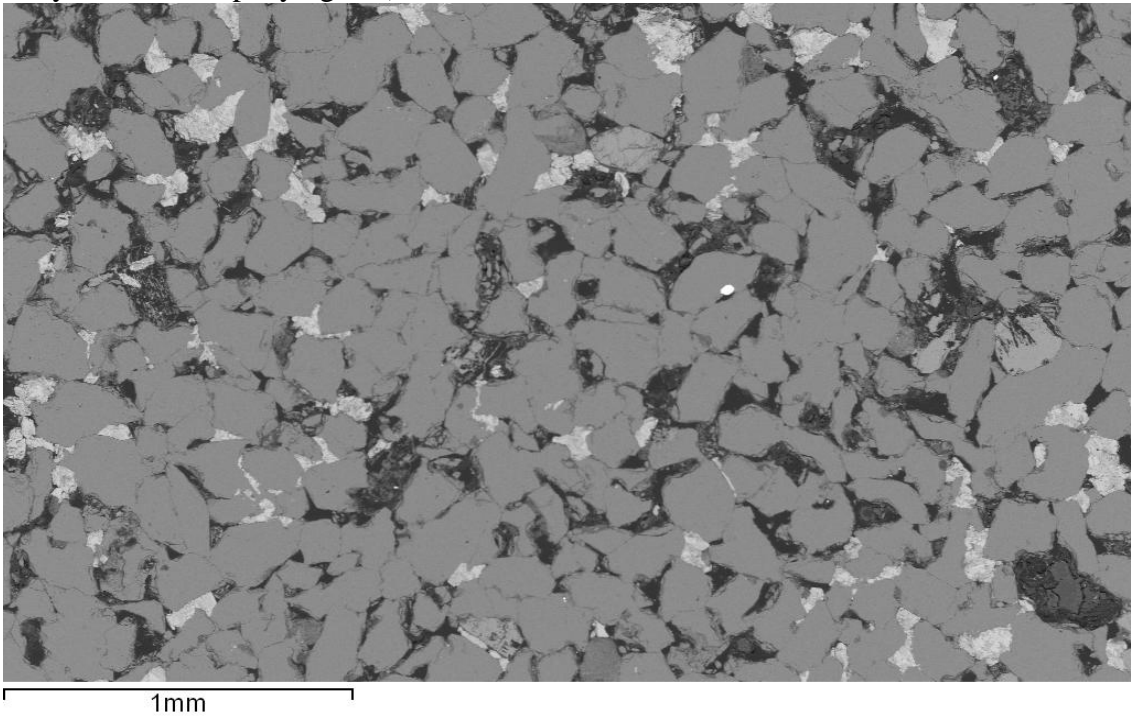
Medium- fine grained sandstone sample, poorly sorted, with sub-rounded grains, quartz-rich with individual well-rounded, clay grains, and little-to-no visible porosity. Cement dominantly composed of clay, with some siderite in patches (more noticeable on the SEM image). Some grain-coating clay and some quartz overgrowths are visible in the SEM analysis.



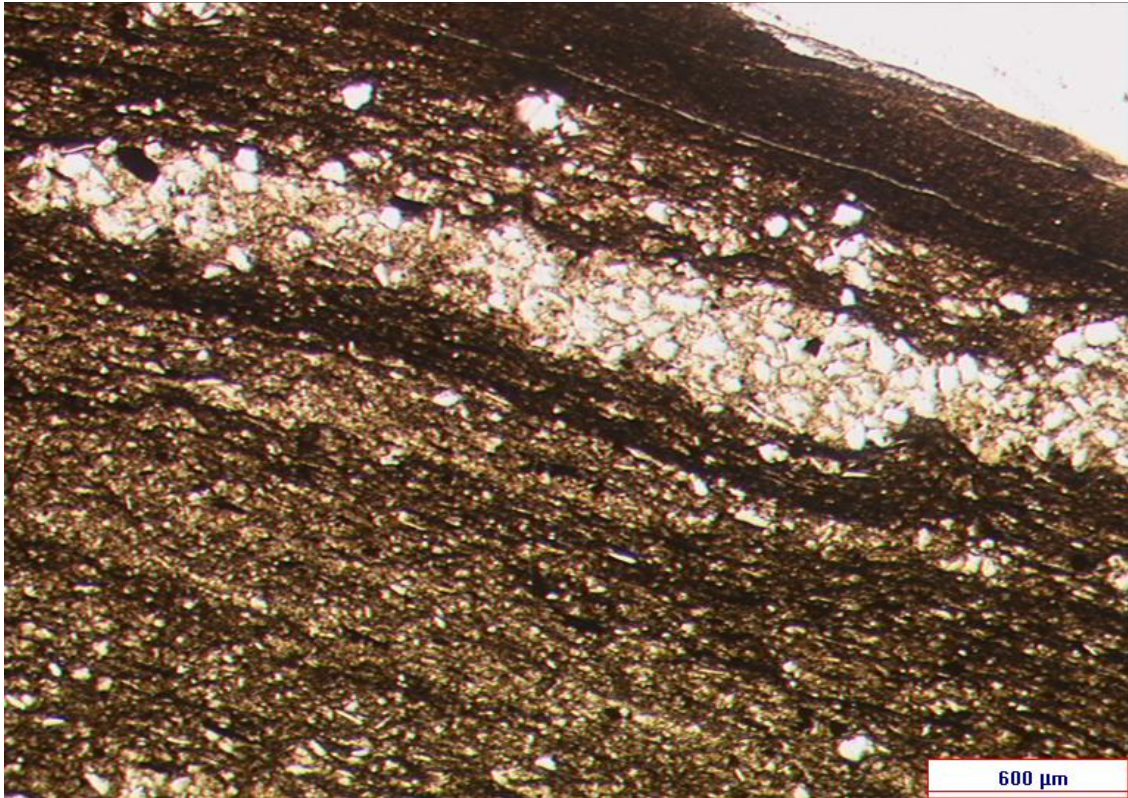
MLNW-2: 3469.70m



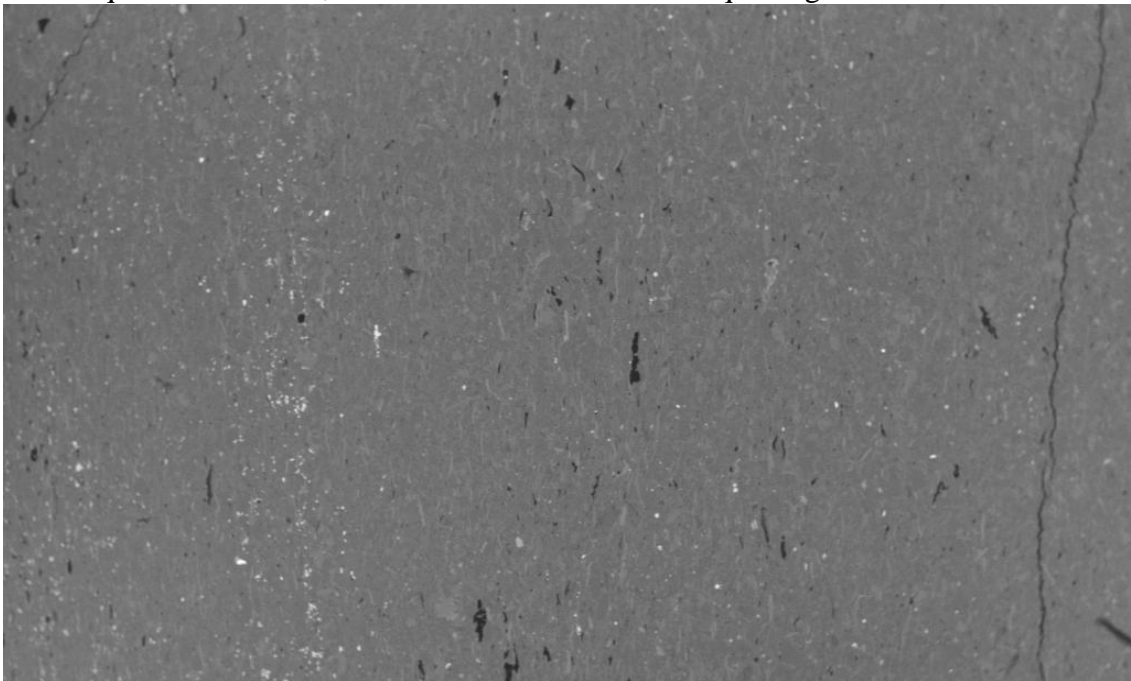
Medium-grained sandstone sample, with sub-angular quartz grains, occasional rounded clay grains, and little visible porosity. Minor grain-coating clays are visible on the SEM image, and a siderite cement is observed (siderite cement confirmed by SEM spectra analysis on accompanying CD).



MLNW-2: 3472.70m

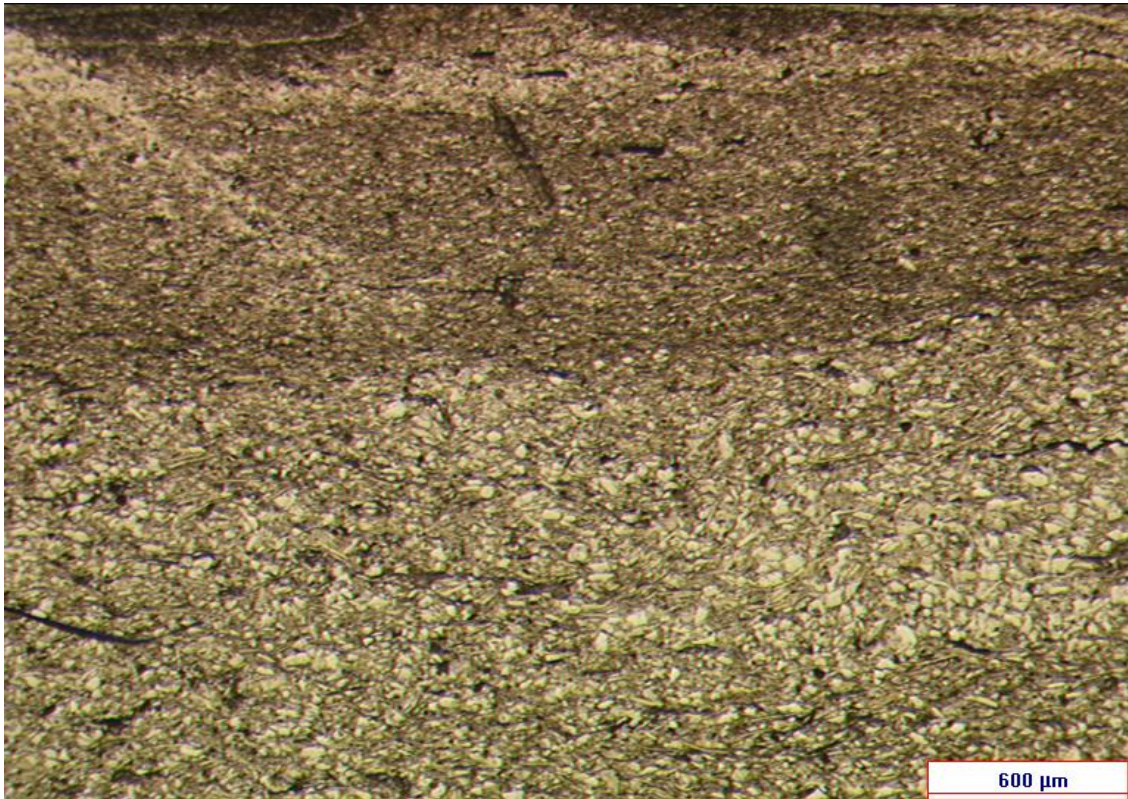


Very fine-grained mudstone sample, dominated by the brown, clay and mica rich matrix, with occasional visible quartz grains in the matrix, the sample also exhibits coarser quartz-rich bands, with rounded to sub-rounded quartz grains dominant.

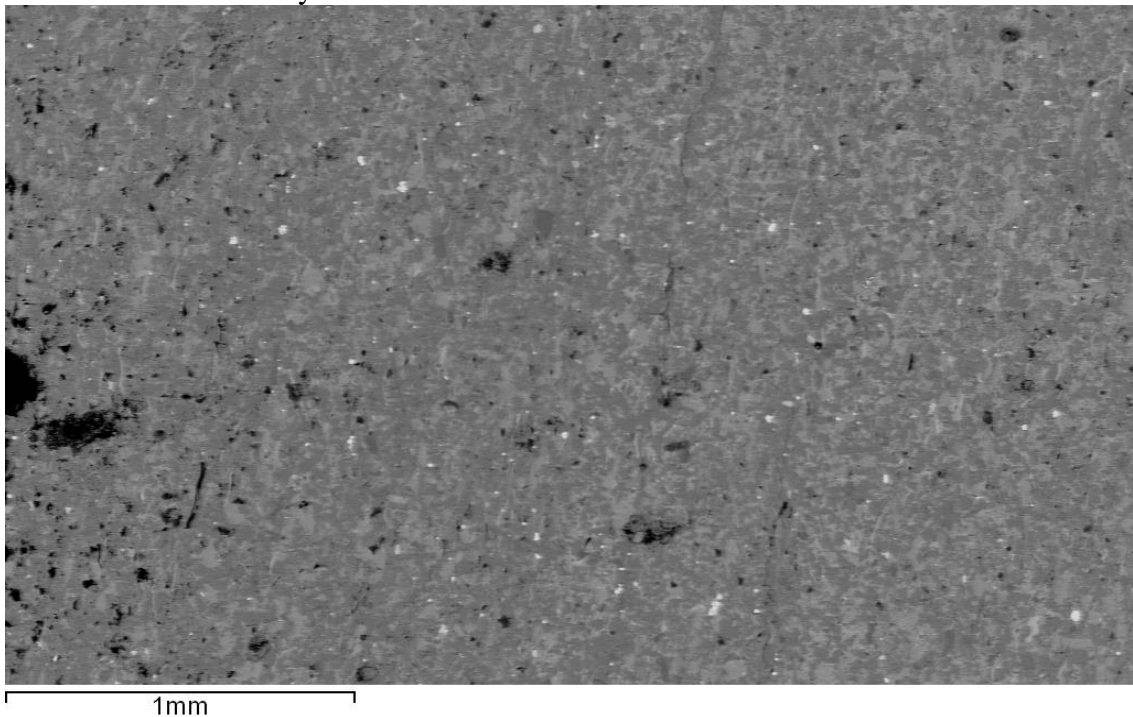


1mm

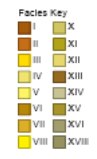
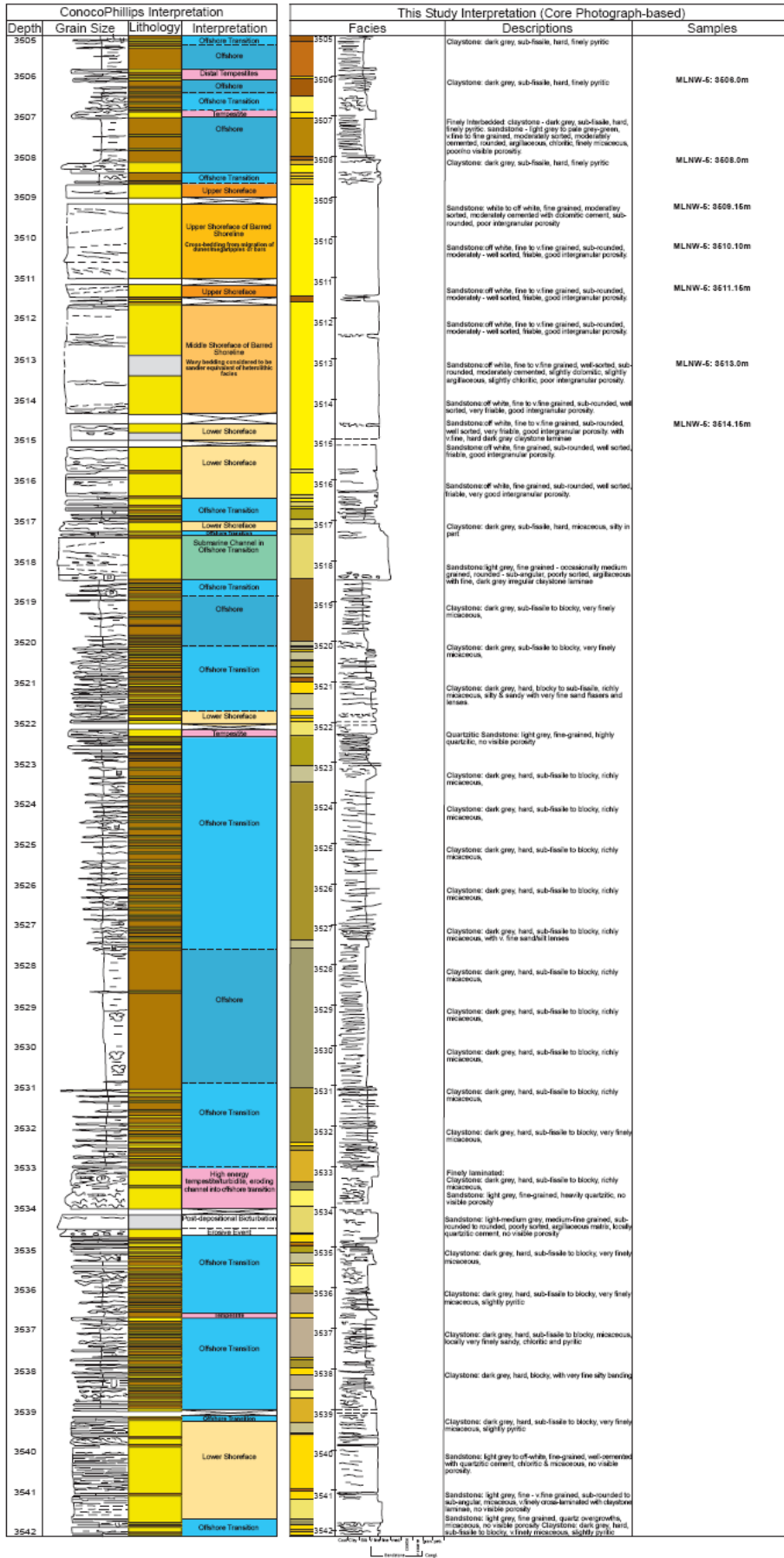
MLNW-2: 3473.45m



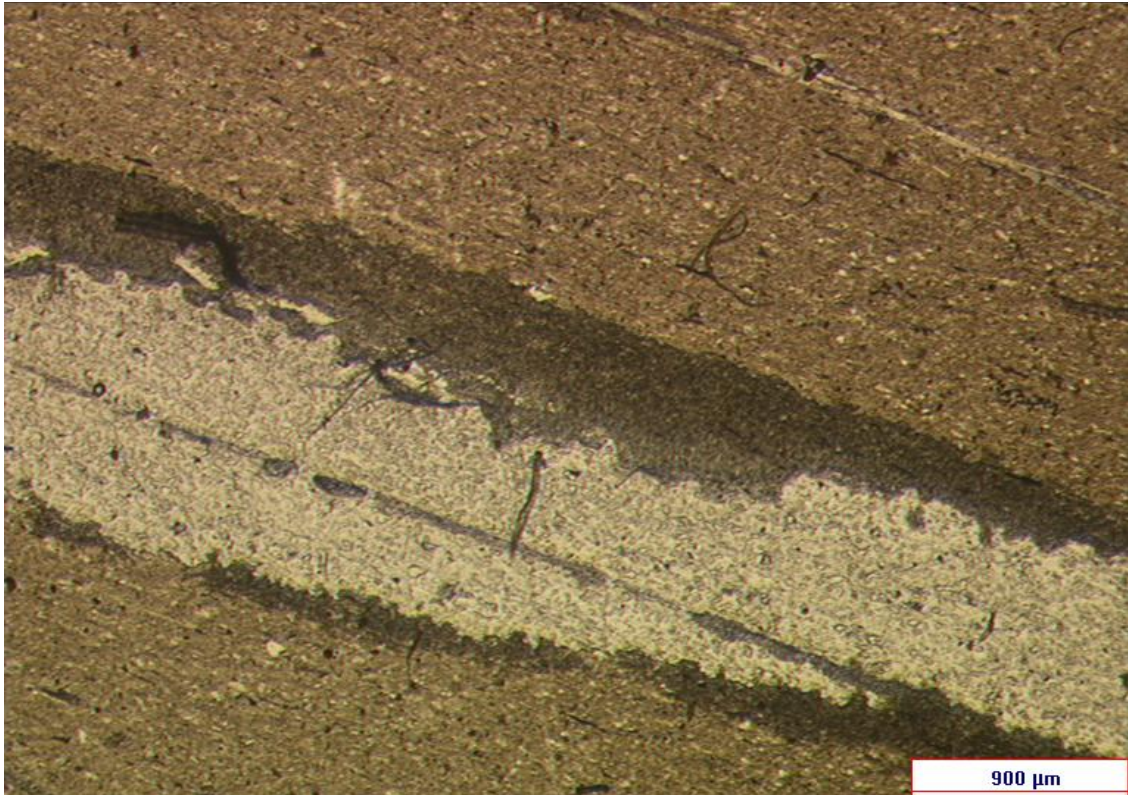
Very fine-grained mudstone sample, exhibiting banding between very fine-grained and extremely fine grained layers, with minor visible porosity most notable in the SEM image. The matrix is dominantly clay and mica grains, with the individual quartz grains visible in the coarser layers.



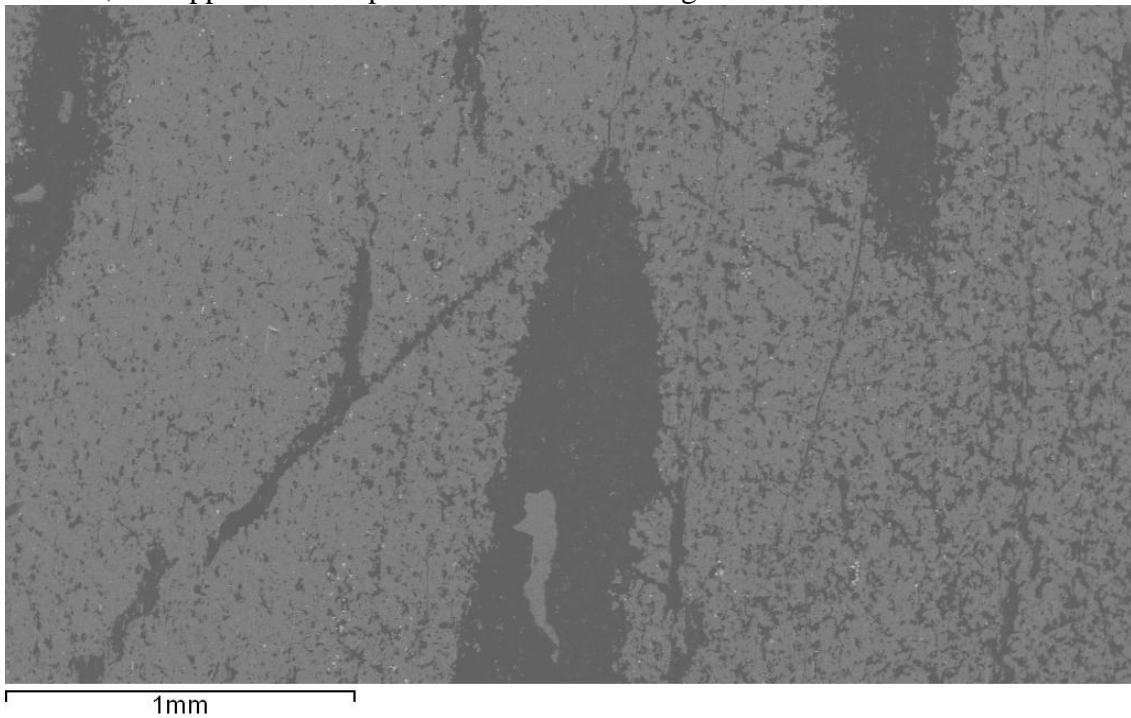
MLNW-5



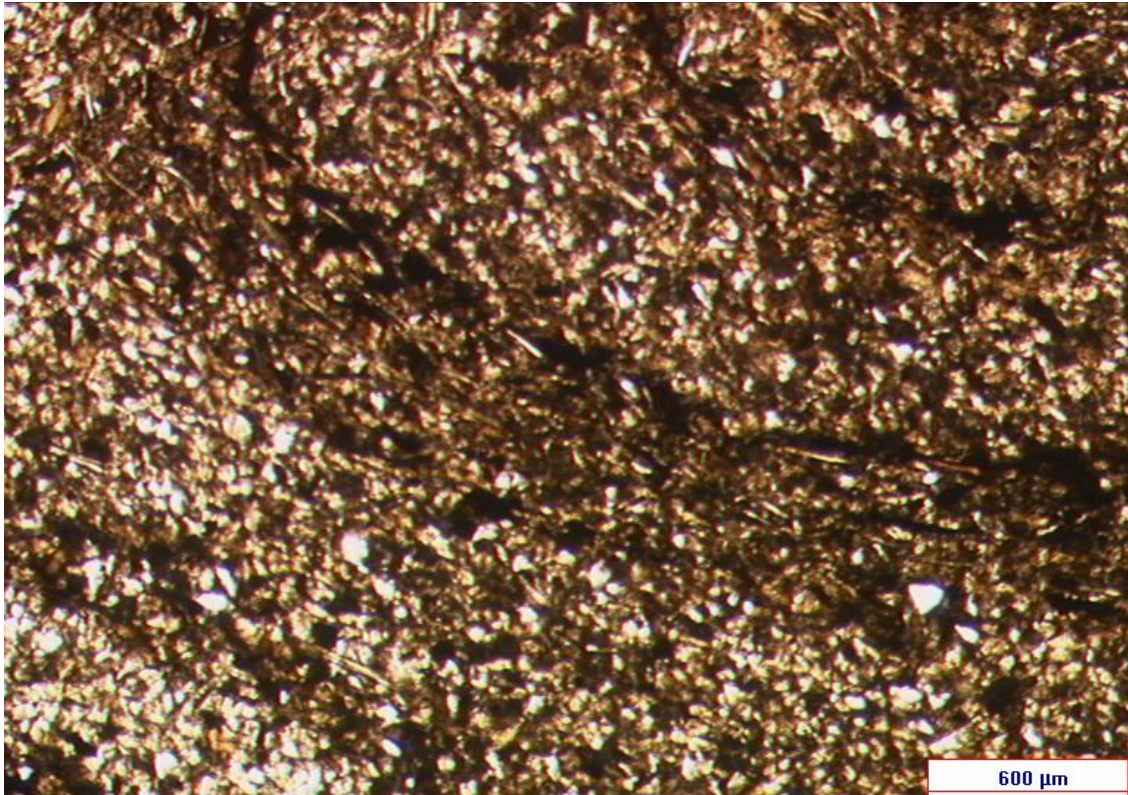
MLNW-5: 3506.0m



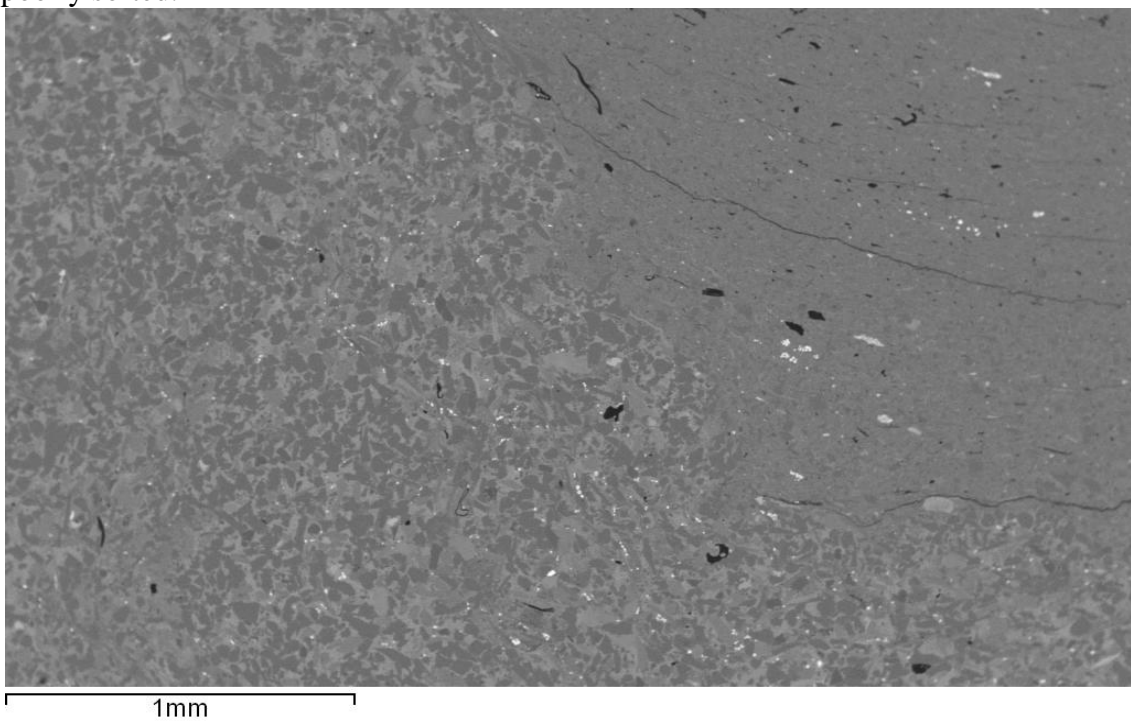
Extremely fine-grained mudstone sample with barely visible grains and a dominant dark brown matrix. The sample exhibits unusual pale bands, which contain amorphous green patches, these bands and patches are surrounded by very dark, very fine grained material, and appear as dark patches on the SEM image.



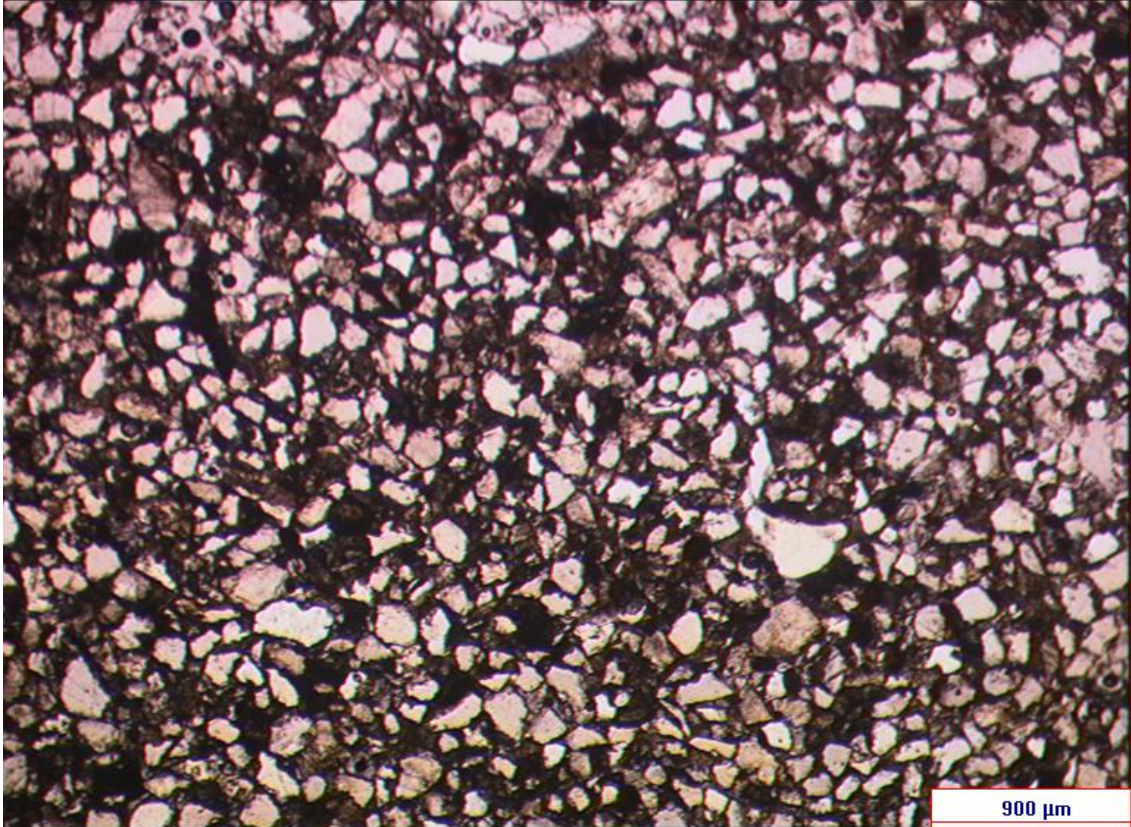
MLNW-5: 3508.0m



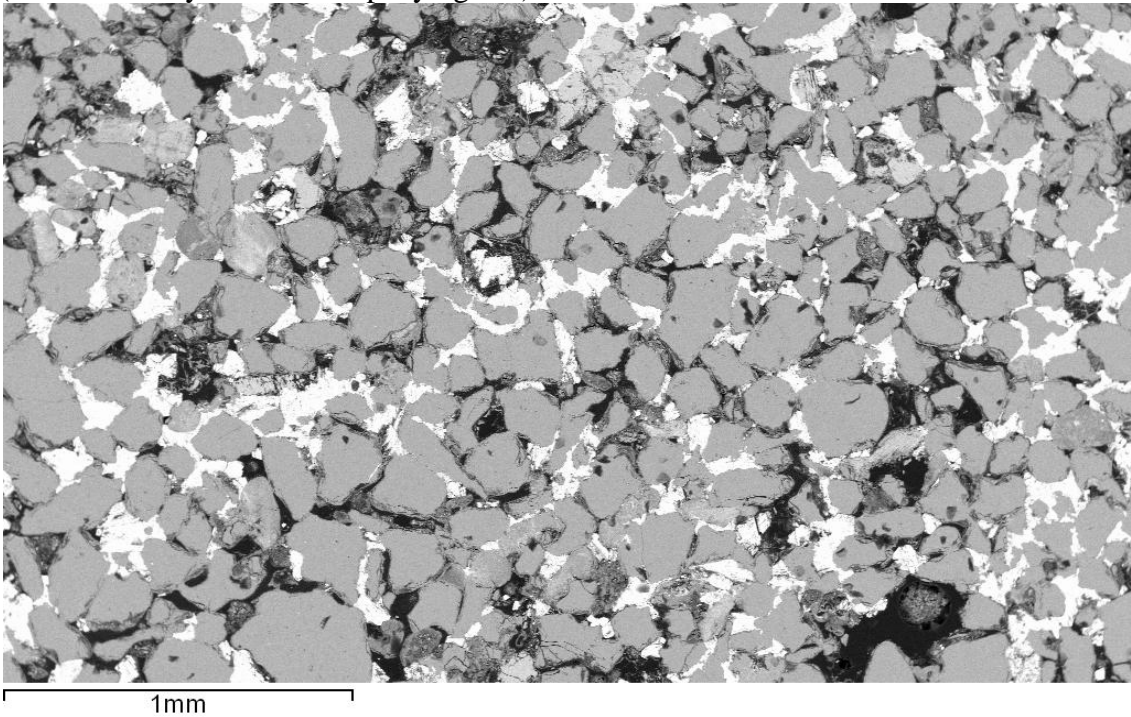
Very fine-grained mudstone sample, with visible quartz and mica grains, the mica grains exhibit some alignment and the quartz grain are sub-rounded to sub-angular and poorly sorted.



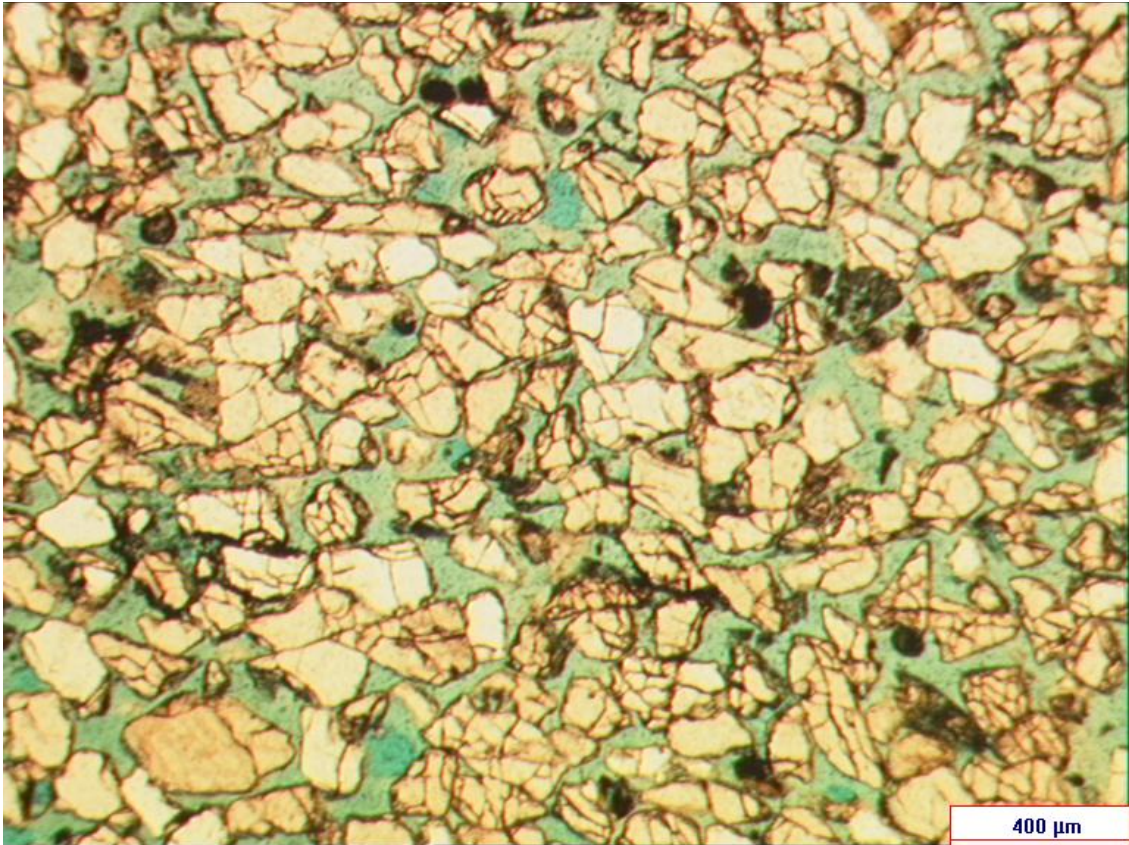
MLNW-5: 3509.15m



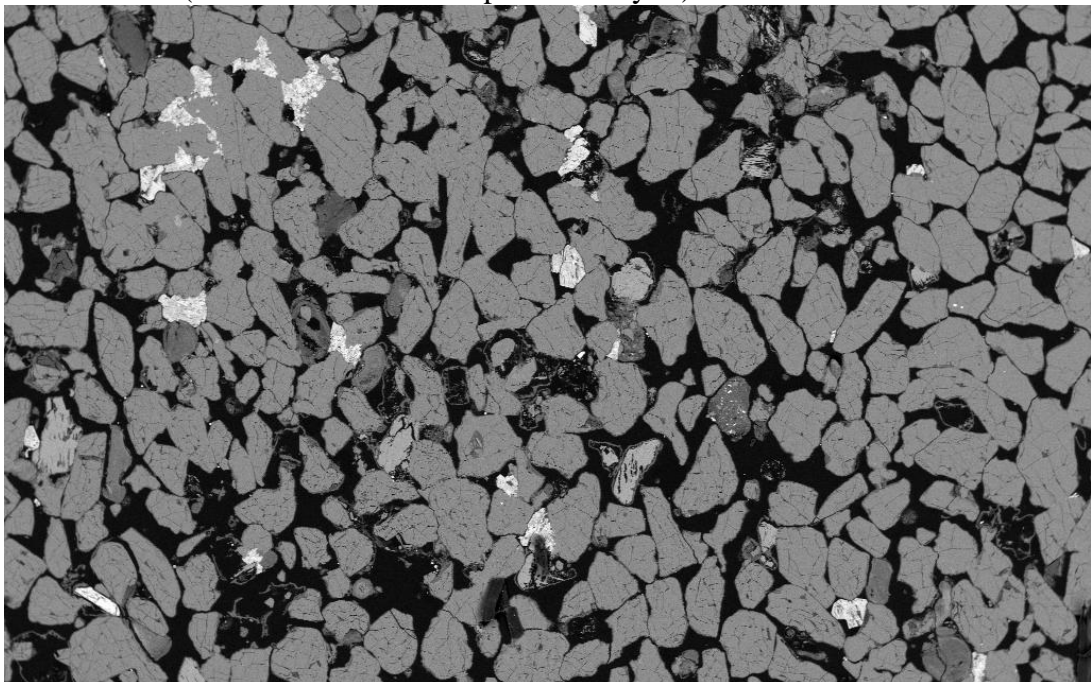
A quartz-rich medium – fine-grained sandstone sample, with sub-angular to sub-rounded poorly sorted grains, a siderite cement is abundant (confirmed with SEM spectra analysis) as are grain-coating clays, which appear to pre-date the siderite cement (see SEM analysis on accompanying CD).



MLNW-5: 3510.10m

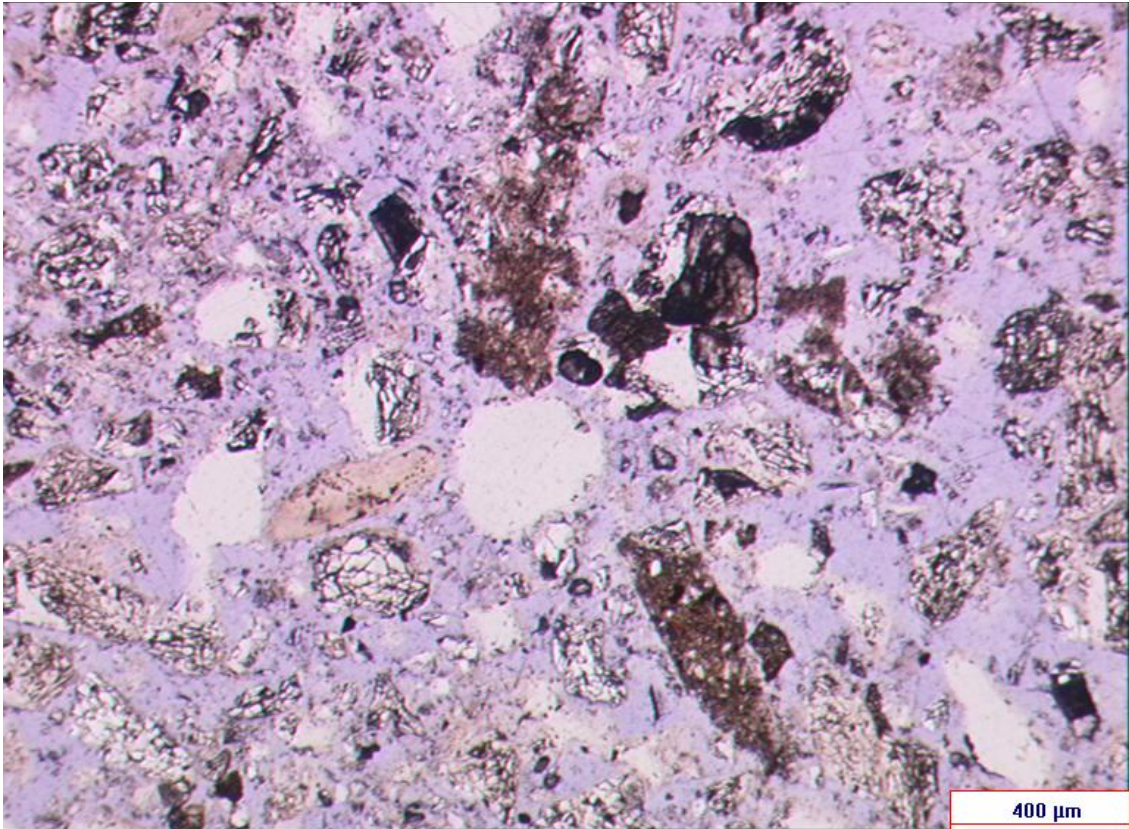


Quartz-rich medium – coarse-grained sandstone sample, poorly sorted with angular to sub-rounded grains, occasional individual clay grains are visible, and visibly highly porous. The SEM analysis indicates minimal grain-coating clays present and occasional siderite cement (confirmed with SEM spectral analysis).



1mm

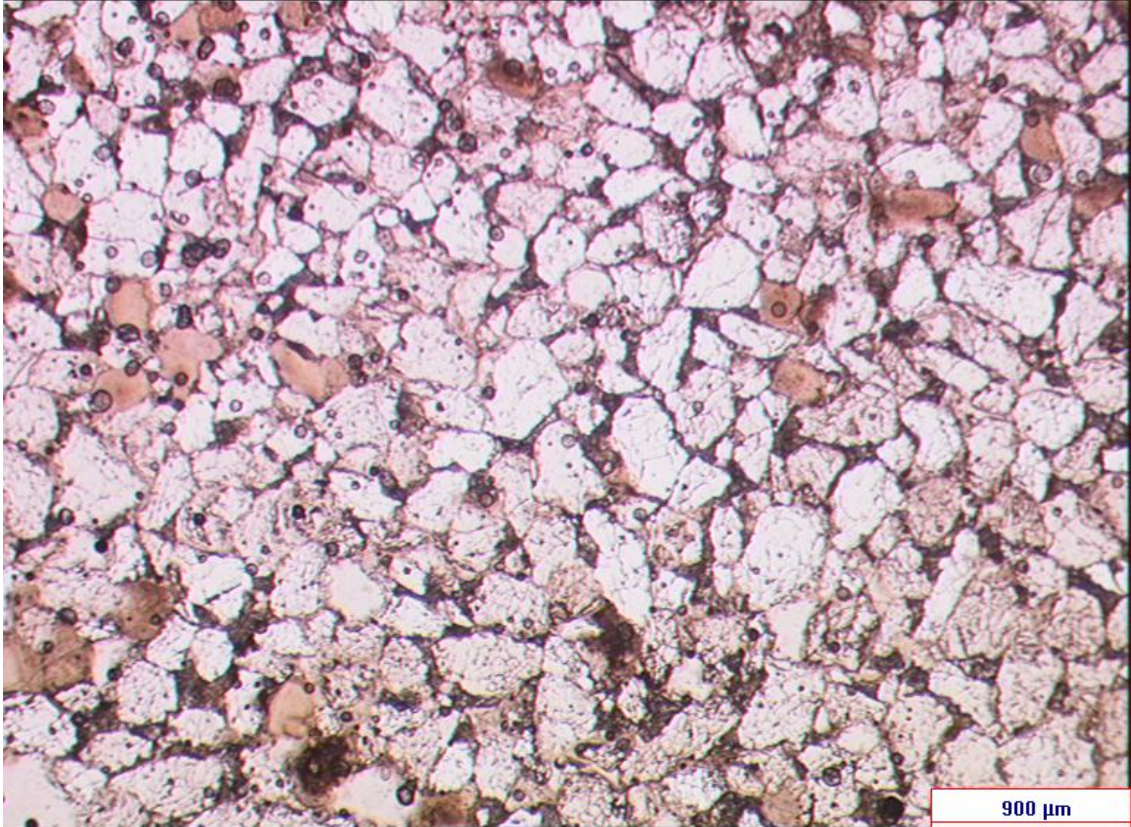
MLNW-5: 3511.15m



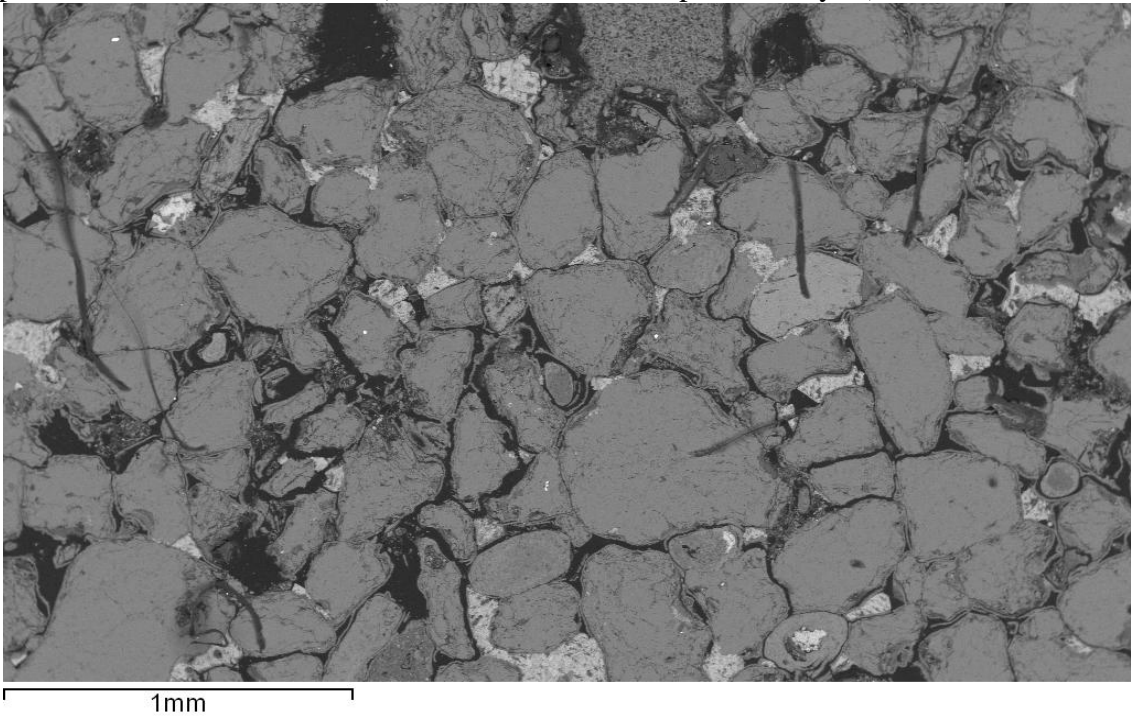
Due to the unconsolidated nature of the sample, the distribution of grains within this slide bears no relation to the sorting of the sandstone, and therefore no SEM analysis was done. It illustrates the grain shape, size and composition. The sandstone sample is fairly coarse grained, dominated by quartz, which is often highly fractured; individual clay grains are present and some calcite/siderite grains which may have been cement.

NO SEM IMAGE AVAILABLE

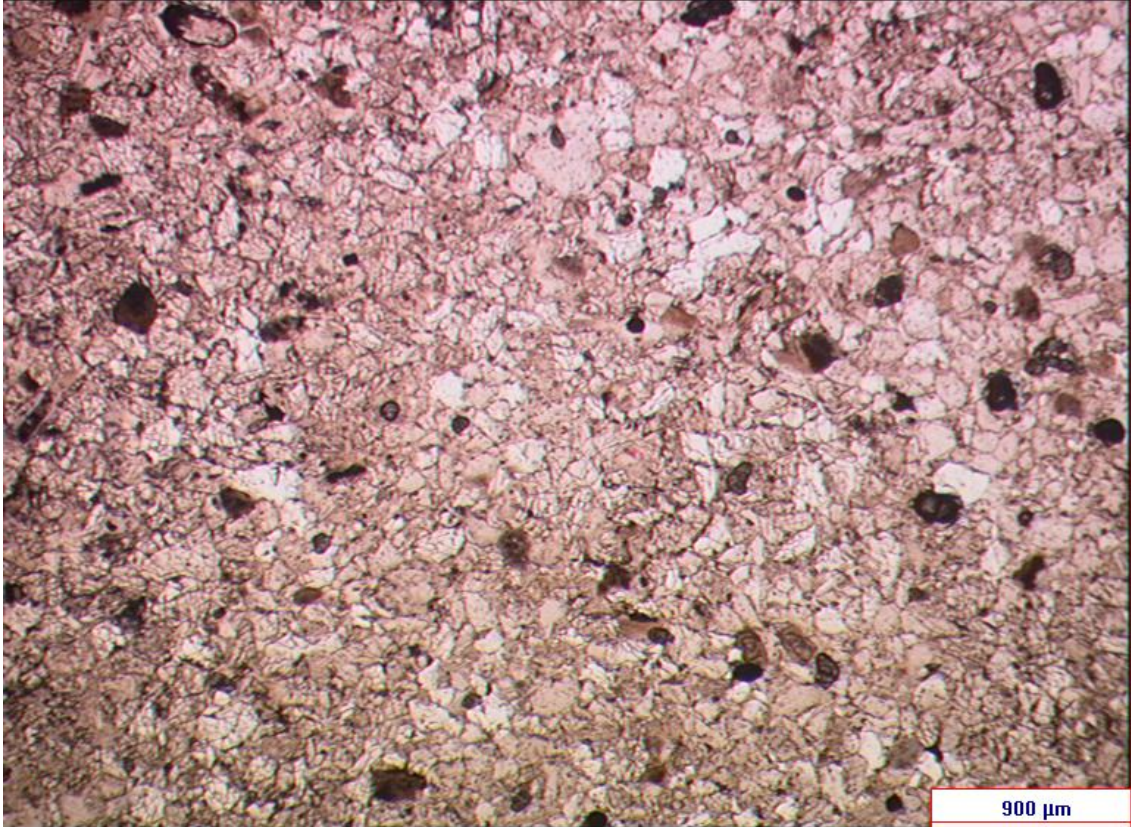
MLNW-5: 3513.0m



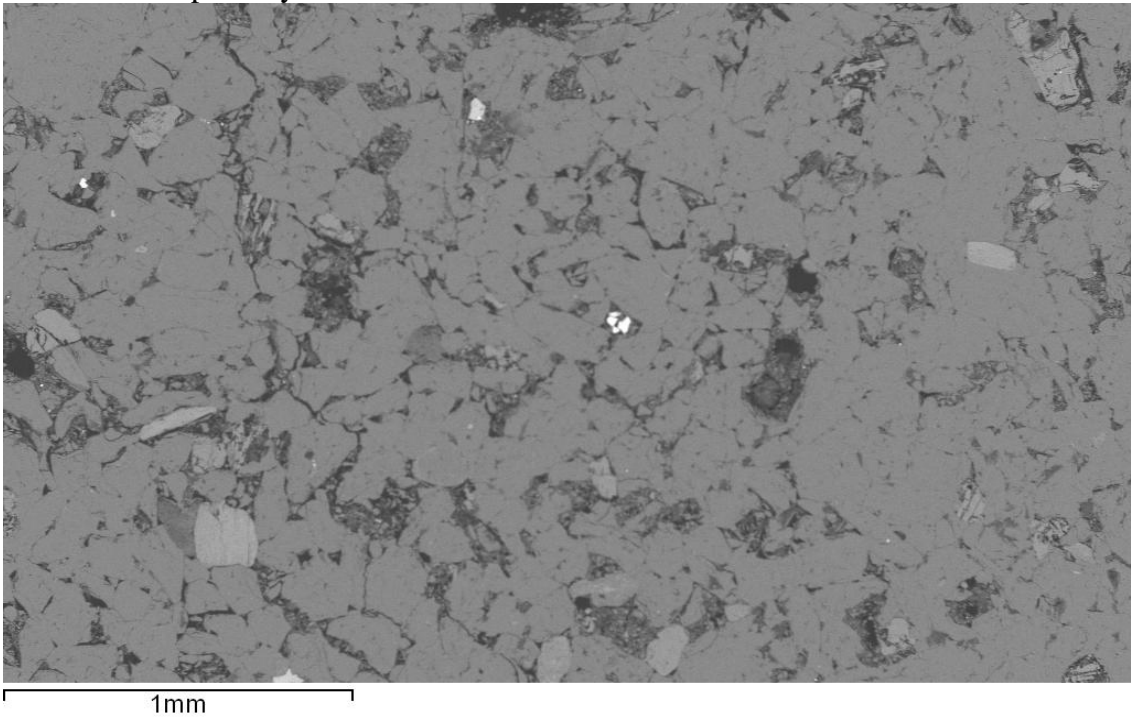
Moderately coarse-grained, well-sorted, quartz rich sandstone sample, exhibiting visible porosity, and an abundance of individual clay grains and grain coating clays, where present the cement is siderite (confirmed with SEM spectra analysis).



MLNW-5: 3514.54m



Quartz-rich, medium – fine-grained sandstone sample, with sub-angular to sub-rounded moderately well-sorted grains, occasional individual clay grains are present, the sample is well cemented with both grain-coating clays and quartz overgrowths, and exhibits limited visible porosity.

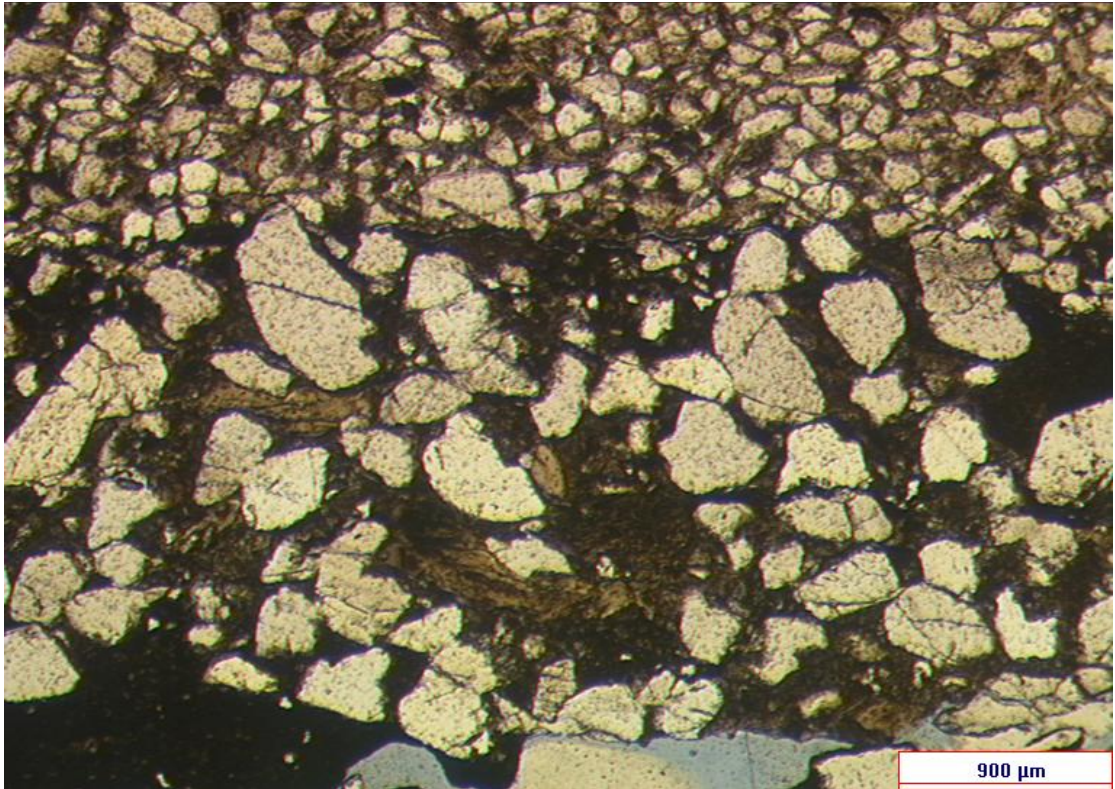


MLN-5

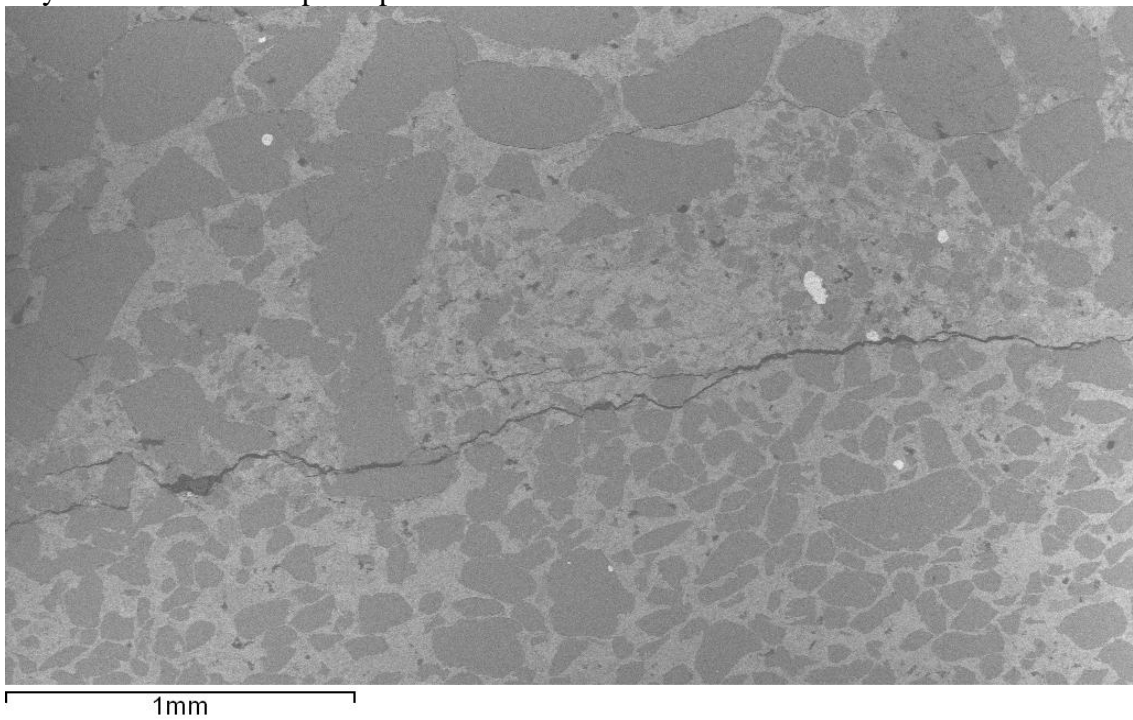
ConocoPhillips Interpretation				This Study Interpretation (Core Photograph-based)		
Depth	Grain Size	Lithology	Interpretation	Facies	Descriptions	Samples
3515			Offshore - offshore transition			
3516			Offshore			
3517			storm-influenced shelf (offshore transition)			MLN-5: 3517.40m
3518			Offshore			
3519			Hiatus in sedimentation			
3520			Upper shoreface of longshore bar			
3521			Cross-bedding due to no channel fill or migration of bar			
3522			Tempestite			MLN-5: 3522.20m
3523			Upper shoreface of Longshore bar			
3524			Tidal Inlet			MLN-5: 3524.62m
3525			Upper shoreface of Longshore bar			
3526			Minor Tidal Inlet			
3527			Upper shoreface			
3528			Tidal Inlet			
3528			Marine Transition			
3528			Tidal channels			
3529			Lower to Upper shoreface			
3530			Lower shoreface?			
3531			Offshore			
3532			Lower shoreface			
3533			Offshore			
3534			Offshore			
3535			Offshore transition above storm wave base, shallowing upwards to lower shoreface			
3536						
3537						
3538						
3539			Tempestite			
3540			Offshore			
3541						
3542						
3543			Lower shoreface			

Not Applicable
Due to Lack of
Core
Photographs

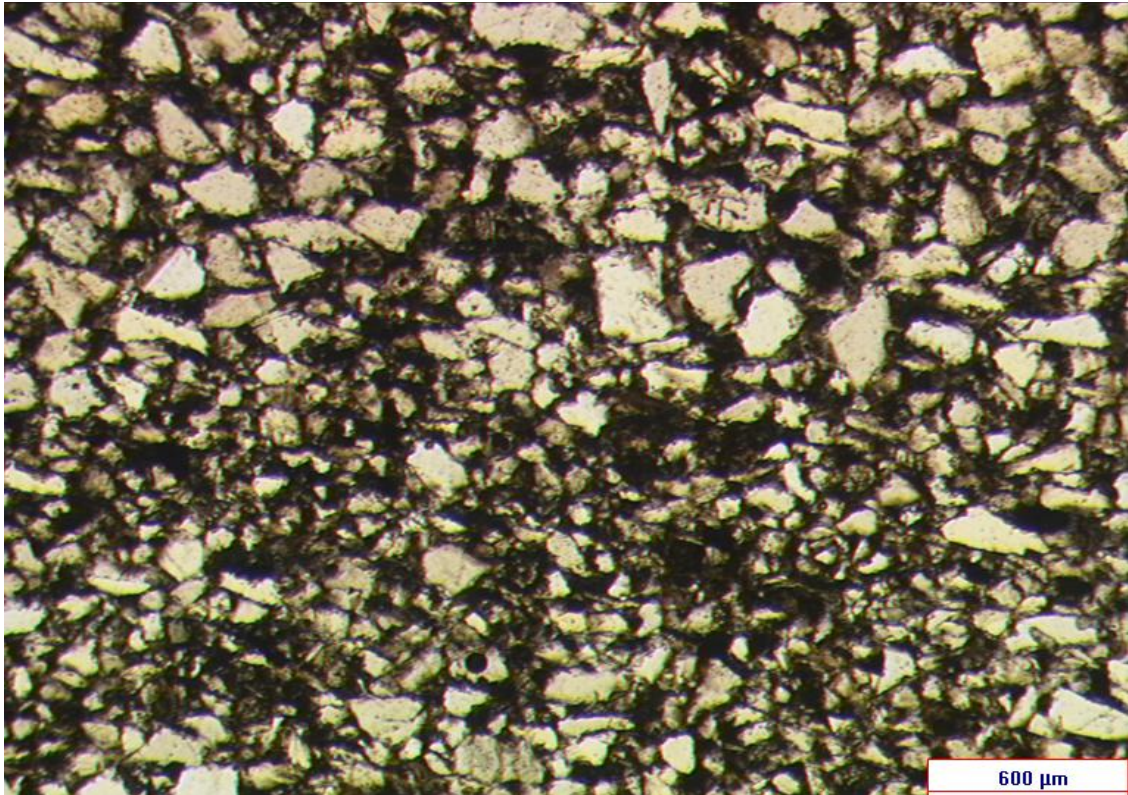
MLN-5: 3517.40m



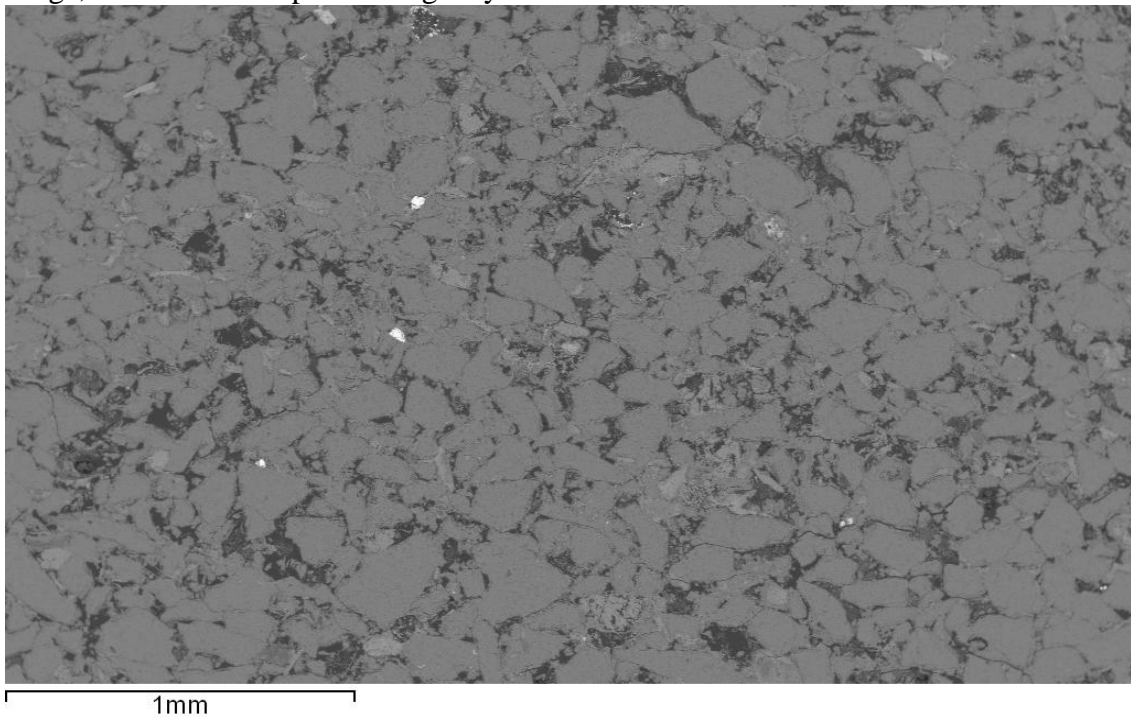
Quartz-rich, banded sandstone sample, exhibiting two different layers: on the above image the “top” layer is moderately fine-grained, with abundant clay-rich cement, and is moderately well-sorted. The “bottom” layer is coarse-grained, with shale lithic fragments, visible as dark brown patches; this layer also exhibits clay-rich cement and only occasional visible pore space.



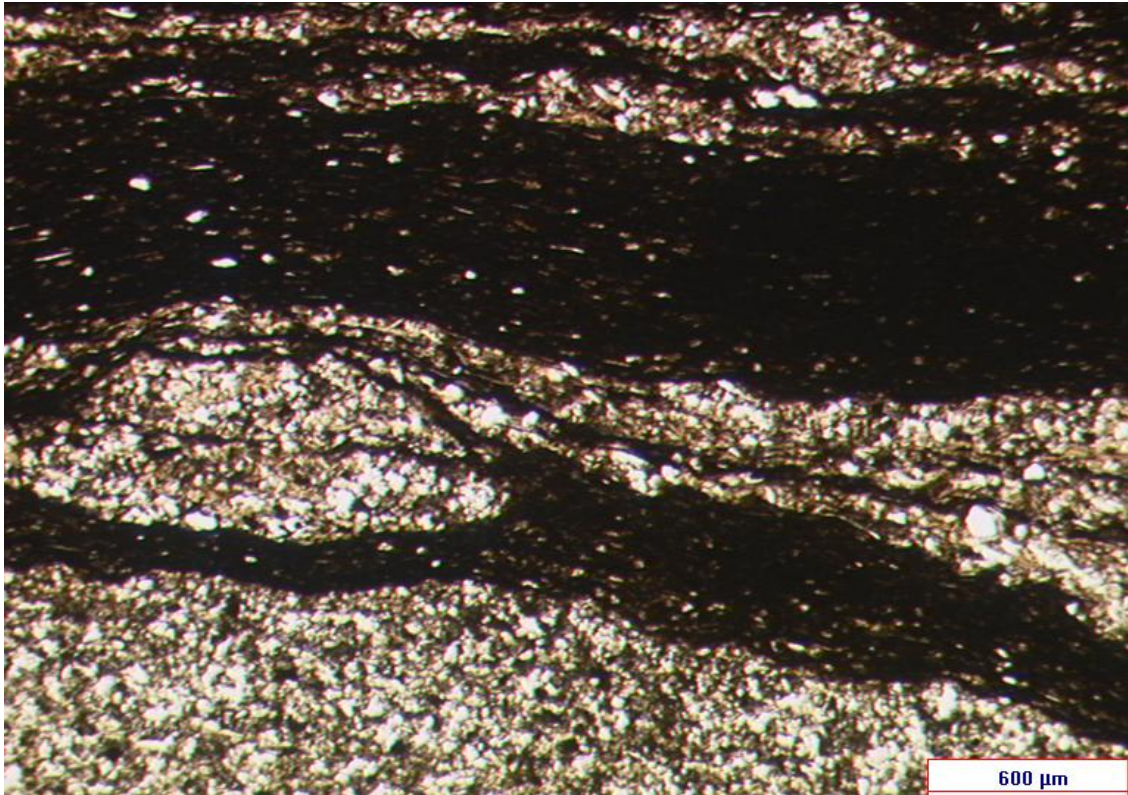
MLN-5: 3522.20m



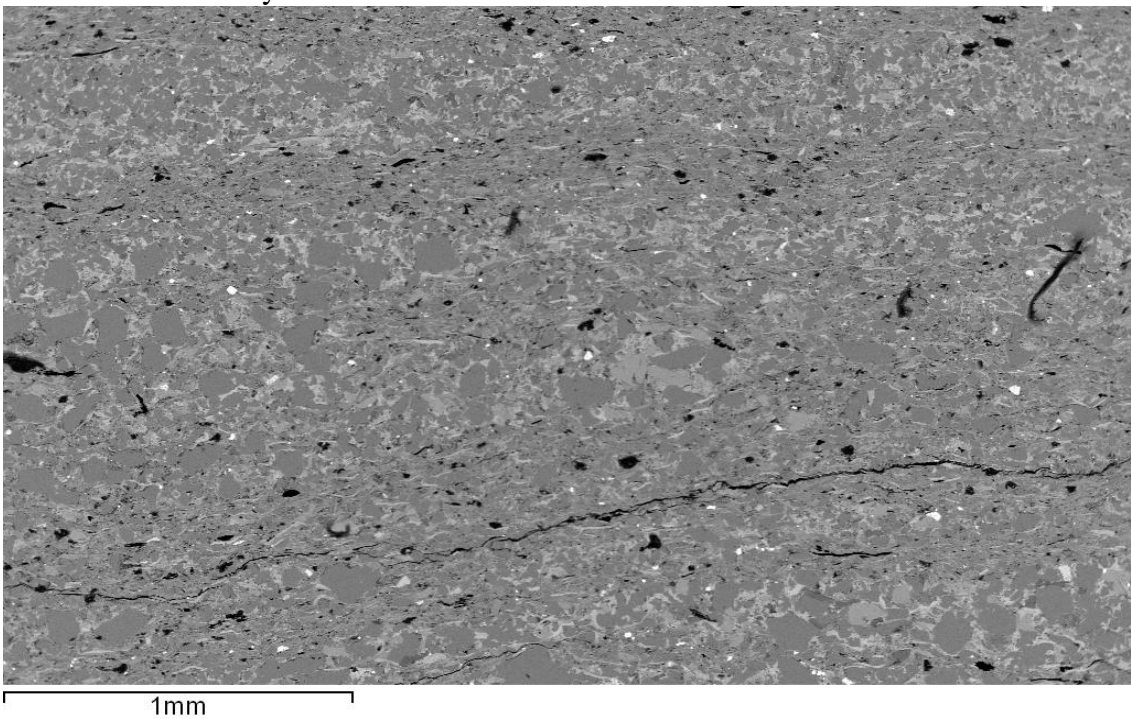
Quartz-dominated very fine-grained sandstone sample, exhibiting poorly-sorted, sub-angular grains and with little-to-no visible porosity, the sample is well-cemented and clay-rich, with abundant grain-coating clays, which are more noticeable in the SEM image, and occasional pore-filling clays.



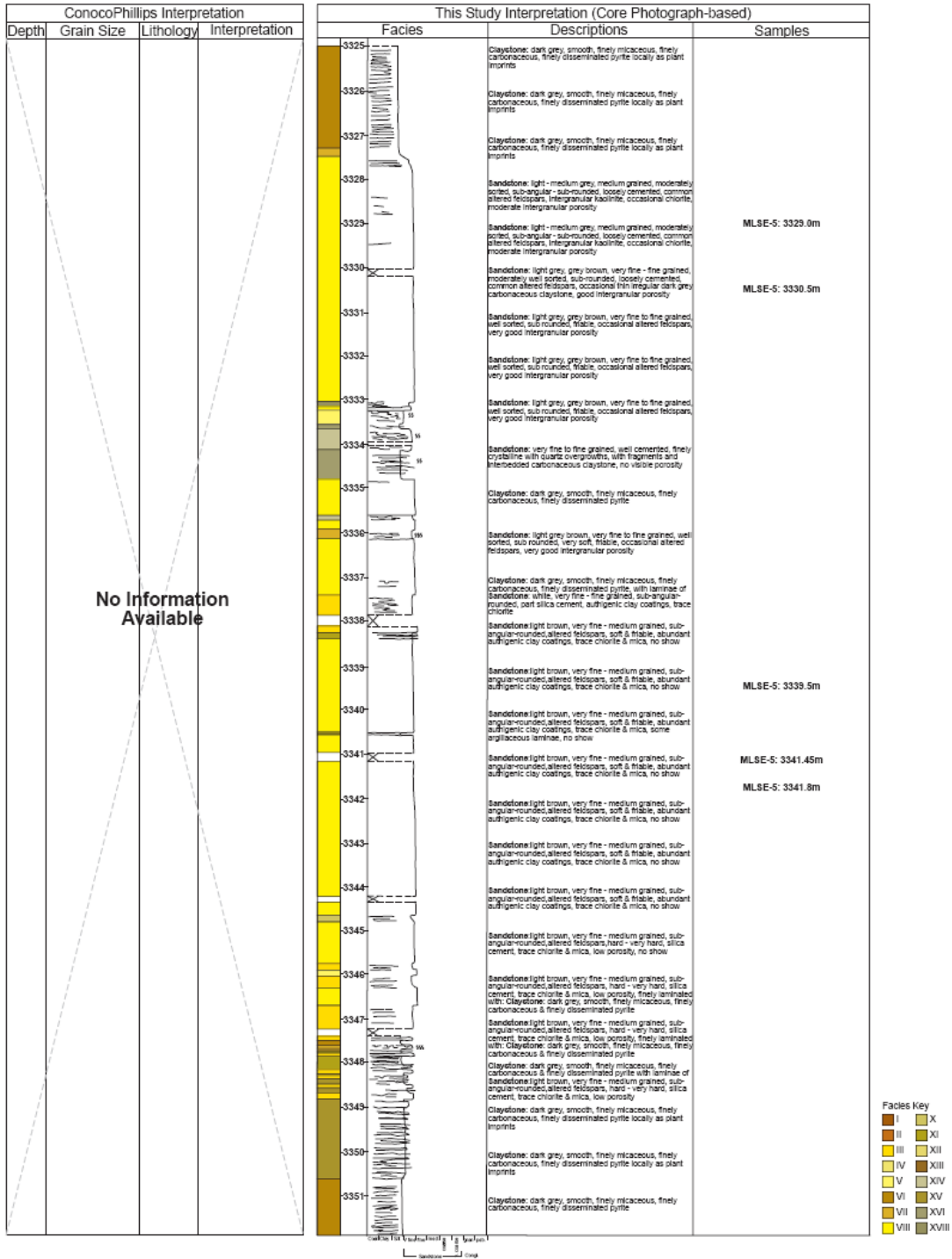
MLN-5: 3524.62m



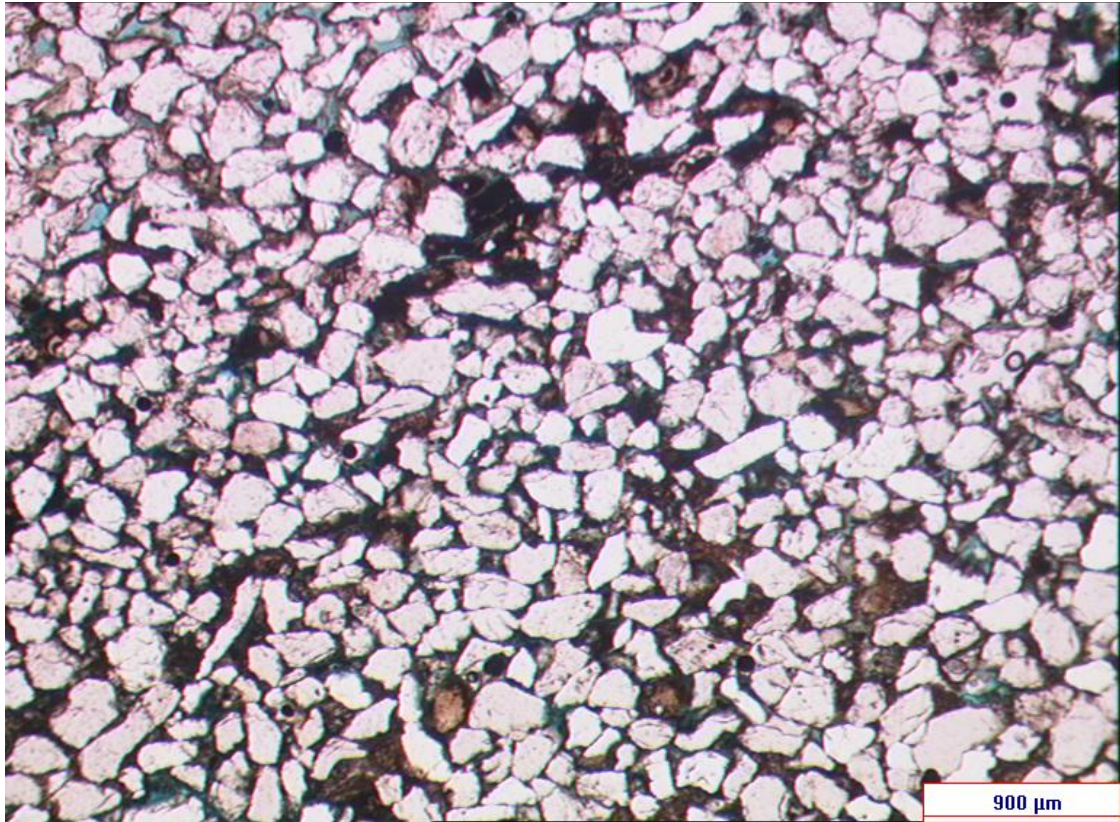
Mudstone sample with extremely fine-grained dark bands, with only occasional visible quartz grains and coarser grained quartz-rich bands, which have visible quartz grains, and are mica and clay-rich.



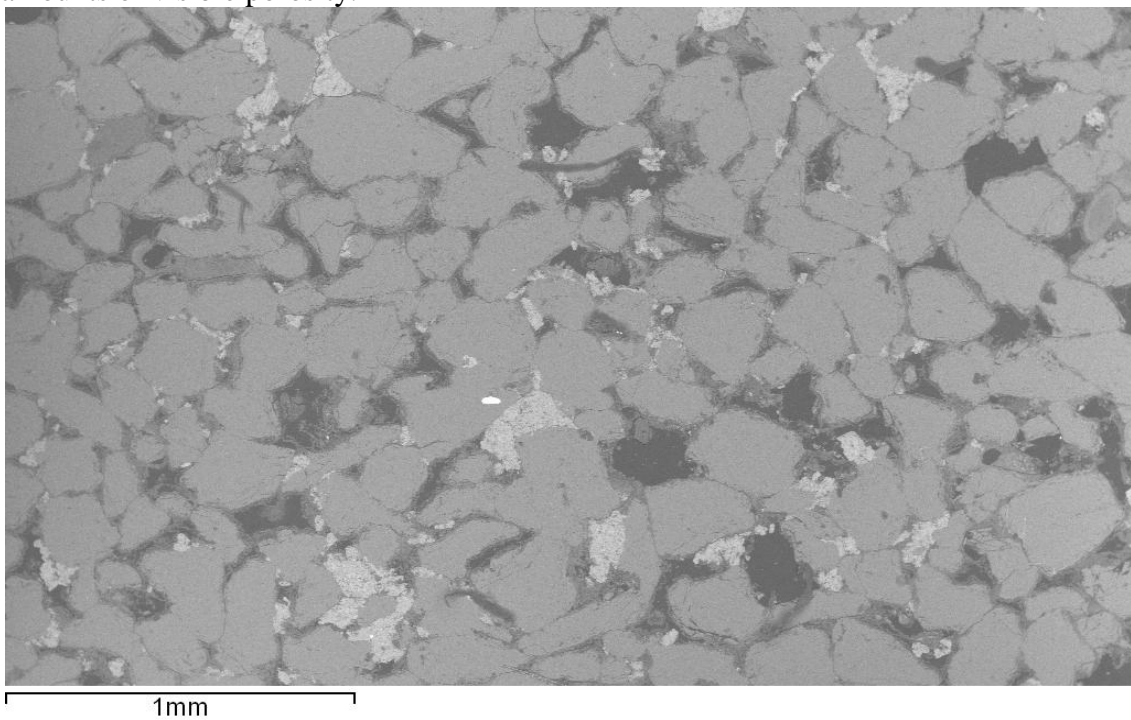
MLSE-5



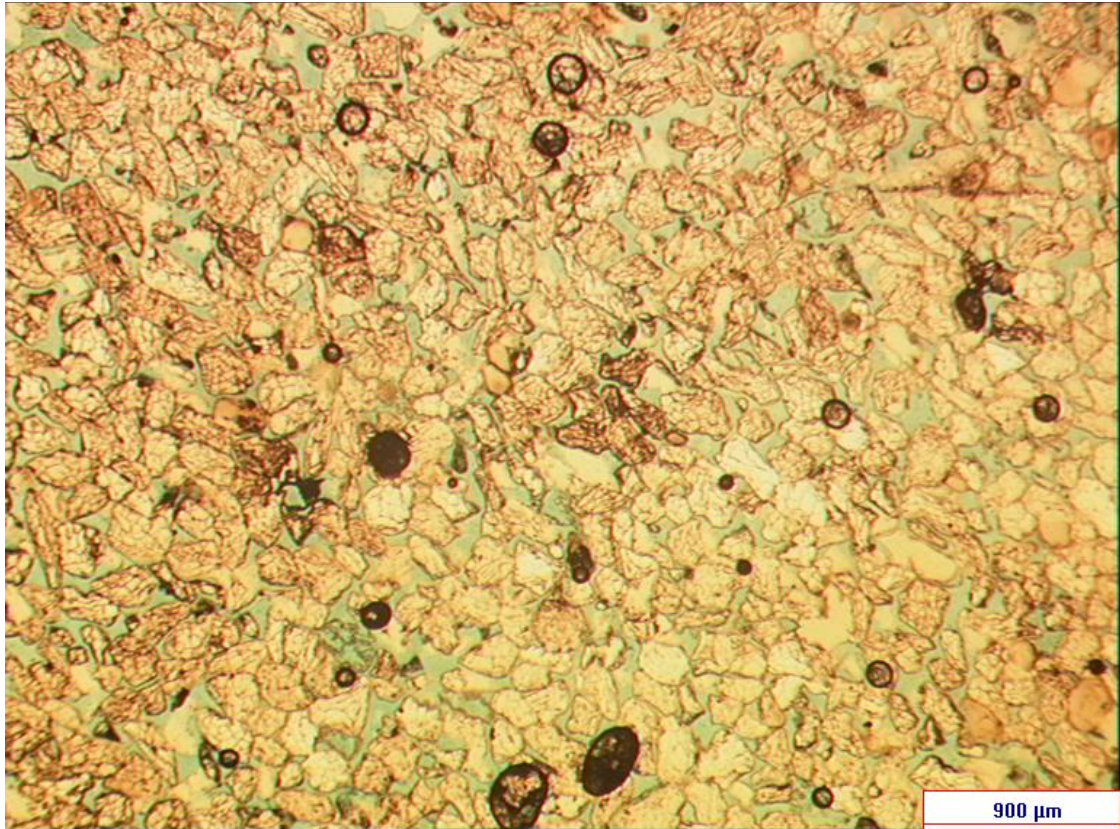
MLSE-5: 3329.0m



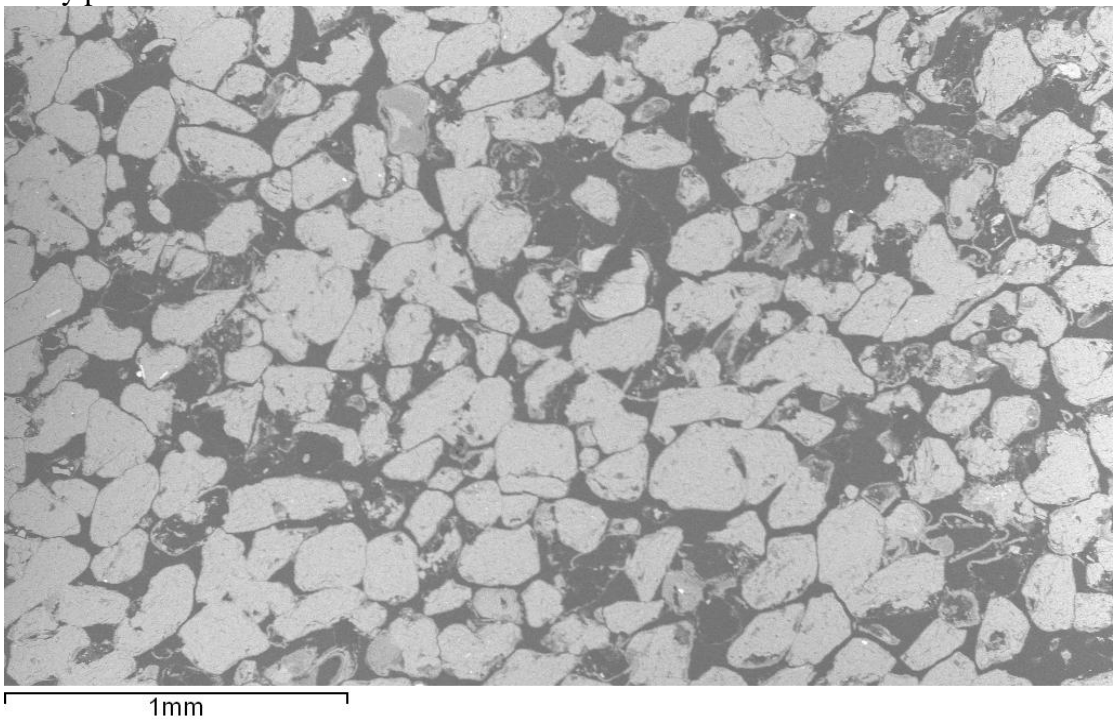
A medium grained, poorly sorted sandstone sample, dominated by sub-angular to rounded quartz grains, with occasional individual clay grains, patchy siderite cement (see SEM spectra analysis on accompanying CD), grain-coating clays and minor amounts of visible porosity.



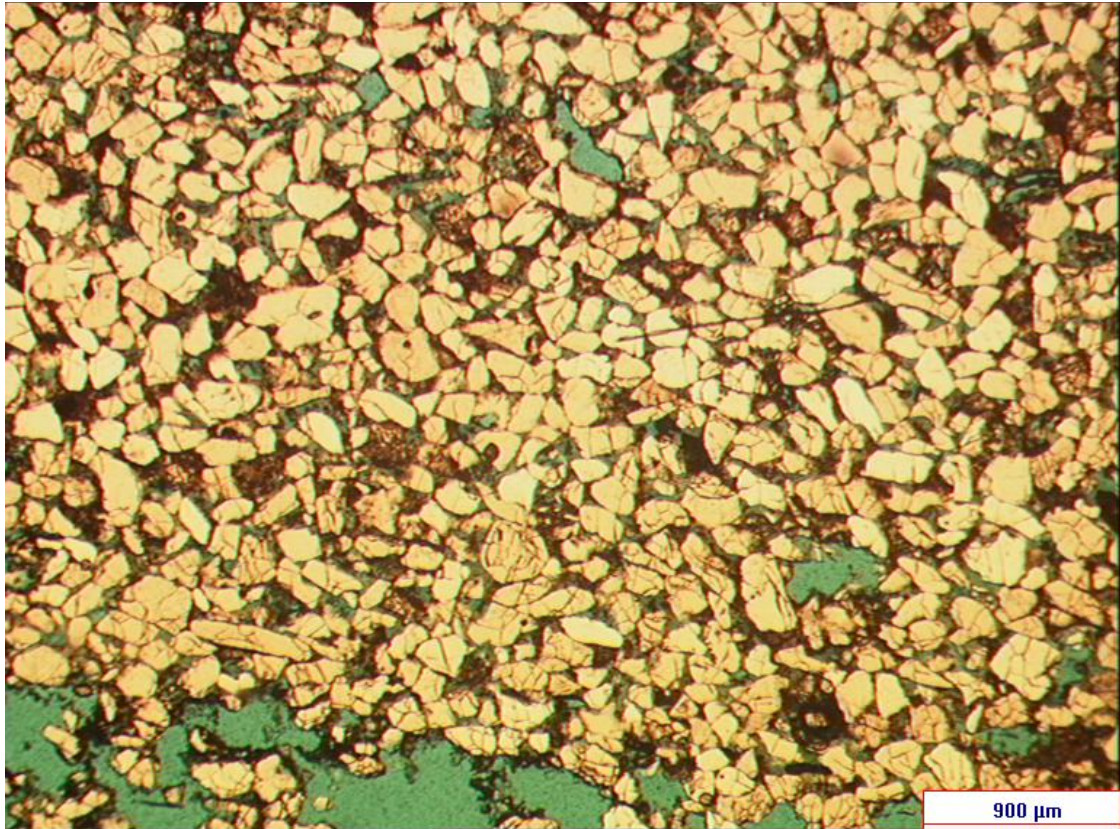
MLSE-5: 3330.5m



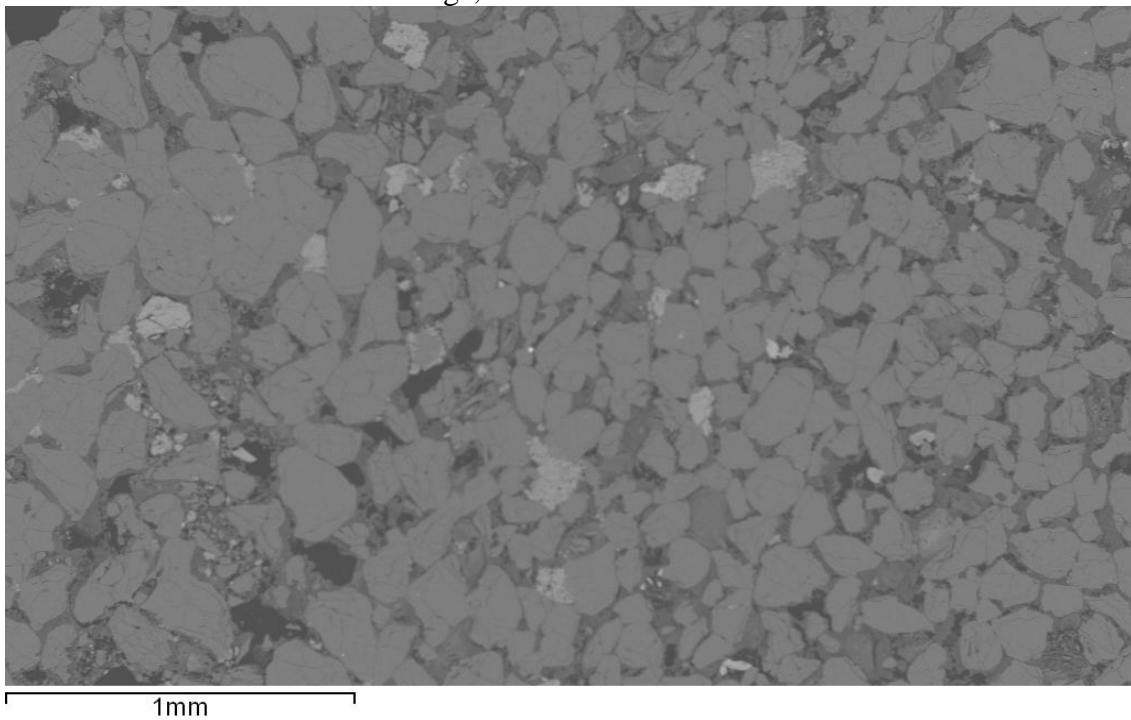
Quartz-dominated medium – fine-grained sandstone sample with sub-rounded to elongate grains, some of the quartz is highly fractured (possible effect of polishing), grain-coating clays are abundant when viewed under the SEM, and the sample is highly visibly porous.



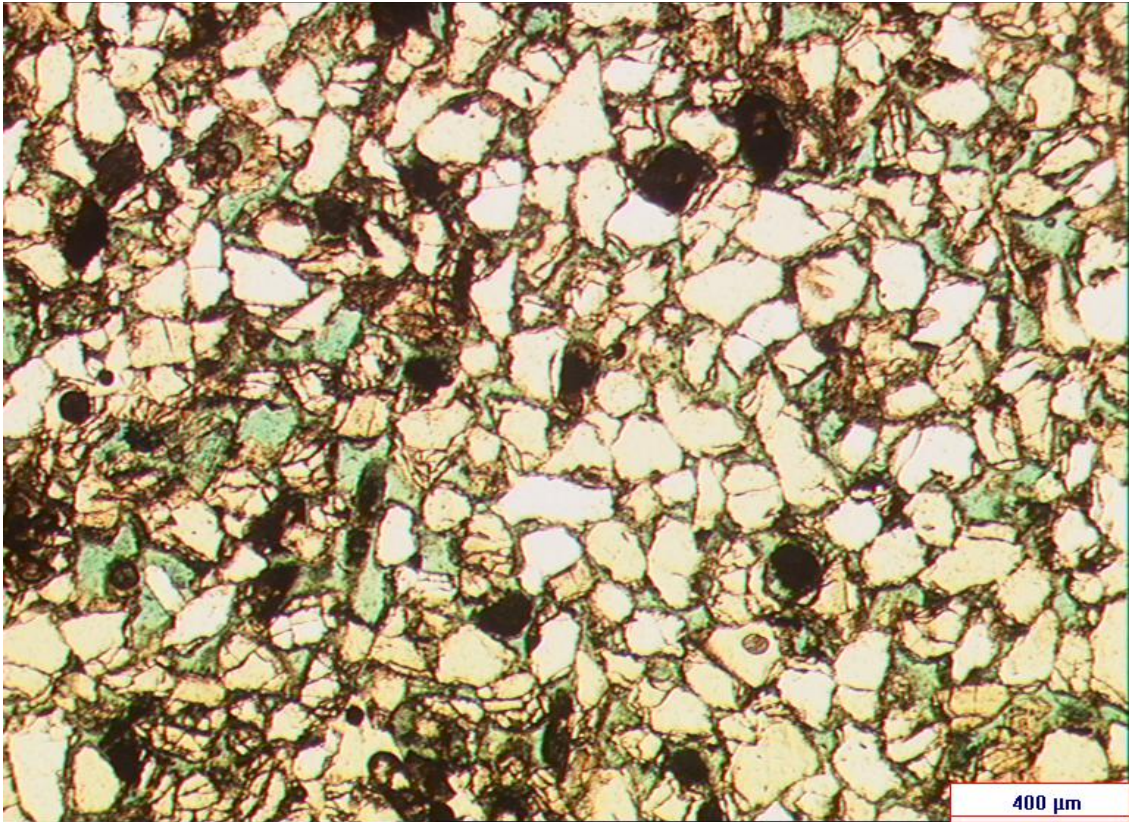
MLSE-5: 3339.5m



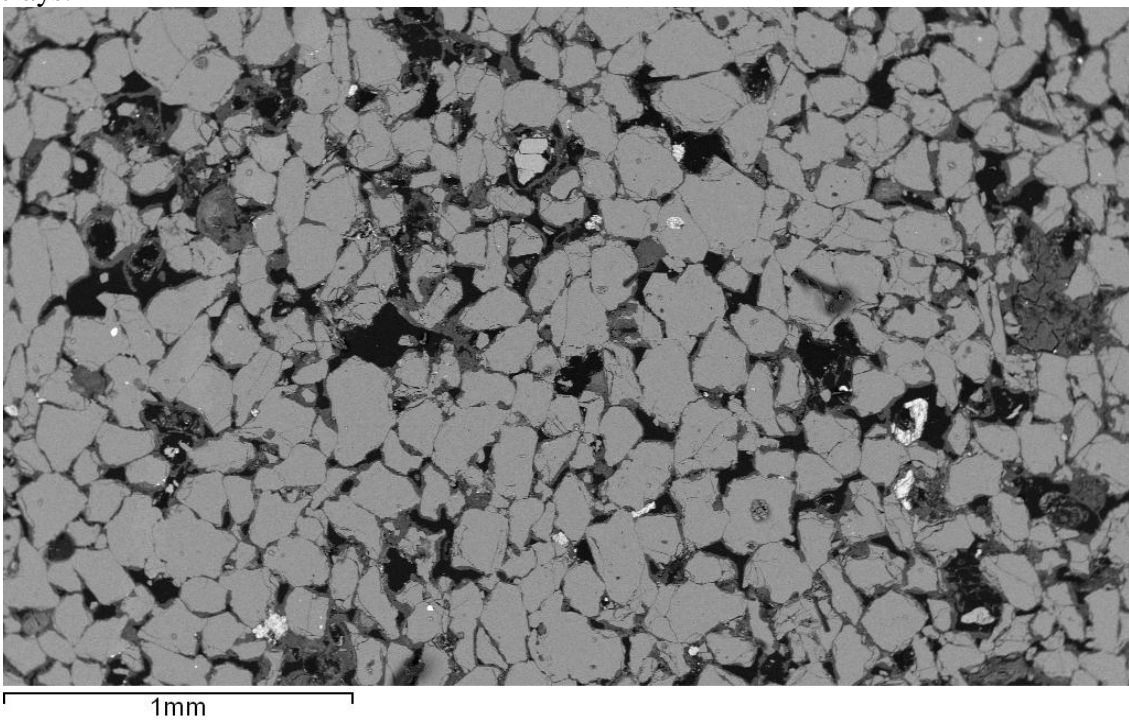
Quartz-rich highly porous sandstone sample, with sub-rounded high sphericity grains to elongate angular grains, with occasional calcite and feldspar grains, individual clay grains are present and also occur as grain-coatings, occasional patches of siderite cement are visible in the SEM image, but are of minor occurrence.



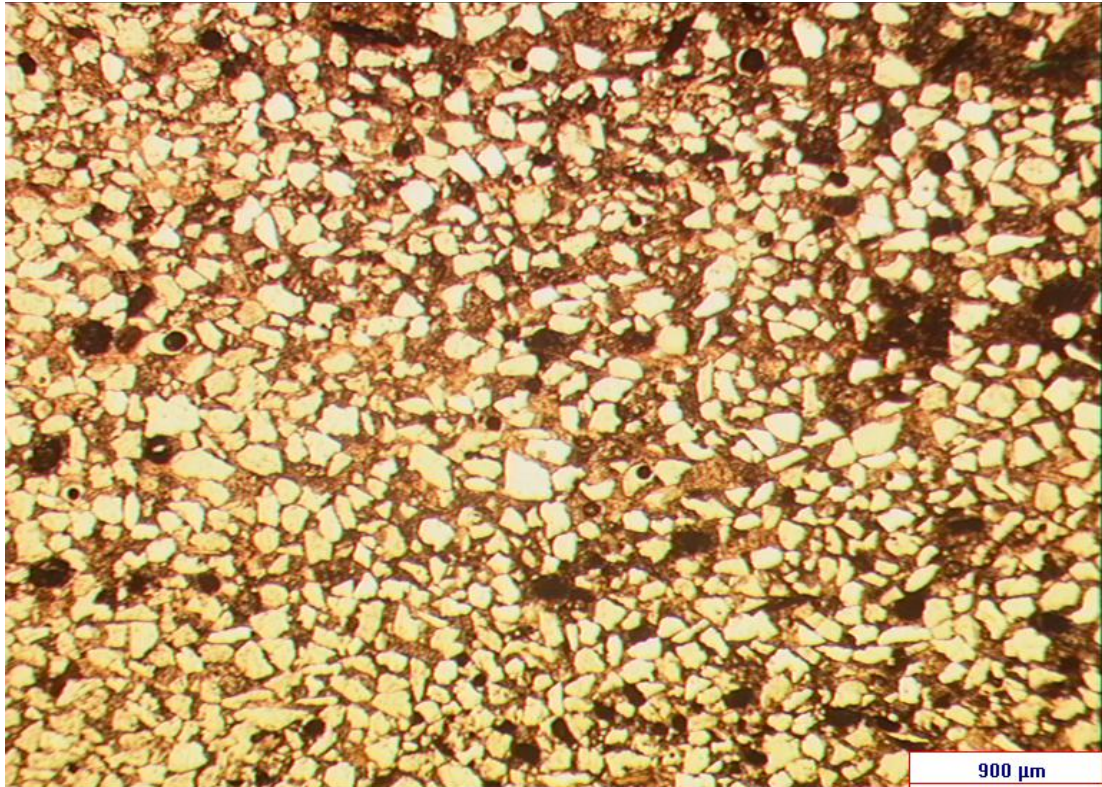
MLSE-5: 3341.45m



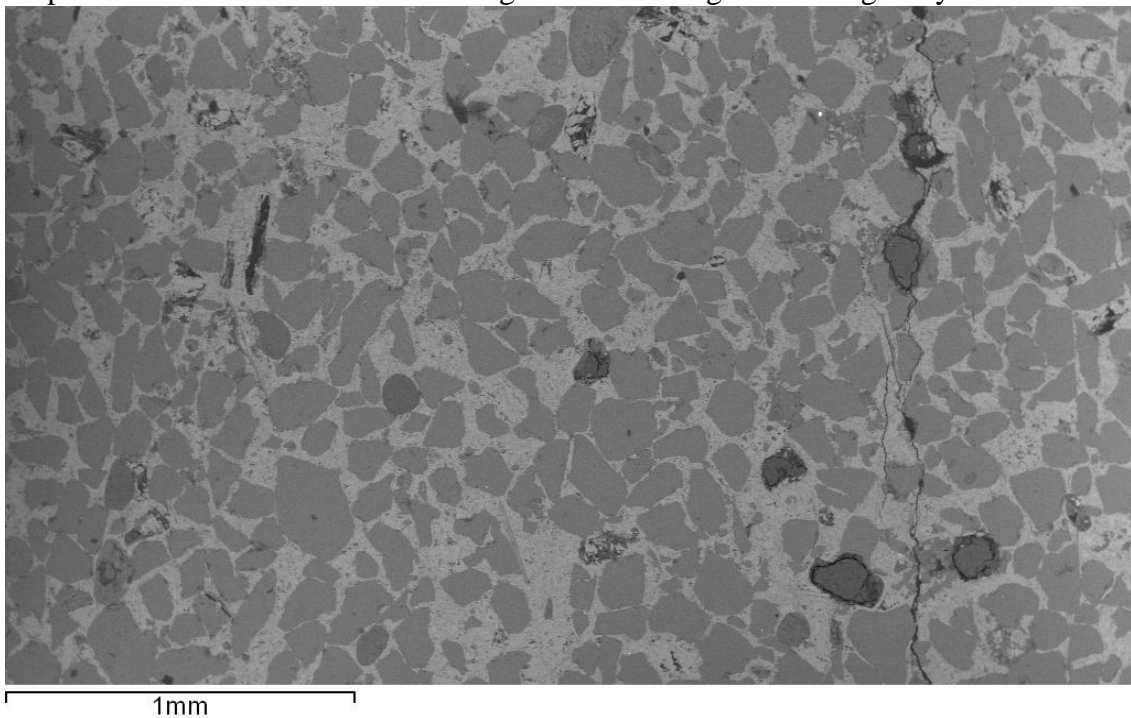
Quartz rich sandstone sample exhibiting angular and elongate to sub-rounded with moderate-to-high sphericity grains, occasional clay and feldspar grains, and visible porosity; the cement, where present, is dominated by grain-coating and pore-filling clays.



MLSE-5: 3341.8m



Fine-grained quartz-rich sandstone sample is well cemented with very little visible porosity, the quartz grains are moderately well-sorted, angular to sub-rounded, the cement is carbonate-rich siderite (confirmed with SEM spectra analysis), and the clays are present as individual well-rounded grains with few grain-coatings clays.



Appendix III. Resistivity Index Graphs

Raw data for the calculation of the saturation exponents from the provided resistivity index data.

To calculate the field average the samples were grouped for the fields and each samples n value were totalled and averaged (Table III.1).

Field	Sample Depth	Sample n	Average
<i>MLNW-5</i>	3509.08	1.9361	2.146633
	<i>MLNW-2</i>	3459.13	
	3497.07	2.5735	
<i>MLSE-5</i>	3330.1	2.0344	
	3338.14	2.1559	
	3341.07	1.9137	
	3347.02	2.1449	
<i>MLN-5</i>	3521.1	2.4562	2.178633
	3521.2	1.7788	
	3523.13	2.3009	

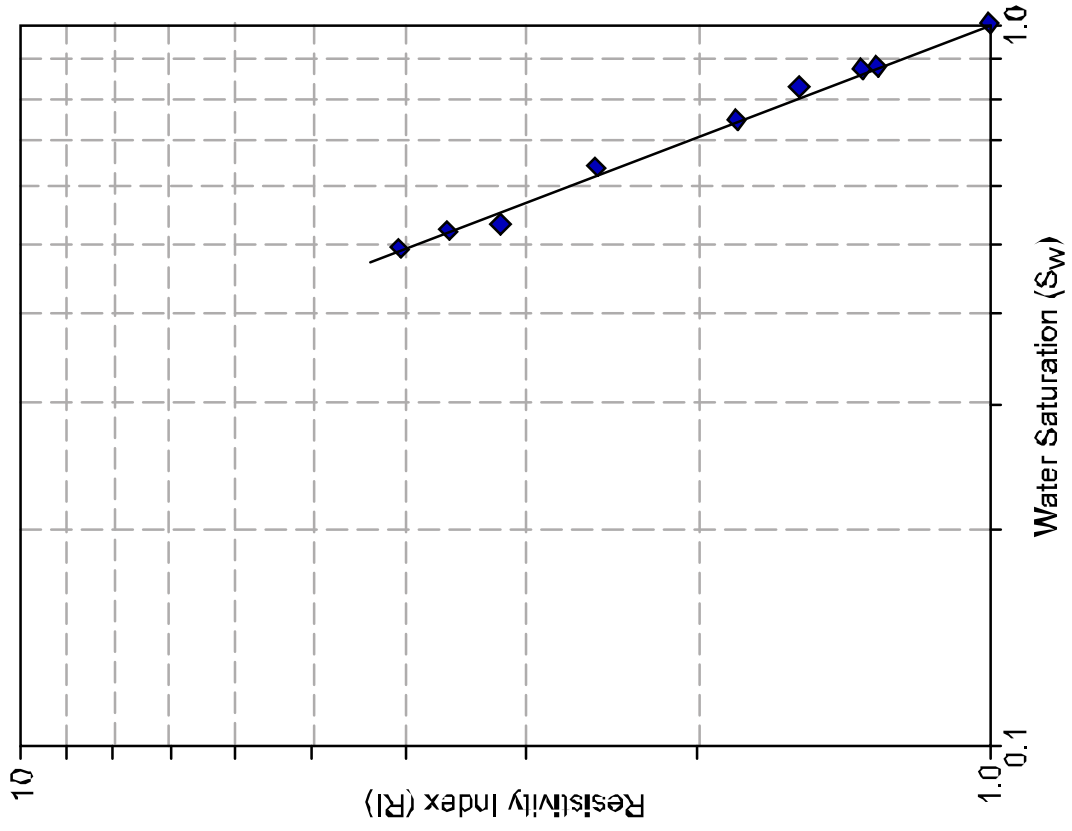
Table III.1: samples grouped for the field and averaged

To calculate the facies average the samples were grouped for the facies defined in chapter 4, and each samples n value were totalled and averaged (Table III.2).

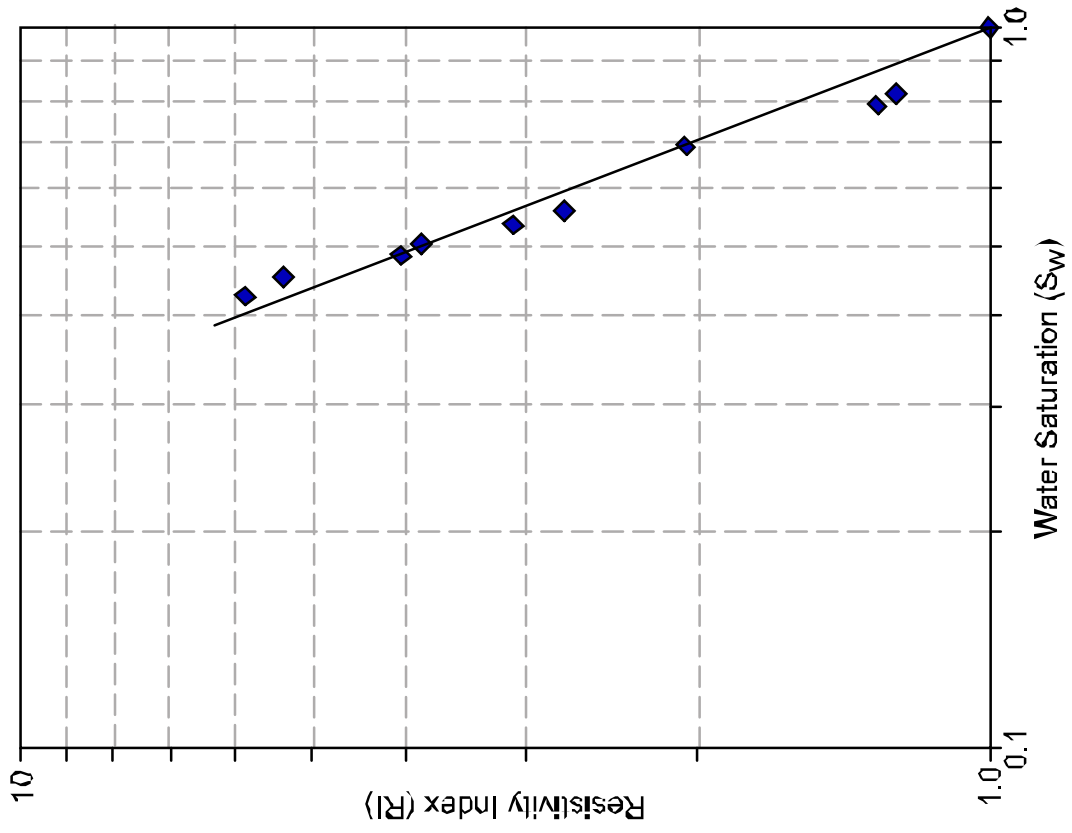
Facies	Well	Sample Depth	Sample n	Facies average
<i>III</i>	<i>MLNW-2</i>	3497.07	2.5735	2.235033
	<i>MLSE-5</i>	3338.14	2.1559	
	<i>MLSE-5</i>	3347.02	2.1449	
	<i>MLN-5</i>	3521.1	2.4562	
	<i>MLN-5</i>	3521.2	1.7788	
	<i>MLN-5</i>	3523.13	2.3009	
<i>VIII</i>	<i>MLNW-5</i>	3509.08	1.9361	1.953625
	<i>MLNW-2</i>	3459.13	1.9303	
	<i>MLSE-5</i>	3330.1	2.0344	
	<i>MLSE-5</i>	3341.07	1.9137	

Table III.2: samples grouped for the sedimentary facies and average

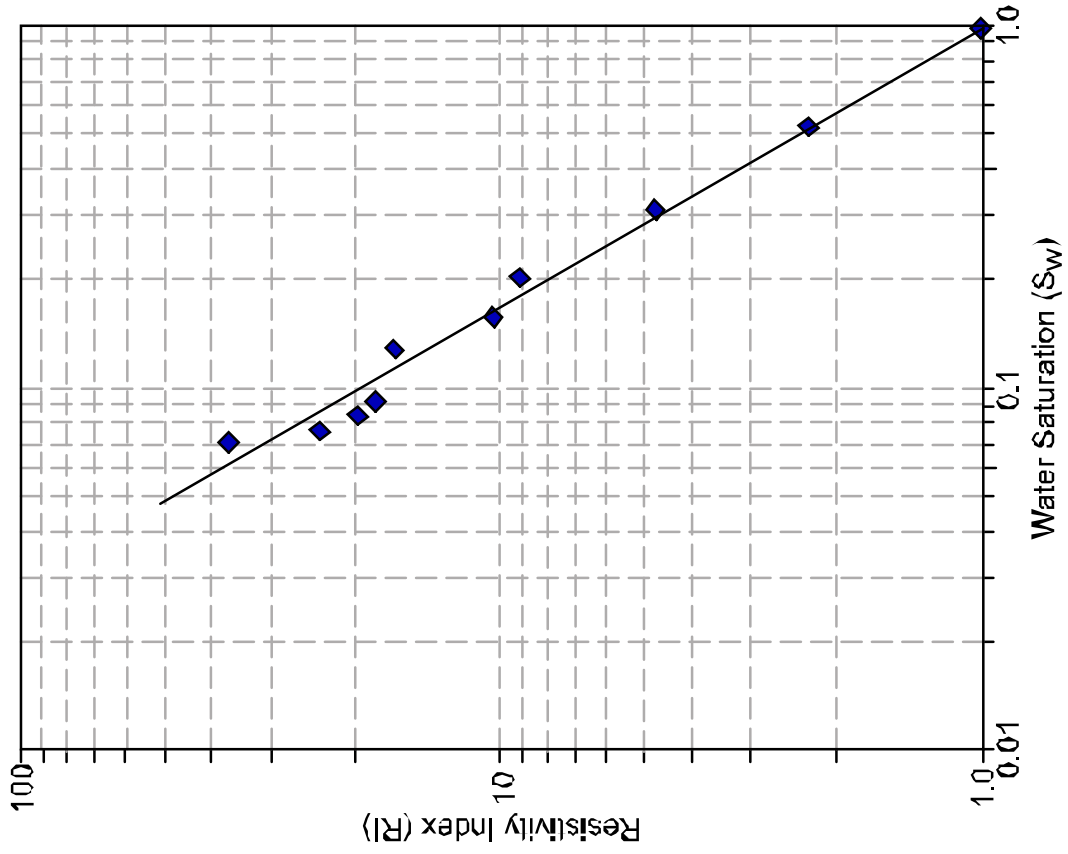
MLNW-5: 3509.08m



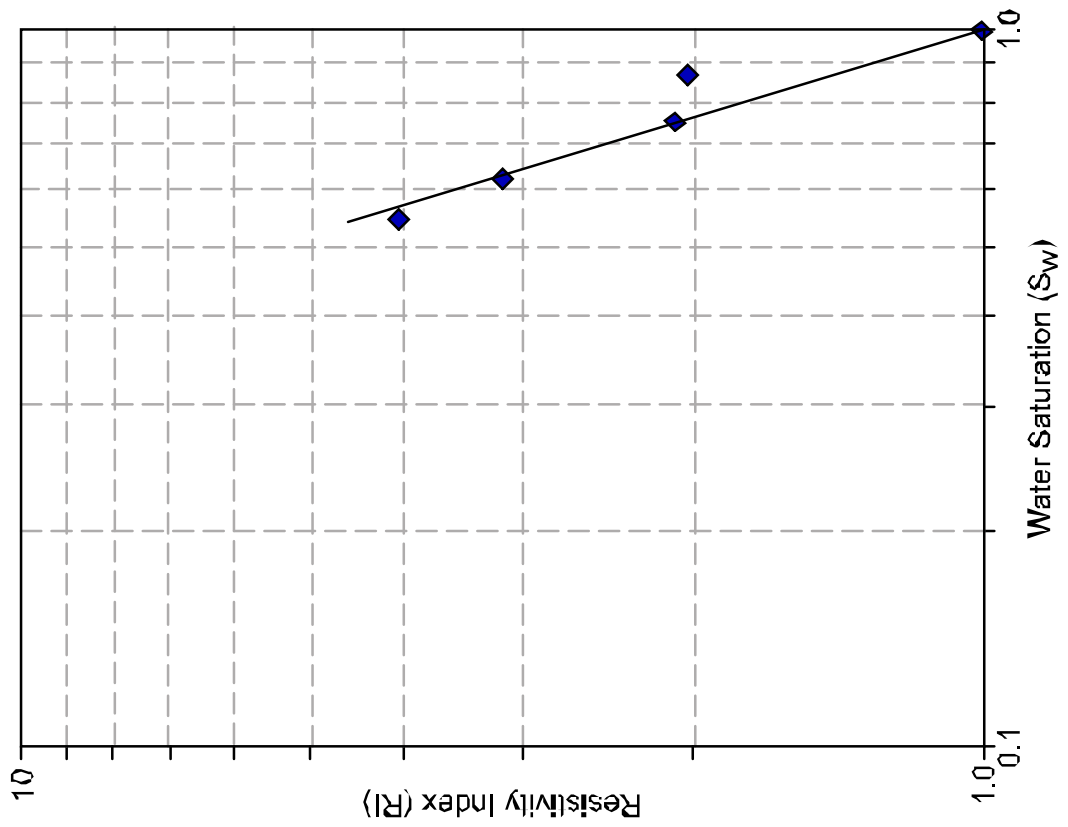
MLNW-2: 3459.13m



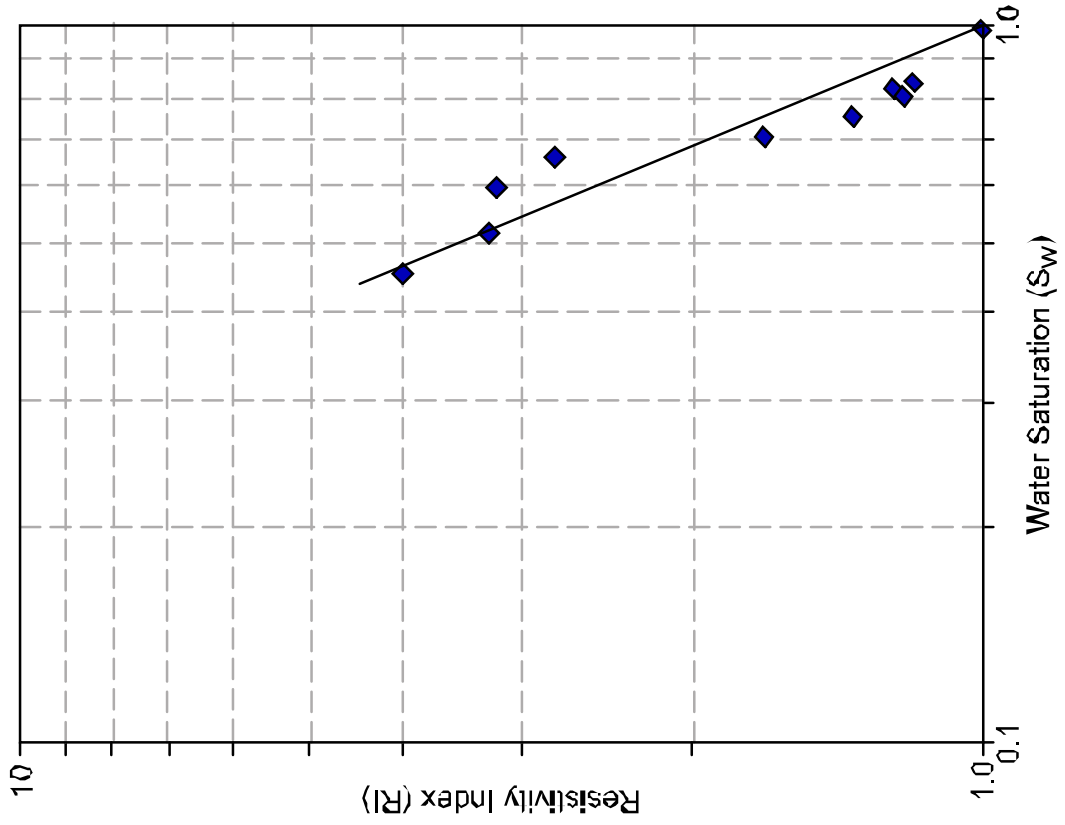
MLNW-2: 3497.07m



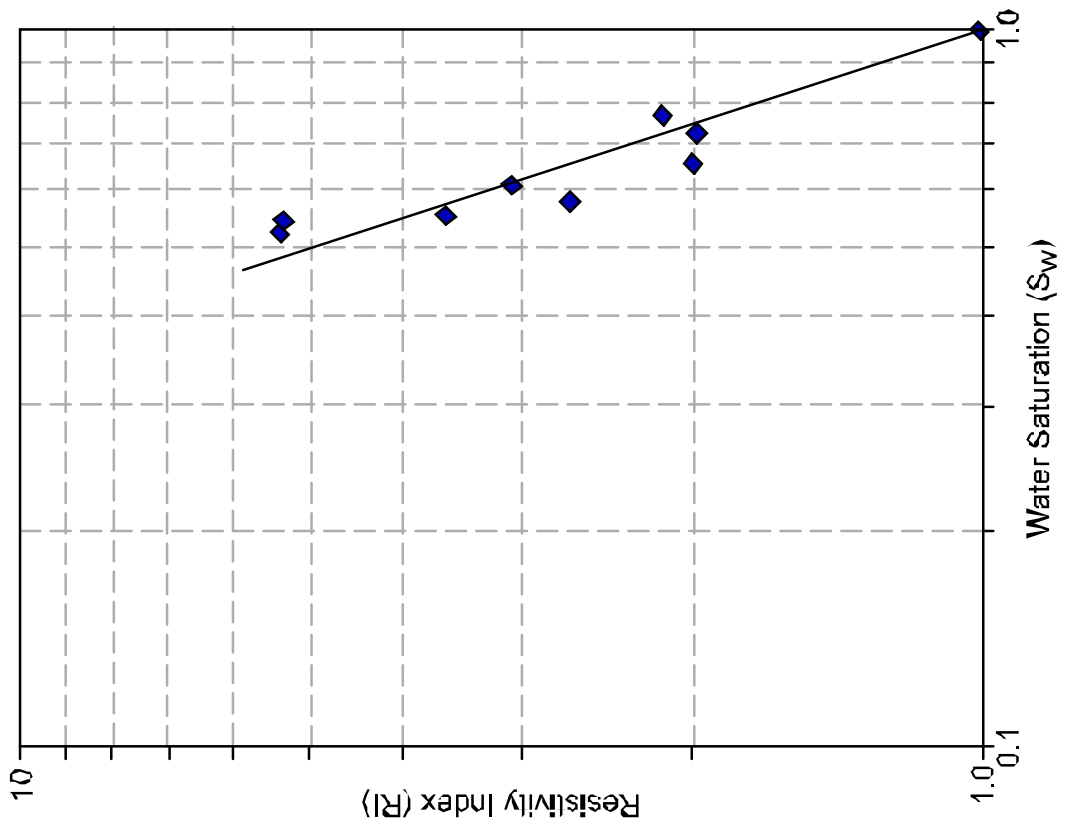
MLN-5: 3521.1m



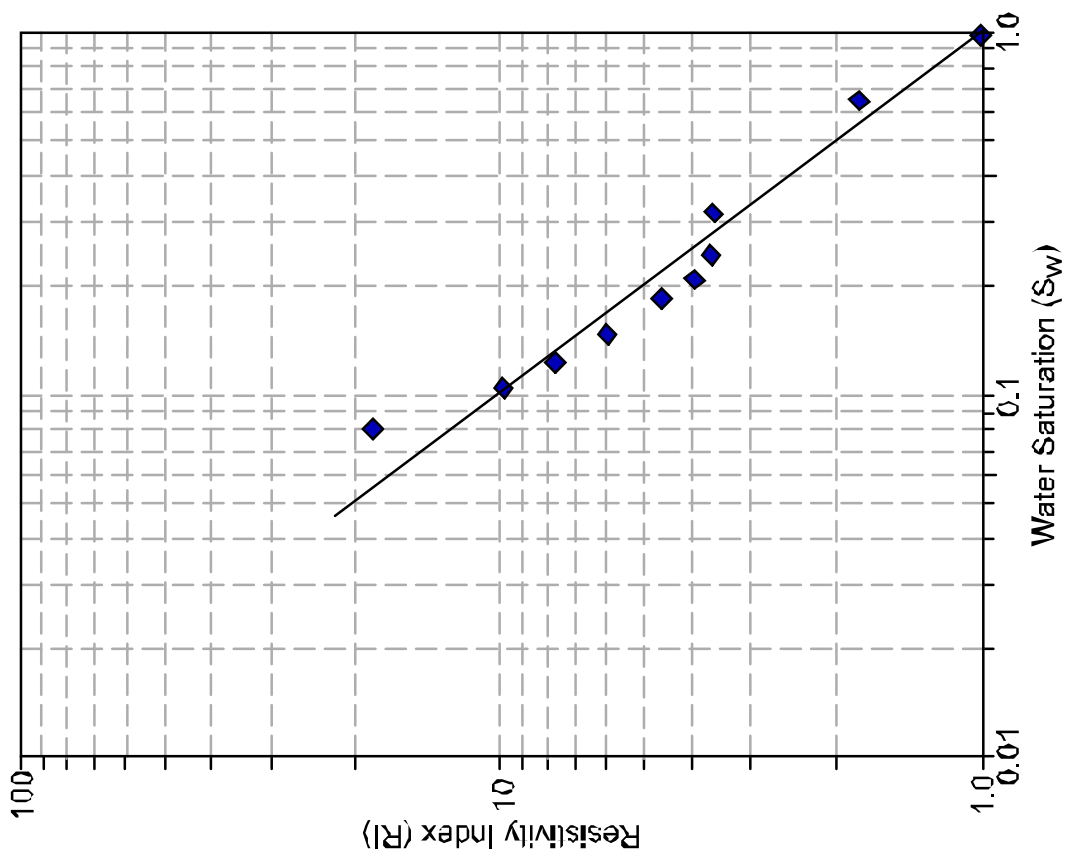
MLN-5: 3521.2m



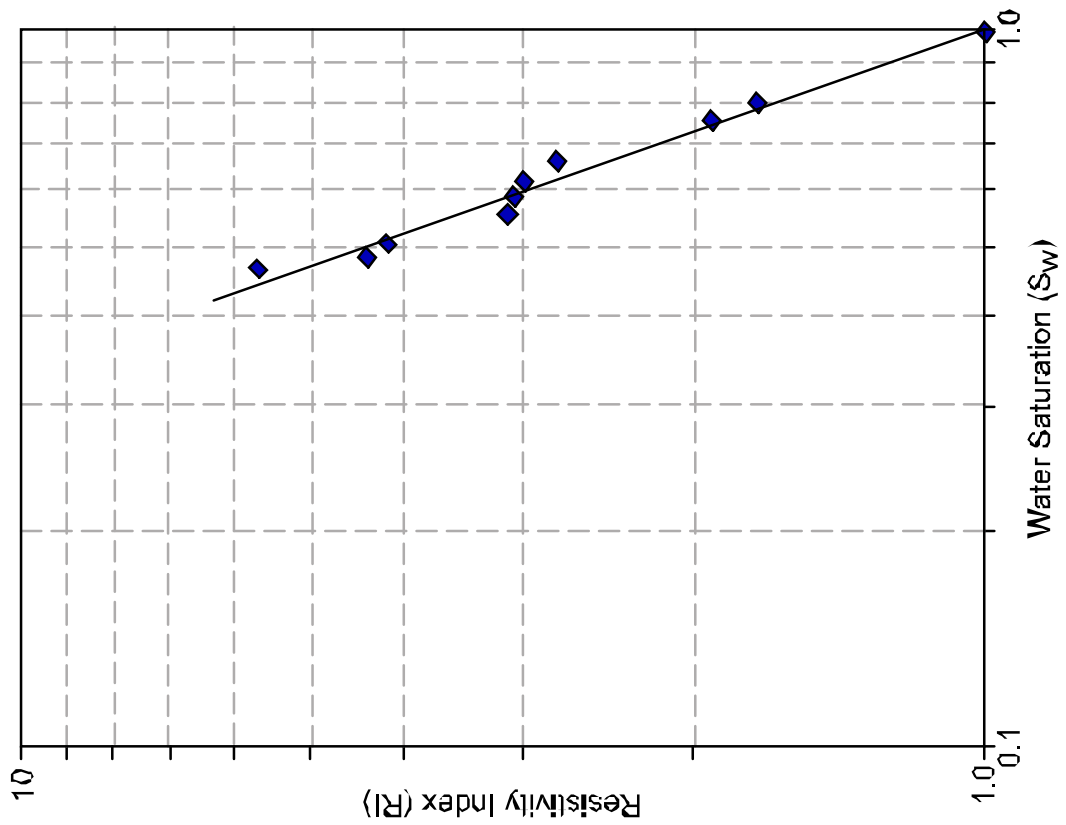
MLN-5: 3523.13m



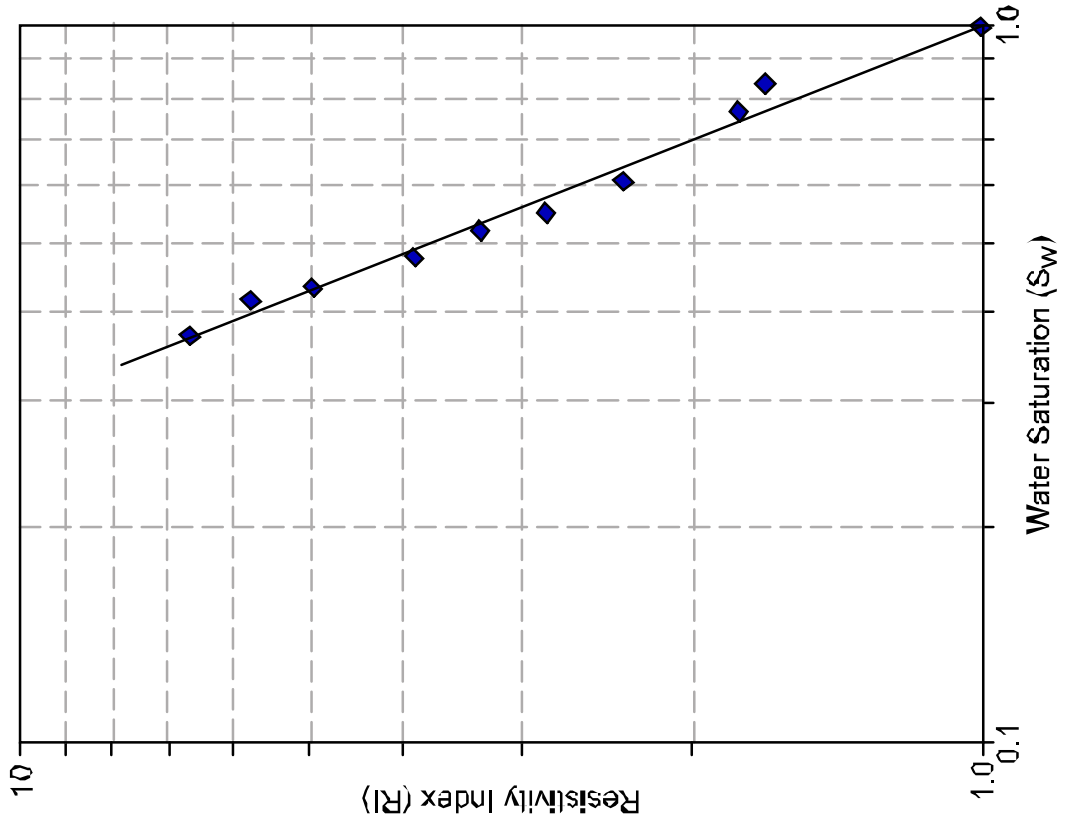
MLSE-5: 3330.1m



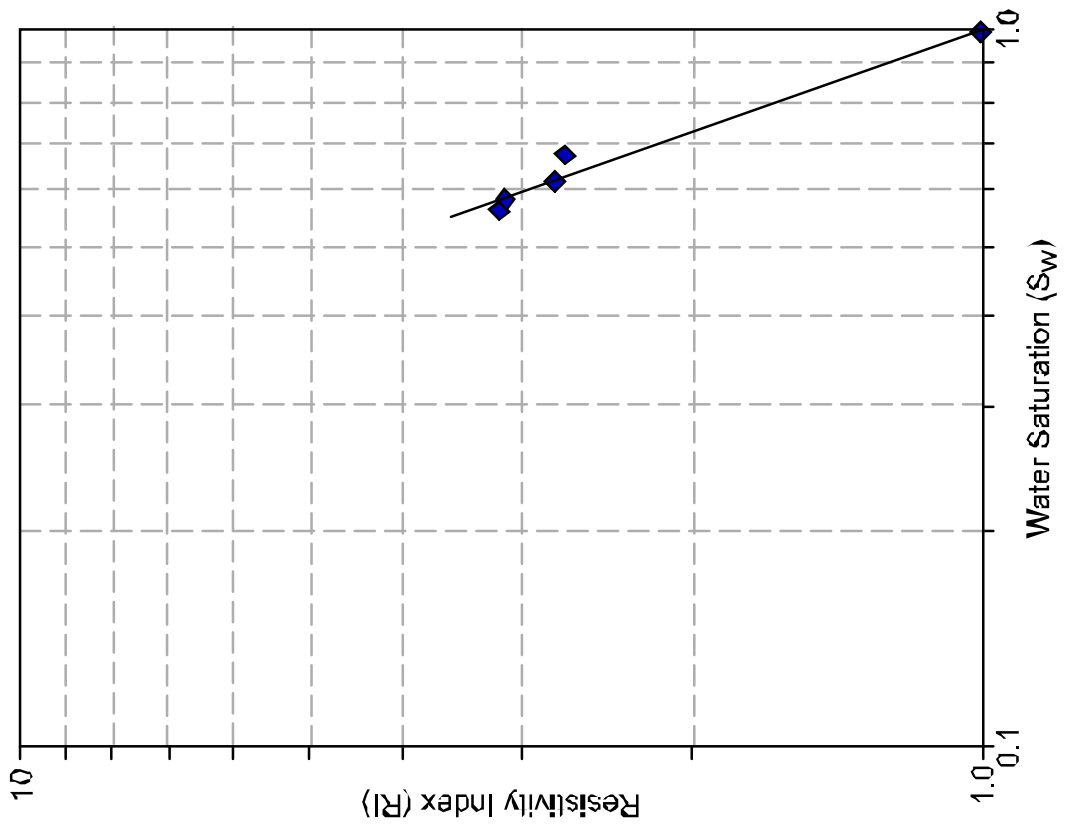
MLSE-5: 3338.14m



MLSE-5: 3341.07m



MLSE-5: 3347.02m



Appendix IV. Capillary Pressure Curves

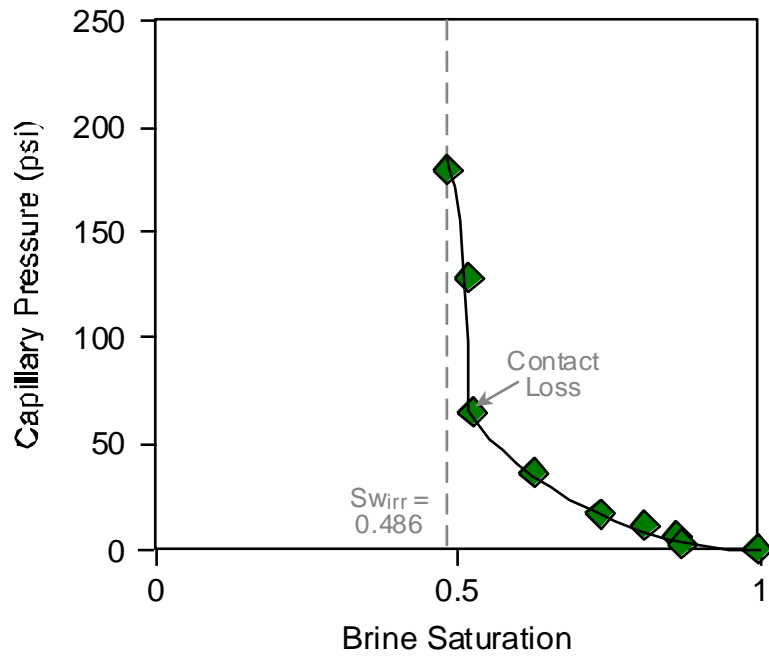
The available capillary pressure curves were provided by ConocoPhillips as part of the initial data set. Measurements were made using both the centrifuge method and the porous plate method. Table IV.1 below documents which samples were analysed with which method. The capillary-pressure based irreducible water saturations are also presented, and summarised in table IV.1.

Method	Well	Sample Depth	Irreducible Water Saturation
<i>Porous Plate</i>	<i>MLNW-5</i>	3509.08	0.486
	<i>MLNW-2</i>	3459.13	0.264
		3497.07	0.424
		3330.1	0.285
	<i>MLSE-5</i>	3338.14	0.467
		3341.07	0.373
		3347.02	0.564
		3521.1	0.547
	<i>MLN-5</i>	3521.2	0.451
		3523.13	0.526
<i>MLNW-5</i>		3509.03	0.475
<i>Centrifuge</i>	<i>MLNW-2</i>	3459.09	0.637
	<i>MLSE-5</i>	3497.03	0.245
		3330.05	0.300
		3332.06	0.259
		3334.06	0.763
	3341.13	0.320	

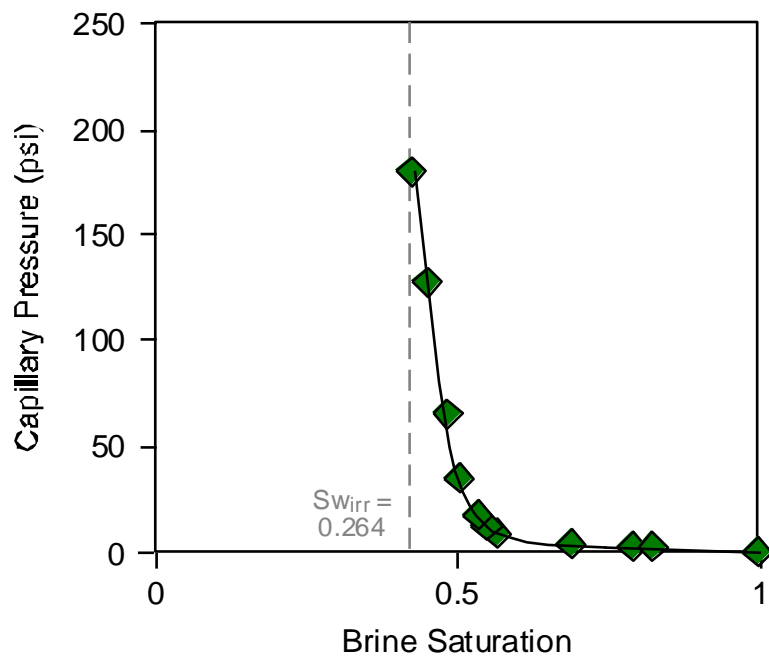
Table IV.1: Capillary pressure samples split for method used, and their irreducible water saturations

Porous Plate Graphs:

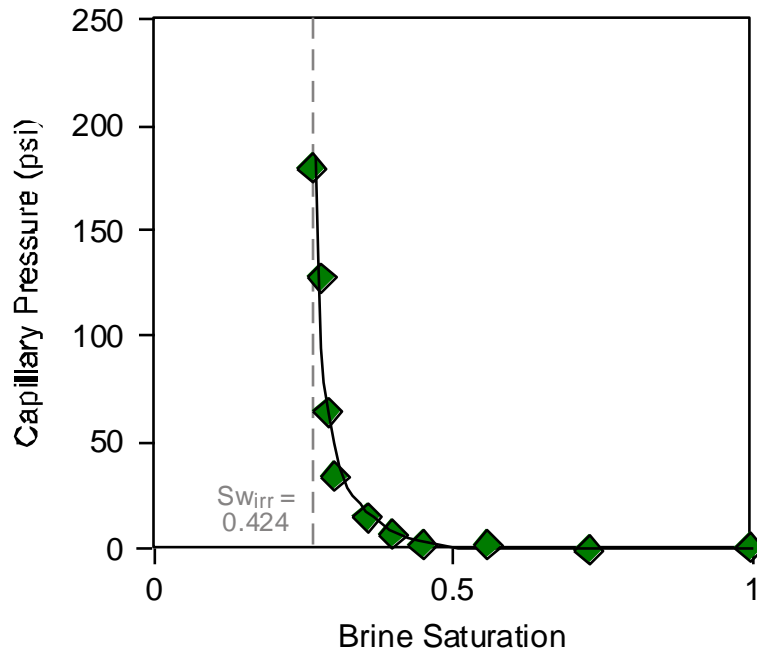
MLNW-5: 3509.08m



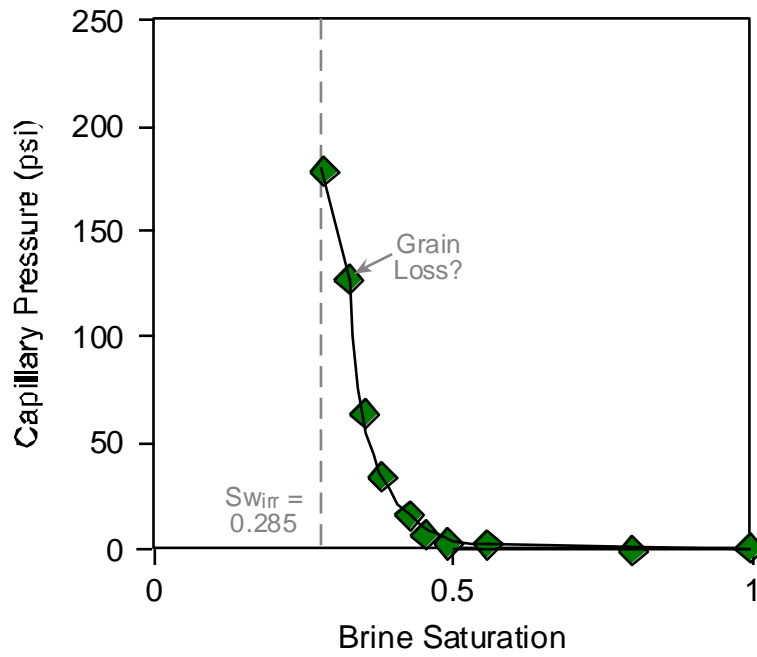
MLNW-2: 3459.13m



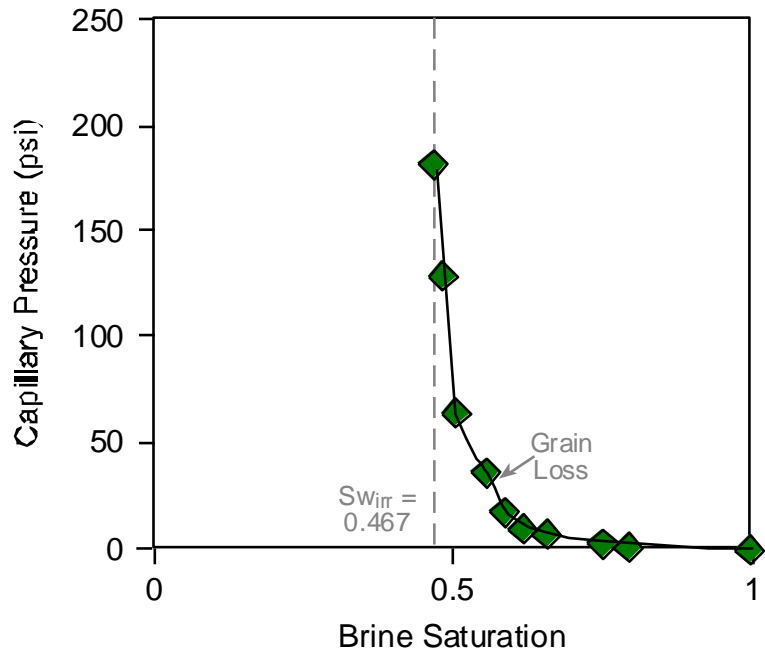
MLNW-2: 3497.07m



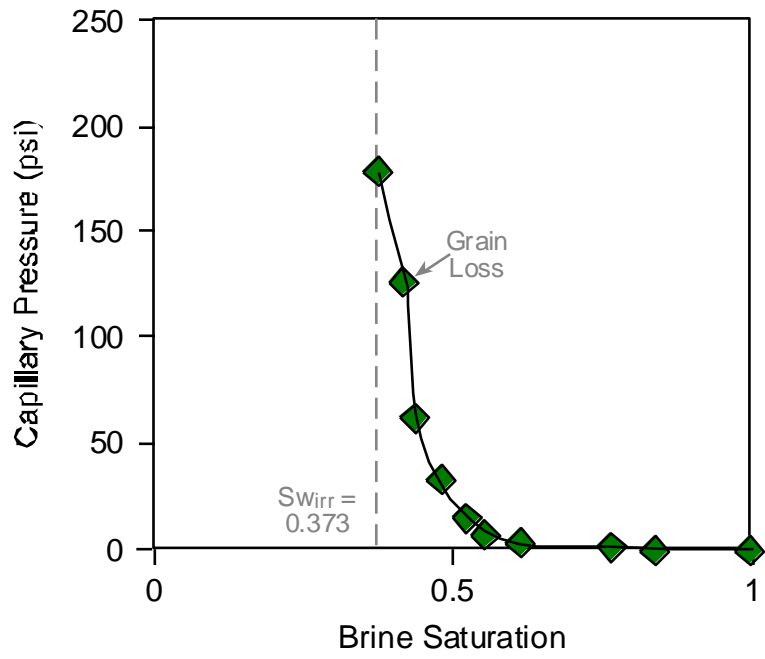
MLSE-5: 3330.1m



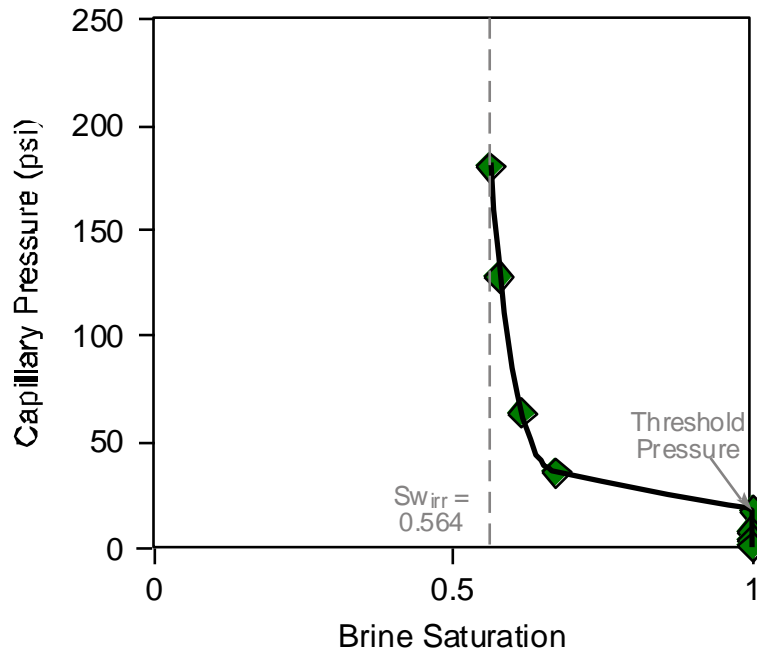
MLSE-5: 3338.14m



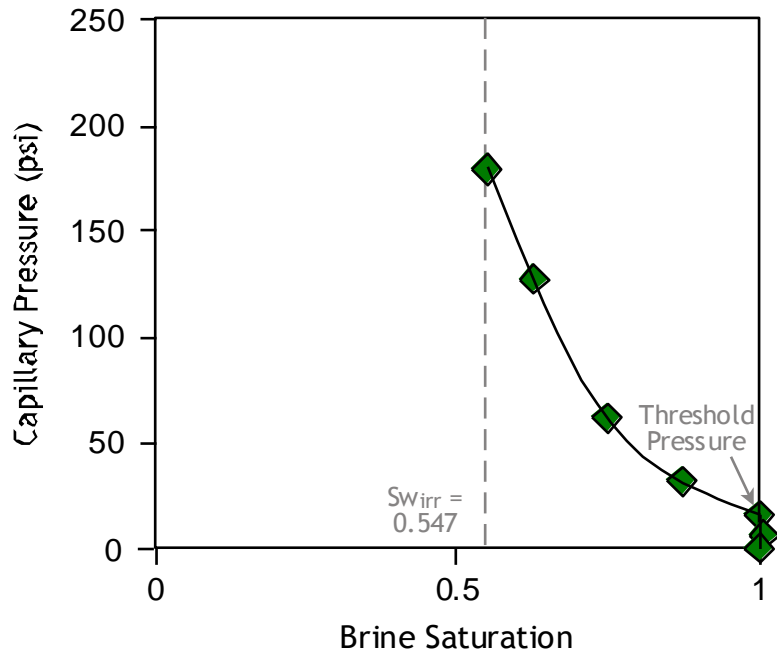
MLSE-5: 3341.07m



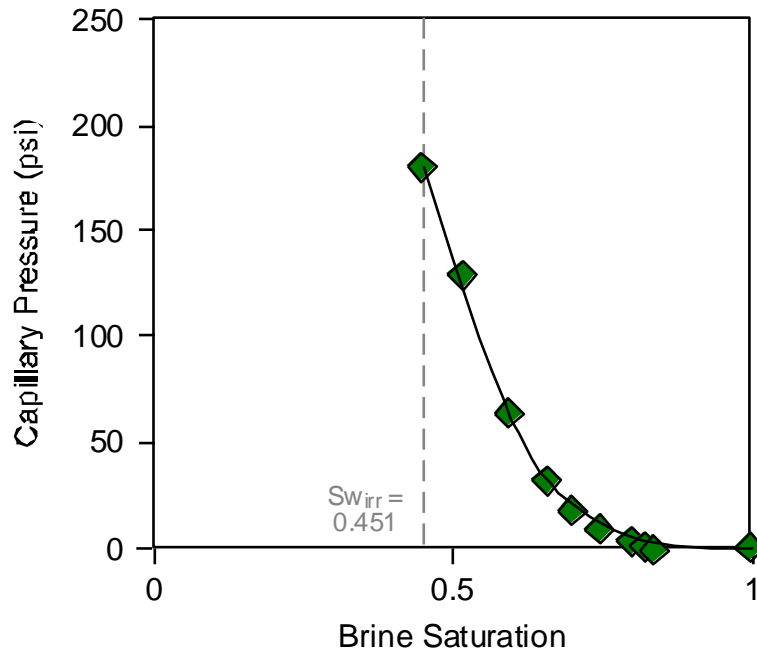
MLSE-5: 3347.02m



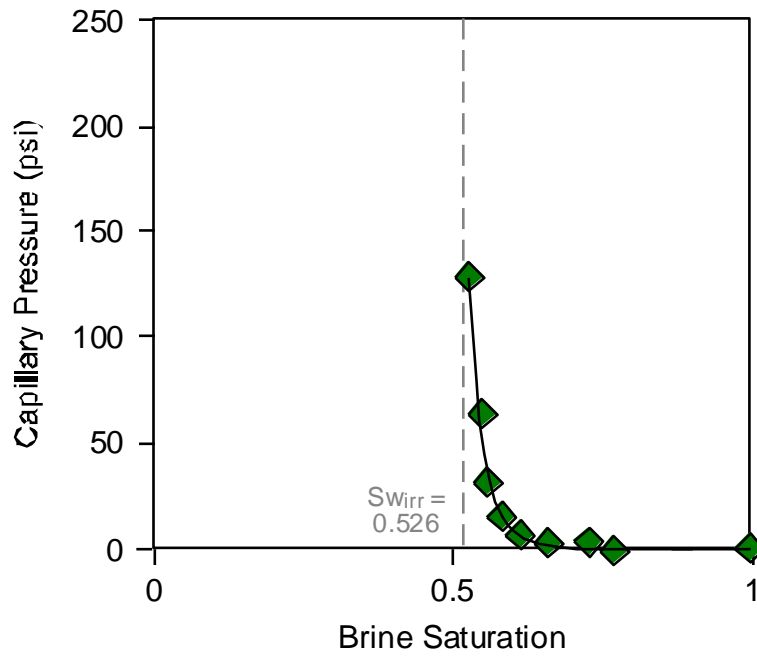
MLN-5: 3521.1m



MLN-5: 3521.2m

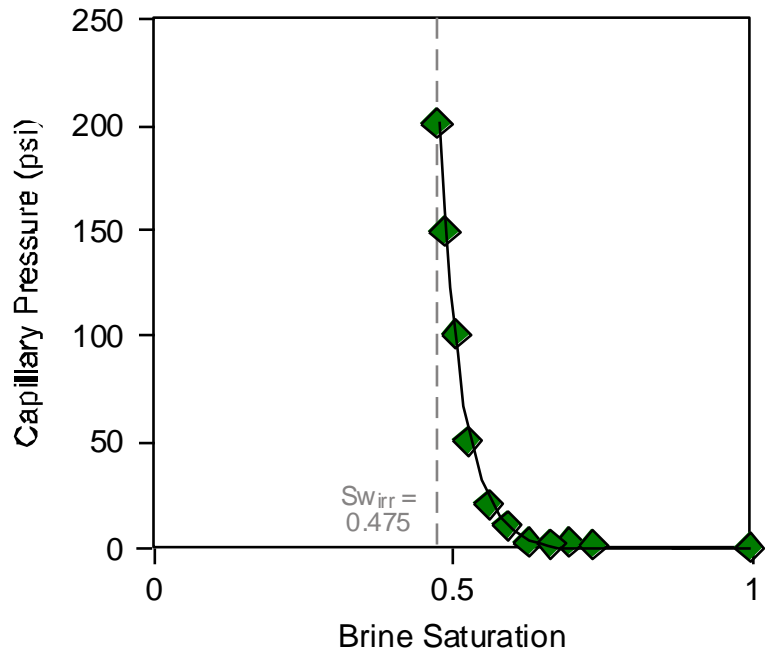


MLN-5: 3523.13m

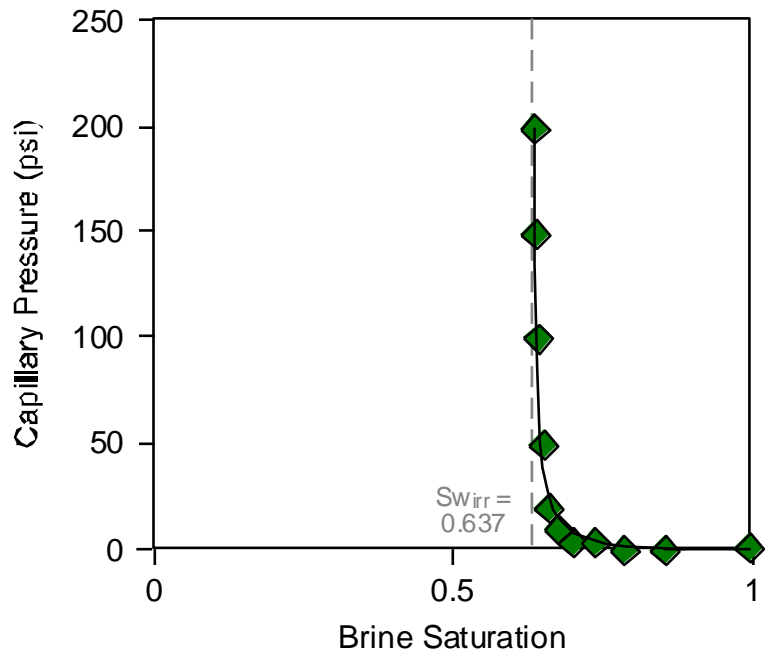


Centrifuge Graphs:

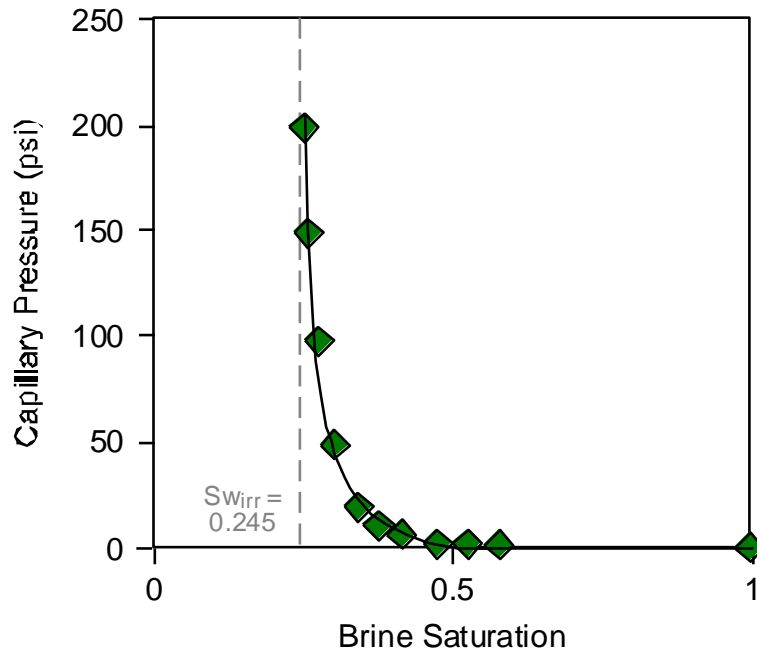
MLNW-5: 3509.03m



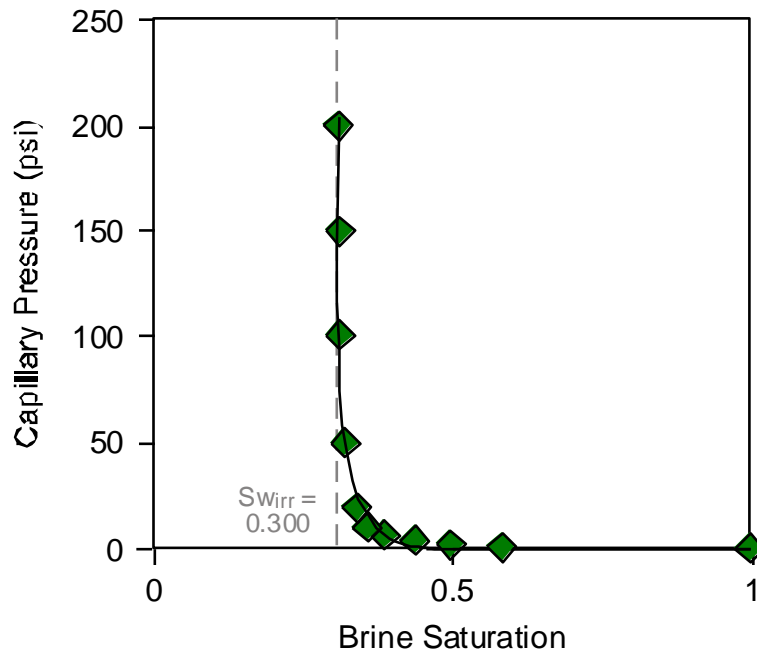
MLNW-2: 3459.09m



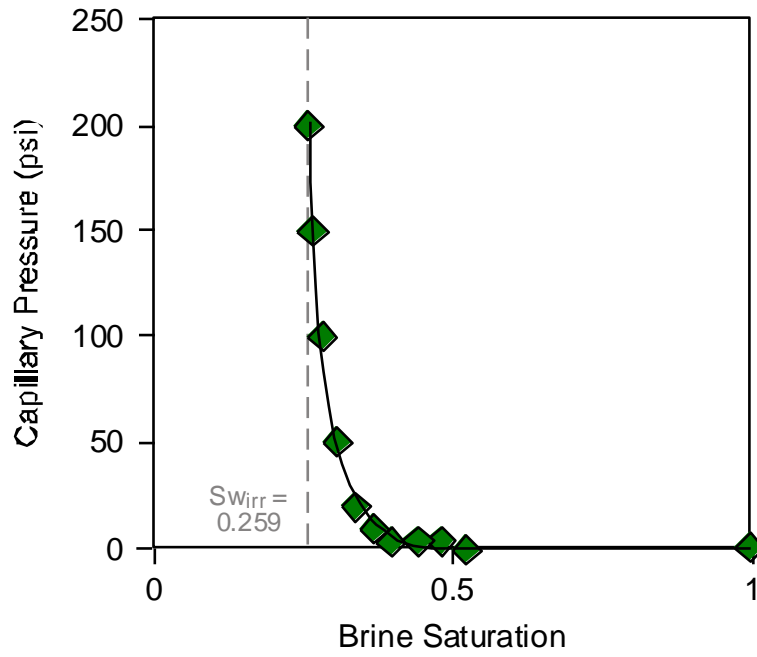
MLNW-2: 3497.03m



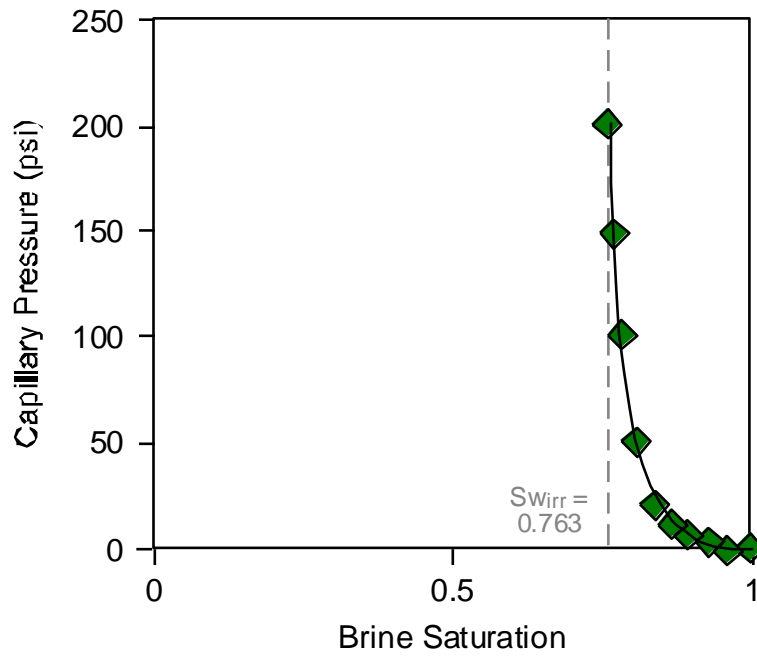
MLSE-5: 3330.05m



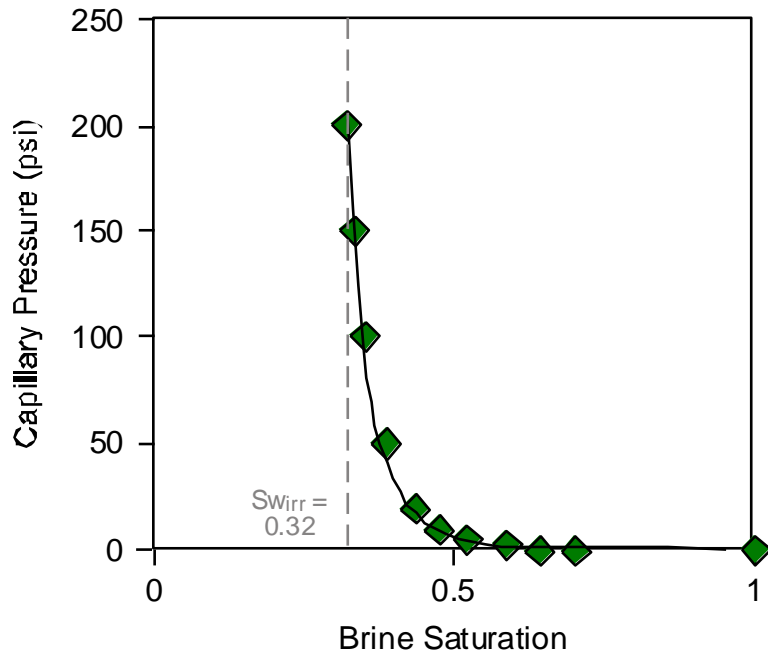
MLSE-5: 3332.06m



MLSE-5: 3334.06m



MLSE-5: 3341.13m



Appendix V. Oil Density Calculations

The oil density of the hydrocarbon filling the three Carboniferous (Tournaisian) reservoirs was available in well-test data. The measurements were made in API units, but for use in the J-function calculations the oil density needs to be in g/cc. A simple conversion exists between the API and the specific gravity of oil density (Schlumberger, 2000) at approximately 60°C:

$$API = \frac{141.5}{SpecificGravity - 131.5}$$

The specific gravity is approximately equal to g/cc, and is considered adequate enough for the calculations. To calculate the specific gravity from API the above equation is rearranged:

$$SpecificGravity = \frac{141.5}{API + 131.5}$$

To obtain the oil density for the F1 reservoirs each value is converted to specific gravity and the averaged value is used (Table V.1).

Well	Formation	Perforation Depth (mRT)	Oil API (deg)	Oil Density – Specific Gravity
<i>MLN-4</i>	Tournaisian A & B	3499.5 - 3516	44.2	0.805
<i>MLN-5</i>	Tournaisian A & B	3515 - 3527	44	0.806
<i>MLN-8</i>	A	3510-3523	43	0.811
<i>MLNW-1</i>	Tournaisian A & B	3477 – 3497.5	42.2	0.814
<i>MLNW-2</i>	A	3465 - 3477	41	0.82
	B	3494 – 3505	48.6	0.786
	C	3533.5 - 3543	49.8	0.78
<i>MLNW-5</i>	C	3579 - 3589	46	0.797
<i>MLSE-4</i>	Tournaisian A	3371-3379	48	0.788
<i>MLSE-5</i>	A	3338 - 3348	52 – 55	0.771 – 0.759
<i>MLW-1</i>	Tournaisian A & B	3461 - 3470	42.3	0.814

Table V.1: Wells, formations and oil density values

Average Specific Gravity = 0.796

Appendix VI. Bibliography

- Aagaard, P., et al. (2000), Formation of grain-coating chlorite in sandstones: Laboratory synthesized vs. natural occurrences, *Clay Minerals*, 35, 261-269.
- Amaefule, O. J., et al. (1993), Enhanced reservoir description: Using core and log data to identify hydraulic (flow) units and predict permeability in uncored intervals/wells, *SPE 26436*.
- Anjos, S. M. C., et al. (2003), Chlorite authigenesis and porosity preservation in the Upper Cretaceous marine sandstones of the Santos Basin, offshore eastern Brazil, in *Clay Mineral Cements in Sandstones*, edited by R. H. Worden and S. Morad, pp. 291 - 316, International Association of Sedimentologists.
- Archie, G. E. (1942), The electrical resistivity log as an aid in determining some reservoir characteristics, *Transactions of the American Institute of Mining and Metallurgical Engineers*, 146, 54-62.
- Berger, A., et al. (2009), Porosity-preserving chlorite cements in shallow-marine volcanoclastic sandstones: Evidence from Cretaceous sandstones of the Sawan gas field, Pakistan, *AAPG Bulletin*, 93, 595 - 615.
- Bertozzi, W., et al. (1981), The physical foundation of formation lithology logging with gamma rays, *Geophysics*, 46, 1439 - 1455.
- Bjorlykke, K. (1998), Clay mineral diagenesis in sedimentary basins - a key to the prediction of rock properties: examples from the North Sea Basin, *Clay Minerals*, 33, 15-34.
- Boles, J. R., and S. G. Franks (1979), Clay diagenesis in Wilcox Sandstones of southwest Texas - Implications of smectite diagenesis on sandstone cementation, *Journal of Sedimentary Petrology*, 49, 55 - 70.

Boote, D. R. D., et al. (1998), Palaeozoic petroleum systems of North Africa, in *Petroleum Geology of North Africa*, edited by D. S. MacGregor, et al., pp. 7 - 68, Geological Society Special Publication No. 132.

Braaksma, H., et al. (2003), Controls on acoustic properties of Upper Jurassic siliclastic rocks (Boulonnais, northern France), *Geophysics*, 68, 58 - 69

Brindley, G. W. (1952), Identification of Clay Minerals by X-Ray Diffraction Analysis, *Clays and Clay Minerals*, 1, 119 - 129.

Brindley, G. W., and G. Brown (Eds.) (1980), *Crystal Structures of Clay Minerals And Their X-ray Identification*, 495 pp.

Calhoun, J. C., Jr, et al. (1949), Experiments on the capillary properties of porous solids, *Transactions of the American Institute of Mining and Metallurgical Engineers*, 189, 189-196.

Chow, J. J., et al. (2005), Geophysical Well Log Study on the Paleoenvironment of the Hydrocarbon Producing Zones in the Erchungchi Formation, Hsinyin, SW Taiwan, *Terrestrial, Atmospheric and Oceanic Sciences*, 16, 531 - 545

Clavier, C., et al. (1984), Theoretical and Experimental Bases for the Dual Water Model for Interpretation of Shaly Sands, *Society of Petroleum Engineers Journal*, 24, 153-168.

Cochran, M. D., and L. E. Petersen (2001), Hydrocarbon exploration in the Berkiné Basin, Grand Erg Oriental, Algeria, in *Petroleum provinces of the twenty-first century*, edited by M. W. Downey, et al., pp. 531 - 557.

Craig, A. (2003), Advanced Rock Properties Study For Burlington Resources: Well MLNW-5, MLNW-2, Core Laboratories (U.K) Ltd.

Cuddy, S., et al. (1993), A Simple, Convincing Model For Calculating Water Saturations in Southern North Sea Gas Fields, paper presented at SPWLA Symposium Transactions.

Davis, J. C. (2002), *Statistics and data analysis in geology*, Third Edition ed., 638 pp., J. Wiley & Sons

Deer, W. A., et al. (1992), *An Introduction to the rock-forming minerals*, Second ed., 696 pp., Longmann Scientific and Technical Press.

Dixon, S. A., et al. (1989), Diagenesis and preservation of porosity in Norphlet Formation (Upper Jurassic), Southern Alabama, *AAPG Bulletin*, 73, 707 - 728.

Doveton, J. H. (1994), *Geologic Log Analysis Using Computer Methods*, AAPG Computer Applications in Geology, No. 2.

Durand, C., et al. (2001), Effect of pore-lining chlorite on petrophysical properties of low-resistivity sandstone reservoirs, *SPE Reservoir Evaluation and Engineering*, 231 - 239.

Edmundson, H. N. (1988a), Archie's Law: Electrical Conduction in Clean, Water-bearing Rock, *The Technical Review*, 36, 4 - 13.

Edmundson, H. N. (1988b), Archie II: Electrical Conduction in Hydrocarbon-Bearing Rock, *The Technical Review*, 36, 12-21.

Edmundson, H. N., and L. L. Raymer (1979), Radioactive logging parameters for common minerals, in *SPWLA 20th Annual Logging Symposium*, edited, p. Paper O.

Ehrenberg, S. N. (1993), Preservation of anomalously high porosity in deeply buried sandstones by grain-coating chlorite; examples from the Norwegian continental shelf., *The American Association of Petroleum Geologists Bulletin*, 77, 1260-1286.

Ellis, D. (2003a), Formation porosity estimation from density logs, *Petrophysics*, 44, 306-316.

Ellis, D. (2003b), Tutorial - Porosity from Neutron Logs I - Measurement, *Petrophysics*, 44.

Ellis, D. (2004), Tutorial - Porosity from Neutron Logs II - Interpretation, *Petrophysics*, 45.

Ellis, D. V. (1987), *Well Logging for Earth Scientists*, 532 pp., Elsevier Science Publishing Co., Inc.

Fekirine, B., and H. Abdallah (1998), Palaeozoic lithofacies correlatives and sequence stratigraphy of the Saharan Platform, Algeria, in *Petroleum Geology of North Africa*, edited by D. S. MacGregor, et al., pp. 97-108, Geological Society Special Publication No. 132.

Gall, B. L., et al. (1983), Semiautomated method for cation-exchange-capacity determination of reservoir rocks, *Society of Petroleum Engineers*, 23, 231 - 237.

Grigsby, J. D. (2001), Origin and growth mechanism of authigenic chlorite in sandstones of the Lower Vicksburg Formation, south Texas, *Journal of Sedimentary Research*, 71, 27 - 36.

Gross, J. S., et al. (1995), Reservoir distribution and exploration potential of the Spiro Sandstone in the Choctaw Trend, Arkoma Basin, Oklahoma and Arkansas, *AAPG Bulletin*, 79, 159 - 185.

Gupta, R., and H. D. Johnson (2001), Characterization of heterolithic deposits using electrofacies analysis in the tide-dominated Lower Jurassic Cook Formation (Gulfaks Field, offshore Norway), *Petroleum Geoscience*, 7, 321 - 330.

Harrison, B., and X. D. Jing (2001), Saturation Height Methods and Their Impact on Volumetric Hydrocarbon in Place Estimates, *Society of Petroleum Engineers*.

Hearst, J. R., et al. (1999), *Well Logging for Physical Properties: A Handbook for Geophysicists, Geologists and Engineers*, Second Edition ed., John Wiley & Sons, Ltd.

Henn, F., et al. (2001), Are pore-lining chlorites a cause of low resistivity in sandstones?, *SCA 2001*, 34.

Heslop, A. (1974), Gamma-ray log response of shaly sandstones, *The Log Analyst*, XV, 16 - 21.

Hill, H. J., and J. D. Milburn (1956), Effect of clay and water salinity on electrochemical behaviour of reservoir rocks, *Transactions of the American Institute of Mining and Metallurgical Engineers*, 207.

Hillier, S. (1994), Pore-lining chlorites in siliclastic reservoir sandstones: electron microprobe, SEM and XRD data, and implications for their origin., *Clay Minerals*, 29, 665-679.

Hinton, P. R. (2004), *Statistics Explained*, 379 pp., Routledge.

Hoffman, N. W., and H. J. Tobin (2004), An empirical relationship between velocity and porosity for underthrust sediments in the Nankai Trough Accretionary Prism, in *Proceedings of the Ocean Drilling Program, Scientific Results*, edited by H. Mikada, et al.

Houseknecht, D. W., and T. A. McGilvery (1990), Red Oak Field, in *Structural Traps II. Atlas of Giant Oil and Gas Fields*, edited by E. A. Beaumont and N. H. Foster, pp. 201 - 225, American Association of Petroleum Geologists.

Howard, J. J. (1992), Influence of authigenic-clay minerals on permeability, in *Origin, Diagenesis, and Petrophysics of Clay Minerals in Sandstones*, edited by D. W. Houseknecht and E. D. Pittman, pp. 257 - 264, Society for Sedimentary Geology, Special Publication No. 47.

Hook, J. R. (2003), An Introduction to Porosity, *Petrophysics*, 44, 205 - 212.

Hughes, A., et al. (2003), edited, Burlington Resources / ConocoPhillips.

Humphreys, B., and G. K. Lott (1990), An investigation into nuclear log responses of North Sea Jurassic sandstones using mineralogical analysis, in *Geological Applications of Wireline Logs*, edited by A. Hurst, et al., pp. 223 - 240, The Geological Society.

Humphreys, B., et al. (1989), Authigenic chlorite in late Triassic sandstones from the Central Graben, North Sea, *Clay Minerals*, 24.

Hurst, A. (1990), Natural gamma-ray spectrometry in hydrocarbon-bearing sandstones from the Norwegian Continental Shelf, in *Geological Applications of Wireline Logs*, edited by A. Hurst, et al., pp. 211-222, The Geological Society Special Publication Classics.

Islam, M. A. (2009), Diagenesis and reservoir quality of Bhuben sandstones (Neogene), Titas Gas Field, Bengal Basin, Bangladesh, *Journal of Asian Earth Sciences*, 35, 89 - 100.

Juhász, I. (1979), The central role of Qv and formation-water salinity in the evaluation of shaly formations, *Transactions of the SPWLA Twentieth Annual Logging Symposium*, AA1-AA26.

Klett, T. R. (2000), Total petroleum systems of the Trias/Ghadames province, Algeria, Tunisia and Libya - The Tanezzuft-Oued Mya, Tanezzuft-Melrhir and Tanezzuft-Ghadames, *U.S. Geological Survey Bulletin* 2002-c.

Larsen, O. H., and H. Friis (1991), Petrography, diagenesis and pore-water evolution of the shallow marine sandstone (Hasle Formation, Lower Jurassic, Bornholm, Denmark), *Sedimentary Geology*, 72, 269 - 284.

Lasswell, P., M. (2006), Core Analysis for Electrical Properties, *Petrophysics*, 47, 191 - 213.

Le Heron, D. P., et al. (2009), Ancient glaciations and hydrocarbon accumulations in North Africa and the Middle East, *Earth Science Reviews*, 93, 47 - 76.

Leverett, M. C. (1941), Capillary Behavior in Porous Solids, *Transactions of the American Institute of Mining and Metallurgical Engineers*, 142, 152-169.

Lindsay, C. (2002), Advanced Rock Properties Study For Burlington Resources: Well MLNW-1, Core Laboratories (U.K.) Ltd.

Lofts, J., and G. Page (Eds.) (2002), *Defining Thin Beds and Improving Net Pay with Modern Logging and Core-interpretation Techniques*, 39-53 pp.

Longstaffe, F. J. (1986), Oxygen isotope studies of diagenesis in the Basal Belly River Sandstone, Pembina I-pool, Alberta, *Journal of Sedimentary Petrology*, 56, 77-88.

Lumsden, D. N., et al. (1971), Sedimentation and petrology of Spiro and Foster Sands (Pennsylvanian), McAlester Basin, Oklahoma, *AAPG Bulletin*, 55, 254 - 266.

Luo, J. L., et al. (2009), Impact of diagenesis on reservoir-quality evolution in fluvial and lacustrine-deltaic sandstones: evidence from Jurassic and Triassic sandstones from the Ordos Basin, China, *Journal of Petroleum Geology*, 32, 79 - 102.

Manghnani, M. H., and J. Hower (1964), Glauconites: Cation Exchange Capacities and infrared spectra, *The American Mineralogist*, 49, 586 - 598.

Market, J. (2008), Broad frequency LWD multipole tools provide high quality compressional and shear data in a wide variety of formations, *Petrophysics*, 49, 146-158.

McPhee, C. (2009), *Special Core Analysis*, Senergy Energy.

Milliken, K. L. (2003), Microscale distribution of kaolinite in Breathitt Formation sandstones (middle Pennsylvanian): implications for mass balance, in *Clay Mineral Cements in Sandstones*, edited by R. H. Worden and S. Morad, International Association of Sedimentologists Special Publication 34.

Milodowski, A. E., and J. A. Zalasiewicz (1991), The origin and sedimentary, diagenetic and metamorphic evolution of chlorite-mica stacks in Llandovery sediments of central Wales, U.K, *Geological Magazine*, 128, 263 - 278.

Moore, D. M., and C. R. Reynolds, Jr. (1997), *X-ray Diffraction and the Identification and Analysis of Clay Minerals*, Second Edition ed., 378 pp., Oxford University Press.

McNeill, I. (2006), Personal Communication, edited.

Nadeau, P. H. (2000), The Sleipner Effect: a subtle relationship between the distribution of diagenetic clay, reservoir porosity, permeability and water saturation, *Clay Minerals*, 35, 185 - 200.

Nashawi, I. S., and A. Malallah (2009), Improved Electrofacies characterization and permeability prediction in sandstone reservoirs using a data mining and expert system approach, *Petrophysics*, 50, 250 - 268

Needham, S.J., Worden, R.H., and McIlroy, D., 2005, Experimental production of clay rims by macrobiotic sediment ingestion and excretion processes: *Journal of Sedimentary Research*, v. 75, p. 1028 - 1037.

Newman, A. C. D. (Ed.) (1987), *Chemistry of Clay and Clay Minerals*, 480 pp.

Norry, M. J., et al. (1994), Mineralogy and geochemistry of the Peterborough Member, Oxford Clay Formation, Jurassic, UK: element fractionation during mudrock sedimentation, *Journal of the Geological Society, London*, 151, 195 - 207.

Parkinson, N. (2001), MLNW-1 Core Shifts, *Burlington Resources Internal Publication*.

Pay, M. D., et al. (2000), Clay mineral distribution in the Devonian-Carboniferous sandstones of the Clair Field, West of Shetland, and its significance for reservoir quality, *Clay Minerals*, 35.

Pelling, R., et al. (1991), Statistical Analysis of Geochemical Logging Tool Data from Hole 735B, Atlantis Fracture Zone, Southwest Indian Ocean, *Proceedings of the Ocean Drilling Program*, 118, 271 - 283.

Pickett, G. R. (1966), A review of current technologies for determination of water saturation from logs, *SPE Journal of Petroleum Technology*, 1425 - 1435.

Pirmez, C., et al. (1997), Clay content, porosity and velocity of Amazon Fan sediments determined from ODP Leg 155 cores and wireline logs, *Geophysical Research Letters*, 24, 317-320.

Pittman, E. D. (1988), Diagenesis of Terry Sandstone (Upper Cretaceous), Spindle Field, Colorado, *Journal of Sedimentary Petrology*, 58, 785 - 800.

Pittman, E. D., et al. (1992), Clay coats: Occurrence and relevance to preservation of porosity in sandstones, in *Origin, Diagenesis and Petrophysics of clay minerals in sandstones*, edited by D. W. Houseknecht and E. D. Pittman, SEPM (Society for Sedimentary Geology).

Poulos, S. E., et al. (1996), Deltaic sedimentation, including clay mineral deposition patterns, associated with small mountainous rivers and shallow marine embayments of Greece (SE Alpine Europe), *Journal of Coastal Research*, 12, 940-952.

Poupon, A., et al. (1970), Log analysis of sand-shale sequences - a systematic approach, *Journal of Petroleum Technology*, 22, 867 - 881

Poupon, A., and J. Leveaux (1971), Evaluation of water saturation in shaly formations, *The Log Analyst*, 7, 3 - 8.

Rabaute, A., et al. (2003), In situ mineralogy and permeability logs from downhole measurements: Application to a case study in chlorite-coated sandstones, *Journal of Geophysical Research*, 108.

Raymer, L. L., et al. (1980), An improved sonic transit time-to-porosity transform, *SPWLA 21st Annual Logging Symposium*.

Revil, A., et al. (1998), Electrical conductivity in shaly sands with geophysical applications, *Journal of Geophysical Research - Solid Earth*, 103, 23925 - 23936.

Rider, M. (2004), *The Geological Interpretation of Well Logs*, Second ed., 280 pp., Whittles Publishing.

Ringen, J. K., et al. (2001), Reservoir water saturation measured on cores; case histories and recommendations, *Proceedings of the 6th Nordic Symposium on Petrophysics*, 1 - 13.

Ryan, P. C., and S. Hillier (2002), Berthierine/chamosite, corrensite and discrete chlorite from evolved verdine and evaporite-associated facies in the Jurassic Sundance Formation, Wyoming, *American Mineralogist*, 87, 1607-1615.

Ryan, P. C., and R. C. Reynolds (1996), The origin and diagenesis of grain-coating serpentine-chlorite in Tuscaloosa Formation sandstone, US Gulf Coast, *American Mineralogist*, 81, 213 - 225.

Sahagian, D. (1988), Epeirogenic motions of Africa as inferred from Cretaceous shoreline deposits, *Tectonics*, 7, 125 - 138.

Saner, S., et al. (2006), Mineralogical, pore and petrophysical characteristics of the Devonian Jauf sandstone reservoir, Hawiyah Field, Eastern Saudi Arabia *Journal of Petroleum Geology*, 29, 257 - 272.

Schlumberger (2000), *Log Interpretation Charts*.

Schmid, S., et al. (2004), Diagenesis and reservoir quality of the Sherwood Sandstone (Triassic), Corrib Field, Slyne Basin, west of Ireland, *Marine and Petroleum Geology*, 21, 299 - 315.

Serra, O., and L. Serra (2003), *Well Logging and Geology*.

Skelt, C., and B. Harrison (1995), An Integrated Approach to Saturation Height Analysis.

Stiles, J. (1998), Using special core analysis in reservoir engineering.

Sullivan, K. B., and E. F. McBride (1991), Diagenesis of sandstones at shale contacts and diagenetic heterogeneity, Frio Formation, Texas, *AAPG Bulletin*, 75, 121 - 138.

Sundberg, K. (1980), Effect of impregnating waters on electrical conductivity of soils and rocks, *The Log Analyst*, XXI, 19 - 30.

Theys, P. (1991), *Log Data Acquisition And Quality Control*, 330 pp., Editions Technip, Paris.

Thomas, E. C., and S. J. Stieber (1975), The distribution of shale in sandstones and its effect upon porosity, *SPWLA 16th Annual Logging Symposium, Paper T*.

Tiab, D., and E. C. Donaldson (1996), *Petrophysics: Theory and practice of measuring reservoir rock and fluid transport properties*, 706 pp., Gulf Publishing Company, Houston.

Tillman, R. W., and W. R. Almon (1979), Diagenesis of Frontier Formation offshore bar sandstones Spearhead Ranch Field, Wyoming, in *Aspects of Diagenesis*, edited by P. A. Scholle and P. R. Schluger, pp. 337 - 378, SEPM Special Publication No. 26.

Tudge, J., et al. (2009), Petrophysically determined lithofacies at the Nankai Trough Accretionary Prism: NanTroSEIZE, IODP Expedition 314, *Journal of the Geological Society, London*, 166, 961 - 968.

Underdown, R., and J. Redfern (2008), Petroleum generation and migration in the Ghadames Basin, north Africa: A two-dimensional basin-modeling study, *AAPG Bulletin*, 92, 53 - 76.

van Olphen, H., and J. J. Fripiat (Eds.) (1979), *Data handbook for clay materials and other non-metallic minerals*, 346 pp., Pergamon Press.

Velde, B. (1985), *Clay Minerals: A Physico-chemical explanation of their occurrence*, 421 pp., Elsevier.

Velde, B. (1992), *Introduction to clay minerals*, 198 pp., Chapman & Hall.

Welton, J. E. (1984), *SEM Petrology Atlas*, American Association of Petroleum Geologists.

Waxman, M. H., and L. J. M. Smits (1968), Electrical conductivities in oil-bearing shaly sands, *The Society of Petroleum Engineers*, 8, 107-122.

Weibel, R. (1999), Effects of burial on the clay assemblages in the Triassic Skagerrak Formation, Denmark, *Clay Minerals*, 34, 619 - 635.

Welton, J. E. (1984), *SEM Petrology Atlas*, American Association of Petroleum Geologists.

Worthington, P. F. (1985), The Evolution of Shaly-sand concepts in reservoir evaluation, *The Log Analyst*, 26, 23-40.

Worthington, P. F. (2000), Recognition and evaluation of low-resistivity pay, *Petroleum Geoscience*, 6, 77-92.

Worthington, P. F. (2002), Application of Saturation-height Functions in Integrated Reservoir Description, in *Geological Applications of Well Logs: AAPG Methods in Exploration*, No. 13, edited by M. A. Lovell and N. Parkinson, pp. 75-89.

Worthington, P. F. (2004), Characterisation of the intrinsic porosity exponent through dual-salinity measurements of electrical conductivity, *Petrophysics*, 45, 499 - 516.

www.bakerhughesdirect.com Baker Atlas, edited.

www.slb.com Schlumberger, edited.

www.statsoft.com/textbook Statistica Electronic Textbook, edited,
www.statsoft.com.

Wyllie, M. R. J., et al. (1958), An experimental investigation of factors affecting elastic wave velocities in porous media, *Geophysics*, 23, 459 - 493.

Wyllie, M. R. J., et al. (1956), Elastic wave velocities in heterogeneous and porous media, *Geophysics*, 21, 41 - 70.

Xiao, J., et al. (2002), Petrophysics-based Resolution Matching for Induction Logs, in *Geological Applications of well logs: AAPG Methods in Exploration No. 13*, edited by M. A. Lovell and N. Parkinson, pp. 27-38.

Yang, S. L., et al. (2006), Statistical Analysis of Well Logs Compared with Geotechnical Data in Storegga Slide Area *Marine Georesources and Geotechnology*, 24, 237 - 250.

Zhu, Z., et al. (2008), Experimental studies of monopole, dipole, and quadrupole acoustic logging while drilling (LWD) with scaled borehole models, *Geophysics*, 73, E133-E143.